PROTON THERAPY IN CANCER TREATMENTS: CLINICAL EVIDENCE AND CONTROVERSIES

EDITED BY: Jérôme Doyen, Beate Timmermann and Antony John Lomax
PUBLISHED IN: Frontiers in Oncology

frontiers Research Topics

Frontiers eBook Copyright Statement

The copyright in the text of individual articles in this eBook is the property of their respective authors or their respective institutions or funders. The copyright in graphics and images within each article may be subject to copyright of other parties. In both cases this is subject to a license granted to Frontiers.

The compilation of articles constituting this eBook is the property of Frontiers.

Each article within this eBook, and the eBook itself, are published under the most recent version of the Creative Commons CC-BY licence. The version current at the date of publication of this eBook is CC-BY 4.0. If the CC-BY licence is updated, the licence granted by Frontiers is automatically updated to the new version.

When exercising any right under the CC-BY licence, Frontiers must be attributed as the original publisher of the article or eBook, as applicable.

Authors have the responsibility of ensuring that any graphics or other materials which are the property of others may be included in the CC-BY licence, but this should be checked before relying on the CC-BY licence to reproduce those materials. Any copyright notices relating to those materials must be complied with.

Copyright and source acknowledgement notices may not be removed and must be displayed in any copy, derivative work or partial copy which includes the elements in question.

All copyright, and all rights therein, are protected by national and international copyright laws. The above represents a summary only. For further information please read Frontiers' Conditions for Website Use and Copyright Statement, and the applicable CC-BY licence.

ISSN 1664-8714
ISBN 978-2-88974-026-0
DOI 10.3389/978-2-88974-026-0

About Frontiers

Frontiers is more than just an open-access publisher of scholarly articles: it is a pioneering approach to the world of academia, radically improving the way scholarly research is managed. The grand vision of Frontiers is a world where all people have an equal opportunity to seek, share and generate knowledge. Frontiers provides immediate and permanent online open access to all its publications, but this alone is not enough to realize our grand goals.

Frontiers Journal Series

The Frontiers Journal Series is a multi-tier and interdisciplinary set of open-access, online journals, promising a paradigm shift from the current review, selection and dissemination processes in academic publishing. All Frontiers journals are driven by researchers for researchers; therefore, they constitute a service to the scholarly community. At the same time, the Frontiers Journal Series operates on a revolutionary invention, the tiered publishing system, initially addressing specific communities of scholars, and gradually climbing up to broader public understanding, thus serving the interests of the lay society, too.

Dedication to Quality

Each Frontiers article is a landmark of the highest quality, thanks to genuinely collaborative interactions between authors and review editors, who include some of the world's best academicians. Research must be certified by peers before entering a stream of knowledge that may eventually reach the public - and shape society; therefore, Frontiers only applies the most rigorous and unbiased reviews.
Frontiers revolutionizes research publishing by freely delivering the most outstanding research, evaluated with no bias from both the academic and social point of view. By applying the most advanced information technologies, Frontiers is catapulting scholarly publishing into a new generation.

What are Frontiers Research Topics?

Frontiers Research Topics are very popular trademarks of the Frontiers Journals Series: they are collections of at least ten articles, all centered on a particular subject. With their unique mix of varied contributions from Original Research to Review Articles, Frontiers Research Topics unify the most influential researchers, the latest key findings and historical advances in a hot research area! Find out more on how to host your own Frontiers Research Topic or contribute to one as an author by contacting the Frontiers Editorial Office: frontiersin.org/about/contact

PROTON THERAPY IN CANCER TREATMENTS: CLINICAL EVIDENCE AND CONTROVERSIES

Topic Editors:
Jérôme Doyen, Centre Antoine Lacassagne, France
Beate Timmermann, Essen University Hospital, Germany
Antony John Lomax, Paul Scherrer Institut (PSI), Switzerland

Citation: Doyen, J., Timmermann, B., Lomax, A. J., eds. (2022). Proton Therapy in Cancer Treatments: Clinical Evidence and Controversies.
Lausanne: Frontiers Media SA. doi: 10.3389/978-2-88974-026-0

Table of Contents

frontiers in Oncology

EDITORIAL
published: 28 January 2022
doi: 10.3389/fonc.2021.791302

Editorial: Proton Therapy in Cancer Treatment: Clinical Evidence and Controversies

Beate Timmermann *

Department of Particle Therapy, University Hospital Essen, West German Proton Therapy Centre Essen (WPE), West German Cancer Center (WTZ), Germany, German Cancer Consortium (DKTK), Essen, Germany

Keywords: proton therapy, cancer, clinical evidence, treatment, clinical controversies

Editorial on the Research Topic

Proton Therapy in Cancer Treatment: Clinical Evidence and Controversies

INTRODUCTION

When speaking about proton therapy (PT), we typically walk between two lines. On the one hand we have a well-established radiotherapy modality representing a standard method for demanding entities like chordomas and chondrosarcomas of the base of skull and spine as well as uveal melanomas over the last 70 years already. More recently, also childhood cancer was understood to be an important target of PT. On the other hand, we have to acknowledge that there are still significant technical developments in progress to achieve the same standards in image guidance and robustness as are established in photon therapy for quite some time already. Therefore, the drive for further research but also controversies are typically arising either from the quest of getting PT into a broader clinical use for other (and more common) entities or from the ambition to successfully promote further technical progress. This present issue is truly reflecting the current status of proton therapy. It highlights the fact that the clinical role of PT in entities other than chordomas and eye tumours is definitely increasing. Still, this issue also clearly illustrates that physicists are still busy working on optimizing the technical aspects of proton beam therapy in areas like moving targets, robustness and range verification.

The Research Topic covers in total 11 articles on PT reflecting technical, biological and clinical questions. Any broader use of PT will be based on fundamental technical developments, helping to overcome current restrictions and addressing the challenges of a greater extent of uncertainties and the vulnerability of the static dose plan due to range uncertainties or to intrafractional interplay effects. If the superior physical characteristics of PT are supposed to lead to further clinical advantage, efficient control of uncertainties and better understanding of potential plan degradation have to be achieved. It is therefore conclusive that two studies within this Research Topic are focussing on lung tumours being the most challenging targets for proton beam therapy.

Wei et al. present an analysis of methods for mitigating interplay effects. Their retrospective study is focussing on the most modern proton modality, spot scanning proton beam therapy (i.e. pencil beam scanning [PBS]). Here it was used to deliver stereotactic body radiotherapy with repainting after robust 4-D optimization as a strategy to overcome uncertainties resulting from respiratory motion.

Another strategy to safely treat lung tumours by using particle radiation therapy (PRT) is presented by Emert et al., investigating motion-mitigation either by enhanced deep-inspiration breath hold (eDIBH) or

OPEN ACCESS

Edited and reviewed by:
Timothy James Kinsella, Warren Alpert Medical School of Brown University, United States

***Correspondence:**
Beate Timmermann
beate.timmermann@uk-essen.de

Specialty section:
This article was submitted to Radiation Oncology, a section of the journal Frontiers in Oncology

Received: *08 October 2021*
Accepted: *13 October 2021*
Published: *28 January 2022*

Citation:
Timmermann B (2022) Editorial: Proton Therapy in Cancer Treatment: Clinical Evidence and Controversies. Front. Oncol. 11:791302. doi: 10.3389/fonc.2021.791302

high-frequency percussive ventilation (HFPV). Applicability, effectiveness, reproducibility, and subjects' acceptance were assessed and proven to be both effective and feasible.

Besides mitigating interplay effect, also improving lateral penumbra of pencil beam proton therapy is of major concern since one of the few disadvantages of active scanned versus passive scattered protons is the inferior lateral dose fall-off as the scanned pencil beams have typical widths larger than 1 cm. Therefore, investigations of adding apertures to PBS proton therapy is of major interest for the community. Bäumer et al. describe the clinical implementation of brass apertures in combination with active scanning proton delivery, proving that sharpening of the beam and improved sparing of organs at risk could be achieved.

The attractive dose distributions of proton fields can only be fully exploited in clinics if the uncertainties of the stopping-power estimation are well under control. Positron emission tomography (PET) range verification was understood as a method that can help to provide the confidence in PT for clinical applications. Zhang et al. implemented two verification methods of off-line PET verification and applied it to clinical breast cancer cases. It turned out, that both methods evaluated could quantify the accuracy of PT to the millimetre level.

Very much alike a summary of the most relevant current issues, Mazal et al. list various limitations of protons in clinical practice, like uncertainties in range, lateral penumbra, deposition of higher LET outside the target, organ movements and eventually cost. In their review, interesting and innovative methods to mitigate those pitfalls are proposed to be further studied, such as "FLASH" irradiation, mini-beams, rotational techniques and, gantry-less treatment approaches.

He also highlights the importance of improving the biological understanding of particle therapy. Therefore, studies like presented by Suckert et al. seem very much appropriate. The authors describe a preclinical model to reveal biological mechanisms caused by precise high-dose proton irradiation of a brain sub-volume and try to derive a dose–response model in order to optimise future experiments and to potentially support evaluation of brain toxicity after proton therapy.

In general, in the field of medicine, but particularly in the field of PT, focussing research on clinical needs is of crucial importance, thus delivering positive impact on improved individual patient treatment. Even with fantastic instruments being accessible, we may not always use them in the best way. The study from Sha et al. reflect how new treatment techniques could be realised, by adopting long-used historical strategies. Here, the authors have managed to improve cardiac sparing by separating the PTV of the right and left lung rather than using one PTV on both lungs.

In proton beam therapy, the body of clinical evidence is rapidly growing, also caused by the increasing number of facilities and therefore greater capacity to perform clinical studies. Hence, we could include a number of clinical papers in this Research Topic, both reviews and original studies.

Jazmati and colleagues report on their findings on neuroblastoma from a large prospective paediatric proton registry. In their study, PT was well tolerated and effective in young children with neuroblastoma. The authors still remind us, that any RT has to be regarded in the view of the multidisciplinary treatment regimen and that particularly in very young children open questions remain to be studied in order to balance risks for adverse events against gain in tumour control.

Doyen et al. are dealing with a very different cohort. They reviewed 127 patients with both benign and malignant tumours retrospectively, having received high dose rate pulsed PT with 10 Gy per second. The authors could not reveal a major decrease in acute and subacute toxicity. However, they discuss the need for further investigation and the chances arising from "FLASH" radiotherapy for patients as it was suggested by preclinical studies.

Our Research Topic also includes one clinical review. Weber et al. summarise findings in PT for recurrent and primary meningioma. They conclude that PT is routinely used for treatment of meningiomas and that it may not be limited to volumetrically challenging tumours, non-benign histology or for the re-irradiation of recurrent and progressive tumours. They still state, that some scenarios may need to be discussed on a case by case basis also taking into account age and tumour grading.

Interestingly, the question of patient selection on a case by case basis is also addressed in this Research Topic from a very different, computational perspective. As the area of artificial intelligence and big data has further evolved over time, machine learning may help clinicians in making qualified decisions. Qiu et al. present an original study on predicting outcome for high grade glioma (HGG) patients, by using machine learning to provide a tool of reference for counselling PBS as a treatment option for HGG.

CONCLUDING REMARKS

We are convinced, that the ambition and eagerness to answer the open questions in proton beam therapy - reflected by this Research Topic – will finally lead to a wider PT offered to a higher number of cancer patients in critical scenarios. Besides improving survival rates, also lowering the price of survival is of particular importance for cancer patients. Both are understood as being the fundamental aims when incorporating PT into a wider range of oncological strategies. Still, as the financial effort to offer PT is significantly higher when compared to photon radiotherapy, it will be crucial to gain further clinical evidence in order to convince policy makers.

We are eager to follow the future evolution of PT in science and clinics.

AUTHOR CONTRIBUTIONS

The author confirms being the sole contributor of this work and has approved it for publication.

Conflict of Interest: The author declares that the research was conducted in the absence of any commercial or financial interest.

Publisher's Note: All claims expressed in this article are solely those of the authors and do not necessarily represent those of their affiliated organizations, or those of the publisher, the editors and the reviewers. Any product that may be evaluated in

this article, or claim that may be made by its manufacturer, is not guaranteed or endorsed by the publisher.

Copyright © 2022 Timmermann. This is an open-access article distributed under the terms of the Creative Commons Attribution License (CC BY). The use, distribution or reproduction in other forums is permitted, provided the original author(s) and the copyright owner(s) are credited and that the original publication in this journal is cited, in accordance with accepted academic practice. No use, distribution or reproduction is permitted which does not comply with these terms.

frontiers in Oncology

ORIGINAL RESEARCH
published: 09 October 2020
doi: 10.3389/fonc.2020.574605

Mitigation of the Interplay Effects of Combining 4D Robust With Layer Repainting Techniques in Proton-Based SBRT for Patients With Early-Stage Non-small Cell Lung Cancer

Long Wei[1†], Haijiao Shang[2,3,4†], Fu Jin[5*] and Yuenan Wang[6]*

[1] School of Computer Science and Technology, Shandong Jianzhu University, Jinan, China, [2] Shanghai Institute of Applied Physics, Chinese Academy of Sciences, Shanghai, China, [3] University of Chinese Academy of Sciences, Beijing, China, [4] RaySearch, Shanghai, China, [5] Department of Radiation Oncology, Chongqing University Cancer Hospital, Chongqing Cancer Hospital, Chongqing Cancer Institute, Chongqing, China, [6] Department of Radiation Oncology, National Cancer Center, National Clinical Research Center for Cancer, Cancer Hospital & Shenzhen Hospital, Chinese Academy of Medical Sciences, Peking Union Medical College, Shenzhen, China

Objective: The objective of this study was to evaluate the interplay effects in proton-based stereotactic body radiotherapy (SBRT) using 4D robust optimization combined with iso-energy layer repainting techniques for non-small cell lung cancer (NSCLC).

Materials and Methods: Twelve patients with early-stage NSCLC who underwent 4DCT were retrospectively selected. A robust CTV-based 4D plan was generated for each based on commercial Treatment planning system (TPS), considering patient setup errors, range uncertainties, and organ motion. The 4D static dose (4DSD) and 4D dynamic dose (4DDD) were calculated using a hybrid deformable algorithm and simulated proton delivery system. An index $\Delta I_M^R(\%)$ was developed to quantitatively evaluate the interplay effects. The interplay effects of the 4D robust plan and multiple iso-energy layers (3, 4, 5, 6, and 7) of the robust repainting 4D plan were calculated based on $\Delta I_M^R(\%)$ to select the optimal times for layer repainting.

Results: Due to the interplay effects, the mean target values D_2 and D_5 increased to 1.28 and 1.01%, and the target values D_{98} and D_{95} decreased to 2.01 and 1.77%, respectively, for the 4D Robust SBRT plan. After multiple iso-energy repainting times, the interplay effects of the target values D_{98} and D_{95} tended to migrate, from 2.01 to 0.92% in target value D_{98} and from 1.77 to 0.89% in target value D_{95}, respectively. Moreover, a positive linear correlation was observed between the optimal interplay effect mitigation and target range of motion.

OPEN ACCESS

Edited by:
Antony John Lomax, Paul Scherrer Institut (PSI), Switzerland

Reviewed by:
Sergio Jaramillo, Willis-Knighton Cancer Center, United States
Tsair-Fwu Lee, National Kaohsiung University of Science and Technology, Taiwan

***Correspondence:**
Haijiao Shang
haijiao.shang@raysearchlabs.com
Fu Jin
jfazj@126.com

† These authors have contributed equally to this work

Specialty section:
This article was submitted to Radiation Oncology, a section of the journal Frontiers in Oncology

Received: *20 June 2020*
Accepted: *15 September 2020*
Published: *09 October 2020*

Citation:
Wei L, Shang H, Jin F and Wang Y (2020) Mitigation of the Interplay Effects of Combining 4D Robust With Layer Repainting Techniques in Proton-Based SBRT for Patients With Early-Stage Non-small Cell Lung Cancer. Front. Oncol. 10:574605. doi: 10.3389/fonc.2020.574605

Conclusion: In proton-based 4D Robust SBRT, the interplay effects degraded the target dose distribution but were mitigated using iso-energy layer repainting techniques. However, there was no significant correlation between the number of repainting layers and improvements in the dose distributions. The optimal layer repainting times based on the interplay effect index were ascertained according to the patient characteristics.

Keywords: lung cancer, proton SBRT, 4D robust optimization, interplay effects, layer repainting

INTRODUCTION

Proton spot scanning-based stereotactic body radiotherapy (SBRT) has been shown to outperform photon-based SBRT in patients with early-stage non-small cell lung cancer (NSCLC). Proton has a superior Bragg peak increasing the dose delivered to tumors and sparing healthy organs, such as the lungs, esophagus, and spinal cord (1, 2). However, patient setup errors and range and target motion uncertainties must be addressed to make full use of the advantages of proton-based SBRT for lung cancer (3).

The motion of lung tumors has been evaluated based on 4DCT imaging. Most lung tumors have limited motion, less than 5 mm, especially in locally advanced NSCLC (4). Patient setup and range uncertainties are the primary factors to consider during IMPT planning. In early-stage NSCLC, approximately 50% of lung tumors move more than 5 mm and some even move more than 2 cm in the superior–inferior direction (5), where interplay effects caused by the interference between the beam spot and intra-fractional respiratory motion is dominant and should be taken into account. Otherwise, the quality of the dose distribution can be severely degraded. The effects should be minimized as much as possible. Robust optimization combining with 4DCT imaging (4DRP) (6, 7) mitigates the interplay effects. The appropriate repainting strategy (8, 9) can also manage the interplay effects. However, there are few clinical reports on the effectiveness of combining 4DRP and repainting with proton-based SBRT for IMPT in patients with early-stage NSCLC. Moreover, an interplay index for quantitative evaluation is needed to assess the effectiveness of combining 4DRP and repainting. The interplay effects can be estimated by calculating the single-fraction 4D static dose (4DSD) and single-fraction 4D dynamic dose (4DDD) based on 4DCT images (10, 11). The 4DSD is calculated based on the assumption that the tumor moves in 4DCT images without considering the delivery system's time dependence. The 4DDD is calculated by taking into account the delivery system's time dependence. However, this method is not very intuitive and cannot provide changes in the target volume or organs at risk (OARs), such as target conformity, homogeneity, and OAR volume dosimetry.

In the current study, a 4D Robust plan was generated for selected patients. The interplay effects were quantitatively evaluated using a target index and OAR index. A multiple iso-energy layer repainting strategy was also used to further mitigate the interplay effects to explore the optimal mitigation outcomes.

Abbreviations: 4DDD, 4D dynamic dose; 4DRP, 4D robust optimization plans; 4DSD, 4D static dose; CTVs, clinical target volumes; DIR, deformable image registration; DVF, deformation vector field; IMPT, intensity-modulated proton therapy; ITVs, internal target volumes; NSCLC, non-small cell lung cancer; OARs, organs at risk; SBRT, stereotactic body radiotherapy.

MATERIALS AND METHODS

Patient Characteristics

A total of 12 patients with early-stage (IA/IB) NSCLC were selected for this study, which was approved by the local institutional research review board. The clinical target volumes (CTVs) were contoured by the attending radiation oncologists at each 4DCT phase. The internal target volumes (ITVs) were created by encompassing the extent of 10 CTV motions in 10 4DCT phases. The patients' information is summarized in **Table 1**. The inclusion criteria were as follows: (i) the tumor was small with no distant metastasis, each <5 cm in diameter, (ii) the patients' body surface was more than 4 cm away from the tumor and did not require the use of a range shifter, and (iii) the patients underwent specialized respiratory training to maintain a stable respiratory cycle for approximately 3–5 s.

Target Range of Motion

The target range of motion was obtained by calculating the maximum deformation vector lengths (DVLs) in the target area (9, 12). The maximum inhale phase T_0 and maximum exhale phase T_{50} were used for deformable image registration (DIR) (13) to obtain the DVL. The DIR algorithm was developed by RaySearch and performs well in lung applications (14). Voxels in the CTVs were selected and the target range of motion was calculated according to the DVL formula:

$$DVL_i = \sqrt{(x_{T_{0,i}} - x_{T_{50,i}})^2 + (y_{T_{0,i}} - y_{T_{50,i}})^2 + (z_{T_{0,i}} - z_{T_{50,i}})^2}$$

where $x_{T_{0,i}} - x_{T_{50,i}}, y_{T_{0,i}} - y_{T_{50,i_i}}, z_{T_{0,i}} - z_{T_{50,i}}$ are the components in voxel i of the deformation vector field between the T_0 and T_{50} phase images in the 4DCT images.

4D Robust Treatment Planning

Spot Scanning SBRT

Pencil beam scanning proton plans were generated for the patients via RayStation (RaySearch Laboratories, Version 6.1 sp1, Stockholm, Sweden) using proton energies between 70 and 225 MeV with beam data from a typical pencil beam scanning dedicated nozzle manufactured by IBA (Ion Beam Applications S.A., Louvain-la-Neuve, Belgium). The spot sizes at the iso-center in air varied between 2.5 mm at 225 MeV and 6.8 mm at 70 MeV. At least greater than 95% of the CTV received a prescribed dose of 60 Gy [RBE] in five fractions. Two or three suitable oblique

TABLE 1 | Summary of patient characteristics including tumor location, size, and motion range.

Patient No.	Diagnosis	CTV Volume (Mean ± SD)	Breathing Period(s)	Motion Range (DVF) (cm)
1	NSCLC/IB	40.1 ± 1.67 (cc)	4.2	0.75
2	NSCLC/IA	20.4 ± 1.35 (cc)	4.5	1.02
3	NSCLC/IA	10.5 ± 0.61 (cc)	3	1.12
4	NSCLC/IA	10.3 ± 0.65 (cc)	3.5	1.62
5	NSCLC/IB	22.3 ± 0.71 (cc)	3.8	1.08
6	NSCLC/IA	23.2 ± 1.56 (cc)	3.6	1.27
7	NSCLC/IA	20.9 ± 1.18 (cc)	3.8	0.84
8	NSCLC/IA	21.7 ± 0.56 (cc)	4.2	0.57
9	NSCLC/IA	28.3 ± 0.56 (cc)	4.8	0.68
10	NSCLC/IA	13.8 ± 1.75 (cc)	3.9	1.35
11	NSCLC/IA	20.3 ± 0.66 (cc)	4.8	0.68
12	NSCLC/IB	36.4 ± 1.25 (cc)	4.5	0.75
Median (Range)		21.3 (10.3–40.1)	4.05	0.93

coplanar beams were used for the plan with the beam direction according to the tumor location. Then, a 4D Robust optimization algorithm (7) was used based on the 4DCT images considering the patient setup, range uncertainties, and target motion. Before optimization, the minimum and maximum spot weights were 0.02 and 4 MU, respectively.

Uncertainty Modeling

Proton-based SRBT is sensitive to the patient setup, range uncertainties, and organ motion, so all of the uncertainties should be considered in the model. Inter-fractional patient setup uncertainties were simulated by shifting the patient iso-center in the antero–posterior (A–P), superior–inferior (S–I), and right–left (R–L) directions by 5 mm, yielding six dose distributions and the corresponding influence matrices (the beamlet dose distributions per unit intensity). Range uncertainties were simulated by scaling the stopping power ratios by ±3.5% to generate two additional dose distributions and influence matrices corresponding to the minimum and maximum proton ranges, respectively. The organ motion uncertainty was considered using 4DCT images consisting of 10 respiratory cycle phases to generate 10 dose distributions with each respiratory cycle phase.

4D Robust Optimization

The 4D Robust optimization plans (4DRP) were generated by optimizing the CTV dose in 10 4DCT phases considering the modeling uncertainties. Robust optimization taking into account the set S of scenarios was implemented using minimax optimization (15). The objective function was

$$min_{x\in X} max_{s\in S} \sum_{i=1}^{n} w_i f_i \left(d\left(x; s\right)\right)$$

where X is the set of feasible variables (spot weights for spot scanning IMPT), $d\left(x; s\right)$ is the dose distribution as a function of variable x, scenario s, and $f_i$is the i structure's penalty function. The robust optimization objective were used in CTV with a minimum dose objective of 60 Gy [RBE] (weight 100) and a maximum dose objective of 60 Gy [RBE] (weight 60). A dose fall-off function from 60 Gy [RBE] to 10 Gy [RBE] over 1 cm (weight 10) was used to lower the dose to the normal tissue as much as possible. The equivalent uniform dose (EUD) (16) on the normal lung was approximately 5 Gy [RBE] with a dose volume effect parameter of 1 (A = 1). In the final dose calculation, the Monte Carlo dose engine was used with 0.5% statistical uncertainty and a 3 mm× 3 mm× 3 mm dose grid resolution.

Interplay Effect Calculation

An overview of the interplay effect process is shown in **Figure 1**. The black flowchart shows how the 4DSD was produced, while the blue flowchart shows how the 4DDD was produced.

The quantitative interplay effect index was represented by the differences in the DVH metrics (ΔI_M^R) between 4DSD and 4DDD over 4DSD for each region of interest (ROI).

$$\Delta I_M^R\,(\%) = \frac{4\mathrm{DDD}\left[\mathrm{DVH}_M^R\right] - 4\mathrm{DSD}\left[\mathrm{DVH}_M^R\right]}{4\mathrm{DSD}\left[\mathrm{DVH}_M^R\right]} \times 100\%$$

where $4\mathrm{DSD}\left[\mathrm{DVH}_M^R\right]$ and $4\mathrm{DDD}\left[\mathrm{DVH}_M^R\right]$ are specific DVH metrics for one ROI in the 4DSD distribution or 4DDD distribution. $4\mathrm{DSD}\left[\mathrm{D}_{95\%}^{\mathrm{CTV}}\right]$ represents the 4DSD at 95% of the CTV volume. If the value of ΔI_M^R was positive, the DVH metrics increased in the 4DDD distribution and vice versa.

We used the CTV and lung minus ITV (lung – ITV) as the ROIs to obtain the quantitative interplay effects. The DVH metrics in the CTV included the minimum target dose (D_{98}[cGy(RBE)]: dose at 98% of the target volume), prescription dose (D_{95}[cGy(RBE)]: dose at 95% of the target volume), and maximum dose (D_2[cGy(RBE)]: dose at 2% of the target volume). The target EUD (A = 10) metrics were also included for interplay evaluation. For lung – ITV, the DVH metrics of the lungs included V_5, V_{20}, and V_{30}, which were the percentage volume of lungs receiving 500 cGy [RBE], 2000 cGy [RBE], and 3000 cGy [RBE], respectively. The lung – ITV average dose and EUD (A = 1.2) (17) were also calculated for evaluation.

Iso-Energy Layer Repainting

The repainting strategy used for the 4D robust plans was layered repainting, where each energy layer is rescanned several times before switching to the next energy level. Zenklusen et al. (8)

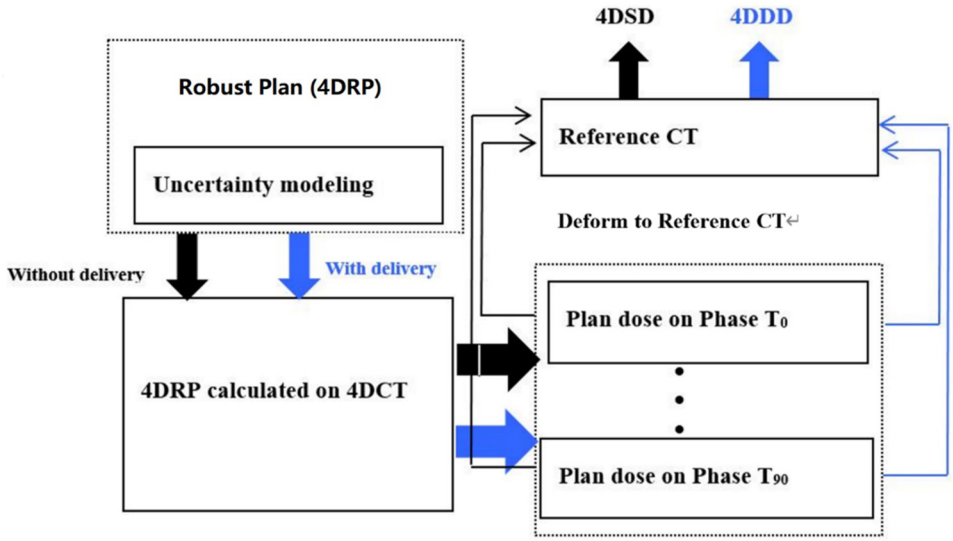

FIGURE 1 | Flowchart of the 4D static dose (4DSD) and 4D dynamical Dose (4DDD) for 4D robustly SBRT plan.

proposed two different methods to divide a plan into layers: scaled and iso-layered repainting. Scaled repainting involves simply dividing each layer in a present number of layers. In contrast, in iso-layered repainting, the MU per spot is limited by the maximum value. In this study, we segmented 4DRP by scaling the repainting 3, 4, 5, 6, or 7 times and obtained new repainting plans called 4DRP-SN3, 4DRP-SN4, 4DRP-SN5, 4DRP-SN6, and 4DRP-SN7, respectively. The layers were divided with respect to the minimum MU per spot, which means that some spots with the same energy levels consecutively contained fewer and fewer spots, but the minimum number of spots was not smaller than the limited minimum MU per spot. For the current study, the machine's minimum MU (0.02 MU) was used during the division to ensure that all of the spots in the rescans were directly deliverable.

The optimal interplay effect mitigation in the 12 patients was assessed by comparing the value of interplay effect index $\Delta I_{D_{98}}^{CTV}$ and $\Delta I_{D_{95}}^{CTV}$ to obtain the minimum index of $\Delta I_{D_{98}}^{CTV}$ and $\Delta I_{D_{95}}^{CTV}$ over five different iso-energy repainting plans. In other words, the smaller the interplay effect index, the better the interplay effect mitigation outcome.

Statistical Analysis

Student's *t*-test was used to compare the following results between 4DRP(**SN3**), 4DRP(**SN4**), 4DRP(**SN5**), 4DRP(**SN6**), and 4DRP(**SN7**), respectively: (1) the interplay effect in the target DVH metrics (D_2, D_5, D_{95}, D_{98}, and Target EUD) and (2) the interplay effect in lung minus ITV DVH metrics (V_5, V_{20}, V_{30}, and EUD); $p < 0.05$ was considered statistically significant. We compared (1) and (2) to investigate whether increasing the number repainting layers mitigated the interplay effects in the target and lungs. A linear regression model was used to evaluate the correlation between the optimal interplay mitigation vs. the tumor range of motion. This study was conducted using a linear model created with Excel software version (v.2016, Microsoft, Redmond, WA, United States)[1] to predict the correction.

RESULTS

Interplay Effects of the 4DRP

As shown in **Figure 2**, the DVH target and OAR metrics changed in the 4D robust plan due to the interplay effects. Targets D_2 and D_5 increased while D_{98} and D_{95} obviously decreased.

The mean value of $\Delta I_{D_2}^{CTV}$ and $\Delta I_{D_5}^{CTV}$ increased to 1.28 and 1.01% according to the interplay index, and $\Delta I_{D_{98}}^{CTV}$ and $\Delta I_{D_{95}}^{CTV}$ decreased to 2.01 and 1.77%, respectively. For the OARs, the mean value of $\Delta I_{V_5}^{Lung}$, $\Delta I_{V_{20}}^{Lung}$, and $\Delta I_{V_{30}}^{Lung}$ increased less than 1%.

Interplay Effects After Repainting

Using patient #2's treatment plan as an example, the 4DSD distribution, 4DDD distribution of the 4DRP, and 4DDD distributions of the 4DRP(**SN3**), 4DRP(**SN4**), 4DRP(**SN5**), 4DRP(**SN6**), and 4DRP(**SN7**) were investigated. In the 4DSD distribution, the isodose line of the prescription dose (PD) basically covered the tumor volume (**Figure 3a**). Considering the interplay effects, the distribution of the dose lines markedly deteriorated, and the PD isodose lines failed to cover the target area (**Figure 3b**). Further executing the repainting at different layer repainting times, the target area was again covered by the isodose lines of the PD dose lines (**Figures 3c–g**). No significant changes occurred in the isodose lines of the lungs.

Figure 4 shows the static interplay effect index in the target and lung DVH metrics. The interplay effect index $\Delta I_{D_{98}}^{CTV}$ and $\Delta I_{D_{95}}^{CTV}$ decreased as the number of layers increased

[1]https://www.microsoft.com

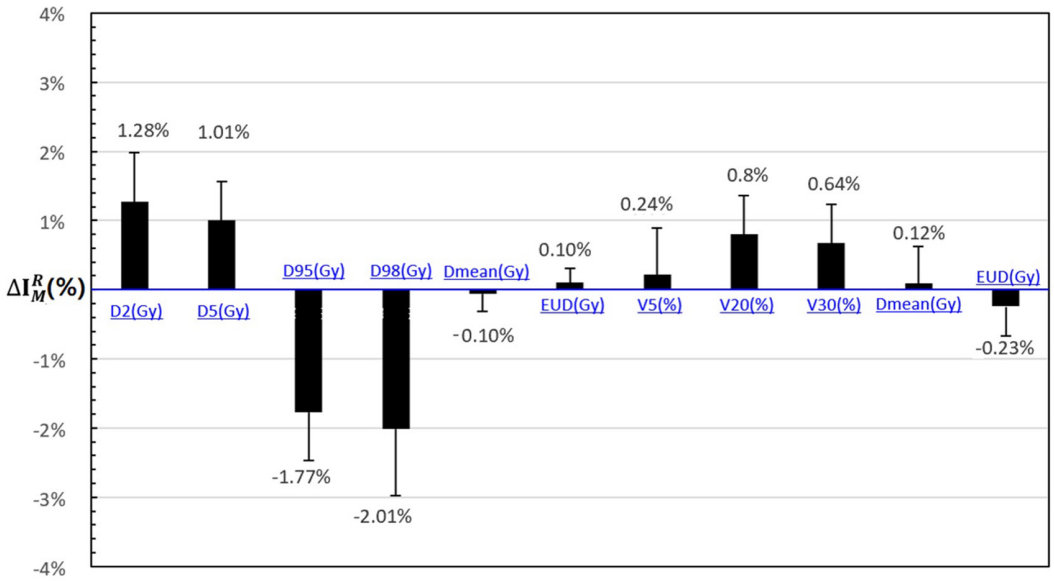

FIGURE 2 | The statistical difference with DVH metrics of interplay index between 4D static dose (4DSD) and 4D dynamical dose (4DDD) for all the patients.

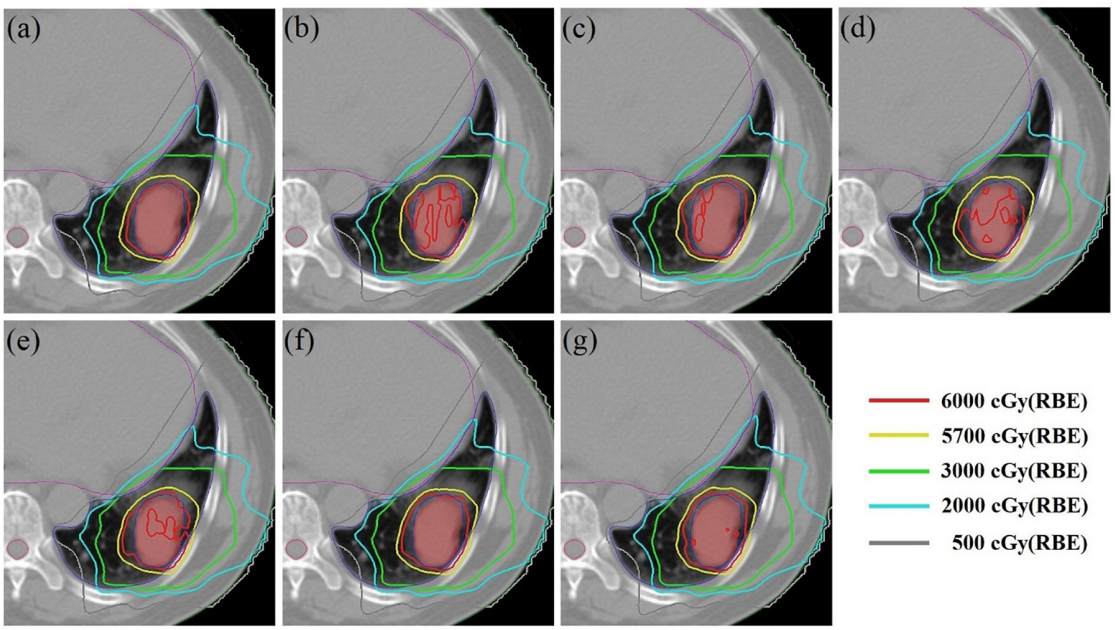

FIGURE 3 | The 4D static dose distribution 4DSD **(a)** and 4D dynamical dose distribution 4DDD **(b)** in the transverse plane for patient #2 of the 4D robust plan 4DRP and 4DDD in the five numbers of layer repainting plan based on 4DRP, marked as 4DRP(SN3) **(c)**, 4DRP(SN4) **(d)**, 4DRP(SN5) **(e)**, 4DRP(SN6) **(f)**, and 4DRP(SN7) **(g)**. The target CTV is red filled and PD line is 6000 cGy (Red), shown as the legend from the dose line.

(**Figure 4A**). Specifically, the mean values of $\Delta I_{D_{98}}^{CTV}$ were 2.01, 1.48, 1.21, 1.03, 1.01, and 0.92% and the mean values of $\Delta I_{D_{95}}^{CTV}$ were 1.77, 1.42, 1.13, 1.01, 0.91, and 0.89% for 4DRP(**SN3**), 4DRP(**SN4**), 4DRP(**SN5**), 4DRP(**SN6**), and 4DRP(**SN7**), respectively. Compared to $\Delta I_{D_{95}}^{CTV}$ and $\Delta I_{D_{98}}^{CTV}$ in 4DRP, 4DRP(**SN3**) was lower, with a significant difference ($p < 0.05$), whereas no significant differences in the other metrics were observed in the target. In the normal tissue lung, as shown in **Figure 4B**, the interplay effect index $\Delta I_{V_5}^{Lung}$ and $\Delta I_{V_{20}}^{Lung}$ increased when three layers repainting was conducted on 4DRP. The average value was 3% for 4DRP vs. 4.5% for 4DRP(**SN3**) in $\Delta I_{V_5}^{Lung}$ and 3.4% for 4DRP vs. 5.1% for 4DRP(**SN3**) in $\Delta I_{V_{20}}^{Lung}$, but no significant difference was observed when the number of iso-energy layers was more than three.

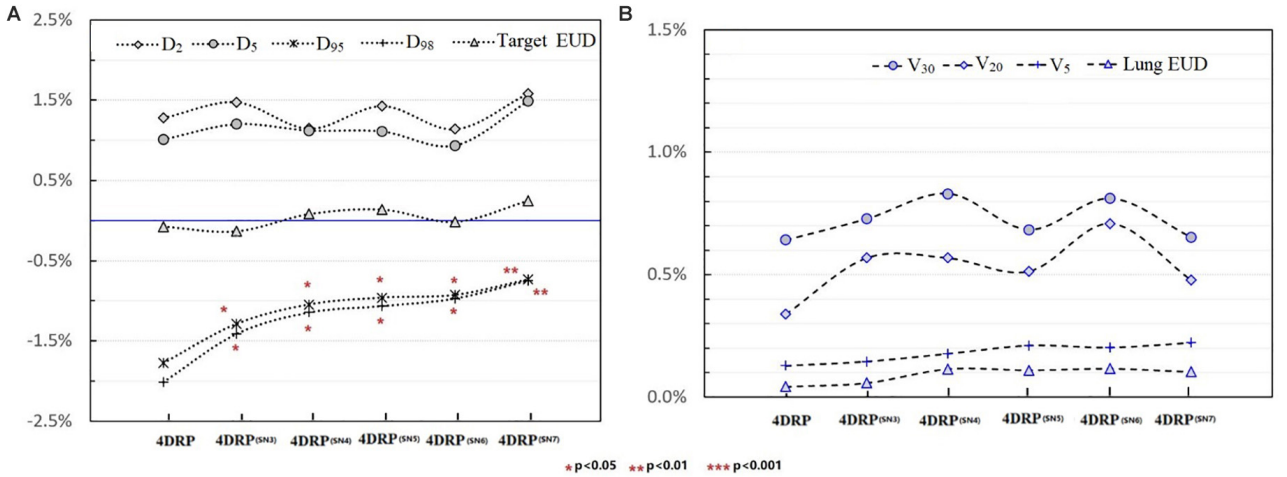

FIGURE 4 | (A) The tendency of interplay effect index on DVH metrics of target and **(B)** shows the tendency of interplay effect index of OAR.

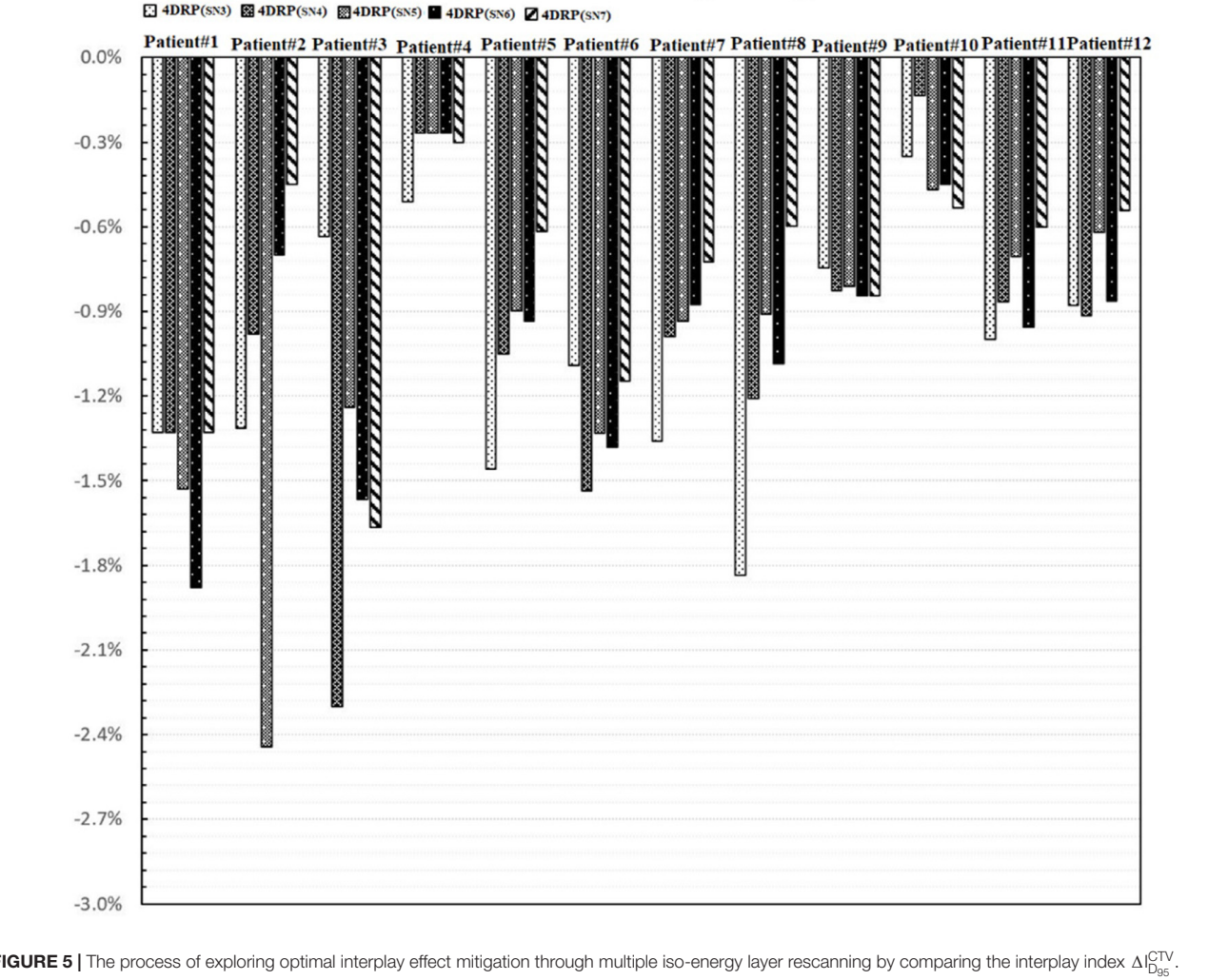

FIGURE 5 | The process of exploring optimal interplay effect mitigation through multiple iso-energy layer rescanning by comparing the interplay index $\Delta I_{D_{95}}^{CTV}$.

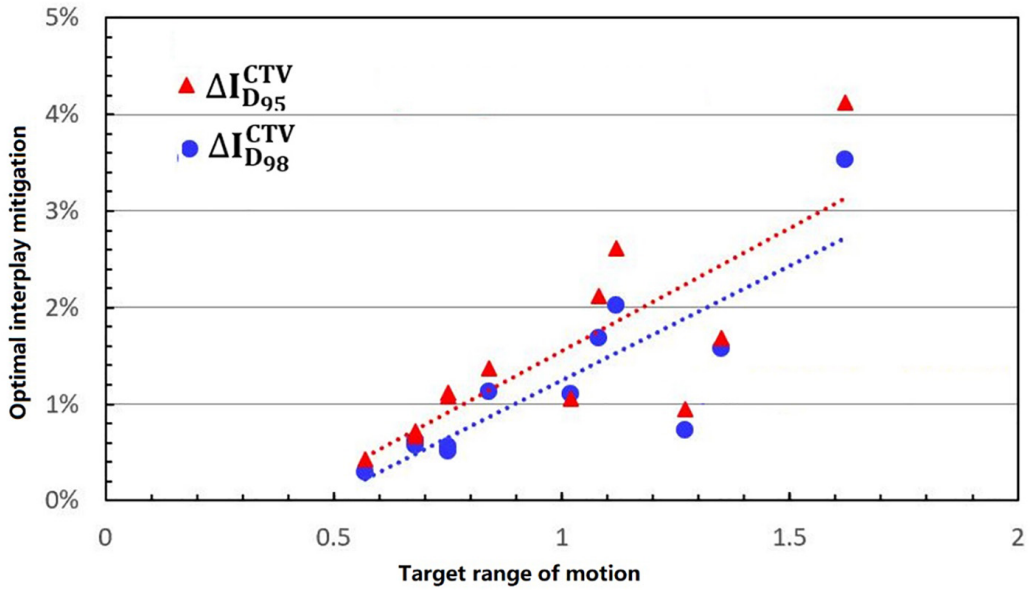

FIGURE 6 | The linear relationship between the optimal interplay effect mitigation on target (D95, D98) and motion range.

Relationship Between the Optimal Interplay Effect Mitigation and Target Range of Motion

Figure 5 shows the process of exploring optimal interplay effect mitigation via multiple iso-energy layer repainting for target coverage metrics. The optimal interplay effect mitigation was attained by comparing the ΔI_{D95}^{CTV} index among 4DRP(**SN3**), 4DRP(**SN4**), 4DRP(**SN5**), 4DRP(**SN6**), and 4DRP(**SN7**) with the smallest absolute value. Then, a statistical correlation study was conducted to evaluate the correlation between the optimal interplay mitigation and target range of motion that showed a linear relationship between the two (**Figure 6**). For ΔI_{D98}^{CTV}, the expression was $\Delta I_{D98}^{CTV} = 2.25DVF - 0.75$, $(R^2 = 0.63)$, while for ΔI_{D95}^{CTV}, it was $\Delta I_{95}^{CTV} = 2.21DVF - 1.12$, $(R^2 = 0.73)$, where DVF is the maximum deformation vector field or target range of motion. A positive correlation was observed between the optimal interplay effect index and target range of motion.

DISCUSSION

4D Robust optimization has been proven to mitigate the interplay effects of IMPT planning and can make the difference between the planned dose and delivery dose less than the established criterion (for example, 3%) (18). However, compared to conventional IMPT planning, proton-based SBRT has led to more consideration of the interplay effects and should have strict standards (19). Therefore, it might be ineffective to rely only on 4D Robust optimization alone to mitigate the interplay effects. Thus, we proposed 4D Robust optimization combined with an iso-energy layer repainting strategy in early-stage NSCLC patients.

In the current study, 4D robust plans were evaluated based on the quantitative interplay index for patients with early-stage NSCLC. The results showed that the target coverage decreased due to the interplay effects (**Figures 2**, **3**). Multiple iso-energy layer repainting was subsequently used to mitigate the interplay effects. The target coverage increased as the number of iso-energy repainting layers increased (**Figure 4**), but this was not applicable for specific patients. Therefore, the optimal iso-energy repainting times were explored based on the quantitative interplay index. A positive linear relationship occurred between the optimal interplay effect mitigation and target range of motion. Our results confirmed that 4D Robust optimization combined with iso-energy layer repainting technology further mitigated the interplay effects, which has important clinical significance.

The motion of lung tumors was evaluated based on 4DCT images. Only 35 to 39% of the tumors moved more than 5 mm in locally advanced NSCLC, but the percentage increased to 50% for early-stage NSCLC (5). In the current study, the target range of motion was assessed using the maximum DVLs of the DIR within the target. The results showed that all of the patients had a more than 5-mm range of motion, which was also evaluated by the difference between the ITV volume and mean CTV volume over all phases (the CTV change rate in the 4DCT images). **Figure 6** shows that there was a positive linear relationship between the tumor range of motion and CTV change rate. Thus, the target range of motion was obtained based on the differences in the ITV and CTV contours in the 4DCT images. DIR errors should be considered. Anaconda, implemented in RayStation, is a hybrid method utilizing a combination of image intensities and controlling structures from contoured image sets (13). Anaconda demonstrates a good performance in the thoracic region compared to other commercially available algorithms based on previous studies (14).

In practice, when using spot scanning, the number of spot rescans should be proportional to the patients' spot weights in a range of motion up to 5 mm. However, the optimal number of repainting layers remains debatable due to patient- and machine-specific parameters, such as the patient breathing cycle, energy switch times, and other factors (20). Seco et al. (21) investigated a phase-controlled repainting and breathing-sampled strategy in which the number of rescans was decided using a motion-monitoring system. Engwall et al. (9) investigated offline breath-sampled layered repainting methods in which the number of iso-energy layers was spread uniformly throughout the breathing cycle, the optimal method of mitigating interplay effects. In the current study, multiple iso-energy layer repainting times were used to explore the optimal number of interplay mitigation rescans based on the quantitative metrics (**Figure 5**). A positive linear correlation occurred between the optimal interplay effect mitigation and target range of motion, demonstrating that breathing motions are dominated by the interplay effect.

One limitation of this study was associated with the method of simply dividing each layer in the present number of layers, which resulted in small weighted spots that might have been deleted after multiple iso-energy rescans. The dose distribution before and after the iso-energy rescans was compared to avoid this scenario in this study.

CONCLUSION

In proton-based SBRT, interplay effects degrade the target dose distribution and can be mitigated using iso-energy layer repainting techniques. However, in this study, there was no significant correlation between the number of repainting layers and improvement in the dose distributions. We recommend using the optimal layer repainting times based on the interplay effect index according to the patient characteristics.

DATA AVAILABILITY STATEMENT

The raw data supporting the conclusion of this article will be made available by the authors, without undue reservation.

ETHICS STATEMENT

Ethics approval for this study was obtained from the Chongqing University Cancer Hospital's Ethics Committee. All patients gave written informed consent, and all methods were performed in accordance with the relevant guidelines and regulations.

AUTHOR CONTRIBUTIONS

HS conceived and designed the study, and collected and sorted the data. LW and HS wrote the manuscript. LW carried out the experiments, data analysis, and statistical analysis with guidance from HS. FJ and YW assisted with statistical analysis. All authors edited the manuscript, and critically reviewed and approved the manuscript.

FUNDING

This work was supported by the National Natural Science Foundation of China under grant nos. 11575038 and 11805025. and the Doctoral Research Fund of Shandong Jianzhu University, grant number X20070Z0101.

REFERENCES

1. Bush DA, Cheek G, Zaheer S, Wallen J, Mirshahidi H, Katerelos A, et al. High-dose hypo-fractionated proton beam radiation therapy is safe and effective for central and peripheral early-stage non-small cell lung cancer: results of a 12-year experience at Loma Linda University Medical Center. *Int J Radiat Oncol Biol Phys.* (2013) 86:964–8. doi: 10.1016/j.ijrobp.2013.05.002
2. Makita C, Nakamura T, Takada A, Takayama K, Suzuki M, Azami Y, et al. High-dose proton beam therapy for stage I non-small cell lung cancer: clinical outcomes and prognostic factors. *Acta Oncologica.* (2015) 54:307–14. doi: 10.3109/0284186X.2014.948060
3. Paganetti H. Range uncertainties in proton therapy and the role of Monte Carlo simulations. *Phys Med Biol.* (2012) 57:R99. doi: 10.1088/0031-9155/57/11/R99
4. Liu HH, Balter P, Tutt T, Choi B Zhang J, Wang C, et al. Assessing respiration-induced tumor motion and internal target volume using four-dimensional computed tomography for radiotherapy of lung cancer. *Int J Radiat Oncol Biol Phys.* (2007) 68:531–40. doi: 10.1016/j.ijrobp.2006.12.066
5. Yu ZH, Lin SH, Balter P, Zhang L, Dong L. A comparison of tumor motion characteristics between early stage and locally advanced stage lung cancers. *Radiother Oncol.* (2012) 104:33–8. doi: 10.1016/j.radonc.2012.04.010
6. Wei L, Schild SE, Chang JY, Liao Z, Liu Z, Li H, et al. Impact of respiratory motion on worst-case scenario optimized intensity modulated proton therapy for lung cancers. *Int J Radiat Oncol Biol Phys.* (2016) 95:523–33.
7. Engwall E, Fredriksson A, Glimelius L. 4D robust optimization including uncertainties in time structures can reduce the interplay effect in proton pencil beam scanning radiation therapy. *Med Phys.* (2018a) 45:4020–29. doi: 10.1002/mp.13094
8. Zenklusen SM, Pedroni E, Meer D. A study on repainting strategies for treating moderately moving targets with proton pencil beam scanning at the new gantry 2 at PSI. *Phys Med Biol.* (2010) 55:5103–512. doi: 10.1088/0031-9155/55/17/014
9. Engwall E, Glimelius L, Hynning E. Effectiveness of different rescanning techniques for scanned proton radiotherapy in lung cancer patients. *Phys Med Biol.* (2018b) 63:095006. doi: 10.1088/1361-6560/aabb7b
10. Kardar L, Li Y, Li X, Li H, Cao W, Chang JY, et al. Evaluation and mitigation of the interplay effects of intensity modulated proton therapy for lung cancer in a clinical setting. *Pract Radiat Oncol.* (2014) 4:e259–68. doi: 10.1016/j.prro.2014.06.010
11. Yu J, Zhang X, Liao L, Li H, Zhu R, Park PC, et al. Motion-robust intensity-modulated proton therapy for distal esophageal cancer. *Med Phys.* (2016) 43:1111. doi: 10.1118/1.4940789
12. Inoue T, Widder J, van Dijk LV, Takegawa H, Li H, Zhu R, Park PC, et al. Limited impact of setup and range uncertainties, breathing motion, and Interplay effects in robustly optimized intensity modulated proton therapy for stage III non-small cell lung cancer. *Int J Radiation Oncol Biol Phys.* (2016) 96:661–9. doi: 10.1016/j.ijrobp.2016.06.2454

13. Weistrand O, Svensson S. The anaconda algorithm for deformable image registration in radiotherapy. *Med Phys.* (2015) 42:40–53. doi: 10.1118/1.4894702
14. Kadoya N, Nakajima Y, Saito M, Miyabe Y, Kurooka M, Kito S, et al. Multi-institutional validation study of commercially available deformable image registration software for thoracic images. *Int J Radiat Oncol Biol Phys.* (2016) 96:422–31. doi: 10.1016/j.ijrobp.2016.05.012
15. Fredriksson A, Forsgren A, Hardemark B. Minimax optimization for handling range and setup uncertainties in proton therapy. *Med Phys.* (2011) 38:1672–84. doi: 10.1118/1.3556559
16. Niemierko A. A generalized concept of equivalent uniform dose (EUD). *Med Phys.* (1999) 26:1100.
17. D'Andrea M, Strolin S, Ungania S, Cacciatore A, Bruzzaniti V, Marconi R, et al. Radiobiological optimization in lung stereotactic body radiation therapy: are we ready to apply radiobiological models. *Front Oncol.* (2018) 7:321. doi: 10.3389/fonc.2017.00321
18. Chang JY, Zhang X, Knopf A, Li H, Mori S, Dong L, et al. Consensus guidelines for implementing pencil-beam scanning proton therapy for thoracic malignancies on behalf of the PTCOG thoracic and lymphoma subcommittee. *Int J Radiat Oncol Biol Phys.* (2017) 99:41–50. doi: 10.1016/j.ijrobp.2017.05.014
19. Madhava RK, Neil D, Shankar PG. Stereotactic body radiation therapy in lung. *Transl Cancer Res.* (2015) 4:435–48.
20. Schatti A, Zakova M, Meer D, Lomax AJ. Experimental verification of motion mitigation of discrete proton spot scanning by re-scanning. *Phys Med Biol.* (2013) 58:8555–72. doi: 10.1088/0031-9155/58/23/8555
21. Seco J, Robertson D, Trofimov A, Paganetti H. Breathing interplay effects during proton beam scanning: simulation and statistical analysis. *Phys Med Biol.* (2009) 54:N283. doi: 10.1088/0031-9155/54/14/N01

Conflict of Interest: HS was employed by the company RaySearch.

The remaining authors declare that the research was conducted in the absence of any commercial or financial relationships that could be construed as a potential conflict of interest.

Copyright © 2020 Wei, Shang, Jin and Wang. This is an open-access article distributed under the terms of the Creative Commons Attribution License (CC BY). The use, distribution or reproduction in other forums is permitted, provided the original author(s) and the copyright owner(s) are credited and that the original publication in this journal is cited, in accordance with accepted academic practice. No use, distribution or reproduction is permitted which does not comply with these terms.

frontiers in Oncology

ORIGINAL RESEARCH
published: 30 October 2020
doi: 10.3389/fonc.2020.551420

A Comparison Study of Machine Learning (Random Survival Forest) and Classic Statistic (Cox Proportional Hazards) for Predicting Progression in High-Grade Glioma after Proton and Carbon Ion Radiotherapy

Xianxin Qiu[1,2], *Jing Gao*[1,2], *Jing Yang*[1,2], *Jiyi Hu*[1,2], *Weixu Hu*[1,2], *Lin Kong*[1,3*] *and Jiade J. Lu*[1,2*]

[1] *Shanghai Engineering Research Center of Proton and Heavy Ion Radiation Therapy, Shanghai, China,* [2] *Department of Radiation Oncology, Shanghai Proton and Heavy Ion Center, Shanghai, China,* [3] *Department of Radiation Oncology, Shanghai Proton and Heavy Ion Center, Fudan University Cancer Center, Shanghai, China*

OPEN ACCESS

Edited by:
Antony John Lomax, Paul Scherrer Institut (PSI), Switzerland

Reviewed by:
Alexander F. I. Osman, Al-Neelain University, Sudan
Wei Zhao, Stanford University, United States

***Correspondence:**
Jiade J. Lu
jiade.lu@sphic.org.cn
Lin Kong
lin.kong@sphic.org.cn

Specialty section:
This article was submitted to Radiation Oncology, a section of the journal Frontiers in Oncology

Received: *13 April 2020*
Accepted: *29 September 2020*
Published: *30 October 2020*

Citation:
Qiu X, Gao J, Yang J, Hu J, Hu W, Kong L and Lu JJ (2020) A Comparison Study of Machine Learning (Random Survival Forest) and Classic Statistic (Cox Proportional Hazards) for Predicting Progression in High-Grade Glioma after Proton and Carbon Ion Radiotherapy. Front. Oncol. 10:551420. doi: 10.3389/fonc.2020.551420

Background: Machine learning (ML) algorithms are increasingly explored in glioma prognostication. Random survival forest (RSF) is a common ML approach in analyzing time-to-event survival data. However, it is controversial which method between RSF and traditional cornerstone method Cox proportional hazards (CPH) is better fitted. The purpose of this study was to compare RSF and CPH in predicting tumor progression of high-grade glioma (HGG) after particle beam radiotherapy (PBRT).

Methods: The study enrolled 82 consecutive HGG patients who were treated with PBRT at Shanghai Proton and Heavy Ion Center between 6/2015 and 11/2019. The entire cohort was split into the training and testing set in an 80/20 ratio. Ten variables from patient-related, tumor-related and treatment-related information were utilized for developing CPH and RSF for predicting progression-free survival (PFS). The model performance was compared in concordance index (C-index) for discrimination (accuracy), brier score (BS) for calibration (precision) and variable importance for interpretability.

Results: The CPH model demonstrated a better performance in terms of integrated C-index (62.9%) and BS (0.159) compared to RSF model (C-index = 61.1%, BS = 0.174). In the context of variable importance, CPH model indicated that age (P = 0.024), WHO grade (P = 0.020), IDH gene (P = 0.019), and MGMT promoter status (P = 0.040) were significantly correlated with PFS in the univariate analysis; multivariate analysis showed that age (P = 0.041), surgical completeness (P = 0.084), IDH gene (P = 0.057), and MGMT promoter (P = 0.092) had a significant or trend toward the relation with PFS. RSF showed

that merely IDH and age were of positive importance for predicting PFS. A final nomogram was developed to predict tumor progression at the individual level based on CPH model.

Conclusions: In a relatively small dataset with HGG patients treated with PBRT, CPH outperformed RSF for predicting tumor progression. A comprehensive criterion with accuracy, precision, and interpretability is recommended in evaluating ML prognostication approaches for clinical deployment.

Keywords: high-grade glioma, random survival forest, machine learning, particle beam radiotherapy, predictive analytics

INTRODUCTION

High-grade glioma (HGG), including WHO grade III and IV class, is the most common and lethal primary cancer in central nervous system (1). Particle beam (e.g., proton and carbon ion) radiotherapy (PBRT), with both biological and physical advantages (2, 3), can potentially improve the outcome of HGG. Our recent results showed promising efficacy of PBRT in HGG (4). However, the inherent high heterogeneity of HGG, as the dominant factor contributing to general poor treatment efficacy, induces markedly variation of individual outcome (5–7). Adequate outcome prediction, particularly at individual level, is essential but remains challenging for developing precision strategy of PBRT for HGG.

Machine learning (ML), a branch of artificial intelligence, has been employed to predict prognosis in a variety of cancer types. Noticeably, series of studies applying ML algorithms to predict the survival of HGG under standard photon-based radiotherapy have reported good performance in recent years (8–13). However, it is still controversial that which methods among ML algorithms and conventional modeling can achieve better performance in survival analysis, particularly in terms of time-to-event censored data (14–16). Hence, it is a critical need to explore which model can contribute to higher accuracy and precision of survival prediction at patient-level for HGG with PBRT.

The most typical and commonly used model of ML and conventional statistics for cancer censored survival data are random survival forest (RSF) and Cox proportional (CPH), respectively. The RSF is an ensemble ML method constructed with numerous independent decision trees, each of which receives a random subset of samples and randomly selects a subset of variables at each split in the tree for prediction. The final prediction results of a RSF model are the average of the prediction of each individual tree. The CPH model is a well-recognized statistical technique to explore the correlation between the survival time and covariates.

To our knowledge, there was no study to explore whether conventional statistics and ML method differ in the ability to predict progression or survival for HGG patients treated with PBRT. Therefore, we retrospectively collected important clinical characteristics of HGG patients underwent PBRT, as well as fundamental molecular markers and treatment information. Then, all HGG patients were randomly split into training set or testing set, and CPH model and RSF model were compared with their performance to predict progression-free survival (PFS). The model with superior performance was then utilized to build a nomogram as in individual prediction tool of progression for HGG patient underwent PBRT.

METHODS AND MATERIALS

Study Population and Data

Institutional review board (IRB) approval was obtained from the Shanghai Proton and Heavy Ion Center (SPHIC) prior to conducting this study. Variables from three categories: patient-related, disease-related and treatment-related information was retrospectively collected. Patient-related data collected included age, gender, and Karnofsky Performance Score (KPS). Disease-related features included tumor location that was classified as invasion of subventricular zone (SVZ) or non-SVZ (17) invasion and molecular markers, including Isocitrate dehydrogenase (IDH) gene and O[6]-methylguanine-DNA methyltransferase (MGMT) promoter status. Treatment-related information consisted of surgical completeness that was divided into gross-total resection (GTR) and non-GTR (subtotal resection, partial resection, and biopsy), and the target volume for PBRT.

Particle Radiotherapy

Conventional MR was fundamental images for radiation planning of HGG. The l-[methyl-()11C]methionine (MET)/O-(2-[18F]fluoroethyl)-L-tyrosine (FET)-positron emission tomography (PET) was optional and further required after the latest escalating boost trial initiated. In the case of incomplete resection, dose escalation trials utilizing proton followed by carbon-ion boost were encouraged to target residual lesion. Doses of PBRT were measured by Gray Relative Biological Equivalent (GyE) to account for the RBE differences compared to photon beam The clinical target volume (CTV) of high risk (CTVhr) was defined as gross-tumor volume (GTV) in residual lesion detected on imaging studies and surgical bed plus 5-mm expansion, and the CTV for lower risk (CTVlr) consisted of GTV plus 15-mm margin and edema area. The standard protocol of PBRT for all patients was CTVhr with proton beam to 60 GyE, and CTVlr with proton beam to 50 GyE.

Statistical Analysis and Modeling Process

Progression-free survival (PFS) time is defined as the duration between the time of diagnosis and the date of progression. The

Response Assessment in Neuro-Oncology (RANO) criteria (18) with interpretation modifications (19), including parameters for changes in T1-weighted enhancing lesion and non-enhancing T2/fluid attenuated inversion recovery (FLAIR) lesion, were used to determine disease progression.

The statistical analysis was performed using the R software. Baseline differences between the training set and testing set were assessed using the Mann-Whitney U test for continuous variables. Survival curves were plotted using the Kaplan-Meier method and compared using log-rank test.

Prior to constructing CPH and RSF models, the data set was split into two mutually exclusive sets. Nearly 80% of the entire dataset was assigned as the training set, which was utilized to generate the prediction model. The remaining 20% of the data was designated as the testing set, for use in estimating the model's accuracy. During this procedure, a five-fold cross-validation that putted the dataset stratified by progression status and then sorted by survival time was performed for the purpose that the number of patients with progression and the range of survival time should be (roughly) equal across all folds. By creating folds in this way models would be tested on dataset that was mostly representative of what they saw in the training data.

CPH and RSF models were trained using the *RandomForestSRS* and *survival* R packages, respectively. The hyperparameter tuning of RSF model was performed with five-fold cross-validation on the training set. In particular, the RSF model, as an extension of random forest (RF) that ensembles tree method for analyzing time-to-event data, must select two central hyperparameters: number of randomly drawn candidate variables (*mtry*) and number of trees. Given several studies on the influence of hyperparameters on RF model regarding performance and variable importance, *mtry*= or *mtry*=*p*/3 for regression with *p* being the number of predictor variables is reasonable (20, 21). As our dataset contained 10 predictor variables, the *mtry* was set to 3. Considering the number of trees, two studies using real datasets show that 100 trees can often achieve the biggest gain of RF model performance (22, 23). Thus, the present study used 100 trees for RSF approach.

Predictive performance of model was measured with five-fold cross-validation by discrimination and calibration *via* the *pec* R package. The concordance index (C-index), which ranges from 0.5 (random prediction) to 1 (perfect prediction), reflects the discrimination power to rank individuals from low to high risk. The brier score (BS) is a metric of calibration, with lower value representing improved model accuracy. A final nomogram was developed using the method with the greatest predictive accuracy for individualized estimation of survival.

RESULTS

Demographics, Clinical Characteristics, and Treatment of Patients

The entire study cohort consisted of 82 consecutive HGG patients, who underwent PBRT at Shanghai Proton and Heavy Ion Center, between 6/2015 and 11/2019. All 82 patients underwent tumor resection, then PBRT with concurrent TMZ of the Stupp protocol. In total, 10 features, including age, sex, symptom duration, tumor location, WHO grade, surgical intervention, IDH status, MGMT promoter status, CTVhr volume, and CTVlr volume, were collected from each patient. The demographics, molecular markers and PBRT information of the dataset are detailed in **Table 1**.

Survival Analysis of the Entire Cohort of Patients

The median follow-up period was 16.6 months. At the last follow-up, 37 patients (4 grade III, 33 grade IV) had tumor progression. Progression-free survival (PFS) time was censored for 45 patients (54.9%). The 6-, 12-, and 18-month PFS rates were 93.4%, 68.3%, and 46.6% for the total dataset, respectively. The entire cohort was exclusively split into a training set and a testing set of 65 patients (79.3%) and 17 (20.7%) patients,

TABLE 1 | Characteristics of all 82 patients, their condition, and treatment.

Characteristics	No. of patients (N = 82, %)
Sex	
Male	48 (58.5%)
Female	34 (41.5%)
Age (years)	
Median	55.5
Range	19–76
KPS before radiotherapy	
>80	64 (78.0%)
≤80	18 (22.0%)
Tumor Location	
Lesion involving the SVZ	58 (70.7%)
Lesion not involving the SVZ	24 (29.3%)
Histology grade (WHO grade)	
Grade IV	59 (72.0%)
Grade III	23 (28.0%)
Surgical intervention	
Partial resection/Biopsy	17 (20.7%)
Subtotal resection	36 (43.9%)
Total resection	29 (35.4%)
MGMT promoter	
Methylated	27 (32.9%)
Un-methylated	31 (37.8%)
N/A	24 (29.3%)
IDH mutation	
Wild type	16 (19.5%)
Mutant type	66 (80.5%)
CTVhr volume (cm^3)	
Median	98.47
Range	3.72–300.89
CTVlr volume (cm^3)	
Median	220.32
Range	24.00–494.21
Doses of particle radiation (GyE/fractions)	
Proton-60GyE/30	48 (58.5%)
Proton-50 GyE/25+ C-ion-10-12GyE/4-5	14 (17.1%)
Proton-60 GyE/30+ C-ion boost to 9–18 GyE/3	18 (22.0%)
Proton-34 GyE/10+ C-ion boost 9 GyE/3*	2 (2.4%)

**For patients ≥ 65 years only. CTVhr, Clinical target volume of high risk; CTVlr, Clinical target volume of low risk; GyE, Gray relative biological equivalent; IDH, Isocitrate dehydrogenase; KPS, Karnofsky Performance Score; MGMT, O[6]-methylguanine-DNA methyltransferase; SVZ, Subventricular zone.*

respectively. No significantly different PFS was revealed between the training and testing datasets by Kaplan-Meier survival curve (P = 0.680, **Figure 1**).

Comparing the Performance of Cox Proportional Hazard Model With Random Survival Forest

The training set was utilized to build CPH and RSF model. The prediction performance of different models was compared in testing set with both C-index and BS. **Figures 2A, B** respectively illustrated the C-index and BS plots for PFS at various time points. The integrated C-index of CPH and RSF model was 62.9% and 61.1%, respectively. The integrated BS of CPH and RSF was 0.159 and 0.174, respectively (reference = 0.181). **Figure 3** showed the PFS probability with a series time points at 6-, 12-, 18-, and 24- month for each individual in the testing cohort, based on the predicting results of CPH (**Figure 3A**) and RSF (**Figure 3B**) models.

Identification of Prognostic Factors Using CPH and Random Survival Forest

The clinico-pathological features were compared for the correlation to PFS in the training set. According to the CPH model (**Table 2**), univariate analysis documented that age (P = 0.024), WHO grade (P = 0.020), IDH gene (P = 0.019), and MGMT promoter status (P = 0.040) were significantly correlated with PFS; multivariate analysis showed that age (P = 0.041), surgical completeness (P = 0.084), IDH gene (P = 0.057), and MGMT promoter (P = 0.092) had a significant or trend toward the relation with PFS. The RSF model (**Figure 4**) ranked the features in order of importance for PFS, with merely age and IDH status being significantly important variables; meanwhile,

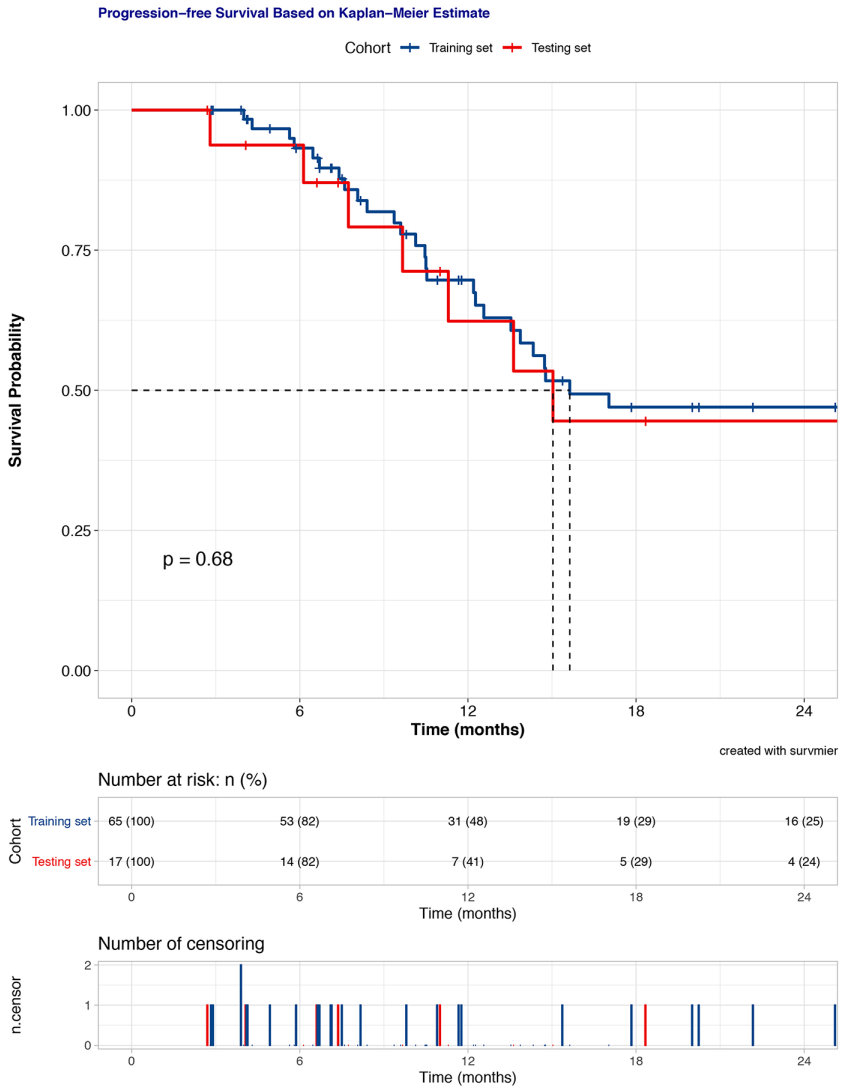

FIGURE 1 | Kaplan-Meier survival curves of progress-free survival for the training and testing set.

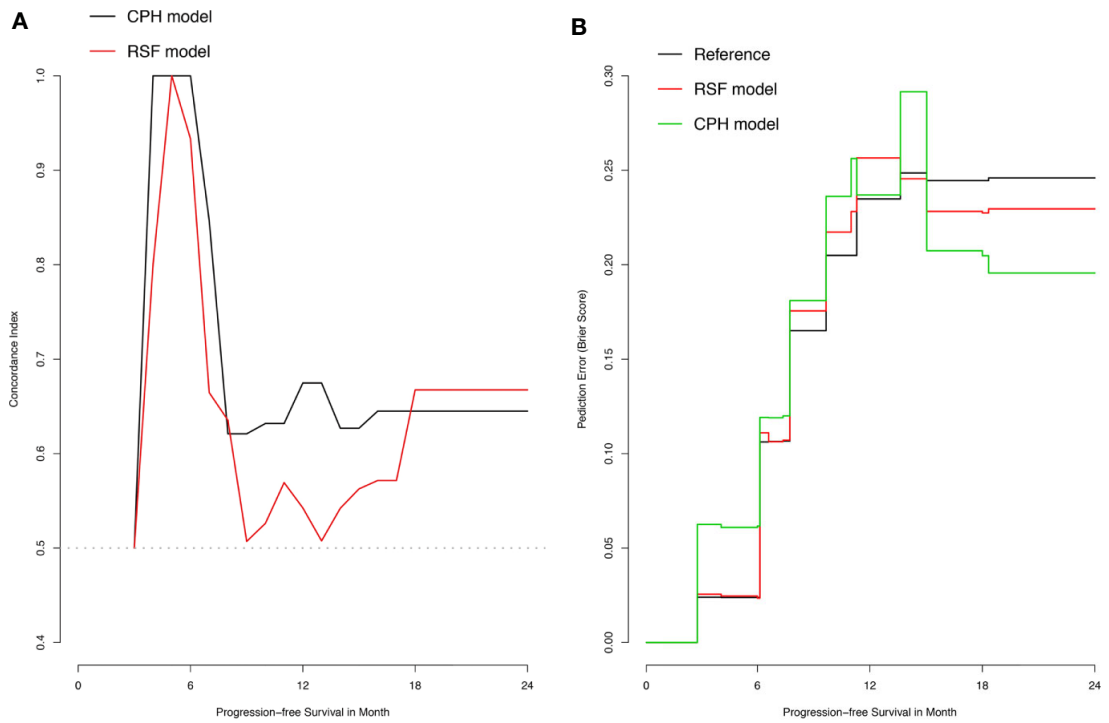

FIGURE 2 | Plots of concordance index (C-index) and brier score (BS) for comparing Cox proportional hazards (CPH) models and random survival forest (RSF) in the testing dataset. **(A)** Plot of C-index; **(B)** Plot of BS.

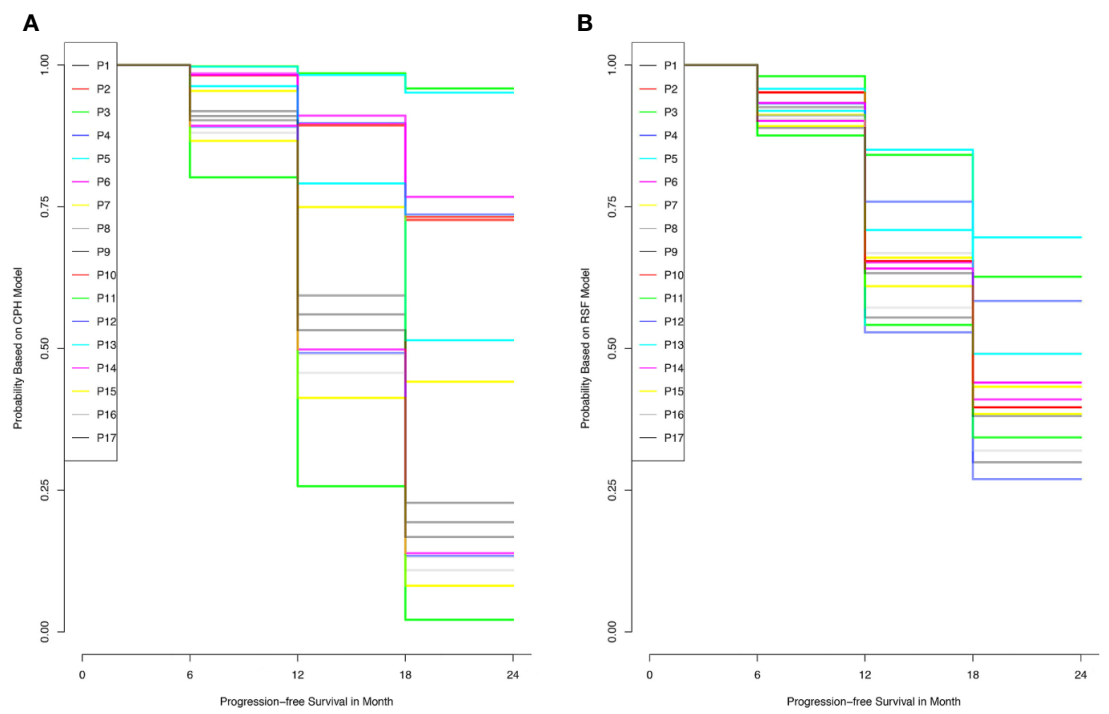

FIGURE 3 | The probability of progress-free survival for each individual in the training data set, according to the results of Cox proportional hazards model **(A)** and random survival forest model **(B)**.

TABLE 2 | Cox proportional hazard regressions for progression-free survival in the training set.

Variables*	Uni-variate analysis		Mulit-variate analysis	
	HR (95% CI)	P- value	HR (95% CI)	P- value
Sex	1.299 (0.616–2.738)	0.492	1.229 (0.510–2.965)	0.646
Age	1.040 (1.005–1.075)	0.024	1.040 (1.002–1.081)	0.041
KPS	1.665 (0.7356–3.770)	0.221	2.233 (0.788–6.321)	0.131
WHO Grade	3.468 (1.200–10.020)	0.020	1.450 (0.418–5.034)	0.559
Tumor Location	0.435 (0.162–1.167)	0.098	0.554 (0.178–1.721)	0.307
Surgical Completeness	1.177 (0.721–1.922)	0.515	1.835 (0.923–3.647)	0.084
IDH gene	4.281 (1.289–14.220)	0.019	4.158 (0.958–18.051)	0.057
MGMT promoter	2.387 (1.041–5.472)	0.040	2.555 (0.857–7.622)	0.092
CTVhr	1.003 (0.998–1.009)	0.253	1.011 (0.997–1.026)	0.123
CTVlr	1.002 (0.999–1.006)	0.236	0.994 (0.985–1.003)	0.195

**The variables were compared in the following ways: sex, female as reference; age as continuous variable; KPS, >80 as reference; WHO grade, grade III as reference; Surgical Completeness, gross total resection as reference; IDH gene, mutant-type as reference; MGMT promoter, methylation as reference; CTVhr (CTVhighrisk), volume as continuous variable; CTVlr (CTVlowrisk), volume as continuous variable. CI, Confidence interval; CTVhr, Clinical target volume of high risk; CTVlr, Clinical target volume of low risk; GyE, Gray relative biological equivalent; HR, Hazard ratio; IDH, Isocitrate dehydrogenase; KPS, Karnofsky Performance Score; MGMT, O[6]-methylguanine-DNA methyltransferase; SVZ, Subventricular zone.*

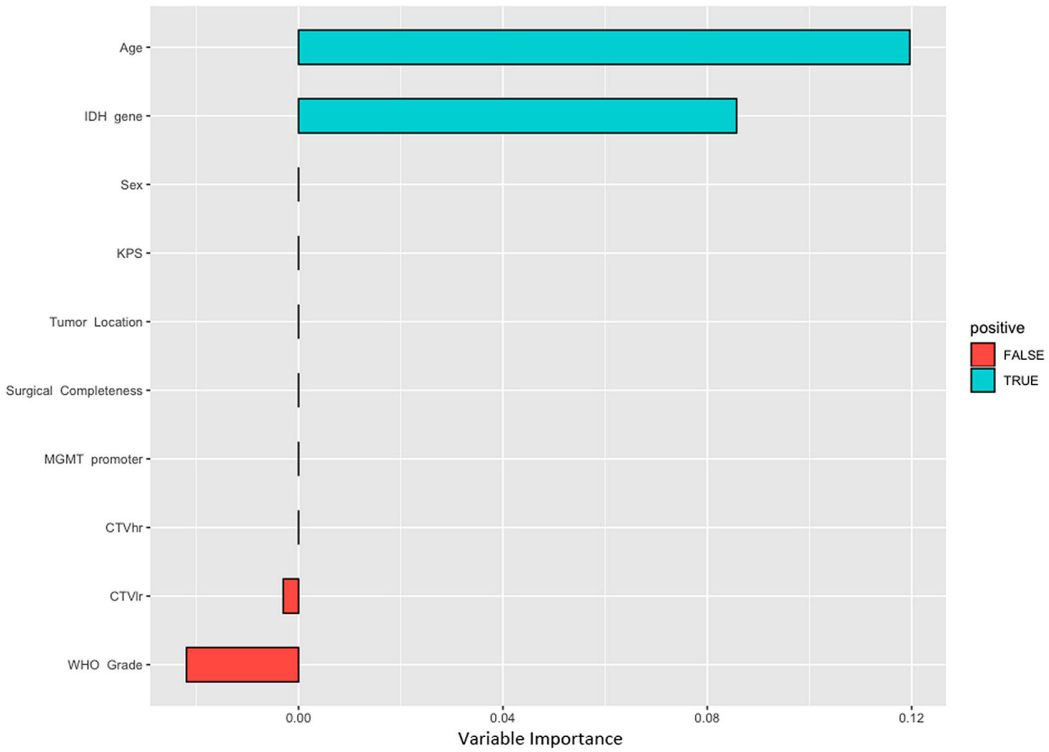

FIGURE 4 | Variable importance of indicated by random forest survival model.

tumor grade showed negative importance, meaning that removing a given feature from the model actually improved the performance.

Nomogram Based on Cox Proportional Hazard Model for Individual PFS Prediction

Given that the CPH model outperformed RSF model in both discrimination and calibration, a nomogram was built on the base of CPH model to predict the progression probability of HGG patients underwent PBRT at individual level. The variables, including age, MGMT promoter, IDH gene, WHO grade and surgical completeness, that were indicated as significant in univariate analysis or significant (or trend forward) in multivariate analysis, were utilized to conduct the nomogram. In the present nomogram (**Figure 5**), each of the variables was given a point according to hazard ratio (HR). By adding up the total score from each variable and locating it onto the total points

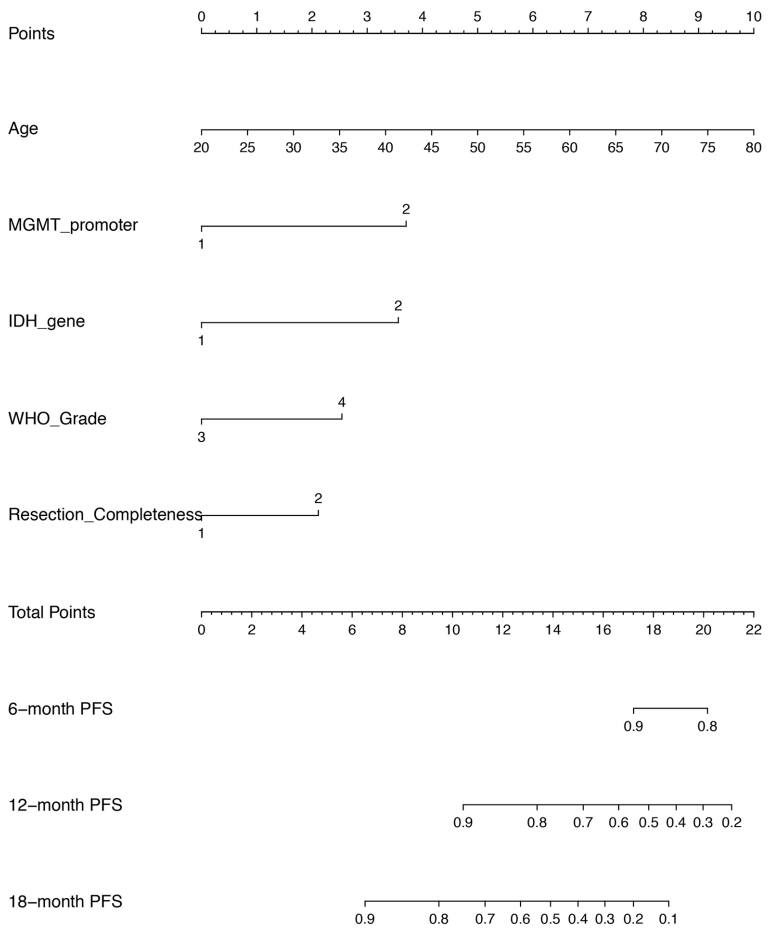

FIGURE 5 | A nomogram of predicting the probability of 6 month-, 12 month-, and 18 month- progression free survival (PFS) at personnel level. The scores of each variable are as follows: age (years) presented as continuous value, MGMT promoter (1 = methylation, 2 = unmethylation/not known), IDH gene (1 = mutant, 2 = wild), WHO grade (3 = Grade III, 4 = Grade IV), resection completeness (1 = gross total resection, 2 = non gross total resection).

scale, the probability of 6-, 12-, and 18- month PFS would be obtained.

DISCUSSION

Prognosis prediction plays a critical role in clinical and personal decision-making for HGG patients, particularly in the condition of considering the rare source of PBRT as alternative treatment. There have been attempts to conduct traditional statistics and ML methodology to predict individual survival. CPH and RSF model are extensively used in application of cancer survival that generally refers to time-to-event censored data. The main objective of this study was to compare the performance between CPH and RSF models for predicting HGG's progression underwent PBRT. Our results showed that CPH model present better fit to predict individual PFS in accuracy, precision, and interpretability. Then, we constructed an individual prediction research tool of nomogram based on CPH model for PFS in HGG patients treated with PBRT.

The main advantage of our study is that it approached progression prediction based on a time-to-event dataset. Indeed, there is increasing studies integrating various ML algorithms into improving the predictability of prognosis for cancer. However, most of ML approaches assume that event status is known for all subjects with the utility limited to continuous or binary model. Indeed, right-censored data, referring to the follow-up ends on a subject prior to a patient experiencing an event (i.e., tumor progression or death), is universal in cancer survival. In application of ML approaches analyzing cancer survival, common strategy is to split the patients' outcome into ordered categorical data based on measuring the disease status at a particular time point. However, this relatively *ad hoc* method does not take the element of time-to-event into account, can merely provide point estimates of outcome and may incur the risk of biasing predication accuracy in the clinical realm (24). The method of RSF utilized in the present study is an extension of random forest for time-to-event data, represents an attractive ML approach that allows for the computation of personnel-level survival prediction

through more granular insight and mitigates the systemic bias associated with incomplete follow-up.

Another advantage of our study is that the performances of different models were graphically compared with a comprehensive aspect of discrimination and calibration at various time points, rather than a fixed time. Discrimination represents the ability of a model to separate observations on subjective-level, whereas calibration is a descriptor of a predictive model that characterizes the agreement between the observed and predicted outcome on a population level. C-index, the main metric quantified of discrimination in this study, reflects the probability that for a random selection of any 2 HGG patients, the patient with earlier tumor progression is ranked with higher risk of progression according to the model. Hence, the C-index takes into account of both the occurrence of the event and the length of follow-up and is particularly well suited for time-to event data analysis. Indeed, any model (i.e., CPH model) with the ability to forecast properly ordered but proportional event times can score high value of C-index (25). Hence, the evaluation of calibration, another metric of prediction accuracy, is essential but unfortunately under-explored in time-to-event models for many studies. Even in studies that performed the assessment of calibration, the method of a calibration plot can only provide information at a specific time point (e.g., 1-year survival probability). Here, in our study, we presented a measurement of BS plot to assess the model performance at various time points. In precise, the BS measures the mean squared difference between the predicted progression probability and the actual outcome for all HGG patients at group level. Note that BS takes on a value between 0 and 1, and the lower of BS indicates that better predictions are calibrated.

The most important finding of the present study is that CPH outperformed RSF with both C-index and BS in the predictability of progression for HGG patients underwent PBRT in a relatively small sample. In terms of C-index, our result was consistent with a study enrolling 289 cases as a testing set and 98 cases as a validation test conducted by Gittleman et al. (16), in which C-index for predicting survival of lower-grade glioma at 60, 90, and 120 months were measured for CPH (0.844, 0.843, 0.841) and RSF (0.806, 0.791, 0.782), respectively. However, it is still controversial which method can consistently achieve better accuracy of predicting prognosis *via* the measurement of C-index in glioma. Audureau et al. (26) conducted a retrospective multi-centric study enrolling 777 patients with recurrent glioblastoma, split into a training set of 407 cases and an external validation set of 370 cases; the results presented the discrimination C-indexes of CPH and RSF as 69.80% and 70.14% in the external validation set, respectively. Based on a larger population from the Surveillance, Epidemiology, and End Results (SEER) database that comprised 20,821 glioblastoma cases split into a training and validation test set with an 80/20 ratio, Senders et al. (14) revealed the integrated C-index of CPH and RSF as 0.69 and 0.68, respectively. On the hands of model calibration, neither of the studies performed such analysis. All these three studies lack the assessment of BS, or any other methods of calibration, for the comparison of CPH and RSF. Our study, to our knowledge, is the first study to directly compare the discrimination and calibration for CPH and RSF in glioma.

In looking at variables with significant relation to survival in our results, CPH model documented that age, MGMT promoter, surgical completeness, IDH gene and KPS had a significant or trend toward relation with tumor progression. In comparison, only IDH status and age were indicated with significant importance affecting PFS according to the RSF model. It should be noted that all the significant variables in our CPH model are well-known prognostic factors in the clinical decision-making of HGG. In brief, the CPH model identified more statistically significant prognostic factors that are generally considered important in decision making in a clinical setting. Hence, we believe that CPH model had a better interpretability as compared to RSF in terms of exploring the critical factors for predicting tumor progression after PBRT. There is a possibility that the relatively small sample and/or the different mathematical underpinnings contributed to this different effect. In principle, RSF model is based on searching for the best variables used to split the node by maximizing the log-rank methods, and the variable importance refers to a measurement of the increase of predicting error when perturbation is added to the variable. While in CPH model, the importance of variables can be interpreted as HR and P-value. Indeed, one common drawback of RSF is a bias toward inclusion of variables with many split points that may lead to a bias in resulting summary of variable importance (27–29).

We also constructed a nomogram based on CPH model due to its superior performance over RSF model. As a pictorial representation that uses various potential prognostic markers to depict a scoring model, nomogram is provided as a visual tool to generate a probability of a clinical outcome for a given individual. Patients' survival-related nomograms for HGG have been developed in series of studies (30–35), but with a common drawback that some critical patient-related, tumor-related or treatment-related information were not incorporated. Moreover, all these studies were only applied for patients treated with photon-based radiotherapy, but not PBRT. In the context of PBRT, previous results from Germany and Japan showed that photon radiation combined with carbon ion boost improved the outcome of HGG patients (3); and recently, we reported our early experience with an encouraging efficacy of PBRT in HGG (4). It is well known that PBRT has been increasingly spread worldwide to treat cancer, and great expectation has been placed with PBRT to improve the dismal outcome of HGG. The present nomogram in our study can provide a tool of reference for counseling PBRT as a treatment option for HGG based on common-used prognostic markers, and may be informative of future precise medicine of PBRT in HGG.

There are several limitations of this study to be discussed. First, due to the retrospective nature of this study, our results were derived from a relatively limited observation database that may introduce some inevitable bias. Statistically, it is of better generalizability to compare methods with a prospective design, or at least external validation dataset. Meanwhile, with a phase III

clinical trial going in our institution (36), the present study provided a blueprint of methodology to perform a prospective validation in the future. Second, our study was designed as a purely academic research to compare the prediction performance of CPH and RSF in discrimination, calibration and interpretability. The present nomogram based on CPH model should not be directly implemented in the clinical practice prior to a prospective validation. Nevertheless, based on our results, we recommend evaluating fitted ML models on several criteria rather than a singular focus on prediction accuracy. Third, though the variables in our studies consisted of systematical information occupying important role in the management of HGG, it should be noted that the critical issue of inherent high heterogeneity within HGG could not be well settled through these features. Noticeably, radiomic, particularly referring to functional brain imaging technique, can provide an integrative and dynamic view of the whole tumor tissue and serve as a reliable tool to tackle the issue of heterogeneity. In this context, our ongoing phase III trial adopts multi-modal imaging, including MET-PET, perfusion weighted imaging (PWI), diffusion tensor imaging (DTI), and MR spectroscopy (MRS), for each patient (36). Thus, more comprehensive models that include imaging parameters will be assessed in the future.

CONCLUSION

This study indicated a superior accuracy of CPH as compared to RSF in a relatively small sample data of HGG patients for predicting tumor progression after PBRT. As more approaches about ML techniques are implemented to glioma prognostication purposes, comprehensive criteria with discrimination and calibration, as well as interpretability, is recommend in evaluating fitted models for clinical deployment.

DATA AVAILABILITY STATEMENT

The raw data supporting the conclusions of this article will be made available by the authors, without undue reservation.

ETHICS STATEMENT

The studies involving human participants were reviewed and approved by Shanghai Proton and Heavy Ion Center. The patients/participants provided their written informed consent to participate in this study.

AUTHOR CONTRIBUTIONS

Conception and design: LK and JL. Acquisition of data: XQ, JG, JY, JH, and WH. Analysis and interpretation of data: XQ, JG, and JH. Drafting or revising the article: XQ, LK, and JL. All authors contributed to the article and approved the submitted version.

FUNDING

The National Key Research and Development Program of China (Project No. 2018YFC0115700 and 2017YFC0108603); The Shanghai Academic/Technology Research Leader Program (Project No. 19XD1432900 and 18XD1423000); Shanghai Hospital Development Center (Joint Breakthrough Project for New Frontier Technologies. Project No. SHDC12016120); Science and Technology Commission of Shanghai Municipality (Project No. 19411951000); Science and Technology Development Fund of Shanghai Pudong New Area (Project No. PKJ2018-Y51, PKJ2017-Y50 and No.PKJ2017-Y49).

REFERENCES

1. Louis DN, Perry A, Reifenberger G, von Deimling A, Figarella-Branger D, Cavenee WK, et al. The 2016 World Health Organization Classification of Tumors of the Central Nervous System: a summary. *Acta Neuropathol* (2016) 131:803–20. doi: 10.1007/s00401-016-1545-1
2. Schlaich F, Brons S, Haberer T, Debus J, Combs SE, Weber KJ. Comparison of the effects of photon versus carbon ion irradiation when combined with chemotherapy in vitro. *Radiat Oncol* (2013) 8:260. doi: 10.1186/1748-717X-8-260
3. Combs SE, Bruckner T, Mizoe JE, Kamada T, Tsujii H, Kieser M, et al. Comparison of carbon ion radiotherapy to photon radiation alone or in combination with temozolomide in patients with high-grade gliomas: explorative hypothesis-generating retrospective analysis. *Radiother Oncol* (2013) 108:132–5. doi: 10.1016/j.radonc.2013.06.026
4. Kong L, Wu J, Gao J, Qiu X, Yang J, Hu J, et al. Particle radiation therapy in the management of malignant glioma: Early experience at the Shanghai Proton and Heavy Ion Center. *Cancer* (2020) 126(12):2802–10. doi: 10.1002/cncr.32828
5. Liu Y, Xu X, Yin L, Zhang X, Li L, Lu H. Relationship between Glioblastoma Heterogeneity and Survival Time: An MR Imaging Texture Analysis. *AJNR Am J Neuroradiol* (2017) 38:1695–701. doi: 10.3174/ajnr.A5279
6. Bernstock JD, Mooney JH, Ilyas A, Chagoya G, Estevez-Ordonez D, Ibrahim A, et al. Molecular and cellular intratumoral heterogeneity in primary glioblastoma: clinical and translational implications. *J Neurosurgery* (2019), 1–9. doi: 10.3171/2019.5.JNS19364
7. Stadlbauer A, Zimmermann M, Doerfler A, Oberndorfer S, Buchfelder M, Coras R, et al. Intratumoral heterogeneity of oxygen metabolism and neovascularization uncovers 2 survival-relevant subgroups of IDH1 wild-type glioblastoma. *Neuro-oncology* (2018) 20:1536–46. doi: 10.1093/neuonc/noy066
8. Mizutani T, Magome T, Igaki H, Haga A, Nawa K, Sekiya N, et al. Optimization of treatment strategy by using a machine learning model to predict survival time of patients with malignant glioma after radiotherapy. *J Radiat Res* (2019) 60:818–24. doi: 10.1093/jrr/rrz066
9. Tan Y, Mu W, Wang XC, Yang GQ, Gillies RJ, Zhang H. Improving survival prediction of high-grade glioma via machine learning techniques based on MRI radiomic, genetic and clinical risk factors. *Eur J Radiol* (2019) 120:108609. doi: 10.1016/j.ejrad.2019.07.010
10. Liu L, Zhang H, Wu J, Yu Z, Chen X, Rekik I, et al. Overall survival time prediction for high-grade glioma patients based on large-scale brain functional networks. *Brain Imaging Behav* (2019) 13:1333–51. doi: 10.1007/s11682-018-9949-2
11. Sanghani P, Ang BT, King NKK, Ren H. Overall survival prediction in glioblastoma multiforme patients from volumetric, shape and texture features using machine learning. *Surg Oncol* (2018) 27:709–14. doi: 10.1016/j.suronc.2018.09.002

12. Lao J, Chen Y, Li ZC, Li Q, Zhang J, Liu J, et al. A Deep Learning-Based Radiomics Model for Prediction of Survival in Glioblastoma Multiforme. *Sci Rep* (2017) 7:10353. doi: 10.1038/s41598-017-10649-8
13. Papp L, Potsch N, Grahovac M, Schmidbauer V, Woehrer A, Preusser M, et al. Glioma Survival Prediction with Combined Analysis of In Vivo (11)C-MET PET Features, Ex Vivo Features, and Patient Features by Supervised Machine Learning. *J Nucl Med* (2018) 59:892–9. doi: 10.2967/jnumed.117.202267
14. Senders JT, Staples P, Mehrtash A, Cote DJ, Taphoorn MJB, Reardon DA, et al. An Online Calculator for the Prediction of Survival in Glioblastoma Patients Using Classical Statistics and Machine Learning. *Neurosurgery* (2020) 86:E184–92. doi: 10.1093/neuros/nyz403
15. Kattan MW. Comparison of Cox regression with other methods for determining prediction models and nomograms. *J Urol* (2003) 170:S6–9; discussion S10. doi: 10.1097/01.ju.0000094764.56269.2d
16. Gittleman H, Sloan AE, Barnholtz-Sloan JS. An independently validated survival nomogram for lower grade glioma. *Neuro-oncology* (2020) 22 (5):665–74. doi: 10.1093/neuonc/noz191
17. Woo P, Ho J, Lam S, Ma E, Chan D, Wong WK, et al. A Comparative Analysis of the Usefulness of Survival Prediction Models for Patients with Glioblastoma in the Temozolomide Era: The Importance of Methylguanine Methyltransferase Promoter Methylation, Extent of Resection, and Subventricular Zone Location. *World Neurosurgery* (2018) 115:e375–85. doi: 10.1016/j.wneu.2018.04.059
18. Wen PY, Macdonald DR, Reardon DA, Cloughesy TF, Sorensen AG, Galanis E, et al. Updated response assessment criteria for high-grade gliomas: response assessment in neuro-oncology working group. *J Clin Oncol* (2010) 28:1963–72. doi: 10.1200/JCO.2009.26.3541
19. Ellingson BM, Wen PY, Cloughesy TF. Modified Criteria for Radiographic Response Assessment in Glioblastoma Clinical Trials. *Neurotherapeutics* (2017) 14:307–20. doi: 10.1007/s13311-016-0507-6
20. Goldstein BA, Polley EC, Briggs FB. Random forests for genetic association studies. *Stat Appl Genet Mol Biol* (2011) 10:32. doi: 10.2202/1544-6115.1691
21. Genuer R, Poggi JM, Tuleau C. Random Forests: some methodological insights. *arXiv preprint arXiv:0811.3619* (2008) [v1]:1–33.
22. Probst P, Boulesteix AL. To tune or not to tune the number of trees in random forest? *ArXiv preprint arXiv:1705.05654* (2017) [v1]:1–20.
23. Oshiro TM, Perez PS, Baranauskas JA. How Many Trees in a Random Forest? In: P Perner, editor. *Machine Learning and Data Mining in Pattern Recognition. MLDM 2012*. Berlin, Germany: Springer (2012). p. 154.
24. Vock DM, Wolfson J, Bandyopadhyay S, Adomavicius G, Johnson PE, Vazquez-Benitez G, et al. Adapting machine learning techniques to censored time-to-event health record data: A general-purpose approach using inverse probability of censoring weighting. *J BioMed Inform* (2016) 61:119–31. doi: 10.1016/j.jbi.2016.03.009
25. Uno H, Cai T, Pencina MJ, D'Agostino RB, Wei LJ. On the C-statistics for evaluating overall adequacy of risk prediction procedures with censored survival data. *Stat Med* (2011) 30:1105–17. doi: 10.1002/sim.4154
26. Audureau E, Chivet A, Ursu R, Corns R, Metellus P, Noel G, et al. Prognostic factors for survival in adult patients with recurrent glioblastoma: a decision-tree-based model. *J Neuro-oncology* (2018) 136:565–76. doi: 10.1007/s11060-017-2685-4
27. Strobl C, Boulesteix AL, Zeileis A, Hothorn T. Bias in random forest variable importance measures: illustrations, sources and a solution. *BMC Bioinf* (2007) 8:25. doi: 10.1186/1471-2105-8-25
28. Wright MN, Dankowski T, Ziegler A. Unbiased split variable selection for random survival forests using maximally selected rank statistics. *Stat Med* (2017) 36:1272–84. doi: 10.1002/sim.7212
29. Nasejje JB, Mwambi H, Dheda K, Lesosky M. A comparison of the conditional inference survival forest model to random survival forests based on a simulation study as well as on two applications with time-to-event data. *BMC Med Res Methodol* (2017) 17:115. doi: 10.1186/s12874-017-0383-8
30. Gittleman H, Lim D, Kattan MW, Chakravarti A, Gilbert MR, Lassman AB, et al. An independently validated nomogram for individualized estimation of survival among patients with newly diagnosed glioblastoma: NRG Oncology RTOG 0525 and 0825. *Neuro-oncology* (2017) 19:669–77. doi: 10.1093/neuonc/now208
31. Zhang X, Lu H, Tian Q, Feng N, Yin L, Xu X, et al. A radiomics nomogram based on multiparametric MRI might stratify glioblastoma patients according to survival. *Eur Radiol* (2019) 29:5528–38. doi: 10.1007/s00330-019-06069-z
32. Peeken JC, Goldberg T, Pyka T, Bernhofer M, Wiestler B, Kessel KA, et al. Combining multimodal imaging and treatment features improves machine learning-based prognostic assessment in patients with glioblastoma multiforme. *Cancer Med* (2019) 8:128–36. doi: 10.1002/cam4.1908
33. Molitoris JK, Rao YJ, Patel RA, Kane LT, Badiyan SN, Gittleman H, et al. Multi-institutional external validation of a novel glioblastoma prognostic nomogram incorporating MGMT methylation. *J Neuro-oncology* (2017) 134:331–8. doi: 10.1007/s11060-017-2529-2
34. Gittleman H, Cioffi G, Chunduru P, Molinaro AM, Berger MS, Sloan AE, et al. An independently validated nomogram for isocitrate dehydrogenase-wild-type glioblastoma patient survival. *Neurooncol Adv* (2019) 1:vdz007. doi: 10.1093/noajnl/vdz007
35. Cheng W, Zhang C, Ren X, Wang Z, Liu X, Han S, et al. Treatment strategy and IDH status improve nomogram validity in newly diagnosed GBM patients. *Neuro-oncology* (2017) 19:736–8. doi: 10.1093/neuonc/nox012
36. Kong L, Gao J, Hu J, Lu R, Yang J, Qiu X, et al. Carbon ion radiotherapy boost in the treatment of glioblastoma: a randomized phase I/III clinical trial. *Cancer Commun (Lond)* (2019) 39:5. doi: 10.1186/s40880-019-0351-2

Conflict of Interest: The authors declare that the research was conducted in the absence of any commercial or financial relationships that could be construed as a potential conflict of interest.

Copyright © 2020 Qiu, Gao, Yang, Hu, Hu, Kong and Lu. This is an open-access article distributed under the terms of the Creative Commons Attribution License (CC BY). The use, distribution or reproduction in other forums is permitted, provided the original author(s) and the copyright owner(s) are credited and that the original publication in this journal is cited, in accordance with accepted academic practice. No use, distribution or reproduction is permitted which does not comply with these terms.

frontiers in Oncology

REVIEW
published: 14 December 2020
doi: 10.3389/fonc.2020.558845

Proton Therapy for Intracranial Meningioma for the Treatment of Primary/Recurrent Disease Including Re-Irradiation

Damien C. Weber[1,2,3]*, *Nicola Bizzocchi*[1], *Alessandra Bolsi*[1] and *Michael D. Jenkinson*[4,5]

[1] Center for Proton Therapy, Paul Scherrer Institute, ETH Domain, Villigen, Switzerland, [2] Radiation Oncology Department, University Hospital Zürich, Zürich, Switzerland, [3] Radiation Oncology Department, University Hospital of Bern, Inselspital, Bern, Switzerland, [4] Department of Neurosurgery, The Walton Centre NHS Foundation Trust, Liverpool, United Kingdom, [5] Institute of Translational Medicine, University of Liverpool, Liverpool, United Kingdom

Meningeal tumors represent approximately 10–25% of primary brain tumors and occur usually in elderly female patients. Most meningiomas are benign (80–85%) and for symptomatic and/or large tumors, surgery, with or without radiation therapy (RT), has been long established as an effective means of local tumor control. RT can be delivered to inoperable lesions or to those with non-benign histology and for Simpson I–III and IV–V resection. RT can be delivered with photons or particles (protons or carbon ions) in stereotactic or non-stereotactic conditions. Particle therapy delivered for these tumors uses the physical properties of charged carbon ions or protons to spare normal brain tissue (i.e. Bragg peak), with or without or a dose-escalation paradigm for non-benign lesions. PT can substantially decrease the dose delivered to the non-target brain tissues, including but not limited to the hippocampi, optic apparatus or cochlea. Only a limited number of meningioma patients have been treated with PT in the adjuvant or recurrent setting, as well as for inoperable lesions with pencil beam scanning and with protons only. Approximately 500 patients with image-defined or WHO grade I meningioma have been treated with protons. The reported outcome, usually 5-year local tumor control, ranges from 85 to 99% (median, 96%). For WHO grade II or III patients, the outcome of only 97 patients has been published, reporting a median tumor local control rate of 52% (range, 38–71.1). Only 24 recurring patients treated previously with photon radiotherapy and re-treated with PT were reported. The clinical outcome of these challenging patients seems interesting, provided that they presented initially with benign tumors, are not in the elderly category and have been treated previously with conventional radiation dose of photons. Overall, the number of meningioma patients treated or-re-irradiated with this treatment modality is small and the clinical evidence level is somewhat low (i.e. 3b–5). In this review, we detail the results of upfront PT delivered to patients with meningioma in the adjuvant setting and for inoperable tumors. The outcome of meningioma patients treated with this radiation modality for recurrent tumors, with or without previous RT, will also be reviewed.

Keywords: meningioma, proton therapy, recurrent disease, primary treatment, reirradiation, pencil beam scanned proton therapy, surgery

OPEN ACCESS

Edited by:
Hailiang Tang,
Huashan Hospital Affiliated to Fudan University, China

Reviewed by:
Xiaoxia Liu,
Fudan University, China
Xuqun Tang,
Huashan Hospital Affiliated to Fudan University, China

****Correspondence:***
Damien C. Weber
damien.weber@psi.ch

Specialty section:
This article was submitted to Radiation Oncology, a section of the journal Frontiers in Oncology

Received: *04 May 2020*
Accepted: *28 October 2020*
Published: *14 December 2020*

Citation:
Weber DC, Bizzocchi N, Bolsi A and Jenkinson MD (2020) Proton Therapy for Intracranial Meningioma for the Treatment of Primary/Recurrent Disease Including Re-Irradiation. Front. Oncol. 10:558845. doi: 10.3389/fonc.2020.558845

INTRODUCTION

Meningiomas are the commonest primary brain tumor and account for 10–25% of all cases (1). The WHO classification describes three different histological grades: WHO grade I meningioma account for up to 80% of cases and have a low recurrence rate; WHO grade II comprise approximately 20–30% of cases and have a recurrence rate of ~30–40%; and grade III meningioma comprise around 1–2% and invariably recur (2). Asymptomatic and incidental meningiomas do not usually require active treatment and can be safely monitored (3, 4). However, for symptomatic or growing tumors, surgery is still the primary treatment modality, can achieve long-term tumor control and in some cases can be curative (5). However, despite advances in surgical techniques not all meningioma are appropriate for surgery (e.g. due to anatomical location) nor are all meningioma amenable to complete resection (e.g. due to proximity to critical neurovascular structures or tumor consistency). Furthermore, even when meningiomas are completely resected, recurrence can still occur. In meningiomas that recur, surgery is more challenging due to scar tissue, and is associated with higher rates of morbidity and mortality. Recently several integrated molecular models to predict the risk of recurrence risk have been developed (6, 7), which, once prospectively validated prospectively, could be used to guide to the use of adjuvant radiotherapy. Due to the risk of recurrence, radiotherapy has a clear role in the management of meningioma in order to achieve durable, long-term control. It is used in the adjuvant setting for most malignant meningioma, for some atypical meningioma and for the occasional benign meningioma. Currently the standard modality is fractionated external beam radiotherapy with photons or radiosurgery for small tumors that are not in direct vicinity of critical structures. The expansion of proton beam facilities has led to increased use of this modality. The main difference between photons, delivered in stereotactic- or non-stereotactic condition, and protons is the remarkable dose distribution obtained with the latter, where the dose is delivered at a narrow area at the distal end of the proton trajectory (i.e. the Bragg Peak). For small target volumes, it may be questionable if proton therapy (PT) delivered with a Gantry obtains a better dose distribution than radiosurgery (8), for larger tumors, for which this latter treatment modality is not an option, protons usually always achieve an improved dose-conformation when compared to photons. The aim of this review is to describe the contemporary experience of using PT for the treatment of intracranial benign- and non-benign meningioma.

PROTON THERAPY FOR BRAIN TUMORS

The dose deposition in tissue of proton beams is described by a sharply defined Bragg peak, where the bulk of the dose is deposited; beyond the peak the deposited dose drops to zero within a few millimeters (9) (**Figure 1**). The maximum depth (proton range) depends only on the initial energy of the proton beams. The resulting PT dose distributions present both superior

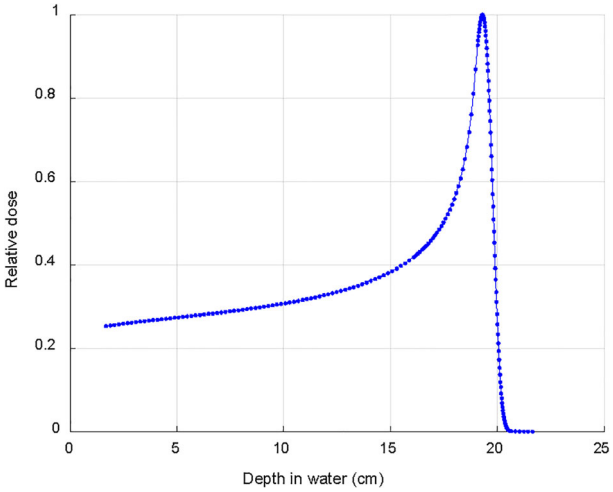

FIGURE 1 | Typical depth dose curve in water for a clinical 170 MeV proton beam used to treat intracranial meningioma.

dose conformality and lower total integral dose when compared to the photon ones. Intensity Modulated Proton Therapy (IMPT) technique (10), available for Pencil Beam Scanning (PBS) systems, can achieve particularly steep dose gradients, thus increasing furthermore the PT advantages. Brain tumors, including meningiomas, typically located in close proximity to many critical organs at risk (OAR), can clearly benefit from PT dose conformality and healthy tissue sparing (11). This rationale is further supported by the dose-dependent relationship for many radiation induced toxicities which develop after RT for brain tumors. This is the case, for instance, of dose to the hippocampus which correlates with memory outcomes (12) and dose to the hypothalamus and pituitary which correlates with the severity of endocrine dysfunction (13). The increased OAR dose sparing and integral dose reduction typical of PT is even more crucial in cases of re-irradiation where PT is frequently the only possible treatment modality. **Figure 2** details such a case treated at the Paul Scherrer Institute with 52.2 GyRBE administered after a photon irradiation for tumor recurrence. Of note, the second irradiation with protons could completely spare the contralateral temporal lobe and optic nerve (**Figure 2**). As shown in the dose–volume histogram (**Figure 2**), PT enabled complete sparing of the initial target volume (i.e. pre-irradiated Isodose line 100%) treated with photons and thus made re-irradiation possible. Many factors such as the tumor location (14), size and shape of the target volumes influence the magnitude of the PT dosimetric advantages compared to photons. A very recent study (15) for skull base meningiomas, comparing VMAT, IMRT and IMPT reported a significant mean dose reduction up to 48% for the bilateral hippocampi for IMPT as compared to VMAT. Similar differences were found when comparing mean dose to the normal brain tissue; the comparison between IMRT and IMPT resulted in even larger differences in dose to OAR, thus possibly leading to a clinically relevant reduction of late neurocognitive side effects.

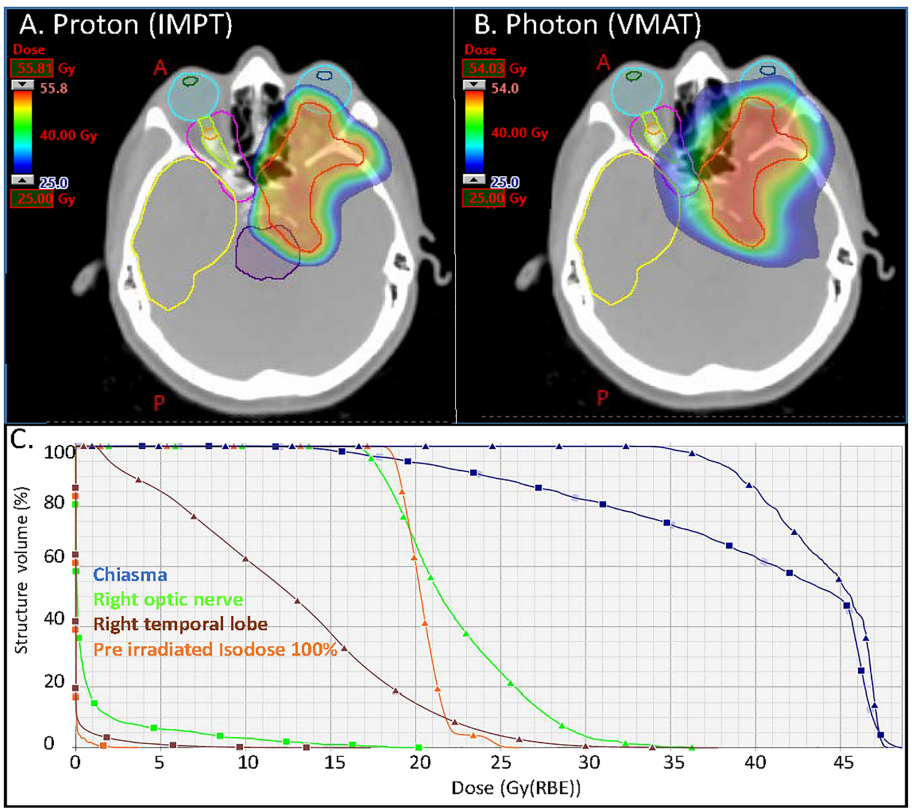

FIGURE 2 | Axial distributions for the **(A)** proton (IMPT) and **(B)** photon (VMAT) plans. In magenta and orange the isodoses lines of the pre irradiation (50% and 100% of 54 Gy respectively); **(C)** DVHs of the optic nerve right, chiasma, right temporal lobe and ROI defined within the 100% isodose line of the pre irradiation (square markers for the proton plan and triangular markers for the photon plan). VMAT, Volumetric modulated Arc Therapy (photon plan); IMPT, Intensity Modulated Proton Therapy (Proton plan).

PT can be administered to meningioma patients with several delivery paradigms. Historically, protons were delivered with a passive scattering system with which the distal end of the proton tracks are controlled/modulated through the use of compensators and the lateral aspect of the proton beam is shaped by brass apertures. In contrast, spot-scanning PT, or as it is called currently pencil beam scanning (PBS) PT, pristine proton pencil beams are scanned in the target volume with different energies to achieve the wanted depth dose distributions. This is in essence a discrete way of administering dose using a 'step and shoot' paradigm. A US group has shown that PBS achieved a better cochlear and lens sparing when compared to passive scattering delivery in brain tumor patients treated with cranio-spinal irradiation (16). Using the same delivery model, radiation volume is virtually divided into numerous slices in dynamic raster scanning, which are subdivided into voxel points. These slices are scanned sequentially but continuously using the focused particle pencil beam.

The steep dose gradients of IMPT, essential to achieve very high dose conformality, are sensitive to range and setup uncertainties, hence potentially affecting the quality of PT delivered dose distributions. Those effects can be mitigated by various techniques, the most effective ones being robust planning (17) and robust optimization (18). The radiation biological characteristic of protons is also a concern in PT, where a constant generic relative biological effectiveness (RBE) value of 1.1 is clinically used. It is anyway well known that RBE increases with increasing Linear Energy Transfer (LET), thus presenting with the highest value in the distal fall-off (19). As proton RBE values are still associated with considerable uncertainties, radiobiological evaluation of PT plans focus preferably on linear energy transfer (LET), a physical parameter which can be calculated quite accurately based on treatment planning information. Adjustment of treatment fields' direction or LET optimization of PT plans can contribute to LET reduction in case of high LET areas localized in critical structures. Research developments in these areas of PT are likely going to further increase its clinical benefits.

PROTON THERAPY FOR WHO GRADE I MENINGIOMA

Table 1 details the PT series delivered to WHO grade I meningioma. Of note, approximately half (n = 237; 45.5%; **Table 1**) of the meningioma patients were treated with either

TABLE 1 | Pencil beam scanning or passive-scattering proton therapy delivered to presumed or histologically-proven WHO grade I tumors.

Author	#Ref	Year	#pts	Median tumor[∞]/target volume[△] (cm^3)[range]	Mean/median follow-up period (months)	Dose (GyRBE) (median/mean)	Delivery modality	Tumor outcome	Proton only	Visual toxicity[#] (%)	Brain necrosis[ŧ] (%)
[△△]Vlachogiannis et al.	(20)	2017	170	[△]13.0 [1–64]	84.0	14–46 [¶] [21.9]	PSPT	PFS***: 85%	Yes	5/170 (2.9%)	5/170 (2.9%)
El Shafie et al.	(21)	2018	102	NR	46.8	50–60 [50.4]	Raster scanning	PFS**: 96.6%	Yes	0/102 (0%)	3/102 (2.7%)
Murray et al.	(22)	2017	61	[∞] 21.4[0–547][○]	56.9	50.4–56.0 [54.0]	PBS only	LC**: 95.7%	Yes	7/96[¥] (7.3%)	3/96[¥] (3.1%)
Noel et al.	(23)	2005	51	NR	25.4	54–64 [60.6]	PSPT only	LC**: 98%	No	0/51 (0%)	0/51 (0%)
[△△]Halasz et al.	(24)	2011	50	[∞] 2.1[0.3–9.7]	32	10.0–15.5[¶] [13.0]	PBS only	LC*: 94%	Yes	0/50 (0%)	2/50 (4%)
Slater et al.	(25)	2012	47	[△]27.6[1–224]	74.0	50.4–66.6	PSPT only	LC**: 99%	Yes	3/72[¥] (4.2%)	2/72[¥] (2.8%)
Wenkel et al.	(26)	2000	46	[∞] 32[2–243]	53.0	53.1–74.1 [59.0]	PSPT only	RFS***: 88%	No	4/46 (8,7%)	4/46 (8.7%)
[△△]Vernimmen et al.	(27)	2001	23	[△]15.6[2.6–63]	40.0	54–61.6 17.3–24.3[¶] [20.3] [¶]	PBS only	LC**: 88%[¶]	Yes	0/27 (0%)	1/27 (3.7%)
Total # patients			**521**								
Median % LC/PFS (Range)								**96%** (85–99%)			
Median % Toxicity (Range)										**2.6%** (0.0–8.7%)	**3.4%** (0.0–8.7%)

Pts, patients; PBS, Pencil Beam Scanning proton therapy; PSPT, Passive-Scattering Proton Therapy; NR, not reported; LC, Local Control; RFS, Recurrence-free Survival; PFS, Progression-free survival.

**3-year.*

***4/5-year.*

****10 year.*

[¥]Total number of WHO grades I–III patients in cohort.

[¶]Stereotactic condition/radiosurgery/Hypo-fractionated PT, horizontal beam.

[#]Including but not limited to ocular adverse events, retinopathy and optic neuropathy.

[ŧ]Radiological brain edema/biopsy proven brain necrosis/epilepsy.

[∞]Tumor volume.

[△]Target volume/Clinical target volume.

[○]WHO grades I and II.

[△△]Fractionated stereotactic proton therapy/proton radiosurgery.

Bold values provided are highlighting the overall results of patients numbers and outcome (Toxicity and tumor outcome).

hypo-fractionated stereotactic PT (SFPT) or with proton radiosurgery (pSRS). For non-SFPT/pSRS series, the Paul Scherrer Institute recently published the results of 61 WHO grade I meningioma patients treated with pencil beam scanning PT to a median dose of 54 GyRBE (**Table 1**) (22). For those patients progressing/recurring, most of them failed within the treatment field. The estimated tumor local control (LC) and overall survival (OS) was 95.7 and 92.1%, respectively (**Table 1**). The difference in LC rates between benign and non-benign tumors were significantly different (p <0.01) in this PT cohort. Only 1/10 WHO grade I patients had a grade CTCAE 3 adverse event during follow-up. Wenkel et al. reported on 46 WHO grade I meningioma patients (median age, 50 years; range, 11–74) treated with combined photon-proton radiotherapy (26). The ratio of median photon and proton dose was 18.4%, but some patients were treated with photon > proton doses depending on the availability of the proton treatment unit on the Harvard–Cambridge campus. Most tumors (29/46; 63%) were treated for recurrence, either after subtotal (n = 19) or gross total resection (n = 10). Only nine (20%) patients were treated postoperatively with protons. Of note, the dose level delivered by the Boston group is substantially higher (median, 59 GyRBE; **Table 1**) than other groups treating these patients with protons worldwide. After a median follow-up of 53 months (range, 12–207) the estimated recurrence-free- and OS were 88 and 77%, respectively. The 10-year toxicity-free survival was 80%. A substantial number of patients (4/46; 8.7%) presented with visual/ocular toxicity (**Table 1**), and dosimetric analysis revealed that these patients received a maximum median dose of 63.2, 67.5 and 67.4 GyRBE to the Chiasma, Optic nerve left- and right, respectively. Of note, no patient died of progressive disease but one patient died (CTCAE grade 5) of brain necrosis 22 months after therapy. Slater et al. reported another series on 72 skull-base WHO grade I-II meningioma and the outcome of 47 patients with benign tumors (25) was detailed in this paper. The median total doses in the entire cohort for patients (age range, 9–87 years) with and without histologic verification were 59 and 57 GyRBE (range, 50.4–66.6). With a median follow-up of 74 months (range, 3–83), the estimated 5-year LC was 99%. Overall, 6 patients developed radiation induced toxicity, which included visual adverse events (n = 3) and brain necrosis (n = 2). The Heidelberg group reported on 102 skull-base histologically proven (WHO grade I, n = 60) or image-defined meningioma patients treated with proton therapy using the raster scanning delivery paradigm (28). The median age of patients (80% female) was 52 years (range 45–59) and after a median follow-up of 46.8 months, four local progressions were observed. As a result of the small number of events, the median PFS was not reached. The estimated 5-year PFS and OS were 96.6 and 96.2%, respectively (**Table 1**). Three (2.7%) patients developed brain necrosis, of which two were symptomatic, but no visual toxicity was observed. Finally, another skull-base meningioma series was published by the Orsay group in Paris reporting on the outcome of 51 patients (42 females; 82.4%) (23). Forty-four (86.3%) patients had histologically proven WHO grade I meningioma and the median age of patients was 56 years (range, 11–75). The mean/median follow-up period was 25.4/21.0 months with a range of 1–90 months and only local failure was observed. The estimated 4-year LC and OS were 98 and 100%, respectively.

For the SFPT/pSRS series, the largest series originates from the Uppsala group which reported the outcome of 170 WHO grade I meningioma patients (mean age, 54.2 years; 22–85) treated with hypo-fractionated (3–4 GyRBE per fraction) SFPT delivered with a horizontal beam (20). Most of these benign meningiomas (155/170; 86.1%) were skull base tumors in female (135/170; 79.4%) patients treated with five fractions of 4 GyRBE, due to the limited availability of the Gustav Werner cyclotron of 10 weeks annually. Median delivered dose was 21.9 GyRBE (14–46). After a median follow-up of 84 months, the estimated 5- and 10-year progression-free survival rates were 93 and 85%, respectively. Only 3 (1.7%) patients died of meningioma. Radiation-induced adverse events were seen in 16 (9.4%) patients, with pituitary insufficiency (37.5% of all toxicities) being the most common. Brain radiation necrosis was observed in 5 (2.9%) patients, most (4/5) being asymptomatic (**Table 1**). Older patients and patients with tumors located in the middle cranial fossa had a lower risk for tumor progression. The Boston group has also been delivering pSRS for benign meningioma and reported the outcome of these patients with a median follow-up of 32 months (range, 6–133) (24). One fraction of 10.0–15.5 GyRBE (median, 13.0) was delivered to histologically proven or image-defined <4 cm (median volume, 2.1 cm^3) meningiomas. Of note, atypical features were observed in 6 (12%) patients but these features did not meet the criteria for a diagnosis of atypical meningioma. Patients with tumor <2 mm from the optic apparatus were not eligible for pSRS. In this series from 2011, the estimated 3-year local tumor control was 94%. Three (6%) patients presented with radiation-induced complications, of which two were brain complications (**Table 1**). Finally, the South African group have reported the results of 23 WHO grade I skull-base meningioma patients (27). SFPT was delivered either in three fractions with mean dose, 20.3 GyRBE to 18 patients. Noteworthy, 16 fractions or more, with a dose range of 54.0–61.6 GyRBE, was delivered to another five patients. Median volume of these meningiomas was 15.6 cm^3. The median follow-up time was 40 months (range, 13–69). For the SFPT group, two local failures were observed and the estimated 5-year local control was 88%. No events were observed in the fractionated group. One (3.7%) patient in the hypo-fractionated group developed temporal lobe epilepsy.

These data show that protons can either be delivered conventionally, with or without a pencil beam scanning paradigm, or in stereotactic conditions (i.e. SFPT and pSRS). The meningiomas treated with SFPT or pSRS were usually smaller than their non-stereotactic PT counterparts, with a median tumor volume reported in the three series listed in **Table 3** of 13.0, 2.1 and 15.6 cm^3, respectively. Interestingly, no increased toxicity (visual toxicity or brain necrosis) was observed with SFPT/pSRS when compared to PT (**Table 1**). Additionally, the outcome was also identical, with the lowest PFS/RFS at 10 years of 85 and 88% for SFPT/pSRS and PT, respectively (**Table 1**).

PROTON THERAPY FOR WHO GRADE II–III MENINGIOMA

The French group has reported on 24 patients (50% females) with non-benign meningioma (atypical, $n = 19$; malignant, $n = 5$) only treated with postoperative proton/photon therapy (29). Most patients (n = 18; 75%) were treated after subtotal resection to a mean/median total photon/proton dose of 65/68 GyRBE. After a median follow-up time of 32.2 months (range, 1–72), 10 (41.7%) progression/recurrences were observed. The mean RFS interval and estimated 5-year local tumor control were 27.2 months and 46.5%, respectively. Noteworthy, survival was significantly associated with dose, with a cut-off of 60 GyRBE. The relative risk of dying of meningioma was 8.3 (1.2–57; $p = 0.029$) for those not treated at this dose level. One patient developed radiation-induced necrosis 16 months after the delivery of 68 GyRBE-Gy, of which 34 Gy was with photons (**Table 2**). The Paul Scherrer Institute has also reported the outcome of 33 grade II and 2 III meningioma patients treated with protons only (22). The median administered dose was 62 GyRBE with a range of 54 to 68. The majority (9/14; 69%) of all treatment failures from the meningioma cohort were non-benign tumors. The estimated 5-year LC was these tumors was 68%. All but 2 (8/10; 80%) in-field treatment failures were of WHO grade II–III histology. Interestingly, only one brain necrosis (CTCAE grade 3) occurred in a WHO grade II patients (**Table 2**), the other brain necrosis (CTCAE grade 5) and brain edema occurred in WHO grade I patients (**Table 1**). Out of the seven observed visual toxicity, only one occurred in a WHO grade II meningioma patient (**Table 2**). In the Heidelberg series (28), all but two WHO grade II or III meningiomas were treated with carbon ion therapy. The outcome of these two patients treated with protons has not been reported separately. Hug et al. reported on 16 patients treated with photon/proton therapy (**Table 2**). These patients were included in the analysis of a larger (n = 31) cohort of patients with non-benign histology treated with high-dose photon and combined photon/proton therapy (31). Interestingly, the local control of patients treated with protons was significantly ($p = 0.003$) higher than those treated with photons. The same statistical result ($p = 0.025$) applied also for those treated at a dose of 60 GyRBE or higher, regardless of the delivery of photons or protons/photons. In this series, two patients developed symptomatic brain necrosis, one of whom was treated with protons/photons to a dose of 72 Gy RBE (**Table 2**). One last patient treated with 68.4 GyRBE combined photon-proton therapy extensive visual field deficits and retained no functional vision. Finally, Mac Donald et al. reported on 22 WHO grade II meningioma patients (30) treated with protons only. Noteworthy, 6 patients had presumed radiation-induced meningiomas. After a follow-up period of 7–104 months (mean, 39.2), five patients progressed/recurred. The estimated 5-year LC was 71.1% (**Table 2**). The authors have seen the same impact on radiation dose and patient's outcome as did the French (29) and other US (31) groups. The 5-year LC of those patients treated with > and ≤60 GyRBE were 87.5 and 50%, respectively ($p = 0.038$). One symptomatic CTCAE grade III temporal lobe necrosis was observed (**Table 2**). No SFPT or pSRS delivery was reported for non-benign meningiomas.

RE-IRRADIATION WITH PROTON THERAPY FOR RECURRENT MENINGIOMA AFTER RADIOTHERAPY

The Heidelberg group reported on 42 recurring patients who underwent prior RT for their meningioma (21). Compatible with the treatment policy of this center, most meningioma patients (34/42; 81%) were considered high-risk patients as a result of tumor volume, WHO grading or individual patient's history, and were thus treated with carbon ion therapy. Only 8 (19%) patients were retreated with PT. For the entire cohort, the median follow-up time was 49.7, with a male/female gender ratio of 0.68. Most patients had a WHO grade II ($n = 25$) or III ($n = 6$) recurring tumor. Due to the limited number of patients, the analysis has been made with the combined carbon ion therapy and PT patients. The 1- and 2-year PFS were 71 and 56.5%, respectively. The median PFS for all patients was 34.3 months. Interestingly, the difference in PFS between WHO grades I and II–III tumors was significant ($p = 0.03$). The estimated median, 1- and 2-year OS was 61 months, 89.6 and 71.4%, respectively. Three (7.1%) patients presented with radiation-induced brain necrosis. All these patients presented with WHO grade II ($n = 1$) and III ($n = 2$) meningiomas and were retreated with 51 GyRBE delivered with carbon ions after an initial photon dose delivery of 54, 60 and 60 Gy, respectively. Additionally, four patients (9.5%) had worsening of their visual symptoms during follow-up.

Another series reported on the outcome of 16 recurring meningioma (WHO grade I, seven; grade II, eight and WHO grade 3, one) patients re-treated with PT (32). The median photon and proton dose for the initial treatment and for the re-irradiation was 54 Gy (range, 13–65.5) and 60 GyRBE (range, 30–66.6), respectively. After a median follow-up of 18.8 months after PT, 7 (44%) intracranial recurrences/progression were observed. The estimated 2-year RFS and OS were 43 and 94%, respectively. Patients with benign recurring meningioma had a significantly ($p = 0.03$) longer PFS than those with non-benign tumors. Of note, the late high-grade toxicity was substantial. Overall, 5 (31%) patients (median age, 72.9 years; range, 58.4–75.1) with WHO grade II ($n = 4$) and I ($n = 1$) tumors presented with late grade 3 toxicity, consisting of hydrocephalus ($n = 3$), seizures ($n = 1$) and carotid stenosis with consequentially cerebrovascular ischemia ($n = 1$). Three, one and one patients received 60, 59.4 and 54 GyRBE proton dose respectively for their re-treatment. No death resulting from this re-irradiation with protons was observed.

DISCUSSION

WHO grade I meningioma accounts for a substantial number of primary brain tumors in adults and are the most prevalent

TABLE 2 | Pencil beam scanning or passive-scattering photon/proton therapy delivered to presumed or histologically-proven WHO grade II-III tumors.

Author	#Ref	Year	#pts	Median tumor[∞]/target volume[△](cm^3)[range]	WHOgrade	Mean/median follow-up period (months)	Dose (GyRBE) [median/mean]	Delivery modality	Tumor outcome	Protononly	Visual toxicity[#](%)	Brainnecrosis[t] (%)
Murray et al.	(22)	2017	35	[∞] 21.4[0–547] [○]	II–III	56.9[¶]	54–68 [62.0]	PBS	LC**: 68.0%	Yes	1/35 (1.5%)	1/35 (2.9%)
Boskos et al.	(29)	2009	24	[∞] 48.3[0–120]	II–III	32.2	0–34[¥] 28.8–68[¥¥] [68.0]	PSPT	LC**: 46.7%	No	0/24 (0%)	1/24 (4.2%)
McDonald et al.	(30)	2015	22	[∞] 8.1[0–89.3]	II only	39.0	54–68.4 [63.0]	PSPT	LC**: 71.1%	Yes	0/22 (0%)	1/22 (4.5%)
Hug et al.	(31)	2000	16	NR	II–III	59.0[∅]	40–72 [62–58] [#]	PSPT	LC**: 38–52%[#]	No	1/16 (6.3%)	1/16 (6.3%)
Total # patients			**97**									
Median % LC/ PFS (Range)									**52%** (38.0–71.1)			
Median % Toxicity (Range)											**0.8%** (0–6.4)	**4.4%** (2.9–6.3)

Pts, patients; WHO, World Health Organization; PBS, Pencil Beam Scanning proton therapy; PSPT, Passive-Scattering Proton Therapy; NR, not reported; LC, Local Control; RFS, Recurrence-free Survival; PFS, Progression-free survival.

***4/5-year.*

[¥]Photon dose.

[¥¥]Proton dose.

[¶]Entire meningioma WHO grades I–III cohort.

[#]Mean dose/local control rate for WHO grades II and III, respectively.

[t]Radiological brain edema/biopsy proven brain necrosis/epilepsy.

[∅]Mean follow-up interval for the photon only and photon/proton treatments.

[∞]Tumor volume.

[△]Target volume/clinical target volume.

[○]WHO grades I and II.

Bold values provided are highlighting the overall results of patients numbers and outcome (Toxicity and tumor outcome).

benign primary neoplasm of the brain. RT has been used with curative attempt in WHO grade meningioma patients whose tumors are not amenable to surgery, for subtotally resected (Simpson >III) tumors, for recurrent tumors or more rarely in the adjuvant setting (33). This treatment modality is an important component of the therapeutic armamentarium for meningioma delivered to mostly elderly patients. However, RT can result in a number of radiation-induced adverse events, including but not limited to cognitive impairment, pituitary dysfunction and secondary cancers. Regarding the former, a systematic review of 11 published series assessing the impact of surgery on the cognitive functioning of meningioma patients observed that most of these patients suffer from deficits in several cognitive domains comparative to the normative values (34). Interestingly, surgery seemed to improve cognitive function in most of these studies. Three series assessed the cognitive function of meningioma patients undergoing RT after surgery. Most of these studies (35, 36) but not all (37), showed that RT with or without surgery had an impact on the patients' visual, verbal and working memory when compared to healthy controls, although the specific cognitive impairment attributable to RT alone was not assessed and no pre-treatment assessment of cognitive function was performed, which are both major disclaimers in the interpretation of these results. Nevertheless, it is safe to say that any radiation modality that could decrease the likelihood of cognitive impairment in elderly patients who are at risk of such a complication would be advisable.

The precise position of the Bragg peak (38) within the meningeal tumor has the possibility to decrease the dose delivered to critical structures within the brain and to decrease the overall brain integral dose. A recent dose comparative planning study assessing photon and proton therapy techniques for 20 meningioma >3 cm in size reported a mean dose and brain volumes receiving intermediate radiation dose (i.e. 20–30 Gy) approximately 50% lower ($p \leq 0.01$) with intensity modulated PT (15). Additionally, the dose delivered to 40% of the bilateral hippocampus was significantly decreased by 74% in this study. These results are in line with other studies (39). Dose comparison analysis of PT *vs.* volumetric modulated arc photon radiotherapy have shown that integral doses were significantly ($p < 0.01$) higher in all photon plans with a reduction of approximately 50% with PT (40). Substantial clinical evidence (41), while not unanimous (42), supports the notion that radiation-induced injury to the hippocampus may correlates with neurocognitive outcome of patients who are treated with RT. As such, PT may decrease the likelihood of long-term cognitive impairment and may be an option for elderly meningioma patients who are at greater risk of cognitive dysfunction or those younger patients with pre-existing clinically relevant neurocognitive impairment (**Table 3**).

The survival of benign meningioma patients is substantial and secondary tumors may be observed after the delivery of adjuvant or radical radiation therapy (44). As such, any therapeutic modality that decreases the risk of radiation-induced tumors should be offered when appropriate. Chung et al. compared the reduction of secondary cancer risk in 558 pediatric and adult proton patients with matched photon patients identified in the SEER database (45). The observed secondary cancer incidence at 10 years was significantly decreased from 8.6% with photons to 5.4% with protons (Hazard ratio of 0.54; p <0.09). Importantly protons were delivered to patients with a passive scattering delivery paradigm that produced more neutrons than PBS (46, 47). The latter delivery may thus produce even less radiation-induced malignancies. It is noteworthy that the majority of meningioma patients managed with protons have been treated with a passive scattering delivery mode, as shown in **Tables 1** and **2**.

Radiation therapy is also a risk factor for developing radiation-induced meningioma and other tumors, and have been observed in 2.4–2.7% of patients in large case-series with a long (i.e. 20 years) follow-up period (48, 49). The use of conformal treatment such as PT may decrease the likelihood of developing secondary neoplasms by decreasing the low-bath dose delivered to the brain. The larger the meningioma is, the highest would be the theoretical advantage, as suggested by other authors (**Table 3**) (50, 51), for tumor induction and the aforementioned cognitive toxicity of this treatment modality. Theoretical tumor induction computations have shown in children that protons significantly decrease the risk of this unwanted complication (52), and the same effect has been

TABLE 3 | Indications for proton therapy in the management of WHO grades I–III meningioma.

Meningioma (WHO grade)	Treatment paradigm	Use of protons	Dose (GyRBE)	Level of evidence*	References
I (Benign)	Decrease in long term toxicity	Should be considered if clinically available for decreasing the probability of tumor induction	50.4–54	5	Bolsi et al. (43)
I (Benign)	Decrease in long term toxicity	Should be considered if clinically available for decreasing the probability of cognitive impairment	50.4–54	5	Florijn et al. (15)
II–III (Atypical/ Malignant)	Dose escalation for tumor control	Should be considered if clinically available	>54.0	3b	McDonald et al. (30), Hug et al. (31), Boskos et al. (29)
Recurring (I–III)	Tumor control and mitigate the risk of radiation-induced adverse events	Should be considered if clinically available and especially if: * Non-elderly patient * Initial Benign histology * Previous irradiation at <60 Gy	≤60 (retreatment)	4	Imber et al. (32) El Shafie et al. (21)

Oxford Centre for Evidence-Based Medicine. http://www.cebm.net/index.aspx?o=5653.

suggested in adults with meningioma (43). Arvold et al. predicted a tumor-induction reduction of 50% with protons in a computational study on benign meningioma (39).

That being said, the potential benefit of PT has to be weighed against its substantial additional costs when compared to photon radiotherapy (53). Over 500 WHO grade I or image-defined meningioma have been treated with PT (**Table 1**). The clinical results (5-year LC >95% and toxicity rates) appear to be in line with the photon series. No cost effectiveness analysis has been made so far for PT delivered to this benign tumor. Based on the limited level of evidence (**Table 3**), PT can be considered for a benign meningioma patients if volumetrically challenging or if the patient has a higher risk of presenting radiation-induced toxicity after treatment.

WHO grade II and III meningiomas are tumors with poorer prognosis than benign meningiomas (54). Although the incidence has been substantially increased with the new 2016 WHO meningioma classification, it is still considerably lower than their benign counterparts. As such, the number of patients treated with protons for non-benign meningioma is substantially lower than for WHO grade I tumors by an order of 5 (**Tables 1**, **2**). These former tumors, especially WHO grade III meningiomas, show a local aggressive behavior, with or without distant brain or non-brain failures (55, 56). Although, the administration of radiation for WHO grade III tumors is certain, the role of radiotherapy for WHO grade II tumors is less clearly defined (57). Several survey have shown that only a minority of centers would recommend RT after Simpson I–III resection for WHO grade II meningioma (58). To address this important question, a phase III intergroup trial (ROAM; EORTC 1308) has been activated in 2016 randomizing Simpson 1–3 WHO grade II meningioma patients between observation and adjuvant RT delivering 59.4 Gy (59). This active study has an accrual target of 190 patients and over 60% of the patients have been currently accrued in this trial in Europe, Australia and New-Zealand. A systematic survey of 10 studies of adjuvant RT for grade II and III tumors showed that incomplete resection and dose delivered of <50 Gy were associated with a poorer 5-year PFS (60). Several retrospective analyses (**Table 2**) (29–31) of PT series have shown that increasing the delivered radiation dose may improve the patient outcomes. This parallels the experience with photon series (61–63). These dose–response observations in various analyses may validate the use of PT used with a dose-escalation paradigm (**Table 3**). A recent prospective European study (EORTC 22042-26042) has shown that the delivery of 60 Gy with photon-RT for Simpson I–III WHO grade II meningioma was associated with substantial toxicity, as grade 3–4 adverse event were observed in 10.7 and 3.6% of patients, respectively (64). This phase II-parallel non-randomized study assessed also the efficacy of high-dose radiotherapy in three other independent cohorts. Although the toxicity of the observational study for Simpson IV–V tumors treated with 70 Gy using photons has never been reported due to the small patients' numbers, the toxicity of photon treatments at this dose level was notable (Weber DC, *personal communication*). As such, if moderate dose escalation is pursued, using the physical advantage of the proton beam's properties to conform the dose deposition at a specific depth, the administration of PT in non-benign meningioma should be considered (**Table 3**). This has been the dose-strategy of all groups delivering PT for non-benign meningioma with doses up to 72 GyRBE (median/mean, 62–68) administered to these patients with no demonstrable increase the reported toxicity (**Table 2**). The reported outcome after PT is good, with a median 5-year LC of 52% for WHO grade II–III tumors (**Table 2**) but caution should be exercised not to over-estimate these results due to the small number (16–35; median 23) of patients and short follow-up intervals of those series (**Table 2**). The level of evidence justifying the administration of PT for non-benign meningioma, as with its benign counterpart, is low (**Table 3**).

The management of recurring or progressing meningioma after RT, especially high-grade tumors, is challenging. The therapeutic strategy is often limited but salvage options may include additional surgery and/or re-treatment with a radiation-modality such as brachytherapy (65, 66), photon radiotherapy including but not limited to normo- or hypo-fractionated radiotherapy/radiosurgery, and PT (32). Systemic therapy, including the administration of check-point inhibitors (67), is usually ineffective and rarely translates into radiological objective responses, although WHO grades II–III meningioma patients appear to benefit more from chemotherapy than whose with grade I disease (5, 68). Re-challenging these patients with radiation therapy again could potentially cause serious radiation-induced adverse events, as the organs at risk, including but not limited to the optic apparatus, brainstem and cochlea, have received a substantial dose of radiation already. As such, re-irradiation should be performed using highly conformal radiation techniques. The dose-deposition of particle therapy offers excellent sparing of organs at risk in direct vicinity of the recurrent tumor (**Figure 2**). Dose comparison analysis of PT *vs.* volumetric modulated arc photon radiotherapy have shown that integral doses were significantly (p <0.01) higher in all photon plans with a reduction of approximately 50% with PT (40) for recurring meningioma treated with re-irradiation. Using these techniques does not however nullify this risk, as illustrated in the Imber et al. study which reported a >30% rate of high-grade late radiation induced adverse events (32). Assessing the characteristics of these patients with late toxicity, it seems that age (median age, 72.9 years) and previous administered dose (median, 60 Gy) are important factors to consider when assessing the possibility of re-irradiating recurrent meningioma treated with prior RT with protons. Thus, one should consider PT for re-irradiation of non-elderly patients with recurring WHO grade I tumors treated previously with 50.4–54 Gy of radiation (**Table 3**), as those have the highest PFS and the lowest toxicity rates after re-irradiation. As for newly diagnosed or recurrent meningiomas treated with upfront PT, with or without surgery, the level of clinical evidence justifying the use of protons for re-irradiation is low (**Table 3**).

Regarding patient outcomes, most series reporting the results of PT for the management of WHO I and II–III tumors have shown that the local tumor control or survival of non-benign meningioma patients is lower than for patients with WHO grade I tumors (**Tables 1**, **2**). The Swiss group demonstrated that the

5-year LC rate was significantly lower (68 *vs.* 95.7%) for non-benign meningiomas when compared to WHO grade I tumors (22). This decrease in outcome-metrics is observed for non-benign meningiomas, even when these challenging tumors are treated with a dose-escalation paradigm (**Table 2**). This observed trend mirrors the results of modern photon RT series that report a PFS for atypical meningioma of approximately 70% (69). As such, we must be aware of developing a zealotry about PT for non-benign meningiomas and health providers must consider all existing published evidence before advocating protons for the management of these tumors. Possible explanation for this finding include but are not limited to the referral bias of large/recurrent tumors treated with PT, the span of multiple eras of proton technology (passive scattering, pencil beam scanning, intensity modulated PT, proton radiosurgery) and imbalances between the photon and proton groups with respect to known (age, gender, Simpson resection grade, tumor size, mitotic index) (69–71) and unknown baseline prognostic factors. Additionally, small patient numbers for this rare tumor and differences in patient cohorts between the photon and proton series complicate the interpretation of these findings.

PT is usually delivered to large and volumetrically complex meningiomas. The mean largest volume in the WHO grade 1 PT series is 193 cm^3 (**Table 1**) and is usually larger than in photon series. It may be highly appropriate to treat these challenging patients with highly conformal radiation with a treatment modality that decreases the integral brain dose. The radiosurgery series have shown undisputedly that the largest the tumor volume is, the highest the likelihood of observing a radiation-induced adverse effect. A recent US series reporting on WHO grade I and II meningiomas treated with radiosurgery, has shown that patients who experienced cerebral edema were more significantly (p = 0–028) likely present with larger tumors on univariate analysis (72). These results are in line with other recent series (73–75). These clinical data legitimate thus the use of protons for selected meningioma patients with large tumors, especially if treated in a dose-escalation paradigm.

Visual toxicity and/or brain necrosis are classical complications of high-dose RT for the treatment of meningioma, too well known to merit a repeat citation here. It is reassuring to observe that proton series with a dose-escalation paradigm have not reported increased toxicity to the optic apparatus or brain (**Table 2**), when compared to photon series (76, 77). Taking the modern PT series, the observed rate of visual or brain toxicity is 0–1.5 and 2.9–4.5%, respectively (**Table 2**). In these PT series, radiation-induced toxicity was usually observed when the dose constraints were relaxed, such as those patients treated with 63.2–67.4 GyRBE to the optic apparatus (26). It is important however to note that adverse events occur with photon or proton radiation even when the dose constraints are consciously met and when the patient has no risk factors (76). In the Swiss series, the only grade 5 brain necrosis occurred in a WHO grade I patient treated with 54 GyRBE with all dose-constraints met. In the same series, the two optic nerve and the two other retinopathy observed were also planned respecting all optic apparatus dose constraints. Regarding the toxicity on these organs at risk, several groups have tried to identify dose metrics predictive of clinically relevant toxicity (78–82) but the results are not robust and the implementation of these constraints is problematic in some patients with WHO grade II or III tumors. Care should be taken that patients should be aware of these rare adverse events in the informed consent process that should adhere to national guidelines.

Our review has a number of limitations that future studies should address. Firstly, all reviewed data are retrospective in nature and are thus subject to a known and unknown biases that have been only partially discussed in this section of the manuscript. The reviewed data lacked prospectively captured patient-reported outcomes and quality of life that are important in the area of modern neuro-oncology. PSI will submit soon the analysis of the QoL of meningioma patients treated with protons using the EORTC C30 and BN20 questionnaires. These data will also enhance substantially our understanding of how exactly PT may distinguish itself clinically from other radiation modalities. Prospective cohort studies from other institutions will greatly benefit our understanding of meningioma patient outcomes treated with protons and are arguably required at this juncture in time. The concept of an international prospective registry, such as the one proposed by the European Particle Therapy Network in its Clinical Work-package 1 (83), performed under a standardized protocol is immeasurably desirable, for it will allow more homogenous data to accumulate from multiple European experiences. These could then bolster our ability to perform more robust bias assessments, assess the true value of protons for this indication and justify any decision-algorithms, with or without cost–benefit analyses. Finally, the relatively short follow-up time and more importantly the limited number of patients in the cohorts limit somehow the generated level of evidence, especially so for secondary malignancies.

CONCLUSIONS

The delivery of PT for the treatment of intracranial meningioma may be discussed in clinical settings including but not limited to volumetrically challenging tumors, non-benign histology or for the re-irradiation of recurring/progressive tumors. Patient with a high-risk of radiation induced toxicity may also benefit from the decrease of dose delivered to critical structures such as the optic apparatus and the brain. The outcome of approximately 500 WHO grade I meningioma patients have been reported with excellent tumor control rates and rare radiation-induced adverse events. For WHO grade II–III meningiomas treated with a dose-escalation paradigm, the toxicity profile is clinically acceptable. Re-irradiation of progressing/recurring tumors with protons should be discussed on a case to case basis and should be limited to those younger patients with benign tumors that should most benefit from protons.

AUTHOR CONTRIBUTIONS

DW, AB, and MJ wrote the paper. NB provided the figures and Legends and wrote one section of the MS. All authors contributed to the article and approved the submitted version.

REFERENCES

1. Wiemels J, Wrensch M, Claus EB. Epidemiology and etiology of meningioma. *J Neuro Oncol* (2010) 99(3):307–14. doi: 10.1007/s11060-010-0386-3
2. Louis DN, Perry A, Reifenberger G, von Deimling A, Figarella-Branger D, Cavenee WK, et al. The 2016 World Health Organization Classification of Tumors of the Central Nervous System: a summary. *Acta Neuropathol* (2016) 131(6):803–20. doi: 10.1007/s00401-016-1545-1
3. Islim AI, Kolamunnage-Dona R, Mohan M, Moon RDC, Crofton A, Haylock BJ, et al. A prognostic model to personalize monitoring regimes for patients with incidental asymptomatic meningiomas. *Neuro-oncology* (2020) 22 (2):278–89. doi: 10.1093/neuonc/noz160
4. Islim AI, Mohan M, Moon RDC, Srikandarajah N, Mills SJ, Brodbelt AR, et al. Incidental intracranial meningiomas: a systematic review and meta-analysis of prognostic factors and outcomes. *J Neuro Oncol* (2019) 142(2):211–21. doi: 10.1007/s11060-019-03104-3
5. Brastianos PK, Galanis E, Butowski N, Chan JW, Dunn IF, Goldbrunner R, et al. Advances in multidisciplinary therapy for meningiomas. *Neuro-oncology* (2019) 21(Suppl 1):i18–31. doi: 10.1093/neuonc/noy136
6. Nassiri F, Mamatjan Y, Suppiah S, Badhiwala JH, Mansouri S, Karimi S, et al. DNA methylation profiling to predict recurrence risk in meningioma: development and validation of a nomogram to optimize clinical management. *Neuro-oncology* (2019) 21(7):901–10. doi: 10.1093/neuonc/noz061
7. Sahm F, Schrimpf D, Stichel D, Jones DTW, Hielscher T, Schefzyk S, et al. DNA methylation-based classification and grading system for meningioma: a multicentre, retrospective analysis. *Lancet Oncol* (2017) 18(5):682–94. doi: 10.1016/S1470-2045(17)30155-9
8. Weber DC, Bogner J, Verwey J, Georg D, Dieckmann K, Escude L, et al. Proton beam radiotherapy versus fractionated stereotactic radiotherapy for uveal melanomas: A comparative study. *Int J Radiat Oncol Biol Phys* (2005) 63 (2):373–84. doi: 10.1016/j.ijrobp.2005.01.057
9. Lomax AJ. Charged particle therapy: the physics of interaction. *Cancer J* (2009) 15(4):285–91. doi: 10.1097/PPO.0b013e3181af5cc7
10. Lomax A. Intensity modulation methods for proton radiotherapy. *Phys Med Biol* (1999) 44(1):185–205. doi: 10.1088/0031-9155/44/1/014
11. Lambrecht M, Eekers DBP, Alapetite C, Burnet NG, Calugaru V, Coremans IEM, et al. Radiation dose constraints for organs at risk in neuro-oncology; the European Particle Therapy Network consensus. *Radiother Oncol* (2018) 128 (1):26–36. doi: 10.1016/j.radonc.2018.05.001
12. Zureick AH, Evans CL, Niemierko A, Grieco JA, Nichols AJ, Fullerton BC, et al. Left hippocampal dosimetry correlates with visual and verbal memory outcomes in survivors of pediatric brain tumors. *Cancer* (2018) 124(10):2238–45. doi: 10.1002/cncr.31143
13. Vatner RE, Niemierko A, Misra M, Weyman EA, Goebel CP, Ebb DH, et al. Endocrine Deficiency As a Function of Radiation Dose to the Hypothalamus and Pituitary in Pediatric and Young Adult Patients With Brain Tumors. *J Clin Oncol* (2018) 36(28):2854–62. doi: 10.1200/JCO.2018.78.1492
14. Adeberg S, Harrabi SB, Bougatf N, Verma V, Windisch P, Bernhardt D, et al. Dosimetric Comparison of Proton Radiation Therapy, Volumetric Modulated Arc Therapy, and Three-Dimensional Conformal Radiotherapy Based on Intracranial Tumor Location. *Cancers (Basel)* (2018) 10(11):401. doi: 10.3390/cancers10110401
15. Florijn MA, Sharfo AWM, Wiggenraad RGJ, van Santvoort JPC, Petoukhova AL, Hoogeman MS, et al. Lower doses to hippocampi and other brain structures for skull-base meningiomas with intensity modulated proton therapy compared to photon therapy. *Radiother Oncol* (2020) 142:147–53. doi: 10.1016/j.radonc.2019.08.019
16. Dinh J, Stoker J, Georges RH, Sahoo N, Zhu XR, Rath S, et al. Comparison of proton therapy techniques for treatment of the whole brain as a component of craniospinal radiation. *Radiat Oncol* (2013) 8:289. doi: 10.1186/1748-717X-8-289
17. McGowan SE, Albertini F, Thomas SJ, Lomax AJ. Defining robustness protocols: a method to include and evaluate robustness in clinical plans. *Phys Med Biol* (2015) 60(7):2671–84. doi: 10.1088/0031-9155/60/7/2671
18. Unkelbach J, Alber M, Bangert M, Bokrantz R, Chan TCY, Deasy JO, et al. Robust radiotherapy planning. *Phys Med Biol* (2018) 63(22):22TR02. doi: 10.1088/1361-6560/aae659
19. Paganetti H. Relative biological effectiveness (RBE) values for proton beam therapy. Variations as a function of biological endpoint, dose, and linear energy transfer. *Phys Med Biol* (2014) 59(22):R419–72. doi: 10.1088/0031-9155/59/22/R419
20. Vlachogiannis P, Gudjonsson O, Montelius A, Grusell E, Isacsson U, Nilsson K, et al. Hypofractionated high-energy proton-beam irradiation is an alternative treatment for WHO grade I meningiomas. *Acta Neurochir (Wien)* (2017) 159(12):2391–400. doi: 10.1007/s00701-017-3352-4
21. El Shafie RA, Czech M, Kessel KA, Habermehl D, Weber D, Rieken S, et al. Evaluation of particle radiotherapy for the re-irradiation of recurrent intracranial meningioma. *Radiat Oncol* (2018) 13(1):86. doi: 10.1186/s13014-018-1026-x
22. Murray FR, Snider JW, Bolsi A, Lomax AJ, Walser M, Kliebsch U, et al. Long-Term Clinical Outcomes of Pencil Beam Scanning Proton Therapy for Benign and Non-benign Intracranial Meningiomas. *Int J Radiat Oncol Biol Phys* (2017) 99(5):1190–98. doi: 10.1016/j.ijrobp.2017.08.005
23. Noel G, Bollet MA, Calugaru V, Feuvret L, Haie-Meder C, Dhermain F, et al. Functional outcome of patients with benign meningioma treated by 3D conformal irradiation with a combination of photons and protons. *Int J Radiat Oncol Biol Phys* (2005) 62(5):1412–22. doi: 10.1016/j.ijrobp.2004.12.048
24. Halasz LM, Bussiere MR, Dennis ER, Niemierko A, Chapman PH, Loeffler JS, et al. Proton stereotactic radiosurgery for the treatment of benign meningiomas. *Int J Radiat Oncol Biol Phys* (2011) 81(5):1428–35. doi: 10.1016/j.ijrobp.2010.07.1991
25. Slater JD, Loredo LN, Chung A, Bush DA, Patyal B, Johnson WD, et al. Fractionated proton radiotherapy for benign cavernous sinus meningiomas. *Int J Radiat Oncol Biol Phys* (2012) 83(5):e633–7. doi: 10.1016/j.ijrobp.2012.01.079
26. Wenkel E, Thornton AF, Finkelstein D, Adams J, Lyons S, De La Monte S, et al. Benign meningioma: partially resected, biopsied, and recurrent intracranial tumors treated with combined proton and photon radiotherapy. *Int J Radiat Oncol Biol Phys* (2000) 48(5):1363–70. doi: 10.1016/S0360-3016(00)01411-5
27. Vernimmen FJ, Harris JK, Wilson JA, Melvill R, Smit BJ, Slabbert JP. Stereotactic proton beam therapy of skull base meningiomas. *Int J Radiat Oncol Biol Phys* (2001) 49(1):99–105. doi: 10.1016/S0360-3016(00)01457-7
28. El Shafie RA, Czech M, Kessel KA, Habermehl D, Weber D, Rieken S, et al. Clinical outcome after particle therapy for meningiomas of the skull base: toxicity and local control in patients treated with active rasterscanning. *Radiat Oncol* (2018) 13(1):54. doi: 10.1186/s13014-018-1002-5
29. Boskos C, Feuvret L, Noel G, Habrand JL, Pommier P, Alapetite C, et al. Combined proton and photon conformal radiotherapy for intracranial atypical and malignant meningioma. *Int J Radiat Oncol Biol Phys* (2009) 75 (2):399–406. doi: 10.1016/j.ijrobp.2008.10.053
30. McDonald MW, Plankenhorn DA, McMullen KP, Henderson MA, Dropcho EJ, Shah MV, et al. Proton therapy for atypical meningiomas. *J Neurooncol* (2015) 123(1):123–8. doi: 10.1007/s11060-015-1770-9
31. Hug EB, Devries A, Thornton AF, Munzenride JE, Pardo FS, Hedley-Whyte ET, et al. Management of atypical and malignant meningiomas: role of high-dose, 3D-conformal radiation therapy. *J Neurooncol* (2000) 48(2):151–60. doi: 10.1023/a:1006434124794
32. Imber BS, Neal B, Casey DL, Darwish H, Lin AL, Cahlon O, et al. Clinical Outcomes of Recurrent Intracranial Meningiomas Treated with Proton Beam Reirradiation. *Int J Part Ther* (2019) 5(4):11–22. doi: 10.14338/IJPT-18-00045.1
33. Day SE, Halasz LM. Radiation therapy for WHO grade I meningioma. *Chin Clin Oncol* (2017) 6(Suppl 1):S4. doi: 10.21037/cco.2017.06.01
34. Meskal I, Gehring K, Rutten GJ, Sitskoorn MM. Cognitive functioning in meningioma patients: a systematic review. *J Neurooncol* (2016) 128(2):195–205. doi: 10.1007/s11060-016-2115-z
35. Waagemans ML, van Nieuwenhuizen D, Dijkstra M, Wumkes M, Dirven CM, Leenstra S, et al. Long-term impact of cognitive deficits and epilepsy on quality of life in patients with low-grade meningiomas. *Neurosurgery* (2011) 69 (1):72–8. discussion 78-9. doi: 10.1227/NEU.0b013e318212badb
36. Dijkstra M, van Nieuwenhuizen D, Stalpers LJ, Wumkes M, Waagemans M, Vandertop WP, et al. Late neurocognitive sequelae in patients with WHO grade I meningioma. *J Neurol Neurosurg Psychiatry* (2009) 80(8):910–5. doi: 10.1136/jnnp.2007.138925
37. van Nieuwenhuizen D, Klein M, Stalpers LJ, Leenstra S, Heimans JJ, Reijneveld JC. Differential effect of surgery and radiotherapy on

neurocognitive functioning and health-related quality of life in WHO grade I meningioma patients. *J Neurooncol* (2007) 84(3):271–8. doi: 10.1007/s11060-007-9366-7
38. Rogers L, Barani I, Chamberlain M, Kaley TJ, McDermott M, Raizer J, et al. Meningiomas: knowledge base, treatment outcomes, and uncertainties. A RANO review. *J Neurosurg* (2015) 122(1):4–23. doi: 10.3171/2014.7.JNS131644
39. Arvold ND, Niemierko A, Broussard GP, Adams J, Fullerton B, Loeffler JS, et al. Projected second tumor risk and dose to neurocognitive structures after proton versus photon radiotherapy for benign meningioma. *Int J Radiat Oncol Biol Phys* (2012) 83(4):e495–500. doi: 10.1016/j.ijrobp.2011.10.056
40. Poel R, Stuessi Lobmaier A, Andratschke N, Unkelbach J, Tanadini-Lang S, Guckenberger M, et al. Dosimetric comparison of protons vs photons in re-irradiation of intracranial meningioma. *Br J Radiol* (2019) 92(1100):20190113. doi: 10.1259/bjr.20190113
41. Gondi V, Deshmukh S, Brown P. Preservation of neurocognitive function (NCF) with Conformal avoidance of the hippocampus during whole-brain radiotherapy (HA-WBRT) for brain metastases: preliminary results of phase III trial NRG Oncology CC001. *Int J Radiat Oncol Biol Phys* (2018) 102:1607. doi: 10.1016/j.ijrobp.2018.08.056
42. Belderbos J, Phd M, De Ruysscher D. OC-0503 Phase III trial of prophylactic cranial irradiation with or without hippocampus avoidance in SCLC. *Radiother Oncol* (2019) 133:S259. doi: 10.1016/S0167-8140(19)30923-5
43. Bolsi A, Fogliata A, Cozzi L. Radiotherapy of small intracranial tumours with different advanced techniques using photon and proton beams: a treatment planning study. *Radiother Oncol* (2003) 68(1):1–14. doi: 10.1016/S0167-8140(03)00117-8
44. Labuschagne JJ, Chetty D. Glioblastoma multiforme as a secondary malignancy following stereotactic radiosurgery of a meningioma: case report. *Neurosurg Focus* (2019) 46(6):E11. doi: 10.3171/2019.3.FOCUS1948
45. Chung CS, Yock TI, Nelson K, Xu Y, Keating NL, Tarbell NJ. Incidence of second malignancies among patients treated with proton versus photon radiation. *Int J Radiat Oncol Biol Phys* (2013) 87(1):46–52. doi: 10.1016/j.ijrobp.2013.04.030
46. Wang X, Poenisch F, Sahoo N, Zhu RX, Lii M, Gillin MT, et al. Spot scanning proton therapy minimizes neutron dose in the setting of radiation therapy administered during pregnancy. *J Appl Clin Med Phys* (2016) 17(5):366–76. doi: 10.1120/jacmp.v17i5.6327
47. Baradaran-Ghahfarokhi M, Reynoso F, Darafsheh A, Sun B, Prusator MT, Mutic S, et al. A Monte Carlo based analytic model of the in-room neutron ambient dose equivalent for a Mevion gantry-mounted passively scattered proton system. *J Radiol Prot* (2020) 40(4):980–96. doi: 10.1088/1361-6498/abaff4
48. Breen P, Flickinger JC, Kondziolka D, Martinez AJ. Radiotherapy for nonfunctional pituitary adenoma: analysis of long-term tumor control. *J Neurosurg* (1998) 89(6):933–8. doi: 10.3171/jns.1998.89.6.0933
49. Minniti G, Traish D, Ashley S, Gonsalves A, Brada M. Risk of second brain tumor after conservative surgery and radiotherapy for pituitary adenoma: update after an additional 10 years. *J Clin Endocrinol Metab* (2005) 90(2):800–4. doi: 10.1210/jc.2004-1152
50. Ahmed SK, Brown PD, Foote RL. Protons vs Photons for Brain and Skull Base Tumors. *Semin Radiat Oncol* (2018) 28(2):97–107. doi: 10.1016/j.semradonc.2017.11.001
51. Kosaki K, Ecker S, Habermehl D, Rieken S, Jakel O, Herfarth K, et al. Comparison of intensity modulated radiotherapy (IMRT) with intensity modulated particle therapy (IMPT) using fixed beams or an ion gantry for the treatment of patients with skull base meningiomas. *Radiat Oncol* (2012) 7:44. doi: 10.1186/1748-717X-7-44
52. Miralbell R, Lomax A, Cella L, Schneider U. Potential reduction of the incidence of radiation-induced second cancers by using proton beams in the treatment of pediatric tumors. *Int J Radiat Oncol Biol Phys* (2002) 54(3):824–9. doi: 10.1016/S0360-3016(02)02982-6
53. Weber DC, Grau C, Lim PS, Georg D, Lievens Y. Bringing Europe together in building clinical evidence for proton therapy - the EPTN-ESTRO-EORTC endeavor. *Acta Oncol* (2019) 58(10):1340–42. doi: 10.1080/0284186X.2019.1624820
54. Weber DC, Lovblad KO, Rogers L. New pathology classification, imagery techniques and prospective trials for meningiomas: the future looks bright. *Curr Opin Neurol* (2010) 23(6):563–70. doi: 10.1097/WCO.0b013e328340441e
55. Bender L, Lhermitte B, Carinato H, Baloglu S, Helali M, Cebula H, et al. Grade III meningioma with gastro-intestinal tract and brain metastases: case report and review of the literature. *World J Surg Oncol* (2019) 17(1):70. doi: 10.1186/s12957-019-1596-6
56. Limarzi F, Solaini L, Ercolani G, Foschini MP, Saragoni L. Liver metastasis from a non-recurrent atypical cranial meningioma: a case report. *Pathologica* (2020) 112(1):46–9. doi: 10.32074/1591-951X-29-19
57. Pereira BJA, de Almeida AN, Paiva WS, Teixeira MJ, Marie SKN. Impact of radiotherapy in atypical meningioma recurrence: literature review. *Neurosurg Rev* (2019) 42(3):631–37. doi: 10.1007/s10143-018-0959-8
58. Simon M, Bostrom J, Koch P, Schramm J. Interinstitutional variance of postoperative radiotherapy and follow up for meningiomas in Germany: impact of changes of the WHO classification. *J Neurol Neurosurg Psychiatry* (2006) 77(6):767–73. doi: 10.1136/jnnp.2005.077974
59. Jenkinson MD, Javadpour M, Haylock BJ, Young B, Gillard H, Vinten J, et al. The ROAM/EORTC-1308 trial: Radiation versus Observation following surgical resection of Atypical Meningioma: study protocol for a randomised controlled trial. *Trials* (2015) 16:519. doi: 10.1186/s13063-015-1040-3
60. Kaur G, Sayegh ET, Larson A, Bloch O, Madden M, Sun MZ, et al. Adjuvant radiotherapy for atypical and malignant meningiomas: a systematic review. *Neuro-oncology* (2014) 16(5):628–36. doi: 10.1093/neuonc/nou025
61. Coke CC, Corn BW, Werner-Wasik M, Xie Y, Curran WJJr. Atypical and malignant meningiomas: an outcome report of seventeen cases. *J Neurooncol* (1998) 39(1):65–70. doi: 10.1023/A:1005981731739
62. Milosevic MF, Frost PJ, Laperriere NJ, Wong CS, Simpson WJ. Radiotherapy for atypical or malignant intracranial meningioma. *Int J Radiat Oncol Biol Phys* (1996) 34(4):817–22. doi: 10.1016/0360-3016(95)02166-3
63. Goldsmith BJ, Wara WM, Wilson CB, Larson DA. Postoperative irradiation for subtotally resected meningiomas. A retrospective analysis of 140 patients treated from 1967 to 1990. *J Neurosurg* (1994) 80(2):195–201. doi: 10.3171/jns.1994.80.2.0195
64. Weber DC, Ares C, Villa S, Peerdeman SM, Renard L, Baumert BG, et al. Adjuvant postoperative high-dose radiotherapy for atypical and malignant meningioma: A phase-II parallel non-randomized and observation study (EORTC 22042-26042). *Radiother Oncol* (2018) 128(2):260–65. doi: 10.1016/j.radonc.2018.06.018
65. Ware ML, Larson DA, Sneed PK, Wara WW, McDermott MW. Surgical resection and permanent brachytherapy for recurrent atypical and malignant meningioma. *Neurosurgery* (2004) 54(1):55–63. discussion 63-4. doi: 10.1227/01.NEU.0000097199.26412.2A
66. Gutin PH, Leibel SA, Hosobuchi Y, Crumley RL, Edwards MS, Wilson CB, et al. Brachytherapy of recurrent tumors of the skull base and spine with iodine-125 sources. *Neurosurgery* (1987) 20(6):938–45. doi: 10.1227/00006123-198706000-00020
67. Bi WL, Wu WW, Santagata S, Reardon DA, Dunn IF. Checkpoint inhibition in meningiomas. *Immunotherapy* (2016) 8(6):721–31. doi: 10.2217/imt-2016-0017
68. Dasanu CA, Samara Y, Codreanu I, Limonadi FM, Hamid O, Alvarez-Argote J. Systemic therapy for relapsed/refractory meningioma: Is there potential for antiangiogenic agents? *J Oncol Pharm Pract* (2019) 25(3):638–47. doi: 10.1177/1078155218799850
69. Keric N, Kalasauskas D, Freyschlag CF, Gempt J, Misch M, Poplawski A, et al. Impact of postoperative radiotherapy on recurrence of primary intracranial atypical meningiomas. *J Neurooncol* (2020) 146(2):347–55. doi: 10.1007/s11060-019-03382-x
70. Fioravanzo A, Caffo M, Di Bonaventura R, Gardiman MP, Ghimenton C, Ius T, et al. A Risk Score Based on 5 Clinico-Pathological Variables Predicts Recurrence of Atypical Meningiomas. *J Neuropathol Exp Neurol* (2020) 79(5):500–7. doi: 10.1093/jnen/nlaa018
71. Wang F, Xu D, Liu Y, Lin Y, Wei Q, Gao Q, et al. Risk factors associated with postoperative recurrence in atypical intracranial meningioma: analysis of 263 cases at a single neurosurgical centre. *Acta Neurochir (Wien)* (2019) 161(12):2563–70. doi: 10.1007/s00701-019-04073-2
72. O'Connor KP, Algan O, Vesely SK, Palejwala AH, Briggs RG, Conner AK, et al. Factors Associated with Treatment Failure and Radiosurgery-Related Edema in WHO Grade 1 and 2 Meningioma Patients Receiving Gamma Knife

Radiosurgery. *World Neurosurg* (2019) 130:e558–e65. doi: 10.1016/j.wneu.2019.06.152
73. Kaprealian T, Raleigh DR, Sneed PK, Nabavizadeh N, Nakamura JL, McDermott MW. Parameters influencing local control of meningiomas treated with radiosurgery. *J Neurooncol* (2016) 128(2):357–64. doi: 10.1007/s11060-016-2121-1
74. Przybylowski CJ, Raper DM, Starke RM, Xu Z, Liu KC, Sheehan JP. Stereotactic radiosurgery of meningiomas following resection: predictors of progression. *J Clin Neurosci* (2015) 22(1):161–5. doi: 10.1016/j.jocn.2014.07.028
75. Aboukais R, Zairi F, Lejeune JP, Le Rhun E, Vermandel M, Blond S, et al. Grade 2 meningioma and radiosurgery. *J Neurosurg* (2015) 122(5):1157–62. doi: 10.3171/2014.9.JNS14233
76. Farzin M, Molls M, Kampfer S, Astner S, Schneider R, Roth K, et al. Optic toxicity in radiation treatment of meningioma: a retrospective study in 213 patients. *J Neurooncol* (2016) 127(3):597–606. doi: 10.1007/s11060-016-2071-7
77. Dawley T, Rana Z, Abou-Al-Shaar H, Goenka A, Schulder M. Major complications from radiotherapy following treatment for atypical meningiomas. *Neurosurg Focus* (2019) 46(6):E5. doi: 10.3171/2019.3.FOCUS1930
78. Weber DC, Chan AW, Lessell S, McIntyre JF, Goldberg SI, Bussiere MR, et al. Visual outcome of accelerated fractionated radiation for advanced sinonasal malignancies employing photons/protons. *Radiother Oncol* (2006) 81(3):243–9. doi: 10.1016/j.radonc.2006.09.009
79. Debus J, Hug EB, Liebsch NJ, O'Farrel D, Finkelstein D, Efird J, et al. Brainstem tolerance to conformal radiotherapy of skull base tumors. *Int J Radiat Oncol Biol Phys* (1997) 39(5):967–75. doi: 10.1016/S0360-3016(97)00364-7
80. McDonald MW, Linton OR, Calley CS. Dose-volume relationships associated with temporal lobe radiation necrosis after skull base proton beam therapy. *Int J Radiat Oncol Biol Phys* (2015) 91(2):261–7. doi: 10.1016/j.ijrobp.2014.10.011
81. Pehlivan B, Ares C, Lomax AJ, Stadelmann O, Goitein G, Timmermann B, et al. Temporal lobe toxicity analysis after proton radiation therapy for skull base tumors. *Int J Radiat Oncol Biol Phys* (2012) 83(5):1432–40. doi: 10.1016/j.ijrobp.2011.10.042
82. Santoni R, Liebsch N, Finkelstein DM, Hug E, Hanssens P, Goitein M, et al. Temporal lobe (TL) damage following surgery and high-dose photon and proton irradiation in 96 patients affected by chordomas and chondrosarcomas of the base of the skull. *Int J Radiat Oncol Biol Phys* (1998) 41(1):59–68. doi: 10.1016/S0360-3016(98)00031-5
83. Grau C, Baumann M, Weber DC. Optimizing clinical research and generating prospective high-quality data in particle therapy in Europe: Introducing the European Particle Therapy Network (EPTN). *Radiother Oncol* (2018) 128(1):1–3. doi: 10.1016/j.radonc.2018.06.021

Conflict of Interest: The authors declare that the research was conducted in the absence of any commercial or financial relationships that could be construed as a potential conflict of interest.

Copyright © 2020 Weber, Bizzocchi, Bolsi and Jenkinson. This is an open-access article distributed under the terms of the Creative Commons Attribution License (CC BY). The use, distribution or reproduction in other forums is permitted, provided the original author(s) and the copyright owner(s) are credited and that the original publication in this journal is cited, in accordance with accepted academic practice. No use, distribution or reproduction is permitted which does not comply with these terms.

frontiers in Oncology

ORIGINAL RESEARCH
published: 11 January 2021
doi: 10.3389/fonc.2020.598360

Late Side Effects in Normal Mouse Brain Tissue After Proton Irradiation

Theresa Suckert[1,2], Elke Beyreuther[2,3], Johannes Müller[2,4], Behnam Azadegan[2,5], Matthias Meinhardt[6], Felix Raschke[2,4], Elisabeth Bodenstein[2], Cläre von Neubeck[1,2,7], Armin Lühr[1,2,4,8], Mechthild Krause[1,2,4,9,10†] and Antje Dietrich[1,2†]*

[1] German Cancer Consortium (DKTK), Partner Site Dresden, and German Cancer Research Center (DKFZ), Heidelberg, Germany, [2] OncoRay - National Center for Radiation Research in Oncology, Faculty of Medicine and University Hospital Carl Gustav Carus, Technische Universität Dresden, Helmholtz-Zentrum Dresden-Rossendorf, Dresden, Germany, [3] Helmholtz-Zentrum Dresden-Rossendorf, Institute of Radiation Physics, Dresden, Germany, [4] Helmholtz-Zentrum Dresden-Rossendorf, Institute of Radiooncology - OncoRay, Dresden, Germany, [5] Department of Physics, Hakim Sabzevari University, Sabzevar, Iran, [6] Neuropathology, Institute of Pathology, University Hospital Carl Gustav Carus, TU Dresden, Dresden, Germany, [7] Department of Particle Therapy, University Hospital Essen, University of Duisburg-Essen, Essen, Germany, [8] Department of Medical Physics and Radiotherapy, Faculty of Physics, TU Dortmund University, Dortmund, Germany, [9] National Center for Tumor Diseases (NCT), Partner Site Dresden, Dresden, Germany, [10] Department of Radiotherapy and Radiation Oncology, Faculty of Medicine and University Hospital Carl Gustav Carus, Technische Universität Dresden, Dresden, Germany

OPEN ACCESS

Edited by:
Antony John Lomax, Paul Scherrer Institut (PSI), Switzerland

Reviewed by:
Elvira V. Grigorieva, Institute of Molecular Biology and Biophysics (RAS), Russia
Junwei Shi, University of Miami, United States

***Correspondence:**
Antje Dietrich
Antje.Dietrich@uniklinikum-dresden.de

[†]These authors share last authorship

Specialty section:
This article was submitted to Radiation Oncology, a section of the journal Frontiers in Oncology

Received: *24 August 2020*
Accepted: *16 November 2020*
Published: *11 January 2021*

Citation:
Suckert T, Beyreuther E, Müller J, Azadegan B, Meinhardt M, Raschke F, Bodenstein E, von Neubeck C, Lühr A, Krause M and Dietrich A (2021) Late Side Effects in Normal Mouse Brain Tissue After Proton Irradiation. Front. Oncol. 10:598360. doi: 10.3389/fonc.2020.598360

Radiation-induced late side effects such as cognitive decline and normal tissue complications can severely affect quality of life and outcome in long-term survivors of brain tumors. Proton therapy offers a favorable depth-dose deposition with the potential to spare tumor-surrounding normal tissue, thus potentially reducing such side effects. In this study, we describe a preclinical model to reveal underlying biological mechanisms caused by precise high-dose proton irradiation of a brain subvolume. We studied the dose- and time-dependent radiation response of mouse brain tissue, using a high-precision image-guided proton irradiation setup for small animals established at the University Proton Therapy Dresden (UPTD). The right hippocampal area of ten C57BL/6 and ten C3H/He mice was irradiated. Both strains contained four groups ($n_{irradiated} = 3$, $n_{control} = 1$) treated with increasing doses (0 Gy, 45 Gy, 65 Gy or 85 Gy and 0 Gy, 40 Gy, 60 Gy or 80 Gy, respectively). Follow-up examinations were performed for up to six months, including longitudinal monitoring of general health status and regular contrast-enhanced magnetic resonance imaging (MRI) of mouse brains. These findings were related to comprehensive histological analysis. In all mice of the highest dose group, first symptoms of blood-brain barrier (BBB) damage appeared one week after irradiation, while a dose-dependent delay in onset was observed for lower doses. MRI contrast agent leakage occurred in the irradiated brain areas and was progressive in the higher dose groups. Mouse health status and survival corresponded to the extent of contrast agent leakage. Histological analysis revealed tissue changes such as vessel abnormalities, gliosis, and granule cell dispersion, which also partly affected the non-irradiated contralateral hippocampus in the higher dose groups. All observed effects depended strongly on the prescribed radiation dose and the outcome, i.e. survival, image changes, and tissue alterations, were very consistent within

an experimental dose cohort. The derived dose–response model will determine endpoint-specific dose levels for future experiments and may support generating clinical hypotheses on brain toxicity after proton therapy.

Keywords: proton therapy, brain irradiation, preclinical mouse model, magnetic resonance imaging (MRI), late side effects, blood–brain barrier (BBB), brain tissue toxicity, radiation dose modeling

INTRODUCTION

Tumors of the central nervous system are still an entity with a very poor prognosis, with a current relative 5-year survival rate of around 19 – 22 % (1). However, patients of younger age (1) as well as those treated for low grade tumors (2) have a substantially better perspective. Preserving cognitive abilities and quality of life is of paramount importance to these patients. For radiotherapy, this requires the reduction of dose delivered to the tumor-surrounding normal tissue below a critical threshold dose.

An advantage of proton therapy (PT) over photon radiotherapy is its inherent physical properties: Particles stop in the tissue after depositing their energy maximum (Bragg Peak), leading to a reduced integral dose (3) and sparing of normal tissue. Thus, brain tumors and pediatric patients are often treated with this modality (4, 5). In recent years, there has been a surge in PT treatment facilities (6), and several smaller cohort studies indicate beneficial effects of PT such as improved overall survival (7) or prevention of brain-volume loss (8). However, data from randomized multi-center clinical trials is still lacking (9).

At the same time, preclinical data and observations from clinical practice call for a better biological understanding of the normal brain tissue toxicities after PT (10). While a constant relative biological effectiveness (RBE) of 1.1 relative to photon radiotherapy is used for treatment planning, several *in vitro* (11) and rare *in vivo* (12) studies suggest a variable and higher RBE. Increased RBE values occur particularly at the field edges, which are usually located in the normal tissue due to clinical safety margins. Additionally, particular brain areas such as the periventricular region (13, 14), the neural stem cell compartment (15, 16), and the corpus callosum (16, 17) are suspected to be more sensitive to radiation. If the higher RBE and the particular radiosensitivity of brain substructures prove to be clinically relevant, treatment planning and dose calculations would have to be adjusted accordingly (18).

Normal tissue toxicities caused by radiotherapy alone are hard to estimate in patients who often receive a combination of surgery, chemo- or immunotherapy (19) and also suffer from residual tumor, tumor recurrence or pseudo progression (20). Nevertheless, radiation-induced brain injury or neurologic complications are known side effects (4, 21). A suitable preclinical model would offer the potential to investigate radiation effects without confounding factors, model accurate predictions, and test effective counteractive measurements. Another advantage of the preclinical setting is the availability of tissue histology, which provides valuable insights into the underlying cellular changes.

Despite recent successes, meaningful *in vitro* models for normal brain tissue still fall short, with extensive cultivation requirements and missing complexity (22, 23). Classical *in vivo* brain irradiation experiments in rodents are performed with photons and designed to treat either the whole or half of the brain (24–27), which is not reflecting the clinical practice, where the irradiated normal tissue is minimized as much as possible. Since there is a strong dose-volume effect of normal tissue toxicities (28), more clinically relevant treatment fields are needed.

We recently established a workflow for high-precision proton irradiation of mouse brains (29, 30) and showed immediate DNA damage induction in a defined subvolume (31). Being able to reproduce clinical fields including a dose gradient and tissue sparing, investigating underlying tissue damaging mechanisms or alternative treatment options is now possible. As radiosensitivity differs not only between humans and mice, but also between mouse strains (32), it is mandatory to define the proton radiation doses that evoke side effects in murine brains comparable to clinical observation in patients. Therefore, the primary endpoints of this pilot study were (i) to determine a dose able to evoke clinically relevant tissue changes, and (ii) to elucidate the time dynamics of these side effects. To avoid age as confounding factor and enable experimental insights within a reasonable time frame, we decided to irradiate mice older than 60 days (33) and use a follow-up period of 6 month.

So far, no experimental data on high-dose proton irradiation of mouse brain subvolumes has been published, thus we relied on photon data of rat brain irradiation as reference point. The dose–response curve for the appearance of necrosis in irradiated rat brains lays between 20 Gy to 80 Gy at 19 month post irradiation (34) and image changes in MRI were observed for doses >30 Gy at 15 month after treatment (35). In the present study, we explored late side effects by applying increasing proton doses in a range of 40 Gy to 85 Gy. The longitudinal follow-up consisted of regular contrast-enhanced (CE) MRI, recording of animal health status, and final histological analysis. To model inter-patient variability, the two mouse strains C57BL/6 and C3H/He were compared as representatives for high radiation resistance and sensitivity (27, 32), respectively. In this way, we comprehensively characterized and established two robust, predictable animal models to tackle future research questions in the field of proton radiobiology.

MATERIAL AND METHODS

Animals

Eight to nine weeks old C57BL/6JRj ("C57BL/6") and C3H/HeNRj ("C3H/He") were delivered from Janvier Labs (Saint

Berthevin Cedex, France) at least one week before starting the experiments. Only female mice were used to exclude potential sex differences. Animals were housed in Euro Standard Type III with up to five animals per cage at a 12:12 h light-dark cycle. Food, water, and Kaolin pellets (K50001, Brogaarden, Lynge, Denmark; "Pica test") were available *ad libitum*. Nesting material as well as polycarbonate tunnels or mouse igloos were offered as cage enrichment. All experiments were approved by the Saxon authorities (Landesdirektion Sachsen, DD24.1-5131/449/32) and are in accordance with institutional, national, and European (EU Directive 2010/63/EU) animal welfare regulations.

Magnetic Resonance Image Acquisition

MR images were acquired with a 1.0 T small animal MR scanner (nanoScan® PET/MRI, Mediso Medical Imaging Systems, Budapest, Hungary) using a mouse head coil. Mice were anesthetized with 1–2 % isoflurane (Baxter Deutschland GmbH Medication Delivery, Unterschleißheim, Germany; vol./oxygen). The eyes were protected with Bepanthen eye cream (Bayer Vital GmbH, Leverkusen, Germany).

A field of view (FOV) covering the mouse brain was defined. In each imaging session, first a T2-weighted (T2w) MR scan was acquired with a 3-dimensional (3D) fast spin echo sequence (transverse slices, repetition time (TR) = 1,000 ms, effective echo time (TE) = 97.7 ms, FOV = 31.3 mm, 128 × 128 matrix size, slice thickness (ST) = 0.23 mm, number of slices (NS) = 90). Afterwards, Magnevist® contrast agent (Bayer Vital, Leverkusen, Germany, ~ 5 µl/g body weight) was injected intraperitoneally (i.p.) 10 min before running a CE 3D gradient echo spoiled T1-weighted (T1w) sequence (transverse slices, TR = 15 ms, TE = 3.1 ms, FA = 25°, FOV = 60 mm, 256 × 256 matrix size, ST = 0.23 mm, NS = 90).

MR scans were recorded in the week prior to irradiation and biweekly thereafter, starting either in the first or second week after treatment. Measurements of the sham-irradiated animals as well as selected internal control scans, i.e. scans before irradiation, can be found in **Supplementary Figure S1**. After three months, the measurement interval was increased to up to five weeks. An additional diagnostic MR scan was acquired in case of decreasing health status of an animal.

Irradiation Setup and Dosimetry

A 90 MeV proton beam was shaped laterally by an aluminum collimator with an aperture of 4 mm. To ensure that the Bragg peak position was in the mouse brain, the proton range was adjusted by a 47.6 mm polycarbonate range compensator. **Figure 1A** shows a schematic representation of the irradiation setup and **Figure 1B** an overview of the experimental design. The thickness of the range compensator was optimized using the Giraffe multilayer ionization chamber detector (IBA Dosimetry, Schwarzenbruck, Germany) to obtain a proton range in water of about 6.3 mm for the C3H/He mice. Because C57BL/6 mice are of smaller size, an additional 1 mm poly(methyl methacrylate) slab was added adjacent to the collimator, resulting in a proton range of about 4.9 mm in water (**Figure S2**). The 3D dose distribution, including the proton range at treatment position, was verified by EBT3 dosimetry film stacks [stopping power ratio 1.3 (36), Ashland Inc., USA, LOT: 04181701] that were calibrated beforehand with ionization chambers (capped Markus chamber, model 34045, PTW, Germany). Film readout was adapted for proton doses higher than 20 Gy through evaluation of the green color channel (37) using the fit procedures described by (38). Monte Carlo beam transport simulations of the 3D dose distribution in mouse brains and film stacks were performed by means of the software "Tool for Particle Simulation" [TOPAS (39),] as described in (31). **Figure 2** shows one representative simulated proton dose distribution for each mouse strain.

For absolute and relative dosimetry during mouse irradiation, a two-step process as described in (31) was applied. Briefly, the treatment dose was defined on the basis of EBT3 film stacks. The mean film dose within the 80% isodose area around the Bragg peak maximum was assumed as treatment dose. For comparison, a TOPAS simulation was performed to calculate the mean dose within the volume circumscribed by the 80% isodose line around the Bragg peak. Both, the dose estimated on basis of 2D films and the 3D simulated dose agreed within 10 %. In a second step, a correlation factor between treatment dose and mouse head entrance dose was determined as basis of the measured depth dose distributions. The entrance dose is easily accessible with EBT3 films placed at treatment position perpendicular to the incoming proton beam. To monitor the dose delivery during treatment, monitor units (MU) measured by the ionization chamber at beam exit (model 34058, PTW, Freiburg, Germany) were correlated to the mouse head entrance dose. Beam delivery was automatically switched off when the requested MU were reached. For mouse irradiation, a dose rate of about 10 Gy/min (Bragg peak) was applied to deliver physical doses ("high", "intermediate", "low") of 80, 60, and 40 Gy to C3H/He mice, and of 85, 65, and 45 Gy to C57BL/6 mice. Each dose group contained three animals; one sham-irradiated animal per strain served as control. The quality assurance of dose delivery included the irradiation of EBT3 films with a defined dose range at entrance position to check for MU-dose correlation, and the irradiation of several film stacks during each campaign to verify the depth dose distribution.

Animal Irradiation

At an age of 11–13 weeks, the right hippocampal area of the mice was irradiated with protons at the experimental beam line of the UPTD as described in (31). A designated mouse bedding unit (29) maintained mouse hygiene status and body temperature.

For treatment planning, a cone-beam computed tomography (CBCT) and orthogonal x-ray images were acquired in the week before radiation (40). We defined the target coordinates with the µRayStation 5 treatment planning software (RaySearch Laboratories, Stockholm, Sweden) using relative coordinates within the brain (cranial-caudal: 0.56, dorsal-ventral: 0.4) in accordance with the Allen Mouse Brain Atlas (41). On the treatment day, mice were anesthetized (i.p. ketamine (100 mg/kg, WDT eG, Garbsen, Germany)/xylazine (10 mg/kg, Serumwerk Bernburg AG, Bernburg, Germany)) and a second planar x-ray image was acquired. The two x-ray images were

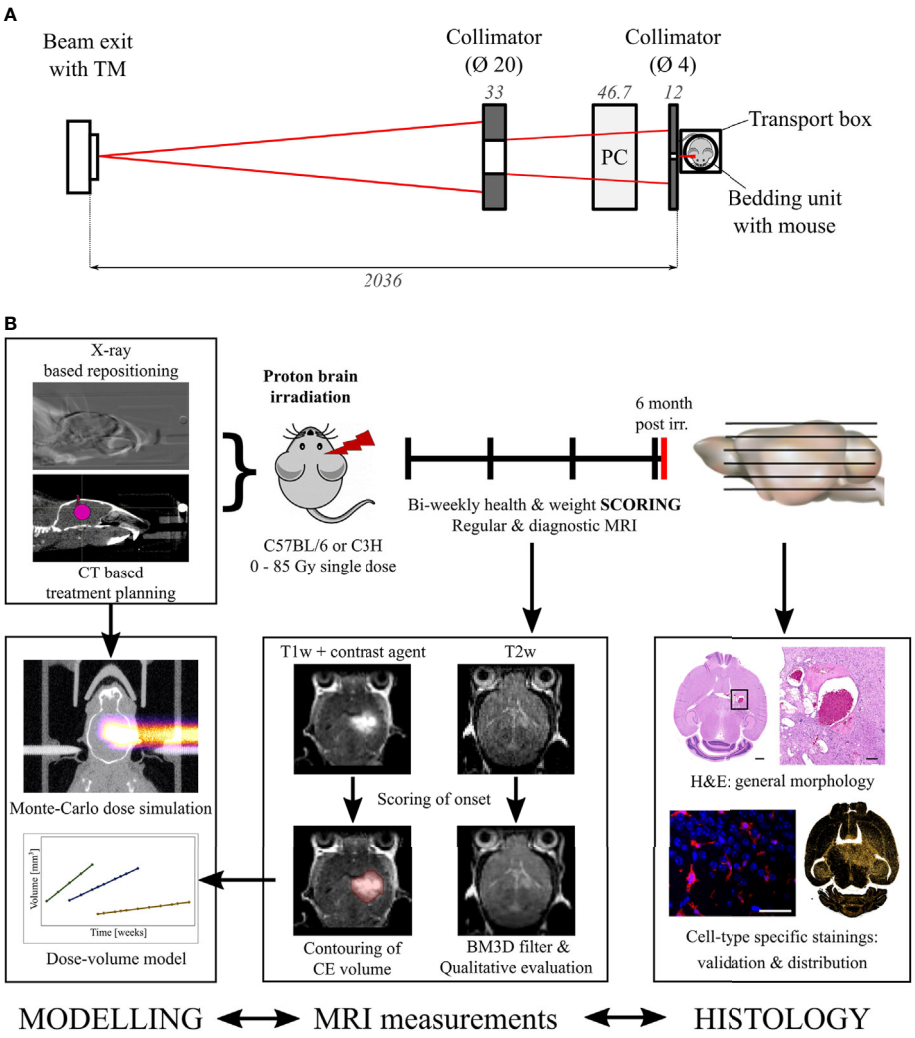

FIGURE 1 | Irradiation setup and experimental procedure. **(A)** Schematic representation of the beam shaping system. Left to right: A 90 MeV proton beam (red) exits the vacuum beam line and passes through a transmission monitor ionization chamber (TM). A brass (left) and an aluminum collimator (right) shape the beam which is range adjusted by a polycarbonate (PC) compensator before irradiating the mouse within the transportation box. Dimensions in mm. **(B)** Overview of the workflow and the specified endpoints. Modelling, MRI measurements, and histology are correlated to find the dose evoking clinically comparable normal tissue toxicities.

used to reposition the animal with the in-house developed RadiAIDD positioning software (https://github.com/jo-mueller/RadiAIDD).

Scoring and Sample Processing

The health status of mice was scored twice per week on a scale from 0–5 considering reduction of body weight, behavior, general appearance, and the skin reaction (grade 0–4). The catalogue of scoring criteria was composed according to guidelines from (42) and (43) and a translation can be found in the Supplement (**Tables S1** and **S2**). To exclude bias and inter-observer variance, a majority of the scorings was performed by the same experienced observer, who was blinded for the applied radiation dose. Substitute observers were trained beforehand. Mice were removed from the experiment by cervical dislocation either when the score revealed deterioration of the animal's health or after the maximum follow-up period of six month was reached. One C3H/He mouse of the 40 Gy group had to be censored in week 24 after irradiation due to a skin injury unrelated to the experiments. Brains were excised and fixed in 4 % formalin overnight at room temperature. Afterwards, tissue samples were processed for paraffin embedding with a semi-enclosed Benchtop Tissue Processor (Leica Biosystems, Wetzlar, Germany).

Histochemistry

In brain areas with T1 contrast agent accumulation, consecutive paraffin sections in the transverse plane of 3 µm thickness were prepared every 100 µm and dried overnight at 37°C. Slices were dewaxed and rehydrated and—for immunohistochemistry—heat-induced antigen retrieval with citrate buffer (pH = 6) was conducted. Hematoxylin and eosin (H&E) staining was performed according to standard procedure.

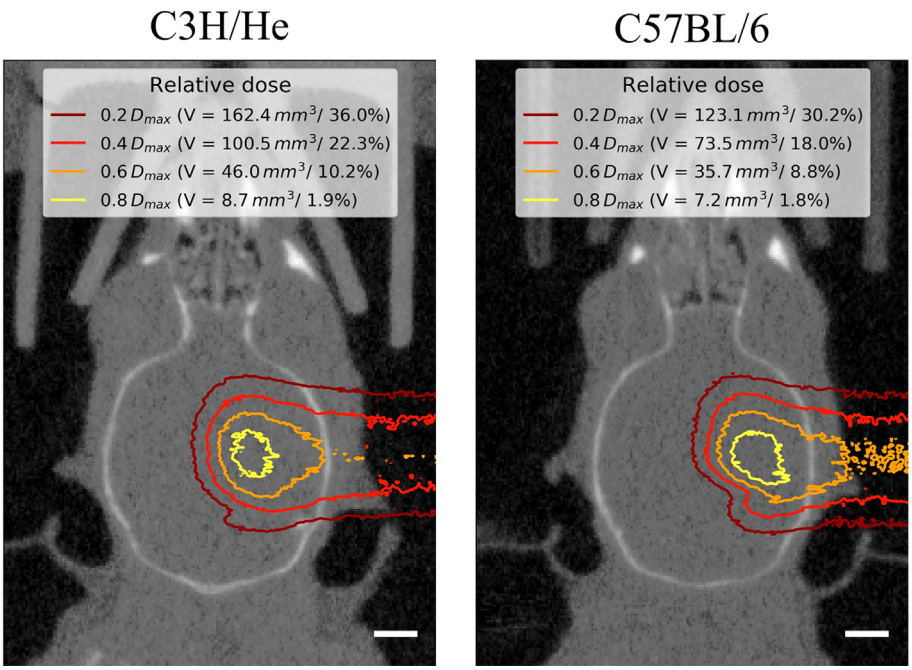

FIGURE 2 | Representative mouse brain CTs in treatment position for one C3H/He and one C57BL/6 mouse with dose distributions from Monte-Carlo beam transport simulations. Little dose was deposited within the contralateral hemisphere. The extent of the brain that received at least a certain fraction of the dose maximum D_{max} is given as absolute volume V and as percentage of the brain volume. Scale bars 2 mm.

For immunofluorescence, sections were blocked for 1 h at room temperature with 1x Rotiblock (Carl Roth, Karlsruhe, Germany, A151) supplemented with 0.1 % Triton X-100 (SERVA Electrophoresis GmbH, Heidelberg, Germany, 37240). Antibodies against glial fibrillary acidic protein (GFAP), ionized calcium-binding adapter molecule 1 (Iba1), Nestin, and the Ki-67 protein as well as their respective secondary antibodies were diluted in 1x Rotiblock and incubated either 1 h at room temperature or overnight at 4°C. After DNA counterstaining with 4′,6-diamidino-2-phenylindole (DAPI, Thermo Fisher Scientific, D3571), sections were embedded with fluorescence mounting medium (Agilent Technologies, Santa Clara, USA, S302380) and dried overnight. Antibody specifications as well as their respective concentrations are listed in **Supplementary Table S3**.

Microscopy Image Acquisition and Analysis

Microscopic images were acquired with a 10x or 40x objective at a ZEISS Axio Scan.Z1 digital slide scanner (Carl Zeiss AG, Oberkochen, Germany) by the Light Microscopy Facility of the Center for Molecular and Cellular Bioengineering (CMCB) and with a 40x objective at an AxioImager M1 or Z2 (Carl Zeiss AG, Oberkochen, Germany). Images were post-processed using Zen 2.3 (blue edition, Carl Zeiss Microscopy GmbH, 2011) or, for visualization of gliosis, with Fiji (ImageJ 1.52p, 64 bit Windows) (44) by applying a background subtraction (rolling ball radius 20 pixel) and the look-up table "Red Hot".

Data Analysis and Statistical Evaluation

Appearing brain tissue changes were categorized by a neuropathologist (MM) in H&E samples. The volumes of regions with CE image signal on the T1w MR images were contoured by two independent experimenters each (**Figure S3**) using the Medical Imaging and Interaction Toolkit [MITK, v2018.04.2 (45)]. Total brain volumes were delineated in the T1w MR images by one observer for three mice per strain. T2w MRI data was filtered using BM3D (46) with a sigma of 1.5 (Matlab R2013a, The Mathworks Inc., Natick, MA, USA) for qualitative analysis, which comprised binary scoring of the presence of abnormal T2 signal intensities (hyper- and hypo-intense). The analysis was performed by three independent observers. GraphPad Prism 7 for Windows (Version 7.02, GraphPad Software, Inc., San Diego, CA, USA) was used for plotting Kaplan-Meier survival curves and survival analysis with a log-rank test. The group size of three animals in this pilot study circumvents any further statistical analysis.

Dose-Volume Response Model

The onset time t_{on} of the first appearance of contrast agent accumulation in the T1w MR images after irradiation as well as the time evolution of the volume V were modelled as a function of irradiation dose D. The onset time,

$$t_{on}(D) = t_1 - t_2 \ln \quad (D/Gy), \tag{1}$$

was assumed to decrease logarithmically with increasing dose. The time constants t_1 and t_2 are model parameters and were obtained by matching Equation (1) to the experimental CE data for the C3H/He mice. The resulting model was then applied to the CE data of the C57BL/6 mice for model validation.

For follow-up time points $t \geq t_{on}(D)$, the logarithm of the CE volume,

$$\log_{10}(V/ml) = a \quad (D - D_0) \quad (t/week)^b, \tag{2}$$

was assumed to increase linearly with dose and with follow-up time t to the power of b. The threshold dose D_0 as well as the parameters a and b were obtained by globally fitting Equation (2) to the CE volume time series of all C3H/He mice. For the C57BL/6 mice data, the values for a and D_0 obtained from the C3H/He data were maintained and only the parameter b was adapted to match the time dependence of the experimental outcome of all C57BL/6 mice. The model is included in the **Supplementary Excel File**.

RESULTS

In the weeks following treatment, general appearance and behavior of the mice remained normal and body weight either increased or remained stable (**Figures 3A, B**). All irradiated mice developed a skin reaction grade 1, i.e. dry desquamation and hair loss, approximately one month after treatment, with a slight delay in the lowest dose group (**Figure 3C**, clinical score change from 0 to 1). Effects appeared strictly within the irradiated area. The regrown fur lost its pigmentation, appearing white thereafter (**Figure S4**). Health deterioration occurred in C3H/He after high- (3/3) and intermediate- (2/3) dose irradiation and in C57BL/6 only in the highest dose group (3/3). If general well-being deteriorated, its decrease was rapid after a certain latency time and mice were sacrificed within few days according to the health scoring (**Figures 3C, D**). The major indicator of health decline was body weight loss; behavioral and appearance changes were recorded only on the last measurement day in most of the mice. Changes in body weight were more apparent in C3H/He animals. This is also reflected by their generally higher weight gain in the measurement period.

The Pica test as indicator for nausea showed no difference between irradiated and non-irradiated animals. Even when the animal suffered from radiation-induced weight loss, no clear indication of nausea, i.e. white colored feces, was observed. Autopsy after euthanasia always revealed an empty digestion tract, but no organ aberrations.

We found prolonged survival for C57BL/6 mice compared to C3H/He mice (**Figures 3**, and **4A, B**) in the highest dose group [C57BL6: (76 ± 13) days, C3H/He: (64 ± 9) days]. All C57BL/6 mice irradiated with intermediate doses reached the maximal follow-up time, while only one out of three C3H/He mice in this dose group survived until the final measurement day. Animals irradiated with the lowest dose as well as the control animals survived until the end of the observation period.

Regardless of the prolonged survival of C3H/He animals, MRI data showed contrast agent accumulation after similar dose-dependent onset times for both animal strains (**Figures 4C–F**). T1w CE appeared consistently before the occurrence of image changes in T2w MRI. We found no T2w hyper-intensities in animals exposed to 45 Gy, 40 Gy, and 0 Gy proton irradiation. Onset of CE was located within the area of the designated dose maximum (**Figures 2** and **5**).

The CE volume increased progressively after its initial occurrence (**Figure 6**). An exception was the lowest dose group

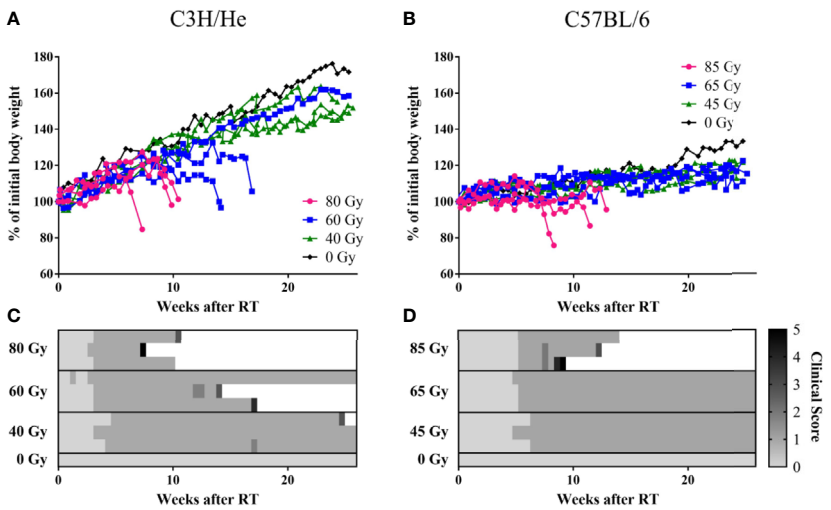

FIGURE 3 | Weight curves of **(A)** C3H/He and **(B)** C57BL/6 shown as percent of initial body weight. **(C, D)** General health scoring of mice included skin reaction (grade 0–4), body weight reduction, general appearance, and behavior, according to a fixed set of criteria. A combined score of 5 was set as the stopping criterion.

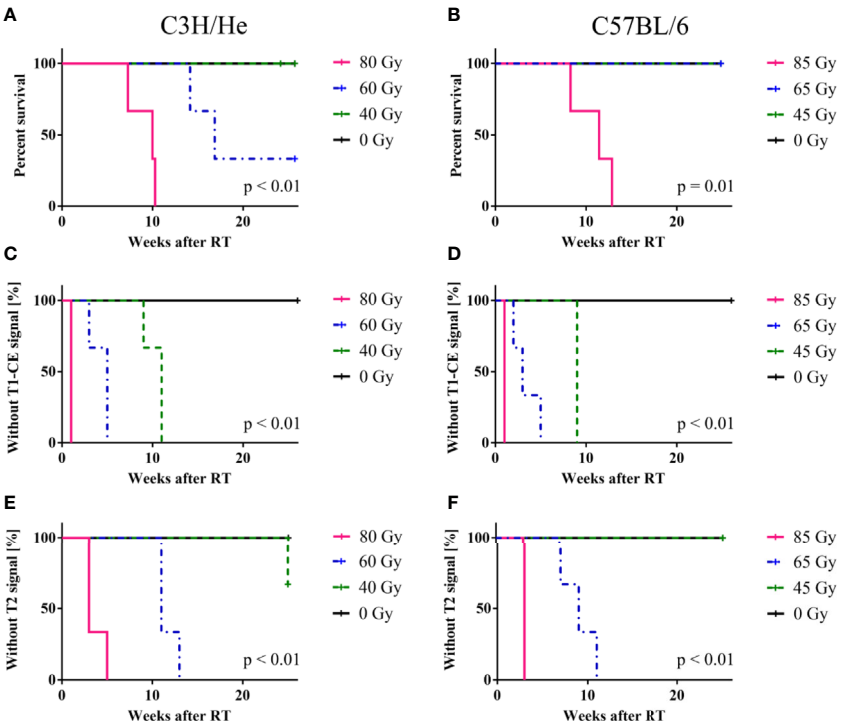

FIGURE 4 | Mouse survival, onset of CE in T1w and signal onset in T2w MRI. **(A, B)** C57BL/6 mice showed an increased survival rate compared to C3H/He, whereas **(C–F)** onset times of MR image changes exhibited a similar pattern in both mouse strains, with a clear dose-dependency. T2w signal only appeared after T1w CE was observed. The log-rank test indicates that there is a significant difference in survival and signal onset in MRI between the dose groups.

(45 Gy) of C57BL/6 mice, where the data indicates an initial progression period followed by a mild recovery at the end of the observation period. The rate of CE volume growth strongly depended on the applied dose as well as on the mouse strain: Progression was faster for higher doses and C3H/He animals. To prevent implicit dependence of the observed effect on differences in total brain size between the two mouse strains, we contoured the total brain volume in three individuals and found comparable sizes (491.4 ± 16.7 mm^3 and 488.6 ± 4.7 mm^3 for C3H/He and C57BL/6, respectively). During the observation period, no noticeable brain volume increase occurred. While longer surviving animals showed slower progression, final CE volumes and health deterioration were within the same magnitude for all animals. In general, as expected for a normal tissue reaction, a high consistency within the dose groups was noted.

The acquired data was used to generate a dose-volume response model to predict the signal onset and the rate of CE volume increase based on Equations (1) and (2), respectively (**Table 1**). The onset time of the first image changes in MRI as function of dose showed for all six dose groups (i.e., both strains) a highly consistent dependence on dose and only small variances within each dose group. Onset time could therefore be precisely estimated by the according model for all 18 mice resulting in high R^2 values of 0.97 and 0.92 for C3H/He and C57BL/6, respectively.

For the modelling of the image change volume over time as a function of dose, in total 153 measured data points were included, that is, on average measured volumes at 8.5 time points were available per mouse. Accordingly, the time dependence of the image change volume was robustly modelled. On the other hand, only three different dose levels entered the modelling per mouse strain. To test model performance, first, a model was built on one cohort (all C3H/He mice, $R^2 = 0.80$) and, second, applied to an independent cohort (all C57BL/6 mice, $R^2 = 0.76$). Despite using two different mouse strains, only one model parameter (i.e., *b*) had to be adapted to fit the smaller CE volume growth rates observed for the C57BL/6 mice.

T2w image changes followed the CE in T1w images with a time delay, but occurred initially within the same brain regions. T2w image changes comprised both T2 hyper- and hypo-intensities and generally had a more diffuse and heterogeneous appearance (**Figure 7**). However, at later time points the extent of T2 hyper-intense signal did outreach the volume with CE. T2 hyper-intensities were never observed in animals of the lowest dose group. On the other hand, one C3H/He animal irradiated with 40 Gy exhibited an area of hypo-intense T2w signal, which was also seen in the three C3H/He mice of the intermediate dose group before onset of hyper-intense signal. In C57BL/6, T2w hypo-intensities appeared as late effect for two animals (85 Gy and 65 Gy).

Selected animals of each dose group were histologically evaluated to validate the MR imaging results and obtain pathologic findings on a microscopic level. H&E staining (**Figure 8**) revealed a broad range of normal tissue toxicities, which predominantly appeared within the irradiated field. We

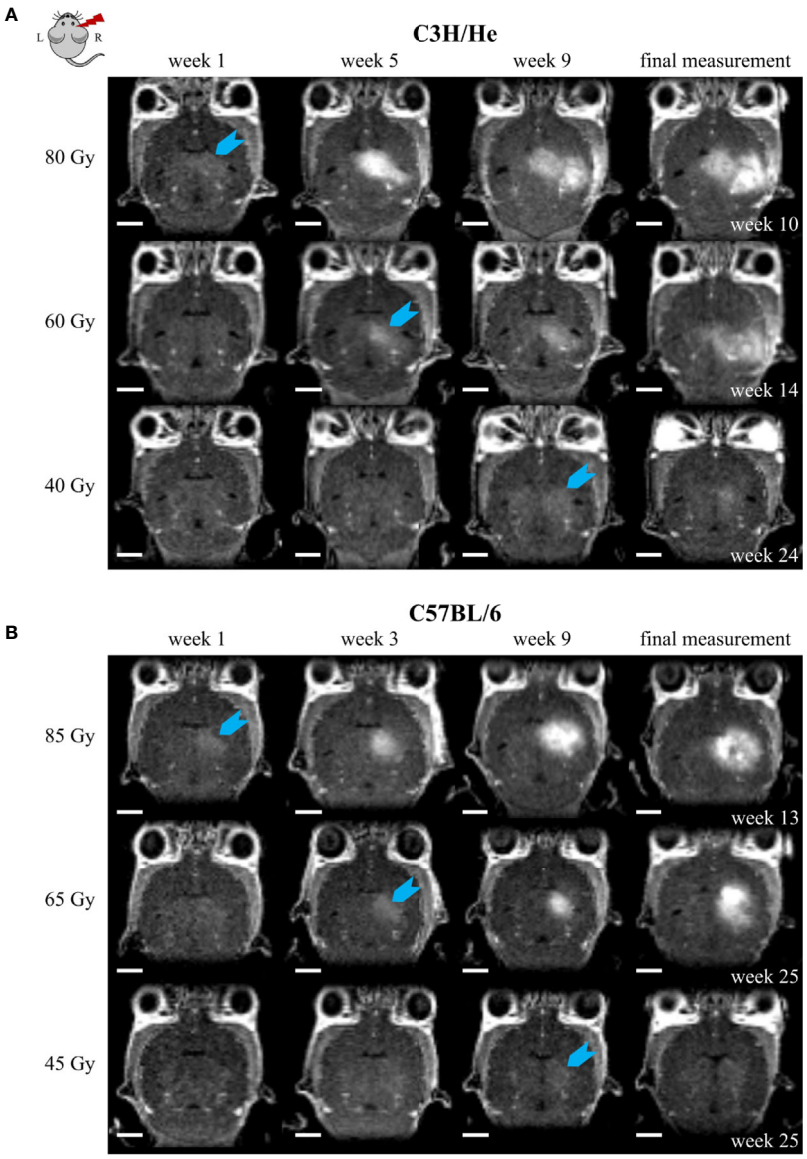

FIGURE 5 | Exemplary CE T1w MR images of **(A)** C3H/He and **(B)** C57BL/6 for one selected mouse per dose group. The time points were chosen to reflect signal onset (blue arrow) in the different treatment groups. CE appeared sooner for higher doses. However, the progression pattern in the mouse strains matched and if the stopping criterion, i.e. health deterioration, was reached, affected volumes corresponded also between different doses. Scale bars 2 mm.

noted gross morphological alterations such as microfocal edema, white matter damage, and cytoplasmic changes. Fibrin extravasation, incomplete necrosis, and small areas of complete necrosis were present. Vessels had started to proliferate strongly and showed indications of dysfunction such as dilatation, chaotic organization, and hyalinosis. Gliosis of astrocytes and microglia occurred as well as microglia-lymphocyte nodules and macrophage invasion, mainly visible by residual siderophages, a sign of past micro-bleedings. Hippocampal sclerosis and granule cell dispersion were induced, especially in hippocampi irradiated with high doses. Incidence and severity of the side effects depended strongly on the delivered dose (**Table 2**). In general, the spatial transition from undamaged tissue to severe tissue alterations and vice versa was narrow and occurred within a range of 300 – 500 μm, which is attributed to the steep dose gradients of the proton beam. The H&E staining revealed only a weak effect in the low dose group.

Comparison of MRI data and histology could correlate image changes with tissue alterations (**Figure 9**). CE in T1w sequences appeared in regions with vessel proliferation and vasodilation. T2w hypo-intense spots were associated with calcification or haemorrhage and fibrin extravasation, whereas hyper-intense signal was linked to edema, angiogenesis, and vessel dilatation.

The microglial immune reaction, astrogliosis, and vessel aberrations were confirmed with further cell-type specific staining. This also revealed previously undetected effects in the

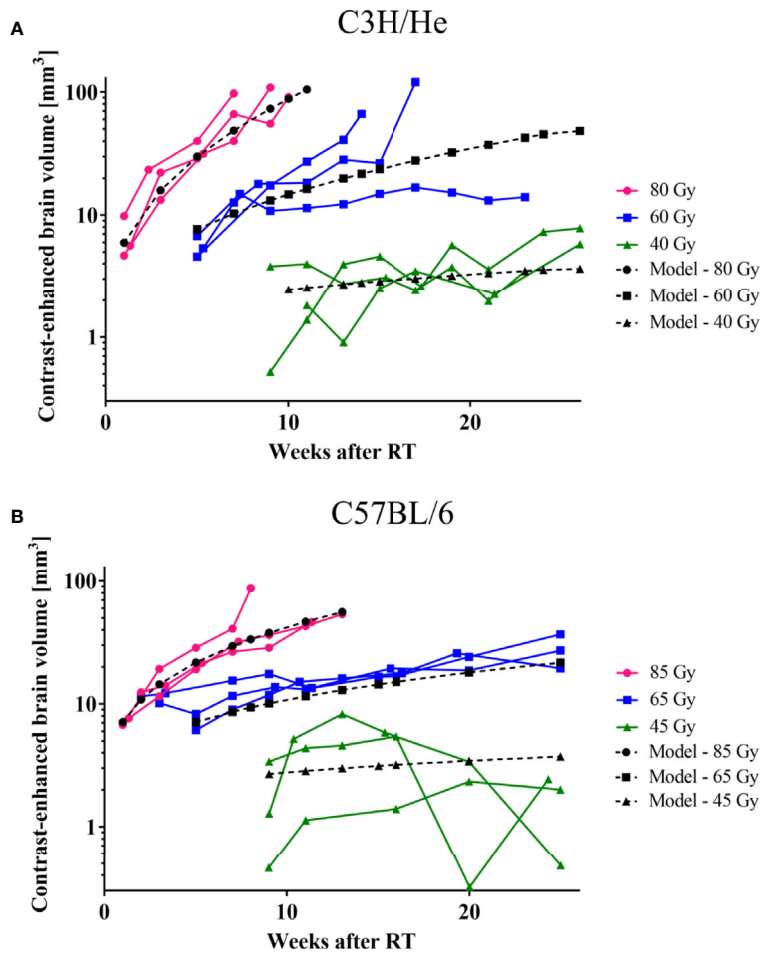

FIGURE 6 | CE-volume increase in T1w MR images and the dose-volume response model (black curves) derived from experimental data for **(A)** C3H and **(B)** C57BL/6 mice. Onset and progression were earlier and faster for higher doses. C57BL/6 progressed at a lower rate than C3H/He animals.

low dose group, where abnormalities were not noticed in H&E histology. Proliferation of microglia (Iba1-positive) and astrocytes (GFAP-positive) occurred in the irradiation field, especially in the hippocampus, the area of the dose maximum, and around edema (**Figure 10**). Astrocytes formed a glial scar around injured tissue. At higher doses, there was—to a lesser extent—also an effect in the contralateral hippocampus with an increased GFAP expression. In general, tissue alterations were more pronounced and spatially widespread at higher doses.

The incidence of reactive gliosis was verified with a co-staining of GFAP and Nestin: double-positive cells, as well as a high number of Nestin-positive vessels were observed predominantly in the irradiated field and particularly within the glial scar tissue (**Figures 11A, B**). Brain areas affected by gliosis showed an increased amount of Ki-67 positive cells, indicating cell proliferation (**Figure 11B**). Brains of mice irradiated with 40 Gy/45 Gy formed no glial scar due to largely absent tissue damage and had only few double-positive cells as well as little reaction outside the irradiated area.

Microglia in the irradiated brain area increased in number and transformed their morphology to an activated state. Control animals show only resting local microglia with round, small cell somas and long, thin processes. Upon proton irradiation, cell shapes change from ramified to amoeboid with decreased cell spread, bushy processes, and increased soma sizes (**Figure 11C**). Again, changes were minor after low-dose (40 Gy/45 Gy) and more pronounced after high-dose (80 Gy/85 Gy) irradiation.

TABLE 1 | Parameters for the dose-volume response model for irradiated brain subvolumes of C3H/He and C57BL/6 mice.

Mouse strain	a [Gy^{-1}]	b	D_0 [Gy]	t_1 [weeks]	t_2 [weeks]
C3H/He	0.0155	0.40	30	55.75	−12.5
C57BL/6	0.0155	0.28	30	55.75	−12.5

DISCUSSION

Normal tissue toxicity following radiotherapy is a clinical challenge, particularly in brain tumor patients, and the

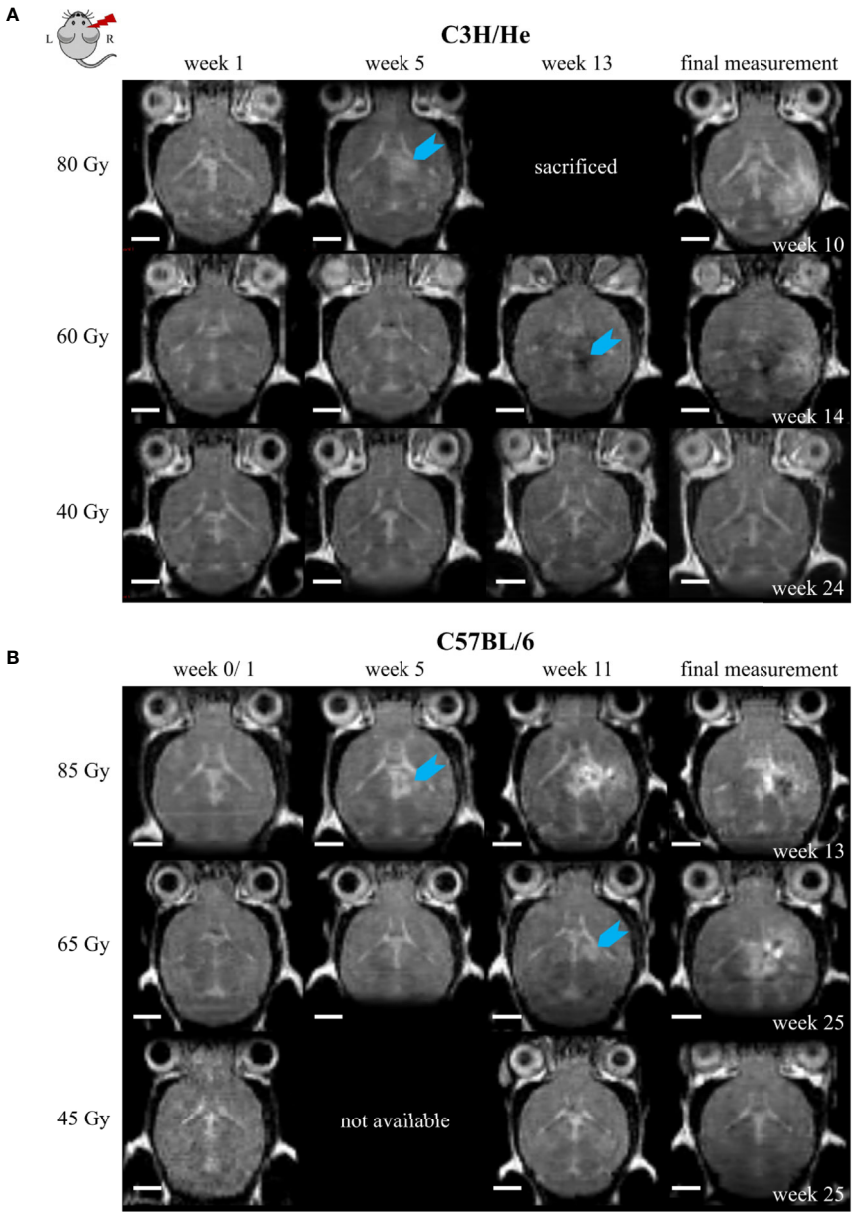

FIGURE 7 | Exemplary T2w MR images of **(A)** C3H/He and **(B)** C57BL/6 for one selected mouse per dose group. Signal onset (blue arrow) occurred faster in high dose animals and did not appear in the lowest dose group. In most animals, the initial T2w image change was a hyper-intense signal; however, hypo-intensities were observed first in C3H/He mice irradiated with 60 Gy. Scale bars 2 mm.

availability of meaningful preclinical models is crucial for understanding the induced side effects. Existing preclinical studies focus on half- (47) or whole-brain irradiation (27) and thereby disregard the dose-volume effect, impairing clinical relevance. In this pilot study, we established and comprehensively characterized a suitable *in vivo* model to investigate long-term side effects after proton irradiation of the hippocampal area as a relevant brain subvolume. For this, we used a follow-up with longitudinal evaluation of MR image changes and general well-being in addition to final histopathological findings.

The incidence, latency period, and severity of observed normal tissue toxicities, i.e. MR image changes, skin reaction, weight reduction, and histological abnormalities, strongly depended on the delivered dose for all investigated endpoints, as found previously (34, 35, 48). Interestingly, all observed effects were very consistent across the different dose groups although the experiments were planned as a pilot study with n = 3 mice per condition. As a first visible side effect, hair loss and subsequent whitening of the fur occurred. This can effectively be used to determine the correct application position of the proton beam.

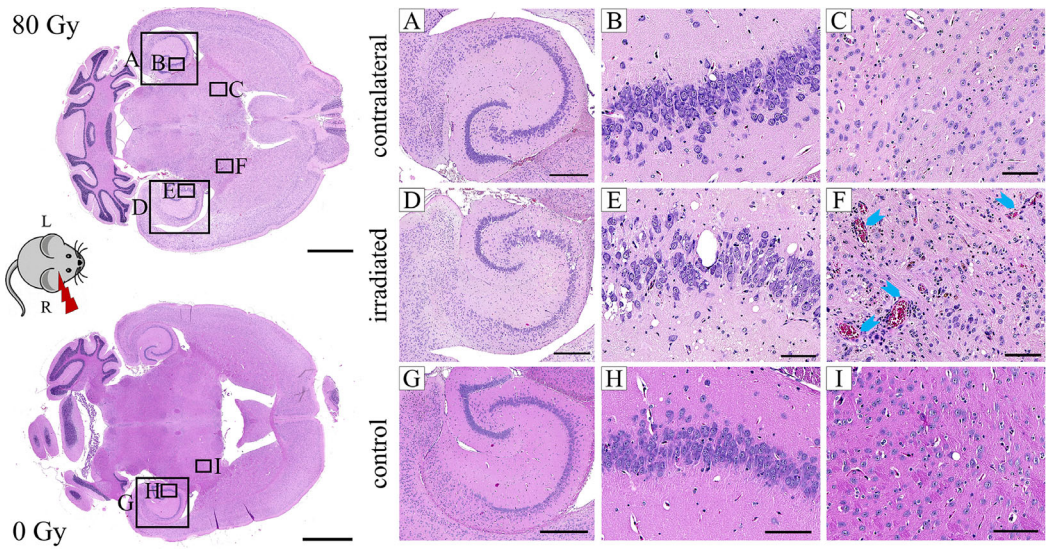

FIGURE 8 | Exemplary H&E images of an 80 Gy proton irradiated **(A–F)** or control **(G–I)** C3H/He brain. The right hemisphere was exposed to proton radiation; the left hippocampus received no dose. Microfocal edema **(D–F)**, vessel proliferation **(D–F)**, hyalinosis and dilatation (**F**, blue arrows) of vessels, incomplete necrosis **(D–F)**, siderophages (**F**, brown color), and white matter damage **(D–F)** were noted in the irradiated brain. The hippocampus had a reduced cell density and granule cell dispersion **(D, E)**. None of these effects were present in the contralateral side **(A–C)** and the control animal **(G–I)**. Pink: parenchyma, violet: cell nuclei, red: erythrocytes, brown: siderophages. Scale bars (left to right): 2 mm, 500 µm, 100 µm, 100 µm.

TABLE 2 | Overview of normal brain tissue toxicities observed after proton irradiation with different doses in C3H/He and C57BL/6.

		C3H/He				C57BL/6		
		40 Gy	60 Gy (a)	60 Gy (b)	80 Gy	45 Gy	65 Gy	85 Gy
Morphology	Complete necrosis							x
	Incomplete necrosis				x		x	x
	White matter damage		x	x	x		x	x
	Edema		x	x	x		x	x
	Fibrin extravasation						x	
	Subarachnoid hemorrhage						x	x
	Calcification	x	x					
Vessels	Proliferation	minor	x	x	x		x	x
	Hyalinosis		x	x	x		x	x
	Vasodilatation	minor	x	x	x		x	x
Cellular changes	Hippocampal granule cell dispersion		minor	x	x		minor	x
	Hippocampal sclerosis		minor	x	x		minor	x
	Gliosis		x	x	x		x	x
	Siderophages		minor		x		x	x

60 Gy (a): mouse survived 6 months observation period; 60 Gy (b): mouse died 17 weeks post irradiation.

The Pica test for detection of nausea or headaches did not reveal any outcome and is thus not helpful to assess animal burden in this context. While apparent behavioral changes occurred late, body weight changes have proven as a reliable indicator for mouse health deterioration after proton brain irradiation. Therefore, a meaningful scoring system for future experiments should consider the weight kinetics. The investigated two mouse strains were chosen to represent a patient population with heterogeneous radiosensitivities (32); the proposedly more radiosensitive C3H/He showed a faster progression of therapy-related BBB damage and weight loss. However, our data may not allow a definite conclusion on that matter, since C3H/He had a larger fraction of their brain volume irradiated, leading to a higher integral dose. In particular the small dimensions of the preclinical setup combined with anatomic differences between the mouse strains complicate the irradiation of identical volumes. Alternatively, a voxel-wise correlation of dose and damage might be a promising approach to reveal strain-specific differences as well as variances in radiation response between the brain regions.

In the MRI measurements, the earliest detectable image change was contrast agent accumulation, which implies leakage

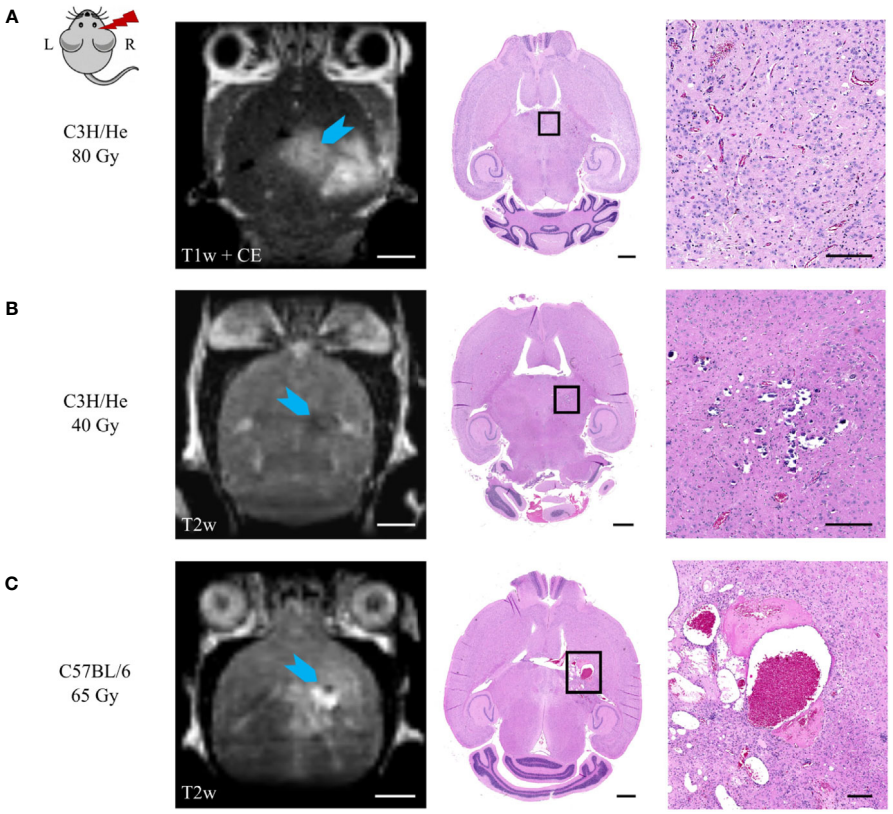

FIGURE 9 | Correlation of MR image data and H&E histology. **(A)** Angiogenesis and vessel dilatation were observed in regions of contrast agent accumulation in T1w MRI. T2 hypo-intense signal could be related to **(B)** calcification or **(C)** fibrin extravasation and haemorrhage. **(C)** Hyper-intense spots in T2w sequences corresponded to edema and immensely dilated vessels. Scale bars (left to right): 2 mm, 1 mm, 200 µm.

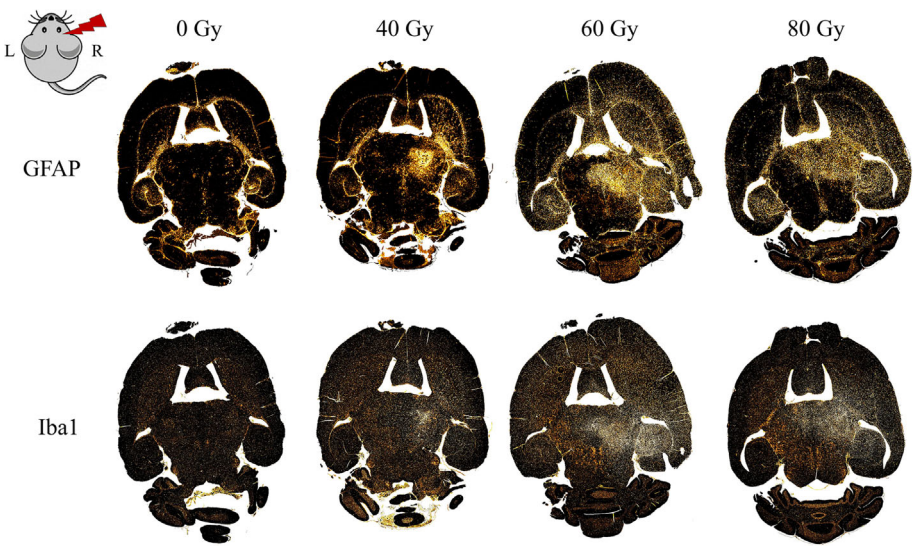

FIGURE 10 | Distribution of gliosis in the proton irradiated C3H/He mouse brain. Gliosis is indicated by an increased number of astrocytes (GFAP, upper row) and microglia (Iba1, lower row) within the irradiated field and, for higher doses, also in the contralateral hippocampus. Staining was either performed within the same slice or in consecutive ones (within 15 µm distance, due to adaption of the staining protocol).

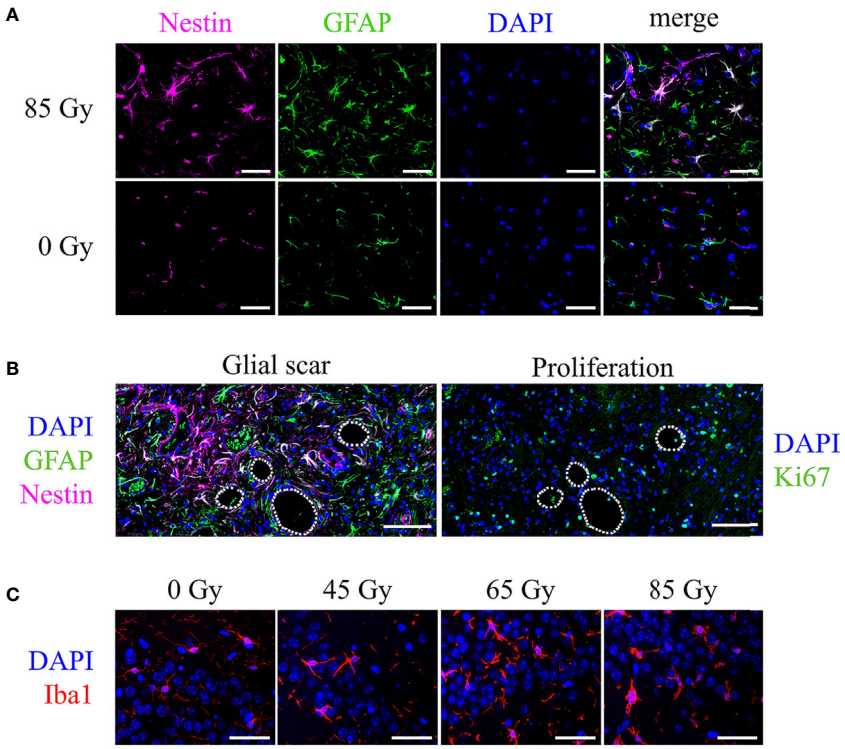

FIGURE 11 | Cell type specific markers and cell nuclei (DAPI, blue) in representative irradiated brain sections of C57BL/6 mice. **(A)** Nestin-positive vessels (pink), GFAP-positive astrocytes (green), and Nestin-GFAP double-positive astrocytes in an animal irradiated with 85 Gy. No double-positive cells appear in the control animal. Scale bar 50 µm. **(B)** Consecutive slices showed the glial scar (left, Nestin-GFAP double-positive cells, green and pink) and proliferating, Ki-67-positive cells (right, green) located in the irradiated brain area, mainly around edema (white lines, 65 Gy). Scale bar 100 µm. **(C)** Iba1-positive microglia (red) increased in number and changed their morphology upon proton irradiation. Higher doses exhibit a bushy or amoeboid-like shape. Scale bar 50 µm.

into the tissue and signifies increased vessel permeability or breakdown of the BBB. CE in T1w MR images was observed in all irradiated animals and formed sharp outlines, thus enabling a clear differentiation from the surrounding brain tissue. On the other hand, T2w hyper-intensities occurred only in intermediate and high dose animals and exhibited a diffuse appearance. Retrospective analysis of H&E staining could verify the existence of white matter damage, edema, and incomplete necrosis in brain areas with CE and hyper-intense MR image signal. In two of the animals with T2w hypo-intensities, histology revealed calcification in the respective region, in another animal subarachnoid hemorrhage and fibrin extravasation were diagnosed. This is in agreement with existing literature: intracerebral bleeding, accumulation of mineral substances, or protein-containing lesions are some morphological changes causing T2w hypo-intensities in patients (49). Origin of the image changes in both sequences was consistently in the region of the dose maximum, but with progressing side effects, surrounding tissue was affected and a T1/T2 mismatch occurred. Above-mentioned MR image changes are classic clinical features of late radiation injury and frequently occurring in patients after brain radiotherapy (50–52) as well as in previous reported preclinical experiments (35, 47, 53, 54).

The distinctive feature of our study is the in-depth comparison of MR image changes with tissue alterations in histology. One restriction was the rather low MRI signal-to-noise ratio combined with a weak T2-weighting of the sequence. This impaired more differentiated evaluation of imaging data and may provide an explanation for the onset of T2w image changes, which appeared consistently after T1-CE. Clinical data frequently describes an inverted course of events with an earlier occurrence of image changes in T2w imaging (52). However, contrast agent accumulation was clearly distinguishable and the onset and qualitative evaluation of image changes in T2w images was possible after applying a BM3D noise reduction filter. Hence, the imaging protocol was deemed feasible as it allowed for high-throughput measurements with acceptable scan times. From the MRI data, we could derive a dose-volume model that consistently predicts onset time and progression of the BBB breakdown as well as animal survival. This model can now be used to choose suitable dose levels for evoking clinically relevant radiation toxicities at realistic preclinical time points in the two mouse strains C3H/He and C57BL/6. Despite the small animal number, we consider the proposed model from this pilot study useful and applicable, due to its consistency and successful validation in an independent

cohort. Especially the finding that increased radiation dose leads to quicker onset of radiation pathology confirms the outcome of earlier *in vivo* mouse photon irradiation studies (55). Additional testing of the model in future experiments with larger cohorts and especially at other dose values is recommended. Future studies could investigate to which extend the modelled behavior also applies to cancer patients suffering from radiation-induced tissue damage, where a similar progression of CE volume increase was observed. In particular, the observed distinct dose dependence of the onset time and velocity of CE volume increase should be tested in an appropriate clinical cohort. Taken together, our findings clearly prove the value of preclinical experiments for interpreting medical imaging results, in turn helping to improve patient diagnosis.

For a deeper understanding of the tissue changes, specific cell types were investigated in greater detail. The strong gliosis observed in H&E staining proved to be originated from both astrocytes and microglia. Ki67-positive cells were present in the respective area, demonstrating active local proliferation. Especially around injured tissue, such as edema or hemorrhages, Nestin-positive astrocytes appeared. These cells are known to form the so-called "glial scar", which is a typical mechanism to self-limit tissue damage that protects against invading inflammatory cells (56). Microglia recruitment to the radiation lesion and cell activation was observed in all dose groups, but the extent showed a clear dose dependence visible in both cell distribution and morphology. Especially after high-dose irradiation, microglia were highly circular with big soma sizes, signifying activation (57). Interestingly, the contralateral hippocampus was affected by gliosis. This has been described before (58) and was attributed to global neuroinflammation resulting from brain irradiation (59). After severe trauma and BBB damage, additional invading immune cells take part in the inflammatory reaction. We did not observe peripheral macrophages after low dose irradiation, whereas specimen of higher doses showed residual siderophages, i.e. blood cell clearing macrophages as a sign of past micro-bleedings, and occasional lymphocyte-microglia nodules. Another prominently changed tissue component is the vasculature, exhibiting vessel dilatation, -hyalinosis, and -angiogenesis. These alterations have also been observed in patient biopsies or autopsies (60, 61) and indicate dysfunctional blood flow and ensuing limited nutrient supply in the respective tissue. The underlying reason could be radiation-induced microvascular injury and a subsequent decline of the vessel population, leading to tissue hypoxia. Apoptosis of CNS vessels as early as 24 h post irradiation has been observed, and experimental data indicates a slow recovery of endothelial cell density with leaky immature vessels (62, 63). Studies on sleep apnoea (64) and brain radiation (65) reveal angiogenesis, reactive gliosis, neuroinflammation, and altered hippocampal neurogenesis as reaction to hypoxic conditions. Vessel proliferation, inflammation, and reactive astrogliosis were indeed confirmed in our final histopathological analysis; and even though altered neurogenesis was not investigated, it is possibly one mechanism contributing to the observed massive gliosis (58). Two hitherto unidentified histological changes following radiation are granule cell dispersion and hippocampal sclerosis, which are known from epilepsy (66) or neurodegenerative diseases (67), but not radiotherapy. Since patient biopsies or autopsies of irradiated hippocampi are very rare, further preclinical studies will be needed to elucidate whether these side effects may contribute to neurocognitive decline after brain radiation.

Our results suggest that alleviating or reversing therapy-related toxicities might be possible; for example by reducing the inflammatory reaction (59) or protecting the vasculature by VEGF blockade (68, 69). The mouse model presents a valuable tool to screen for such potential treatment approaches and characterize their underlying mechanisms before entering clinical trials. Future studies should include longitudinal histology as well as high resolution T1w and T2w MRI together with additional sequences that represent the current clinical standard, such as FLAIR imaging and diffusion weighted imaging. This would allow for improving the link between MR image changes seen clinically after radiotherapy to preclinical MRI and, most importantly, the underlying histological changes. Additionally, high resolution MRI could help to elucidate radiation-induced normal tissue toxicities further, e.g. regarding specific brain regions of interest such as the periventricular area (13, 14) which appears to be particularly radiosensitive. Complementary "omics" analysis or liquid biopsies could reveal suitable biomarkers for predicting the potential onset or the occurrence of late side effects, which could support patient stratification and treatment. Furthermore, the influence of hippocampal-sparing proton irradiation on cognitive abilities, the role of the stem cell niche, and the beneficial potential of exercise during and/or after radiotherapy (70) are interesting research questions which can be tackled using the presented model. This pilot study could therefore achieve its primary endpoints: (i) we defined a dose delivered as a single fraction by a laterally confined 4 mm proton beam in one brain hemisphere within the range of 40 – 50 Gy as suitable for preclinical experiments focused on clinically relevant normal tissue alterations after brain radiotherapy. (ii) The chosen follow-up time of 6 month proved long enough to capture relevant tissue changes while still enabling data analysis within a reasonable time frame. The onset and dynamics of observed MR image changes provide valuable insight for deciding on appropriate analysis time points in longitudinal studies for maximizing the significance of the results while minimizing the number of animals needed.

In summary, we were able to induce normal tissue changes in murine brains similar to clinical observations following partial brain irradiation using a proton beam with a clinically relevant field formation. From MRI measurements, we established a dose–response model, which can be applied for more accurate experimental planning. In addition, histology identified hippocampal sclerosis and granule cell dispersion as potential side effect of radiation which could contribute to neurocognitive decline. With regard to future studies, our model offers the possibility to study existing and generate new clinical hypotheses for radiation-induced brain damage, reveal

underlying mechanisms in greater detail, and, most important, find suitable treatment and prevention strategies.

DATA AVAILABILITY STATEMENT

Contoured MRI volumes and onset times are included in the article as supplementary material. Requests to access MRI raw data and the histology should be directed to the corresponding author.

ETHICS STATEMENTS

The animal study was reviewed and approved by the Saxon authorities (Landesdirektion Sachsen, DD24.1-5131/449/32).

AUTHOR CONTRIBUTIONS

TS, EBe, CV, AL, MK, and AD participated in the conception of the study. Data acquisition was performed by TS, EBe, AL, JM, MM, EBo, and AD. Analysis and interpretation of data were executed by TS, EBe, JM, BA, MM, FR, AL, MK, and AD. JM, FR, and TS provided the software. MK acquired funding. Project supervision was offered by EBe, MK, and AD. Visualization was done by TS and JM. The first draft of the manuscript was written by TS. AL and EBe wrote parts of the manuscript. All authors revised the manuscript and approved the final version

FUNDING

Proton irradiation was done at the University Proton Therapy Dresden (UPTD) which has received funding from the European Union's Horizon 2020 Research and Innovation Programme under Grant Agreement No: 730983 (INSPIRE).

ACKNOWLEDGMENTS

This work was supported by the Light Microscopy Facility, a Core Facility of the CMCB Technology Platform at TU Dresden. The authors thank Gerd Rothe, Peter Zahn and Michael Reiche from the mechanical workshop for their dedicated support. We would like to acknowledge the technical support of Vivien William, Katja Schumann, Anne Kluske, and Elisabeth Jung as well as Dorothee Pfitzmann, Daniela Pollack, and Liane Stolz-Kieslich. We thank Jan Eulitz, Erik Schulz, Gerd Kempermann, Steffen Löck, Emanuel Bahn and Christian Karger for scientific discussion. We further want to acknowledge the UPTD-team and IBA for proton beam support.

SUPPLEMENTARY MATERIAL

The Supplementary Material for this article can be found online at: https://www.frontiersin.org/articles/10.3389/fonc.2020.598360/full#supplementary-material

REFERENCES

1. *Cancer burden statistics and trends across Europe | ECIS* . Available at: https://ecis.jrc.ec.europa.eu/index.php (Accessed August 12, 2020).
2. Claus EB, Walsh KM, Wiencke JK, Molinaro AM, Wiemels JL, Schildkraut JM, et al. Survival and low-grade glioma: The emergence of genetic information. *Neurosurg Focus* (2015) 38:E6. doi: 10.3171/2014.10.FOCUS12367
3. Lühr A, von Neubeck C, Krause M, Troost EGC. Relative biological effectiveness in proton beam therapy – Current knowledge and future challenges. *Clin Transl Radiat Oncol* (2018) 9:35–41. doi: 10.1016/j.ctro.2018.01.006
4. Ahmed SK, Brown PD, Foote RL. Protons vs Photons for Brain and Skull Base Tumors. *Semin Radiat Oncol* (2018) 28:97–107. doi: 10.1016/j.semradonc.2017.11.001
5. Combs SE. Does Proton Therapy Have a Future in CNS Tumors? *Curr Treat Options Neurol* (2017) 19:12. doi: 10.1007/s11940-017-0447-4
6. PTCOG - Home. (2020). Available at: https://www.ptcog.ch/index.php (Accessed March 5, 2020).
7. Jhaveri J, Cheng E, Tian S, Buchwald Z, Chowdhary M, Liu Y, et al. Proton vs. Photon Radiation Therapy for Primary Gliomas: An Analysis of the National Cancer Data Base. *Front Oncol* (2018) 8:440. doi: 10.3389/fonc.2018.00440
8. Petr J, Platzek I, Hofheinz F, Mutsaerts HJMM, Asllani I, van Osch MJP, et al. Photon vs. proton radiochemotherapy: Effects on brain tissue volume and perfusion. *Radiother Oncol* (2018) 128:121—127. doi: 10.1016/j.radonc.2017.11.033
9. Goossens ME, Van den Bulcke M, Gevaert T, Meheus L, Verellen D, Cosset J-M, et al. Is there any benefit to particles over photon radiotherapy? *E Cancer Med Sci* (2019) 13:982. doi: 10.3332/ecancer.2019.982
10. Lühr A, von Neubeck C, Pawelke J, Seidlitz A, Peitzsch C, Bentzen SM, et al. "Radiobiology of Proton Therapy": Results of an international expert workshop. *Radiother Oncol* (2018) 128:56–67. doi: 10.1016/j.radonc.2018.05.018
11. Paganetti H. Relative biological effectiveness ({RBE}) values for proton beam therapy. Variations as a function of biological endpoint, dose, and linear energy transfer. *Phys Med Biol* (2014) 59:R419–72. doi: 10.1088/0031-9155/59/22/r419
12. Saager M, Peschke P, Brons S, Debus J, Karger CP. Determination of the proton RBE in the rat spinal cord: Is there an increase towards the end of the spread-out Bragg peak? *Radiother Oncol* (2018) 128:115–20. doi: 10.1016/j.radonc.2018.03.002
13. Eulitz J, Troost EGC, Raschke F, Schulz E, Lutz B, Dutz A, et al. Predicting late magnetic resonance image changes in glioma patients after proton therapy. *Acta Oncol (Madr)* (2019) 58:1536–9. doi: 10.1080/0284186X.2019.1631477
14. Bahn E, Bauer J, Harrabi S, Herfarth K, Debus J, Alber M. Late Contrast Enhancing Brain Lesions in Proton-Treated Patients With Low-Grade Glioma: Clinical Evidence for Increased Periventricular Sensitivity and Variable RBE. *Int J Radiat Oncol* (2020) 107(3):571–8. doi: 10.1016/j.ijrobp.2020.03.013
15. Monje ML, Palmer T. Radiation injury and neurogenesis. [Miscellaneous Article]. *Curr Opin Neurol* (2003) 16:129–34. doi: 10.1097/01.wco.0000063772.81810.b7
16. Panagiotakos G, Alshamy G, Chan B, Abrams R, Greenberg E, Saxena A, et al. Long-term impact of radiation on the stem cell and oligodendrocyte precursors in the brain. *PLoS One* (2007) 2:e588. doi: 10.1371/journal.pone.0000588
17. Connor M, Karunamuni R, McDonald C, Seibert T, White N, Moiseenko V, et al. Regional susceptibility to dose-dependent white matter damage after brain radiotherapy. *Radiother Oncol* (2017) 123:209–17. doi: 10.1016/j.radonc.2017.04.006
18. Eulitz J, Lutz B, Wohlfahrt P, Dutz A, Enghardt W, Karpowitz C, et al. A Monte Carlo based radiation response modelling framework to assess

variability of clinical RBE in proton therapy. *Phys Med Biol* (2019) 64:225020. doi: 10.1088/1361-6560/ab3841
19. Gunther JR, Sato M, Chintagumpala M, Ketonen L, Jones JY, Allen PK, et al. Imaging changes in pediatric intracranial ependymoma patients treated with proton beam radiation therapy compared to intensity modulated radiation therapy This work was presented previously at the 56th Annual American Society for Radiation Oncology Meetin. *Int J Radiat Oncol Biol Phys* (2015) 93:54–63. doi: 10.1016/j.ijrobp.2015.05.018
20. Walker AJ, Ruzevick J, Malayeri AA, Rigamonti D, Lim M, Redmond KJ, et al. Postradiation imaging changes in the CNS: How can we differentiate between treatment effect and disease progression? *Future Oncol* (2014) 10:1277–97. doi: 10.2217/fon.13.271
21. Greene-Schloesser D, Robbins ME, Peiffer AM, Shaw EG, Wheeler KT, Chan MD. Radiation-induced brain injury: A review. *Front Oncol* (2012) 2:73. doi: 10.3389/fonc.2012.00073
22. Chen HI, Song H, Ming GL. Applications of Human Brain Organoids to Clinical Problems. *Dev Dyn* (2019) 248:53–64. doi: 10.1002/dvdy.24662
23. Suckert T, Rassamegevanon T, Müller J, Dietrich A, Graja A, Reiche M, et al. Applying Tissue Slice Culture in Cancer Research—Insights from Preclinical Proton Radiotherapy. *Cancers (Basel)* (2020) 12:1589. doi: 10.3390/cancers12061589
24. Chiang CS, McBride WH, Withers HR. Radiation-induced astrocytic and microglial responses in mouse brain. *Radiother Oncol* (1993) 29:60–8. doi: 10.1016/0167-8140(93)90174-7
25. Rola R, Raber J, Rizk A, Otsuka S, Vandenberg SR, Morhardt DR, et al. Radiation-induced impairment of hippocampal neurogenesis is associated with cognitive deficits in young mice. *Exp Neurol* (2004) 188:316–30. doi: 10.1016/j.expneurol.2004.05.005
26. Kiehl EL, Stojadinovic S, Malinowski KT, Limbrick D, Jost SC, Garbow JR, et al. Feasibility of small animal cranial irradiation with the microRT system. *Med Phys* (2008) 35:4735–43. doi: 10.1118/1.2977762
27. Yang L, Yang J, Li G, Li Y, Wu R, Cheng J, et al. Pathophysiological Responses in Rat and Mouse Models of Radiation-Induced Brain Injury. *Mol Neurobiol* (2017) 54:1022–32. doi: 10.1007/s12035-015-9628-x
28. Bentzen SM, Parliament M, Deasy JO, Dicker A, Curran WJ, Williams JP, et al. Biomarkers and Surrogate Endpoints for Normal-Tissue Effects of Radiation Therapy: The Importance of Dose-Volume Effects. *Int J Radiat Oncol Biol Phys* (2010) 76:145–50. doi: 10.1016/j.ijrobp.2009.08.076
29. Müller J, Schürer M, Neubert C, Tillner F, Beyreuther E, Suckert T, et al. Multi-modality bedding platform for combined imaging and irradiation of mice. *BioMed Phys Eng Express* (2020) 6(3):037003. doi: 10.1088/2057-1976/AB79F1
30. Müller J, Neubert C, von Neubeck C, Baumann M, Krause M, Enghardt W, et al. Proton radiography for inline treatment planning and positioning verification of small animals. *Acta Oncol (Madr)* (2017) 56:1399–405. doi: 10.1080/0284186X.2017.1352102
31. Suckert T, Müller J, Beyreuther E, Azadegan B, Brüggemann A, Bütof R, et al. High-precision image-guided proton irradiation of mouse brain sub-volumes. *Radiother Oncol* (2020) 146:205–12. doi: 10.1016/j.radonc.2020.02.023
32. Williams JP, Brown SL, Georges GE, Hauer-Jensen M, Hill RP, Huser AK, et al. Animal Models for Medical Countermeasures to Radiation Exposure. *Radiat Res* (2010) 173:557–78. doi: 10.1667/rr1880.1
33. Semple BD, Blomgren K, Gimlin K, Ferriero DM, Noble-Haeusslein LJ, RangeK. Brain development in rodents and humans: Identifying benchmarks of maturation and vulnerability to injury across species. *Prog Neurobiol* (2013) 106–107:1–16. doi: 10.1016/j.pneurobio.2013.04.001
34. Münter MW, Karger CP, Reith W, Schneider HM, Peschke P, Debus J. Delayed Vascular Injury after Single High-Dose Irradiation in the Rat Brain: Histologic, Immunohistochemical, and Angiographic Studies. *Radiology* (1999) 212:475–82. doi: 10.1148/radiology.212.2.r99au42475
35. Karger CP, Münter MW, Heiland S, Peschke P, Debus J, Hartmann GH. Dose–Response Curves and Tolerance Doses for Late Functional Changes in the Normal Rat Brain after Stereotactic Radiosurgery Evaluated by Magnetic Resonance Imaging: Influence of End Points and Follow-up Time. *Radiat Res* (2002) 157:617–25. doi: 10.1667/0033-7587(2002)157[0617:DRCATD]2.0.CO;2
36. Beyreuther E, Baumann M, Enghardt W, Helmbrecht S, Karsch L, Krause M, et al. Research facility for radiobiological studies at the university proton therapy dresden. *Int J Part Ther* (2019) 5:172–82. doi: 10.14338/IJPT-18-00008.1
37. Beyreuther E, Brand M, Hans S, Hideghéty K, Karsch L, Leßmann E, et al. Feasibility of proton FLASH effect tested by zebrafish embryo irradiation. *Radiother Oncol* (2019) 139:46–50. doi: 10.1016/j.radonc.2019.06.024
38. Lewis D, Micke A, Yu X, Chan MF. An efficient protocol for radiochromic film dosimetry combining calibration and measurement in a single scan. *Med Phys* (2012) 39:6339–50. doi: 10.1118/1.4754797
39. Perl J, Shin J, Schümann J, Faddegon B, Paganetti H. TOPAS: an innovative proton Monte Carlo platform for research and clinical applications. *Med Phys* (2012) 39:6818–37. doi: 10.1118/1.4758060
40. Tillner F, Thute P, Löck S, Dietrich A, Fursov A, Haase R, et al. Precise image-guided irradiation of small animals: A flexible non-profit platform. *Phys Med Biol* (2016) 61:3084–108. doi: 10.1088/0031-9155/61/8/3084
41. Lein ES, Hawrylycz MJ, Ao N, Ayres M, Bensinger A, Bernard A, et al. Genome-wide atlas of gene expression in the adult mouse brain. *Nature* (2007) 445:168–76. doi: 10.1038/nature05453
42. Berliner Tierschutzbeauftragter A, Thiel RA. Orientierungshilfe des Arbeitskreises Berliner Tierschutzbeauftragter zur Einstufung in Belastungsgrade (Tab. 1.6.7) für genehmigungspflichtige Tierversuche.
43. Cox JD, Stetz JA, Pajak TF. Toxicity criteria of the Radiation Therapy Oncology Group (RTOG) and the European organization for research and treatment of cancer (EORTC). *Int J Radiat Oncol Biol Phys* (1995) 31:1341–6. doi: 10.1016/0360-3016(95)00060-C
44. Schindelin J, Arganda-Carreras I, Frise E, Kaynig V, Longair M, Pietzsch T, et al. Fiji: An open-source platform for biological-image analysis. *Nat Methods* (2012) 9:676–82. doi: 10.1038/nmeth.2019
45. Wolf I, Vetter M, Wegner I, Nolden M, Bottger T, Hastenteufel M, et al. The medical imaging interaction toolkit (MITK): a toolkit facilitating the creation of interactive software by extending VTK and ITK. *Proc SPIE* (2004) 5367:16–27. doi: 10.1117/12.535112
46. Dabov K, Foi A, Katkovnik V, Egiazarian K. Image denoising by sparse 3-D transform-domain collaborative filtering. *IEEE Trans image Process* (2007) 16:2080–95. doi: 10.1109/TIP.2007.901238
47. Jost SC, Hope A, Kiehl E, Perry A, Travers S, Garbow JR, et al. A novel murine model for localized radiation necrosis and its characterization using advanced magnetic resonance imaging. *Int J Radiat Oncol Biol Phys* (2009) 75:527–33. doi: 10.1016/j.ijrobp.2009.06.007
48. Ruben JD, Dally M, Bailey M, Smith R, McLean CA, Fedele P. Cerebral radiation necrosis: Incidence, outcomes, and risk factors with emphasis on radiation parameters and chemotherapy. *Int J Radiat Oncol Biol Phys* (2006) 65:499–508. doi: 10.1016/j.ijrobp.2005.12.002
49. Zimny A, Neska-Matuszewska M, Bladowska J, Sąsiadek MJ. Intracranial lesions with low signal intensity on T2-weighted MR images - review of pathologies. *Pol J Radiol* (2015) 80:40–50. doi: 10.12659/PJR.892146
50. Kano H, Kondziolka D, Lobato-Polo J, Zorro O, Flickinger JC, Lunsford LD. T1/T2 Matching to Differentiate Tumor Growth From Radiation Effects After Stereotactic Radiosurgery. *Neurosurgery* (2010) 66:486–92. doi: 10.1227/01.NEU.0000360391.35749.A5
51. Valk PE, Dillon WP. Radiation injury of the brain. *Am J Neuroradiol* (1991) 12:45–62. doi: 10.1007/s003290050053
52. Viselner G, Farina L, Lucev F, Turpini E, Lungarotti L, Bacila A, et al. Brain MR findings in patients treated with particle therapy for skull base tumors. *Insights Imaging* (2019) 10:45–62. doi: 10.1186/s13244-019-0784-9
53. Lo EH, Frankel KA, Steinberg GK, Delapaz RL, Fabrikant JI. High-dose single-fraction brain irradiation: MRI, cerebral blood flow, electrophysiological, and histological studies. *Int J Radiat Oncol Biol Phys* (1992) 22:47–55. doi: 10.1016/0360-3016(92)90981-M
54. Jiang X, Yuan L, Engelbach JA, Cates J, Perez-Torres CJ, Gao F, et al. A gamma-knife-enabled mouse model of cerebral single-hemisphere delayed radiation necrosis. *PLoS One* (2015) 10:1–13. doi: 10.1371/journal.pone.0139596
55. Boria AJ, Perez-Torres CJ. Influence of Dose Uniformity when Replicating a Gamma Knife Mouse Model of Radiation Necrosis with a Preclinical Irradiator. *Radiat Res* (2019) 191:352–9. doi: 10.1667/RR15273.1
56. Sofroniew MV. Molecular dissection of reactive astrogliosis and glial scar formation. *Trends Neurosci* (2009) 32:638–47. doi: 10.1016/j.tins.2009.08.002

57. Kozlowski C, Weimer RM. An automated method to quantify microglia morphology and application to monitor activation state longitudinally in vivo. *PLoS One* (2012) 7:1–9. doi: 10.1371/journal.pone.0031814
58. Monje ML, Mizumatsu S, Fike JR, Palmer TD. Irradiation induces neural precursor-cell dysfunction. *Nat Med* (2002) 8:955–62. doi: 10.1038/nm749
59. Monje ML, Toda H, Palmer TD. Inflammatory Blockade Restores Adult Hippocampal Neurogenesis. *Science (80-)* (2003) 302:1760–5. doi: 10.1126/science.1088417
60. Kim JH, Brown SL, Jenrow KA, Ryu S. Mechanisms of radiation-induced brain toxicity and implications for future clinical trials. *J Neurooncol* (2008) 87:279–86. doi: 10.1007/s11060-008-9520-x
61. Rottenberg DA, Chernik NL, Michael DFD, Ellis F, Posner JB. Cerebral necrosis following radiotherapy of extracranial neoplasms. *Ann Neurol* (1977) 1:339–57. doi: 10.1002/ana.410010406
62. Li YQ, Chen P, Haimovitz-Friedman A, Reilly RM, Wong CS. Endothelial apoptosis initiates acute blood-brain barrier disruption after ionizing radiation. *Cancer Res* (2003) 63:5950–6.
63. Ljubimova NV, Levitman MK, Plotnikova ED, Eidus LK. Endothelial cell population dynamics in rat brain after local irradiation. *Br J Radiol* (1991) 64:934–40. doi: 10.1259/0007-1285-64-766-934
64. Rosenzweig I, Glasser M, Polsek D, Leschziner GD, Williams SCR, Morrell MJ. Sleep apnoea and the brain: a complex relationship. *Lancet Respir Med* (2015) 3:404–14. doi: 10.1016/S2213-2600(15)00090-9
65. Miyatake SI, Nonoguchi N, Furuse M, Yoritsune E, Miyata T, Kawabata S, et al. Pathophysiology, diagnosis, and treatment of radiation necrosis in the brain. *Neurol Med Chir (Tokyo)* (2014) 55:50–9. doi: 10.2176/nmc.ra.2014-0188
66. Houser CR. Granule cell dispersion in the dentate gyrus of humans with temporal lobe epilepsy. *Brain Res* (1990) 535:195–204. doi: 10.1016/0006-8993(90)91601-C
67. Amador-Ortiz C, Ahmed Z, Zehr C, Dickson DW. Hippocampal sclerosis dementia differs from hippocampal sclerosis in frontal lobe degeneration. *Acta Neuropathol* (2007) 113:245–52. doi: 10.1007/s00401-006-0183-4
68. Levin VA, Bidaut L, Hou P, Kumar AJ, Wefel JS, Bekele BN, et al. Randomized double-blind placebo-controlled trial of bevacizumab therapy for radiation necrosis of the central nervous system. *Int J Radiat Oncol Biol Phys* (2011) 79:1487–95. doi: 10.1016/j.ijrobp.2009.12.061
69. Gonzalez J, Kumar AJ, Conrad CA, Levin VA. Effect of bevacizumab on radiation necrosis of the brain. *Int J Radiat Oncol* (2007) 67:323–6. doi: 10.1016/j.ijrobp.2006.10.010
70. Rodgers SP, Trevino M, Zawaski JA, Gaber MW, Leasure JL. Neurogenesis, exercise, and cognitive late effects of pediatric radiotherapy. *Neural Plast* (2013) 2013. doi: 10.1155/2013/698528

Conflict of Interest: The authors declare that the research was conducted in the absence of any commercial or financial relationships that could be construed as a potential conflict of interest.

Copyright © 2021 Suckert, Beyreuther, Müller, Azadegan, Meinhardt, Raschke, Bodenstein, von Neubeck, Lühr, Krause and Dietrich. This is an open-access article distributed under the terms of the Creative Commons Attribution License (CC BY). The use, distribution or reproduction in other forums is permitted, provided the original author(s) and the copyright owner(s) are credited and that the original publication in this journal is cited, in accordance with accepted academic practice. No use, distribution or reproduction is permitted which does not comply with these terms.

frontiers in Oncology

ORIGINAL RESEARCH
published: 14 January 2021
doi: 10.3389/fonc.2020.613089

Early Toxicities After High Dose Rate Proton Therapy in Cancer Treatments

Jérôme Doyen[1], Marie-Pierre Sunyach[2], Fabien Almairac[3], Véronique Bourg[4], Arash O. Naghavi[5], Gwenaëlle Duhil de Bénazé[6], Audrey Claren[7], Laetitia Padovani[8], Karen Benezery[7], Georges Noël[9], Jean-Michel Hannoun-Lévi[1], Ferran Guedea[10], Jordi Giralt[11], Marie Vidal[7], Guillaume Baudin[12], Lucas Opitz[13], Line Claude[2] and Pierre-Yves Bondiau[7]*

[1] Université Côte d'Azur, Department of Radiation Oncology, Centre Antoine-Lacassagne, Fédération Claude Lalanne, Nice, France, [2] Department of Radiotherapy, Léon Bérard Cancer Center, Lyon, France, [3] Department of Neurosurgery, Centre Hospitalier Universitaire, University Côte d'Azur, Nice, France, [4] Department of Neurology, Centre Hospitalier Universitaire, University Côte d'Azur, Nice, France, [5] Department of Radiation Oncology, H. Lee Moffitt Cancer Center and Research Institute, Tampa, FL, United States, [6] Department of Pediatric Oncology, Centre Hospitalier Universitaire, University Côte d'Azur, Nice, France, [7] Department of Radiation Oncology, Centre Antoine-Lacassagne, Nice, France, [8] Oncology Radiotherapy Department, CRCM Inserm, UMR1068, CNRS UMR7258, AMU UM105, Genome Instability and Carcinogenesis, Assistance Publique des Hôpitaux de Marseille, Aix-Marseille University, Marseille, France, [9] Department of Radiation Oncology, Institut de cancérologie Strasbourg Europe (Icans), Strasbourg, France, [10] Radiation Oncology Department, Institut Català d'Oncologia (ICO) and University of Barcelona (UB), L'Hospitalet de Llobregat, Barcelona, Spain, [11] Hospital Vall d'Hebron, Vall d'Hebron Institute of Oncology, Barcelona, Spain, [12] Department of Radiology, Centre Antoine-Lacassagne, Nice, France, [13] Department of Anesthesiology, Centre Antoine-Lacassagne, Nice, France

OPEN ACCESS

Edited by:
John Varlotto, University of Massachusetts Medical School, United States

Reviewed by:
John E. Mignano, Tufts University School of Medicine, United States
Corrado Spatola, University of Catania, Italy

***Correspondence:**
Jérôme Doyen
jerome.doyen@nice.unicancer.fr

Specialty section:
This article was submitted to Radiation Oncology, a section of the journal Frontiers in Oncology

Received: *01 October 2020*
Accepted: *23 November 2020*
Published: *14 January 2021*

Citation:
Doyen J, Sunyach M-P, Almairac F, Bourg V, Naghavi AO, Duhil de Bénazé G, Claren A, Padovani L, Benezery K, Noël G, Hannoun-Lévi J-M, Guedea F, Giralt J, Vidal M, Baudin G, Opitz L, Claude L and Bondiau P-Y (2021) Early Toxicities After High Dose Rate Proton Therapy in Cancer Treatments. Front. Oncol. 10:613089. doi: 10.3389/fonc.2020.613089

Background: The conventional dose rate of radiation therapy is 0.01–0.05 Gy per second. According to preclinical studies, an increased dose rate may offer similar anti-tumoral effect while dramatically improving normal tissue protection. This study aims at evaluating the early toxicities for patients irradiated with high dose rate pulsed proton therapy (PT).

Materials and Methods: A single institution retrospective chart review was performed for patients treated with high dose rate (10 Gy per second) pulsed proton therapy, from September 2016 to April 2020. This included both benign and malignant tumors with ≥3 months follow-up, evaluated for acute (≤2 months) and subacute (>2 months) toxicity after the completion of PT.

Results: There were 127 patients identified, with a median follow up of 14.8 months (3–42.9 months). The median age was 55 years (1.6–89). The cohort most commonly consisted of benign disease (55.1%), cranial targets (95.1%), and were treated with surgery prior to PT (56.7%). There was a median total PT dose of 56 Gy (30–74 Gy), dose per fraction of 2 Gy (1–3 Gy), and CTV size of 47.6 ml (5.6–2,106.1 ml). Maximum acute grade ≥2 toxicity were observed in 49 (38.6%) patients, of which 8 (6.3%) experienced grade 3 toxicity. No acute grade 4 or 5 toxicity was observed. Maximum subacute grade 2, 3, and 4 toxicity were discovered in 25 (19.7%), 12 (9.4%), and 1 (0.8%) patient(s), respectively.

Conclusion: In this cohort, utilizing high dose rate proton therapy (10 Gy per second) did not result in a major decrease in acute and subacute toxicity. Longer follow-up and comparative studies with conventional dose rate are required to evaluate whether this approach offers a toxicity benefit.

Keywords: high dose rate, proton therapy, cancer, early, subacute, toxicity

INTRODUCTION

Proton Therapy (PT) is a particle therapy that utilizes a Bragg Peak to reduce the radiation dose received by healthy tissue, as demonstrated by previous *in silico* studies (1). PT is preferred in patients with a long-life expectancy, to mitigate the risk of late sequela (e.g., secondary malignancy, cardiovascular complications, etc.) or in patients where the ideal dose is difficult to achieve without a significant toxicity risk. Several studies have demonstrated a clinical advantage of PT over conventional photon radiotherapy (2–6), with many prospective clinical trials ongoing.

To further improve the therapeutic ratio, several preclinical studies identified a considerable biological advantage to delivering radiation dose rate higher than the conventional 0.01 to 0.05 Gy/second. "FLASH" radiotherapy, or dose rates exceeding 10 Gy per 100 ms, significantly reduced the radiation damage to healthy cells/tissue without a decline in anti-tumoral effect (7–9). This was initially demonstrated with electrons (7–9), but subsequently with photons (10) and protons (11–13). There is a scarcity of clinical data utilizing FLASH radiotherapy, with only 1 case report to date, which showed that electron FLASH reirradiation may mitigate toxicity and allow radiation delivery even if the theoretical cumulative doses to healthy tissue would be exceeded (14).

A recent clinical device (Proteus One©, Ion Beam Application) was designed to deliver pencil-beam scanning with pulsed proton at high dose rate, approximately 200–1,000 times faster than the classical dose rate (125 million protons per pulse leading to approximately 10 Gy/s per spot, depending on the range and energy needed) (15). Toxicity with this dose rate level per spot has not yet been reported.

The purpose of the current study is to analyze the early toxicities for tumors treated pencil-beam scanning with pulsed high dose rate protons.

MATERIALS AND METHODS

Patient Selection

With institutional review board approval, we retrospectively analyzed patients receiving PT at our institution between September 2016 and April 2020. This study included patients that were treated for a benign or malignant tumor, had at least 3 months of clinical follow-up, and received radiation with only PT (without a photon component). Reirradiation was included, defined as an overlap in the previous field with the current GTV. Patients addressed from other centres were not included because of the lack of updated follow-up.

Follow-Up

Patients were followed weekly during PT or more frequently if necessary. A 1-month clinical follow-up was performed after the completion of PT. Benign tumors underwent magnetic resonance imaging (MRI) and clinical follow-up 4 months after completing PT and every 6 months thereafter. Malignant tumors underwent imaging according to the standard of care for that malignancy, which included an MRI of the irradiated region and clinical follow-up every 4 months for 2 years, then every 6 months for 3 years, and a computed tomography (CT) scan of the thorax and abdomen if required (e.g., head and neck cancer, sarcomas, etc.).

Tumor response was evaluated according to RECIST (response criteria in solid tumors) 1.1 criteria (16) and toxicities according to the fifth version of the Common Terminology Criteria for Adverse Events (CTCAE). Toxicity was considered "acute" if occurred during PT or within 2 months of completing PT, and "subacute" if occurred >2 months after completing PT. Late toxicity was not reported due to short follow-up.

Proton Therapy

PT was delivered with Pencil Beam Scanning (PBS), utilizing the Proteus One© device (Ion Beam Application©), which is a synchrocyclotron with active pencil beam scanning and pulsed beam PT. Approximately 125 million protons are delivered per pulse/spot with an energy of 100 to 226 MeV as a function of the target depth. The dose rate per spot is approximately 10 Gy per second, depending on the energy. The characterization of this beam was previously reported by Rossomme et al (15). PT immobilization was performed with a thermoplastic mask for head and neck targets or vacuum body cast for extracranial targets.

The dosimetry was performed using the Raystation treatment planning system © version 6.0 before June 2019 and version 8.0 after June 2019 (Raysearch Laboratories, Stockholm, Sweden). Dose constraints from Feuvret et al (17). and by Marks et al (18). were used for head/neck and extracranial targets, respectively. A relative biologic effectiveness factor for protons of 1.1 was incorporated. PBS plans were calculated using robust

Abbreviations: CT, computed tomography; CTCAE, Common Terminology Criteria for Adverse Events; CTV, clinical target volume; GTV, gross tumor volume; IMPT, intensity modulated proton therapy; LC, local control; LGG, low grade glioma; MRI, magnetic resonance imaging; PBS, Pencil Beam Scanning; PFS, progression-free survival; PT, Proton Therapy; PTV, planning target volume; RECIST, response criteria in solid tumors.

optimization (3% range uncertainties-3 mm positioning uncertainties, for cranial target and 3%–5 mm for extracranial target). Robustness was applied for CTV, brain stem, spinal cord, optic nerves, optic chiasm, femoral head, and digestive tract.

Statistical Analysis

Tumor response was defined by progression, stabilization, partial response, or complete response. Time-to-event outcomes were estimated from the date of last PT fraction to an event or censored at last follow up. This included local control (LC), and progression-free survival (PFS). LC and PFS were evaluated *via* Kaplan-Meier method with a 95% confidence interval (IC 95%). Median follow-up was evaluated by the Schemper method. All statistical analyses were performed using Statistical Package for the Social Sciences (SPSS) version 16.0 on Windows®.

RESULTS

Characteristics of Patients and Treatments

Characteristics of patients and treatments are described in **Table 1**. A total of 127 patients were included. This cohort most commonly consisted of benign disease (55.1%), head and neck location (95.1%), and ECOG ≤ 1 (95.8%). Majority of patients had treatments prior to PT, which included surgery (56.7%), chemotherapy (26%), and previous radiotherapy to the same location (14.2%). Two patients were irradiated with a bifractionated schedule because of previous radiation.

The most common diseases in this study include: meningioma (10.4%), followed by malignant paranasal and nasal sinus tumors (4.3%), and low-grade gliomas (4%).

Chemotherapy was also delivered concomitantly with PT (10.2%) and adjuvant after PT (11%). Concomitant chemotherapy was used for Ewing sarcoma (n=3, vincristine, doxorubicin, ifosfamide), rhabdomyosarcoma (n=6, ifosfamide, vincristine), malignant sinus tumor (n=3, platinum-based chemotherapy), and metastatic lymph node from a vulvar squamous cell carcinoma (n=1, platinum-based chemotherapy). After PT, 1 patient underwent surgical resection.

Among patients with meningioma, malignant sinus tumor and low-grade gliomas, the median total PT dose delivered was 56 Gy (54–60), 68.2 Gy (45–70.4), and 55.8 Gy (54–60), with a median dose per fraction of 2 Gy (1.8–2), 2 Gy (1.8–3), and 2 Gy (1.8–2), and a median CTV size of 41.4 ml (6.7–250.9), 88.2 ml (22.1–572.8), and 65.5 ml (6.2–422.1), respectively.

Among patients with pelvic (n=14) or paraspinal tumors (n=2) the median total PT dose was 65.1 Gy (50.4–73.5), with a median dose per fraction of 2 Gy (1.8–2.4), and a median low risk and high risk CTV size of 437.4 ml (83.2–2,106) and 112.5 ml (14.5–560.9), respectively.

Median follow-up was 14.8 months (3;-42.9). Locally, 5 (3.9%) patients experienced a complete response, 31 (24.4%) a partial response, 71 (55.9%) stabile disease, 5 (3.9%) progressive disease (PD), and 17 (11.9%) did not relapse after combine combination of surgery and PT (local control). The 1-year local

TABLE 1 | Patient and treatment characteristics.

Variable	
Median age (years)	55 (1.6–89)
Gender	
Male	59 (46.5%)
Female	68 (53.5%)
Histology	
Benign brain tumors	
Meningioma	34 (26.7%)
Schwannoma	4 (3.2%)
Paraganglioma	4 (3.2%)
Craniopharyngioma	4 (3.2%)
Pituitary adenoma	7 (5.5%)
Primary orbitary tumors (lymphoma)	2 (1.6%)
Benign vascular tumor	3 (2.4%)
Malignant brain tumors	
Ependymoma	4 (3.2%)
Low grade glioma	13 (10.2%)
Bone tumors	
Chordoma	10 (7.9%)
Chondrosarcoma	3 (2.4%)
Giant cell tumor	1 (0.7%)
Ewing sarcoma	3 (2.4%)
Malignant head and neck tumors	
Malignant paranasal and nasal sinus tumors	14 (11%)
Salivary gland carcinoma	6 (4.7%)
Sarcoma	
Rhabdomyosarcoma	6 (4.7%)
Sarcoma	5 (3.9%)
Other	
Merckel carcinoma	1 (0.7%)
Isolated/local relapse of other cancer*	3 (2.4%)
Tumor location	
Head and neck	111 (95.1%)
Pelvis	14 (4.3%)
Paraspinal	2 (0.6%)
Previous surgery	
Yes	72 (56.7%)
No	55 (43.3%)
Previous chemotherapy	
Yes	33 (26%)
No	94 (74%)
Reirradiation setting	
Yes	18 (14.2%)
No	109 (85.8%)
Concomitant chemotherapy	
Yes	13 (10.2%)
No	114 (89.8%)
Performance Status ECOG**	
At the beginning of Proton Therapy	
0	79 (62.7%)
1	42 (33.1%)
2	5 (3.9%)
Missing	1 (0.8%)
Radiotherapy	
Median residual tumor volume	12.5 ml (0–672)
Median low-risk CTV	47.6 ml (5.6–2106.1)
Median high-risk CTV (if boost, n=46)	35.3 ml (4.1–560.9)
Median dose per fraction	2 Gy (1–3)
Median number of fractions	30 (12–60)
Median total dose	56 Gy (30–74)
Median PT duration	48 days (18–82)
Bifractionated	2 (1.6%)

*Rectal cancer, vaginal squamous cell carcinoma, clear cell carcinoma of the kidney.
**Eastern Cooperative Oncology Group.

control and progression-free survival were 89.2% and 85%, respectively.

Acute Toxicities

Acute toxicities are defined as side-effects that occur during PT or within 2 months of completing PT (**Table 2**). Maximum acute toxicity grade was 0, 1, 2, and 3 for 20 (15.7%), 58 (45.7%), 41 (32.3%), and 8 (6.3%) patients, respectively. There were no grade 4 or 5 acute toxicities.

The most frequent acute toxicity was alopecia (n=40), primarily in targets close to skin or eyelids (88 patients). **Figure 1A** describes an example of alopecia occurring during PT in a patient treated for meningioma (Patient 1). The second most frequent acute toxicity was radiation dermatitis (n=39), which occurred when irradiating close to the skin surface. An example is a vertex angiosarcoma patient treated to 66 Gy (2 Gy per fraction, no concomitant chemotherapy) (**Figure 1B**), who presented with a grade 3 dermatitis at 46 Gy, which slowly healed 1 month after completing PT (Patient 2). Of note 10 out of 13 patients irradiated with concomitant chemotherapy presented with dermatitis.

Only one patient with a head and neck tumor received radiation to their primary and bilateral lymph nodes, whereas all other patients received radiation to only their primary or ipsilateral neck (e.g., salivary gland tumors). **Figure 1C** describes a 79 year-old patient with non-operable cystic adenoid carcinoma irradiated to 73.5 Gy (2.1 Gy per session) (Patient 3). This treatment was well tolerated with only grade 1 oral mucositis and no dysgeusia.

TABLE 2 | Acute toxicities.

	Grade 1	Grade 2	Grade 3	Grade 4	Total
Alopecia	40	0	0	0	40
Dermatitis radiation	24	14	1	0	39
Asthenia	20	6	0	0	26
Headache	20	3	1	0	24
Dry eye	18	6	0	0	24
Nausea	14	3	1	0	18
Sinusitis	8	7	0	0	15
Oral mucositis	9	1	2	0	12
Local pain	6	5	1	0	10
Dysgeusia	6	3	0	0	9
Dry mouth	5	2	0	0	7
Dizziness	5	0	0	0	5
Orbit edema	4	1	0	0	5
Anosmia	5	0	0	0	5
Seizure	1	2	1	0	4
Trismus	4	0	0	0	4
Local bleeding	4	0	0	0	4
Dyspnea	1	2	0	0	3
Diarrhea	3	0	0	0	3
Hearing impaired	2	0	0	0	2
Cranial nerve disorder	0	0	2	0	2
External otitis	2	0	0	0	2
Dysesthesia	1	1	0	0	2
Keratitis	1	0	0	0	1
Esophagitis	1	0	0	0	1
Palpitations	1	0	0	0	1
Cystitis	1	0	0	0	1
Vomiting	0	2	0	0	1

In pelvic and paraspinal tumors (n=16), PT was well tolerated with no grade ≥ 3 gastrointestinal toxicities. Of note, there were only 4 grade 1 gastrointestinal toxicities in this subgroup (3 diarrhea and 1 nausea).

Subacute Toxicities

Subacute toxicity, which occurred >2 months after completing PT, are detailed in **Table 3**. Maximum subacute toxicity grade was 0, 1, 2, 3, and 4 for 50 (39.4%), 39 (30.7%), 25 (19.7%), 12 (9.4%), and 1 (0.8%) patient(s), respectively. There were no grade 5 toxicities.

The most common subacute toxicity was dry eye (n=20, 18% among cranial targets, no grade ≥3 toxicity), followed by seizures (n=14, 12.6% among cranial targets). All patients with grade 3 seizures (n=6) were due to a new onset seizure with no prior seizure history. Seizures were medically manageable for all patients. Histology of patients who presented with a subacute onset seizure was as follows: meningioma (n=7), low grade glioma (n=4), ependymoma (n=1) and pituitary adenoma (n=1). Of these, 8 presented with baseline seizures, 7 of which were on antiepileptic drugs. Median delay to new onset or worsening of seizure was 4.6 months (0.8–34.2) from the end of PT. Of the pelvic and primary tumors, there was 1 grade 3 toxicity (colonic obstruction), in a previously irradiated pelvic sarcoma, requiring hospitalization and resolved with medical management. There was 1 grade 4 toxicity (left optic nerve disorder), which occurred in a 72-year old women treated for skull-based meningioma surrounding optic nerves bilaterally. Left blindness occurred 1 year after PT with no evidence of relapse. D1, D2 and Dmean to the left optic nerve were 53.7 Gy, 53.7 Gy, and 53.3 Gy, respectively.

DISCUSSION

To our knowledge the current study is the first to report early outcomes after high dose rate pulsed proton therapy. The cohort primarily consists of cranial targets and benign disease. The acute toxicities were as expected according to dosimetry, especially for acute onset alopecia and dermatitis.

Unfortunately, the use of high dose rate pulsed PT did not provide a significant "FLASH-like" radioprotective effect.

According to the FLASH electron therapy data, we should have observed a much lower rate and intensity of acute side-effects. In the preclinical setting, Favaudon et al. delivered 15 Gy in a single FLASH dose (60 Gy/s) to the whole lungs without inflammatory infiltration or extracellular matrix deposition after 62 days, whereas mice irradiated with classical dose rates (0.03/s) presented with dense inflammatory infiltrate and extracellular matrix deposition (7).

In our cohort, no patient received lung irradiation and cannot comment on whether our "FLASH effect" might be dependent on the nature of the irradiated tissue. However, Montay-Gruel et al. reported that FLASH photon therapy could also have a protective effect during brain irradiation (8, 10). Unfortunately, we observed seizure rates of 3.6% (n=4 of 111 patients with cranial irradiation) during PT and 12.6% (n=14 of 111 patients

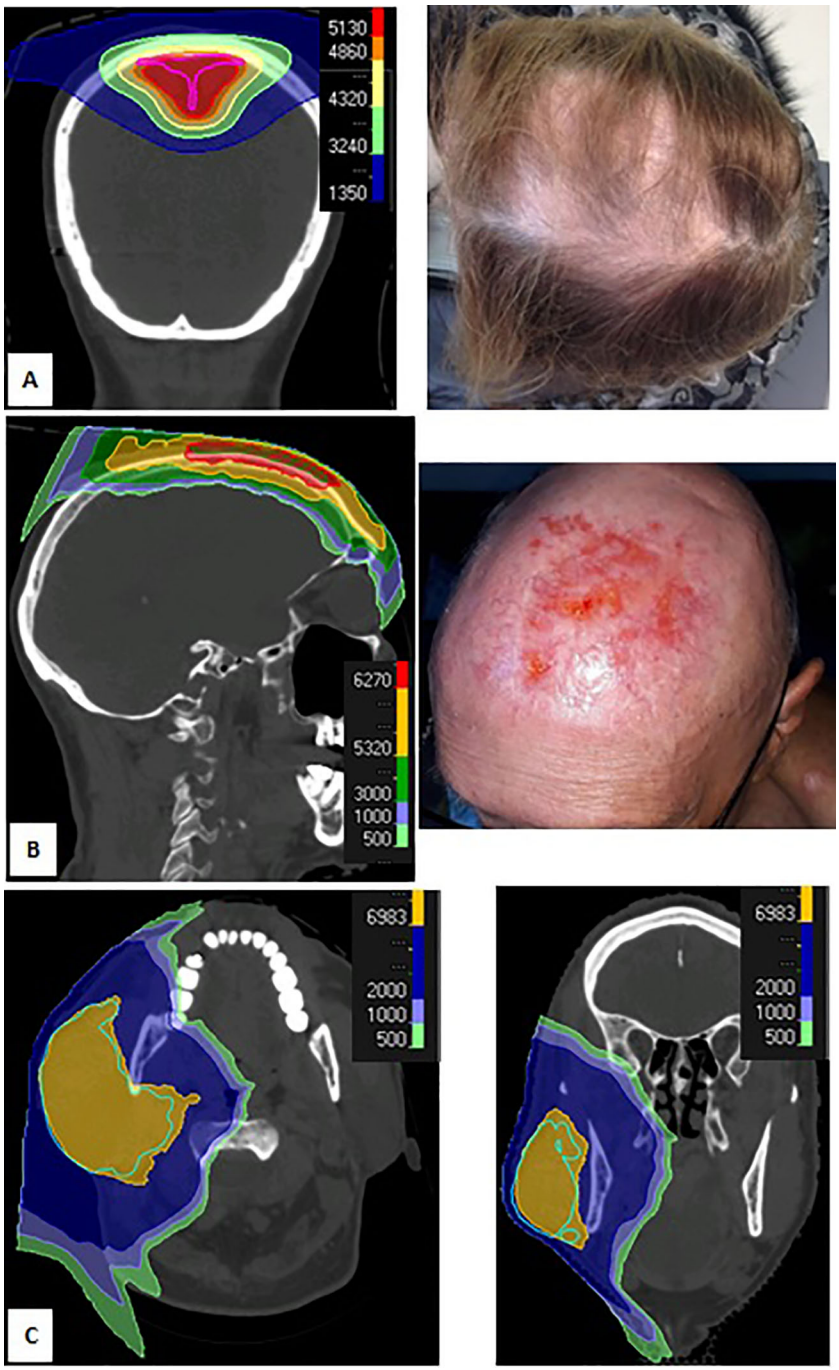

FIGURE 1 | Dose distribution (**A,** left) and grade 1 alopecia (**A,** right) during proton therapy (PT) of patient with meningioma; dose distribution (**B,** Left) and grade 3 dermatitis (**B**, right) 1 month after PT for Merckel carcinoma of the vertex; dose distribution for cystic adenoid carcinoma of the right parotid (**C,** right, axial view; **C,** left, coronal view).

with cranial irradiation) 2 months after PT. Most patients had a previous history of epilepsy (n=8) and we observed six new epilepsy diagnosis after PT. Weber et al. reported a similar rate of post-radiation seizure after radiotherapy (21.5%) for atypical and malignant meningioma (EORTC 22042–26042 phase II study) (19). Lynam et al. observed a cumulative "delayed" seizure (after treatment) rate of 33.8% (n=22 of 65 patients), especially in patients with low grade glioma or meningioma, as seen in our study (20).

We observed a very favourable toxicity profile for Patient 3 treated for non-operable cystic adenoid carcinoma of the parotid (**Figure 1C**). Romesser et al. previously reported that ipsilateral

TABLE 3 | Subacute toxicities.

	Grade 1	Grade 2	Grade 3	Grade 4	Total
Dry eye	16	4	0	0	20
Seizure	4	3	6	0	13
Headache	11	2	0	0	13
Alopecia	12	0	0	0	12
Asthenia	6	5	0	0	11
Sinusitis	4	5	0	0	9
Dry mouth	5	0	0	0	5
Skin pigmentation	5	0	0	0	5
Dizziness	4	0	0	0	4
Orbit edema	3	1	0	0	4
Hearing impaired	1	3	0	0	4
Local pain	2	1	0	0	3
Dermatitis	2	1	0	0	3
Cranial nerve disorder	1	2	0	0	3
Neuropathy	1	2	0	0	3
Dysgeusia	2	0	0	0	2
Trismus	2	0	0	0	2
Brain radionecrosis	1	1	0	0	2
External otitis	2	0	0	0	2
Pulmonary embolism	0	0	2	0	2
Local bleeding	1	0	1	0	2
Brain stroke	2	0	0	0	2
Optic nerve disorder	0	0	0	1	1
Cataract	0	1	0	0	1
Nausea	1	0	0	0	1
Fracture	0	0	1	0	1
Cystitis	1	0	0	0	1
Mastoiditis	0	0	1	0	1
Dysphagia	1	0	0	0	1
Dysphonia	1	0	0	0	1
Dyspnea	1	0	0	0	1
Colonic obstruction	0	0	1	0	1
Cough	1	0	0	0	1
Depression	1	0	0	0	1
Memory loss	1	0	0	0	1

head and neck PT is associated with a dramatic decrease in the rate of acute toxicities when compared with photon therapy, such as grade ≥ 2 dysgeusia (5.6% vs 65.2%, p<0.001) and grade ≥ 2 mucositis (16.7% vs 52.2%, p=0.01) (21). The favorable toxicity profile observed for Patient 3 is likely related to the Bragg Peak advantage. In contrast, Patient 2 was treated for skin cancer of the scalp vertex and presented with prolonged grade 3 toxicity. This is consistent with the unfavorable skin tolerance seen in previously described breast cancer cohorts treated with conventional dose rate PT, with a rapid dose deposit on the skin surface, which may be mitigated with proper dose constraints (22).

Despite the high dose delivered (median of 65.1 Gy [50.4–73.5]) and large irradiated volume (median of 437.4 ml [83.2–2106]), there were limited gastrointestinal sequela for the 16 pelvic and paraspinal tumors, with only 1 grade 3 subacute toxicity (digestive occlusion) reported 4 months after re-irradiation for an 89 year old pelvic sarcoma (65.1 Gy in 31 fractions). This patient required hospitalization but the occlusion quickly resolved with medical management alone. This is consistent with the study by Schneider et al, who described the conventional dose rate PT of 31 paraspinal/retroperitoneal patients, with a mean total dose of 72.3 Gy in 1.8–2 Gy fractions and planning target volume of 560.2 ml, observed no acute or late grade ≥ 2 toxicities (23). Similar to the favorable outcome in Patient 3, toxicity profile of the pelvic/paraspinal cohort is likely due to the Bragg Peak advantage rather than a FLASH-like effect.

Limitations of this study include: its retrospective nature, the relative small number of patients, and short follow-up. With the toxicities (e.g., dermatitis, alopecia, and seizures) observed in this study, we can conclude that the use of high dose rate proton therapy (around 10 Gy/s per spot) does not offer the expected FLASH-like radioprotective effect. It may cause lower grade toxicities but proper comparative studies with conventional dose rate PT are needed. The dose rate might be dependent on the type of irradiation and may be more difficult to obtain with protons than it is for photons or electrons. Larger dose per fraction may also be needed. The FLASH effect of protons was analyzed in the preclinical setting by Buonanno et al, who evaluated various dose rate (0.05, 10, 20, 100, and 1000 Gy/s) effect on normal lung fibroblasts. They found that the proton dose rate had little impact on acute effects, but favorably influenced the 1-month expression of TGF-β (inverse expression with dose rate) and 1-month cell senescence (lower senescence with higher dose rate) (12). Therefore, the FLASH effect of protons might be less pronounced than with other particles and may require an even higher dose rate to be clinically significant. Of note, most of this cohort consisted of head and neck tumors, where toxicity benefit of high dose rate proton therapy may not be as significant as other disease sites, such as abdominal or thoracic treatment sites, which will require further analysis in future studies.

In conclusion, the present study describes the early outcomes with use of high dose rate proton therapy (around 10 Gy/s). Contrary to what was expected in preclinical studies, there was no FLASH-like effect (no lack of toxicities). To identify a clinical difference, when compared to the classical dose rate (<0.05 Gy/s), may require larger cohorts, a match-paired retrospective study or randomized prospective study, longer follow up, or possibly a higher dose rate or dose per session.

DATA AVAILABILITY STATEMENT

The raw data supporting the conclusions of this article will be made available by the authors, without undue reservation.

ETHICS STATEMENT

This study requires a declaration to our French administration (CNIL) and the information of patients by using an information letter. It was performed and the declaration number is as following: 2204177 v 0.

AUTHOR CONTRIBUTIONS

JD and P-YB conceptualized and designed the study. JD and P-YB acquired, analyzed and interpreted the data. JD, M-PS, FA, VB, AN,

GB, LP, J-MH-L, FG, JG, MV, AC, KB, LC, and P-YB drafted/revised the work for intellectual content and context. JD gave the final approval and overall responsibility for the published work. All authors contributed to the article and approved the submitted version.

ACKNOWLEDGMENTS

The authors would like to thank the participating centers and members. This research did not receive any specific grant from funding agencies in the public, commercial, or not-for-profit sectors.

REFERENCES

1. Doyen J, Falk AT, Floquet V, Herault J, Hannoun-Levi JM. Proton beams in cancer treatments: Clinical outcomes and dosimetric comparisons with photon therapy. *Cancer Treat Rev* (2016) 43:104–12. doi: 10.1016/j.ctrv.2015.12.007
2. Baumann BC, Mitra N, Harton JG, Xiao Y, Wojcieszynski AP, Gabriel PE, et al. Comparative Effectiveness of Proton vs Photon Therapy as Part of Concurrent Chemoradiotherapy for Locally Advanced Cancer. *JAMA Oncol* (2019). doi: 10.1001/jamaoncol.2019.4889
3. Brown AP, Barney CL, Grosshans DR, McAleer MF, de Groot JF, Puduvalli VK, et al. Proton beam craniospinal irradiation reduces acute toxicity for adults with medulloblastoma. *Int J Radiat Oncol Biol Phys* (2013) 86:277–84. doi: 10.1016/j.ijrobp.2013.01.014
4. Kahalley LS, Peterson R, Ris MD, Janzen L, Okcu MF, Grosshans DR, et al. Superior Intellectual Outcomes After Proton Radiotherapy Compared With Photon Radiotherapy for Pediatric Medulloblastoma. *J Clin Oncol* (2020) 38:454–61. doi: 10.1200/JCO.19.01706
5. Lin SH, Hobbs BP, Verma V, Tidwell RS, Smith GL, Lei X, et al. Randomized Phase IIB Trial of Proton Beam Therapy Versus Intensity-Modulated Radiation Therapy for Locally Advanced Esophageal Cancer. *J Clin Oncol* (2020) 38:1569–79. doi: 10.1200/JCO.19.02503
6. Patel SH, Wang Z, Wong WW, Murad MH, Buckey CR, Mohammed K, et al. Charged particle therapy versus photon therapy for paranasal sinus and nasal cavity malignant diseases: a systematic review and meta-analysis. *Lancet Oncol* (2014) 15:1027–38. doi: 10.1016/S1470-2045(14)70268-2
7. Favaudon V, Caplier L, Monceau V, Pouzoulet F, Sayarath M, Fouillade C, et al. Ultrahigh dose-rate FLASH irradiation increases the differential response between normal and tumor tissue in mice. *Sci Transl Med* (2014) 6:245ra93. doi: 10.1126/scitranslmed.3008973
8. Montay-Gruel P, Petersson K, Jaccard M, Boivin G, Germond JF, Petit B, et al. Irradiation in a flash: Unique sparing of memory in mice after whole brain irradiation with dose rates above 100Gy/s. *Radiother Oncol* (2017) 124:365–69. doi: 10.1016/j.radonc.2017.05.003
9. Vozenin MC, De Fornel P, Petersson K, Favaudon V, Jaccard M, Germond JF, et al. The Advantage of FLASH Radiotherapy Confirmed in Mini-pig and Cat-cancer Patients. *Clin Cancer Res* (2019) 25:35–42. doi: 10.1158/1078-0432.CCR-17-3375
10. Montay-Gruel P, Bouchet A, Jaccard M, Patin D, Serduc R, Aim W, et al. X-rays can trigger the FLASH effect: Ultra-high dose-rate synchrotron light source prevents normal brain injury after whole brain irradiation in mice. *Radiother Oncol* (2018) 129:582–88. doi: 10.1016/j.radonc.2018.08.016
11. Beyreuther E, Brand M, Hans S, Hideghety K, Karsch L, Lessmann E, et al. Feasibility of proton FLASH effect tested by zebrafish embryo irradiation. *Radiother Oncol* (2019) 139:46–50. doi: 10.1016/j.radonc.2019.06.024
12. Buonanno M, Grilj V, Brenner DJ. Biological effects in normal cells exposed to FLASH dose rate protons. *Radiother Oncol* (2019) 139:51–5. doi: 10.1016/j.radonc.2019.02.009
13. Diffenderfer ES, Verginadis II, Kim MM, Shoniyozov K, Velalopoulou A, Goia D, et al. Design, Implementation, and in Vivo Validation of a Novel Proton FLASH Radiation Therapy System. *Int J Radiat Oncol Biol Phys* (2020) 106:440–48. doi: 10.1016/j.ijrobp.2019.10.049
14. Bourhis J, Sozzi WJ, Jorge PG, Gaide O, Bailat C, Duclos F, et al. Treatment of a first patient with FLASH-radiotherapy. *Radiother Oncol* (2019) 139:18–22. doi: 10.1016/j.radonc.2019.06.019
15. Rossomme S, Horn J, Brons S, Jakel O, Mairani A, Ciocca M, et al. Ion recombination correction factor in scanned light-ion beams for absolute dose measurement using plane-parallel ionisation chambers. *Phys Med Biol* (2017) 62:5365–82. doi: 10.1088/1361-6560/aa730f
16. Eisenhauer EA, Therasse P, Bogaerts J, Schwartz LH, Sargent D, Ford R, et al. New response evaluation criteria in solid tumours: revised RECIST guideline (version 1.1). *Eur J Cancer* (2009) 45:228–47. doi: 10.1016/j.ejca.2008.10.026
17. Feuvret L, Bracci S, Calugaru V, Bolle S, Mammar H, De Marzi L, et al. Efficacy and Safety of Adjuvant Proton Therapy Combined With Surgery for Chondrosarcoma of the Skull Base: A Retrospective, Population-Based Study. *Int J Radiat Oncol Biol Phys* (2016) 95:312–21. doi: 10.1016/j.ijrobp.2015.12.016
18. Marks LB, Yorke ED, Jackson A, Ten Haken RK, Constine LS, Eisbruch A, et al. Use of normal tissue complication probability models in the clinic. *Int J Radiat Oncol Biol Phys* (2010) 76:S10–9. doi: 10.1016/j.ijrobp.2009.07.1754
19. Weber DC, Ares C, Villa S, Peerdeman SM, Renard L, Baumert BG, et al. Adjuvant postoperative high-dose radiotherapy for atypical and malignant meningioma: A phase-II parallel non-randomized and observation study (EORTC 22042-26042). *Radiother Oncol* (2018) 128:260–65. doi: 10.1016/j.radonc.2018.06.018
20. Lynam LM, Lyons MK, Drazkowski JF, Sirven JI, Noe KH, Zimmerman RS, et al. Frequency of seizures in patients with newly diagnosed brain tumors: a retrospective review. *Clin Neurol Neurosurg* (2007) 109:634–8. doi: 10.1016/j.clineuro.2007.05.017
21. Romesser PB, Cahlon O, Scher E, Zhou Y, Berry SL, Rybkin A, et al. Proton beam radiation therapy results in significantly reduced toxicity compared with intensity-modulated radiation therapy for head and neck tumors that require ipsilateral radiation. *Radiother Oncol* (2016) 118:286–92. doi: 10.1016/j.radonc.2015.12.008
22. Liang X, Bradley JA, Zheng D, Rutenberg M, Yeung D, Mendenhall N, et al. Prognostic factors of radiation dermatitis following passive-scattering proton therapy for breast cancer. *Radiat Oncol* (2018) 13:72. doi: 10.1186/s13014-018-1004-3
23. Schneider RA, Vitolo V, Albertini F, Koch T, Ares C, Lomax A, et al. Small bowel toxicity after high dose spot scanning-based proton beam therapy for paraspinal/retroperitoneal neoplasms. *Strahlenther Onkol* (2013) 189:1020–5. doi: 10.1007/s00066-013-0432-0

Conflict of Interest: The authors declare that the research was conducted in the absence of any commercial or financial relationships that could be construed as a potential conflict of interest.

Copyright © 2021 Doyen, Sunyach, Almairac, Bourg, Naghavi, Duhil de Bénazé, Claren, Padovani, Benezery, Noël, Hannoun-Lévi, Guedea, Giralt, Vidal, Baudin, Opitz, Claude and Bondiau. This is an open-access article distributed under the terms of the Creative Commons Attribution License (CC BY). The use, distribution or reproduction in other forums is permitted, provided the original author(s) and the copyright owner(s) are credited and that the original publication in this journal is cited, in accordance with accepted academic practice. No use, distribution or reproduction is permitted which does not comply with these terms.

frontiers in Oncology

ORIGINAL RESEARCH
published: 20 January 2021
doi: 10.3389/fonc.2020.617506

Proton Beam Therapy for Children With Neuroblastoma: Experiences From the Prospective KiProReg Registry

Danny Jazmati[1], Sarina Butzer[2], Barbara Hero[2], Dalia Ahmad Khalil[1], Julien Merta[1], Christian Bäumer[1,3,4], Gina Plum[2], Jörg Fuchs[5], Friederike Koerber[6], Theresa Steinmeier[1], Sarah Peters[1], Jerome Doyen[1], Theresa Thole[7], Matthias Schmidt[8], Christoph Blase[9], Stephan Tippelt[10], Angelika Eggert[7], Rudolf Schwarz[11], Thorsten Simon[2] and Beate Timmermann[1,4]*

[1] Department of Particle Therapy, University Hospital Essen, West German Proton Therapy Centre Essen (WPE), West German Cancer Center (WTZ), Essen, Germany, [2] Children's Hospital, University of Cologne, Cologne, Germany, [3] Faculty of Physics, TU Dortmund University, Dortmund, Germany, [4] Department of Particle Therapy, University Hospital Essen, West German Proton Therapy Centre Essen (WPE), West German Cancer Center (WTZ), German Cancer Consortium (DKTK), Essen, Germany, [5] Department of Pediatric Surgery and Pediatric Urology, University Children's Hospital Tuebingen, Tübingen, Germany, [6] Department of Radiology, University of Cologne, Cologne, Germany, [7] Department of Pediatric Oncology/Hematology, Charité-Universitätsmedizin Berlin, Berlin, Germany, [8] Department of Nuclear Medicine, University Hospital of Cologne, Cologne, Germany, [9] Anästhesienetz Rhein Ruhr, Bochum, Germany, [10] University Hospital of Essen, Paediatrics III, Paediatric Haematology and Oncology, Essen, Germany, [11] Department of Radiotherapy and Radiooncology, Outpatient Center, University Medical Center Hamburg-Eppendorf, Hamburg, Germany

OPEN ACCESS

Edited by:
Minesh P. Mehta, Baptist Health South Florida, United States

Reviewed by:
Ulrich W. Langner, Lifespan, United States
Fiori Alite, Geisinger Commonwealth School of Medicine, United States

***Correspondence:**
Danny Jazmati
danny.jazmati@uk-essen.de

Specialty section:
This article was submitted to Radiation Oncology, a section of the journal Frontiers in Oncology

Received: *14 October 2020*
Accepted: *30 November 2020*
Published: *20 January 2021*

Citation:
Jazmati D, Butzer S, Hero B, Ahmad Khalil D, Merta J, Bäumer C, Plum G, Fuchs J, Koerber F, Steinmeier T, Peters S, Doyen J, Thole T, Schmidt M, Blase C, Tippelt S, Eggert A, Schwarz R, Simon T and Timmermann B (2021) Proton Beam Therapy for Children With Neuroblastoma: Experiences From the Prospective KiProReg Registry. Front. Oncol. 10:617506. doi: 10.3389/fonc.2020.617506

Objective: Radiotherapy (RT) is an integral part of the interdisciplinary treatment of patients with high-risk neuroblastoma (NB). With the continuous improvements of outcome, the interest in local treatment strategies that reduce treatment-related side effects while achieving optimal oncological results is growing. Proton beam therapy (PBT) represents a promising alternative to conventional photon irradiation with regard to the reduction of treatment burden.

Method: Retrospective analysis of children with high or intermediate risk NB receiving PBT of the primary tumor site during first-line therapy between 2015 and 2020 was performed. Data from the prospective in-house registry Standard Protonentherapie WPE – Kinder- (KiProReg) with respect to tumor control and treatment toxicity were analyzed. Adverse events were classified according to CTCAE Version 4 (V4.0) before, during, and after PBT.

Results: In total, 44 patients (24 male, 20 female) with high (n = 39) or intermediate risk NB (n = 5) were included in the analysis. Median age was 3.4 years (range, 1.4–9.9 years). PBT doses ranged from 21.0 to 39.6 Gray (Gy) (median 36.0 Gy). Five patients received PBT to the MIBG-avid residual at the primary tumor site at time of PBT according to the NB-2004 protocol. In 39 patients radiation was given to the pre-operative tumor bed with or without an additional boost in case of residual tumor. After a median follow-up (FU) of 27.6 months, eight patients developed progression, either local recurrence (n = 1) or

distant metastases (n = 7). Four patients died due to tumor progression. At three years, the estimated local control, distant metastatic free survival, progression free survival, and overall survival was 97.7, 84.1, 81.8, and 90.9%, respectively. During radiation, seven patients experienced higher-grade (CTCAE ≥ °3) hematologic toxicity. No other higher grade acute toxicity occurred. After PBT, one patient developed transient myelitis while receiving immunotherapy. No higher grade long-term toxicity was observed up to date.

Conclusion: PBT was a well tolerated and effective local treatment in children with high and intermediate risk NB. The role of RT in an intensive multidisciplinary treatment regimen remains to be studied in the future in order to better define timing, doses, target volumes, and general need for RT in a particularly sensitive cohort of patients.

Keywords: neuroblastoma, proton beam therapy (PBT), radiotherapy—adverse effects, pediatric radiation oncology, childhood cancer, retroperitoneal tumor, survival

INTRODUCTION

Neuroblastoma (NB) is the most common extracranial solid tumor of childhood. It has been identified as a neuroectodermal embryonal malignant tumor affecting the sympathetic nervous tissue. Approximately 50% of all patients are diagnosed already with distant metastases (1). The age of >18 months at diagnosis, the detection of amplification of the oncogene MYCN and the presence of distant metastases are well known risk factors for worse disease control and survival (2). The amplification of the MYCN-gene at least five-fold is found in 20–25% of all NBs (3–5). The different risk groups of NB show a heterogeneous course from spontaneous regression to high mortality. While no indication for radiotherapy (RT) is seen in low risk NBs, RT is an integral part of the interdisciplinary treatment of patients with high-risk disease (6). In addition to RT, the treatment regimen in high-risk NBs includes induction chemotherapy, high-dose chemotherapy including tandem transplant, surgery, and immunotherapy. Despite intensive multimodal therapy, the 5-year survival rate of patients with high-risk NB is below 50% (7). Nevertheless, the treatment of metastatic NB has developed considerably with the use of high-dose chemotherapy and immunotherapy (8–10). With the continuous improvements of prognosis, the interest in local therapeutic strategies that potentially can reduce treatment-related side effects while maintaining high tumor control is increasing. Considering the very young age of the affected children, the position of the tumor close to the radiation sensitive organs, such as kidneys and spinal medulla, and the intensive multi-agent chemotherapy applied prior to radiation, proton beam therapy (PBT) represents a promising alternative to conventional photon irradiation. Planning studies in NB have shown that PBT can considerably reduce the radiation exposure of adjacent healthy tissue, potentially reducing the radiation-induced toxicities (11, 12). Furthermore, there are already clinical data demonstrating the effectiveness and feasibility of PBT for NB patients (13, 14). The current study reports on our experiences when treating patients with NB with special consideration of PBT in an intensive multimodal therapy concept.

METHODS

Patients

Children with high or intermediate risk NB receiving PBT at a single institution during front-line treatment within the prospective in-house registry (Standard Protonentherapie WPE – Kinder- KiProReg; DRKS00005363) were included in this analysis. The high-risk group included all patients with an age of >18 months or >12 months (depending on the study protocol) at diagnosis presenting either with MYCN amplification or with distant metastases. All patients were discussed within the multidisciplinary German NB study board before starting RT. The decision for PBT was considered individually by the national German NB board, which in addition to representatives of pediatric oncology also includes radiation oncology representing both PBT and conventional RT. PBT was typically preferred in younger patients, larger tumors, sites near critical structures, and central sites. Patients treated for a relapse were excluded from this analysis. For all children, data on patients, tumor, treatment, outcome, and toxicity was collected. The registry was approved by the Institutional Ethical Board of the University Duisburg-Essen.

Treatment

Overall strategies were applied within or according to the respective national or international protocols and treatment standards, respectively. In general, first line treatment for high risk disease consisted of induction chemotherapy, high-dose myeloablative chemotherapy followed by autologous stem-cell rescue and post-consolidation treatment of either immunotherapy with the antibody ch14.18 or retinoic acid. In all patients receiving high-dose chemotherapy with busulfan/melphalan (BuMel), a period of 60–90 days was respected before irradiation started. Consolidating immunotherapy started 4 weeks after the end of RT.

Prior to the start of RT, a re-staging consisting of functional imaging using 123I-mIBG or fluorine-18 (18F) fluorodeoxyglucose (FDG), and cross-sectional imaging was performed. In the case of tumor site in the vicinity of the kidney, a renal scintigraphy was performed prior to radiation planning. In addition, before PBT

planning, a central radiological review was performed regarding the preoperative extension and any residual disease in all patients. Furthermore, the surgery reports were evaluated and discussed with the surgeon in case of any uncertainties. A treatment planning computed tomography (CT) was obtained using 1–2 mm slice thickness for all cases. The planning CT was merged with a planning magnetic resonance imaging (MRI) and the initial, preoperative, and most recent previous diagnostic MRIs and MIBGs whenever available. Immobilization of patients for CT-simulation and treatment was ensured using customized immobilization devices depending on the tumor site and geometry. Patients were individually positioned either in prone or supine position. For patients treated according to the "NB 2004 Trial Protocol for Risk Adapted Treatment of Children with Neuroblastoma" (NB 2004/NB2004-HR) (NCT 00410631; NCT 00526318) (15), the extended (by up to 2 cm = CTV) active residual primary tumor was delineated and a total dose of 36–40 Gray (Gy) was delivered to the respective PTV. For patients treated according to High Risk Neuroblastoma Study 1.8 of SIOP-Europe (HRNBL1) (NCT 01704716) protocol or European Low and Intermediate Risk Neuroblastoma Protocol (LINES) (NCT01728155), the gross tumor volume (GTV) included the preoperative extent of the disease adapted to the current anatomy and extended by up to 1 cm in order to account for microscopic spread (CTV). The respective PTV was irradiated up to 21 Gy. Since October 2018, radiation of the primary preoperative tumor region with 21.6 Gy and a tumor boost for the residual tumors with cumulative 36 Gy became the standard in Germany [Association of the Scientific Medical Societies in Germany (AWMF) registration number: 025/008] and was applied in patients not treated in a clinical trial (16). Additionally, in patients with up to three MIBG positive (at the time of RT) osteomedullary metastases, combined irradiation of these lesions was considered. However, the decision to radiate metastases was made very individually by the national interdisciplinary study board. For all dose concepts, a generic relative biological effectiveness (RBE) factor of 1.1 (relative to that of Co-60) was assumed. Proton doses were expressed in terms of Gy (RBE) [Gy (RBE) = proton Gy X 1.1]. After high-dose chemotherapy with Busulfan/Melphalen, the RT planning goals aimed to reduce the maximum dose to gastrointestinal tract, spinal cord, and lung below 30 Gy (RBE). PBT was applied with either uniform (US) or pencil beam scanning (PBS). Treatment planning was carried out with XiO Version 4.80 (Elekta, Stockholm, Sweden) and RayStation© Versions 4.7 to 7.0 (RaySearch Laboratories, Stockholm, Sweden). Typically, two to three beams were used for treatment planning. A multi-field optimization employing intensity modulation was conducted in PBS delivery mode. Typically, the maximum dose of a field was allowed to exceed its nominal dose, i.e. a field configuration with equal weights, by 30%. In order to address potential uncertainties, a density overwrite of the intestine with the average intestine density and a re-computation of the dose distribution was performed. If an interfractional change of the intestine filling had relevant impact on dose robustness, a robust optimization of the treatment plan was conducted simultaneously on the planning CT with or without overwriting intestine density. In addition, the accuracy of dose computation in heterogeneous anatomical regions was taken into account by the Monte-Carlo dose engine as an integral part of the treatment planning system RayStation (17, 18).

Patient set-up, positioning, and treatment were conducted with a ProteusPlus therapy machine (IBA, Lovain-La-Neuve, Belgium). Position verification was facilitated with laser systems, orthogonal X-ray imaging, and a surface tracking camera system (AlignRT, Vision RT Ltd., London, UK). Corrections of the patient set-up were applied to the patient position system, which supports six degrees of freedom. US fields were applied with the IBA universal nozzle which is attached to a 360° gantry. The nozzle was equipped with a Snout180 supporting up two field-specific brass apertures upstream of a range compensator custom milled from an acrylic glass cylinder. PBS fields were applied with a PBS dedicated nozzle which is attached again to a 360° gantry. The PBS delivery proceeded in a step-and-shoot spot scanning mode. The energy and thus, range of the pencil beams was adjusted with an energy-selection system downstream of an isochronous cyclotron.

Whenever tumors in the abdomen and in the thorax displayed relevant respiratory motion, special management to compensate for interplay effect was provided. The motion during the sessions of these cases was monitored with AlignRT. The set-up margin was expanded particularly in cranio-caudal direction. The size of the additional margin was checked against the AlignRT readings. If the respiratory motion was a major concern, also layered repainting was considered resulting in the repeated application of spot segments with the same proton kinetic energy and downscaled fluence (factor of five). Verification MRIs were done on regular basis during treatment, and if any anatomical changes were detected, a new planning CT was obtained with adaptation of contours and plan.

During PBT, regular consultations by radiation oncologists and pediatric oncologists were provided. If patients were too young to consciously cooperate, pediatric anesthesiologists performed deep sedation with i.v. propofol.

Adverse Events and Follow-Up

Adverse events were classified according to Common Toxicities Criteria on Adverse Events (CTCAE) version 4.0. Adverse events were recorded before, during RT, after 90 days and then at least once a year according to the prospective in-house registry. All patients were assessed weekly during PBT. During FU, patients underwent clinical examination, evaluation of tumor markers, bone marrow examination, cross-sectional and functional diagnostic imaging.

Statistical Analysis

Qualitative data was reported as frequency (minimum-maximum and percentage). The cut-off was based on the known cut-off or median. Local recurrence (LR) was used to indicate failure in the irradiated region. Consequently, local control (LC) was determined as the absence of local recurrence. Local metastatic relapse (LMR) was used to describe failure at irradiated metastatic lesions. Accordingly, local metastatic control characterized the absence of failure at irradiated lesions. Progression was defined as any event of tumor

growth or relapse. Therefore, progression free survival (PFS) represents the time from diagnosis until any failure, relapse, or death. Distant metastatic failure (DMF) was defined as a metastatic recurrence occurring at a metastatic non-irradiated site. Distant metastatic free survival (DMFS) was defined as the absence of metastatic recurrence. Overall survival (OS) was defined as the time from diagnosis to death. LC, PFS, DMFS, and OS were calculated and graphically illustrated using the Kaplan-Meier method. Patients were censored at the time of the last follow-up if not having any event. All statistical analyses were carried out with the Statistical Package for the Social Sciences (SPSS) Version 16.0 under Windows®.

Patients and Tumor Characteristics

A total of 44 patients (24 male; 20 female) were evaluable for this analysis. The median age at PBT was 3.4 years (range, 1.4–9.9 years). The cohort included 39 children (89.0%) with high-risk disease and five children (11%) with local intermediate-risk disease. Further information on patients and tumor characteristics is displayed in **Table 1**.

Treatment

Induction chemotherapy was performed either according to the German Society for Paediatric Oncology and Hematology (GPOH) regimen consisting of three N5 (cisplatin, etoposide, and vindesine) and three N6 cycles (vincristine, dacarbacine, ifosfamide, and doxorubicine) (n = 34) (6), according to the SIOPEN protocol with the administration of "rapid COJEC" containing cisplatin, vincristine, carboplatin, etoposide, and cyclophosphamide with subsequent administration of Granulocyte Colony Stimulating Factor (n = 8) or according to the European Low and Intermediate Risk Neuroblastoma Protocol (LINES) which comprises a combination chemotherapy consisting of carboplatin and etoposide as well as cyclophosphamide doxorubicin and vincristine (n = 2).

After induction chemotherapy, high-dose chemotherapy with autologous stem cell rescue was provided to 39 patients (88.6%). For high-dose chemotherapy either busulfan and melphalan (BuMel) (n = 32), melphalan, etoposide, and carboplatin (n = 6) or treosulfan–melphalan (n = 1) was administered.

All but one child (98%) underwent tumor resection before RT. Complete macroscopic excision (CME) was achieved in thirteen patients (29.5%). PBT was performed either according to the NB2004 protocol (n = 4), SIOPEN HRNBL1 protocol (n = 5) SIOPEN LINES protocol (n = 2) or according to the German AWMF guideline (n = 33). Of 31 patients with residual tumor at the time of RT, 25 (80.6%) received a dose of more than 30 Gy (RBE). After RT, 5 children received retinoic acid and 36 children received immunotherapy for consolidation purposes.

Outcome

After a median FU of 27.6 months from diagnosis, the estimated local control, distant metastatic free survival, progression free survival, and overall survival at 3 years was 97.7, 84.1, 81.8, and 90.9% respectively (**Figure 1**). Out of eight patients with disease progression, one experienced local failure only and seven patients experienced progression with distant metastasis without local failure. Four patients died due to tumor progression. No progression was observed at the irradiated metastatic sites (n = 4).

TABLE 1 | Patient and treatment characteristics.

Characteristics		%
Sex	n	
male	24	55%
female	20	45%
Age at diagnosis	years	
Median	2,6	
Min	0.1	
Max	8.7	
Age at start of proton therapy	years	
Median	3.4	
Min	1.4	
Max	9.9	
Risk grouping	n	
high	39	89%
intermediate	5	11%
nMYC Status	n	
amplified	29	66%
non-amplified	15	34%
Induction chemotherapy	n	
yes	44	100%
no	0	0%
Resection status	n	
CME	13	30%
IME	30	68%
none	1	2%
High-dose chemotherapy	n	
none	5	11%
BuMel	32	73%
MEC	6	14%
TreoMel	1	2%
Radiotherapy treatment concept	n	
36–39.6 Gy to residue	4	9%
21.6 Gy to preop.TU; boost to residue to cum. 36 Gy	33	75%
21 Gy to preop. TU	7	16%
Median total PBT dose	Gy	
	36.0	
Median number of fractions	n	
	20	
Consolidation therapy	n	
immunotherapy	36	82%
retino acid	5	11%
none	3	18%

n, number; GPOH regime, German Society for Paediatric Oncology and Hematology (GPOH) regimen [three N5 (cisplatin, etoposide, and vindesine) and three N6 cycles (vincristine, dacarbacine, ifosfamide, and doxorubicine)], Rapid Cojek (cisplatin, vincristine, carboplatin, etoposide, and cyclophosphamide with subsequent administration of Granulocyte Colony Stimulating Factor); CME, Complete macroscopic excision; IME, Incomplete macroscopic excision; BuMel, Busulphan and Melphalan; MEC, Melphalan, Etoposide, and Carboplatin; TreoMel, treosulfan–melphalan.

Treatment Toxicity

Twenty-three patients presented already at baseline (before starting PBT) with one or more conditions such as veno occlusive disease/sinusoidal obstruction syndrome of the liver (n = 8, 18%), sensorineural hearing loss (n = 5, 11.3%), chronic diarrhea (n = 2, 4.5%), neurological impairment (n = 2, 4.5%), necrosis of the femoral head (n = 1, 2.2%), lung function restriction (n = 1, 2.2%), and grade 3 hematotoxicity (n = 3, 6%). The two patients with chronic diarrhea were later diagnosed with an exocrine pancreatic insufficiency.

No higher grade (CTCAE > °2) acute adverse event was observed during the course of PBT except for hematologic toxicity. Higher-grade hematologic toxicity (> CTCAE ° 2) was

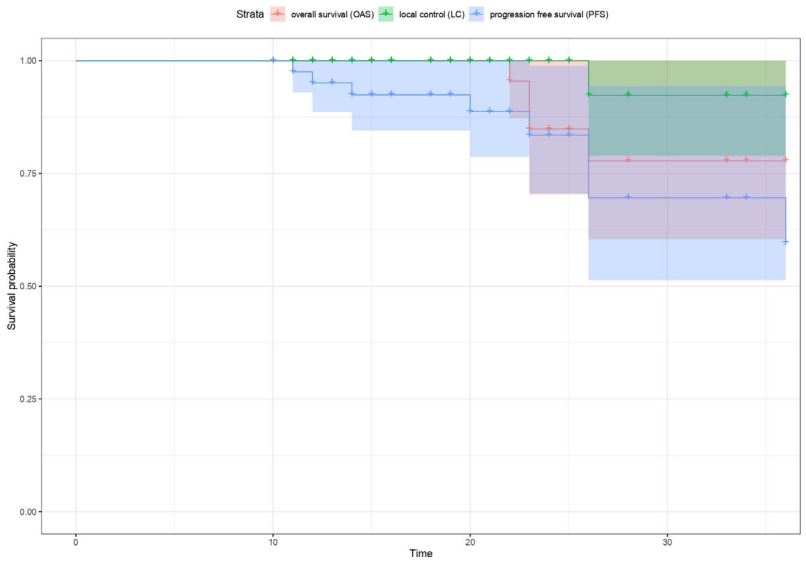

FIGURE 1 | Kaplan-Meier estimates of local control (LC), overall survival (OS) and progression free survival (PFS) respectively for all patients.

reported in seven patients including leukocytopenia (n = 3), thrombocytopenia (n = 3), anaemia (n = 1), and neutropenia (n = 4). One child presented with temporary myelitis (CTCAE ° 3) associated with impaired leg movement and bladder dysfunction following the first block of immunotherapy after PBT, and was considered as early-delayed complication. The diagnostic imaging displayed a hyperintense MRI change of the spinal cord at the level of the radiation field having received near-maximum dose of 24Gy (RBE). Dosimetric analyses showed no overlap between potential regions with high linear energy transfer (LET) and the area of the myelitis. In one out of five fields applied in two irradiation series, the distal edge stops in the proximity of the myelon. The robustness analysis in terms of stopping-power and set-up uncertainties revealed that even in an unfavorable scenario, the dose received by the myelon would be increased by about 4 Gy (RBE) and would, thus, still be far below the acceptable dose limits. After treatment with corticosteroids and immunoglobin, the clinical symptoms improved.

With regard to long-term toxicity, no symptomatic adverse event was observed attributable to PBT so far. In one patient, an asymptomatic image finding of the irradiated parts of the kidney cortex with normal renal function parameters was observed.

DISCUSSION

This study is one of the largest series with standardized data on RT for NB. Our original data displays excellent safety, feasibility and high tumor control gathered from a prospective monoinstitutional registry. Our study complements the existing literature on children undergoing RT for NB confirming high LC and acceptable OS. Local control and survival rates were similar to other studies, which demonstrated a 3- to 5-year LC and OS of 64.7–97% and 35–94% (13, 19–27). In the literature, the most common late effects associated with RT were musculoskeletal abnormalities, gastrointestinal dysfunctions, metabolic disorders, vascular changes, and secondary malignancies (22, 28–31). However, in previous experiences the incidence of RT associated complications was very low, which is consistent with our early results. While the complications of RT in children with NB were only rudimentarily investigated during the early experiences, this study stands out in particular for the close interdisciplinary monitoring and assessment of acute and late effects.

Previously, three comparable studies on PBT for NB have been published. All studies comprised cohorts with similar median age and similar treatment strategies prior to irradiation [9–10, 15]. In all three studies, patients received PBT to the preoperative tumor bed with 21.6–24 Gy (RBE). In two of them, a boost to the residual tumor was administered for a subset of patients. The estimated 3-year local control rate of 97.7% in our study is consistent with the previous PBT experience. Hill et al. reported a local control rate of 97% at 5 years after a median follow-up time of 48.7 months (14). Bagley et al. published on a 5-year local control rate of 87% after a median follow-up of 60.2 months (13). Lim et al. did not experience any local recurrence in their study but having a limited follow-up time of only 14.9 months. As the characteristics of our cohort, and our results are in line with the previous investigations, it confirms that high local control rates can be achieved with PBT in a very sensitive cohort of very young NB patients (32).

PBT was used less frequently in NB compared to other malignancies. First, total doses are relatively low, and second concerns were raised regarding the robustness of PBT plans in the presence of small bowel or diaphragm and lung in or close to the target volume. Protons lose their energy as they pass through

matter and are thereby continuously slowing down. The absorbed dose scales with the inverse of the squared velocity giving rise to an enhancement in ionization near the end of the range, called the Bragg peak. The advantageous depth dose distribution allows for conformal dose coverage of the (static) target and a low radiation burden to healthy tissue. On the other hand, the accurate deposition of dose in the depth domain necessitates concepts to deal with possible variations in geometry or density. These have been considered in the treatment planning of the current study by various measures, individually depending on the tumor site, the amount of respiratory motion or the variability of density of the gastrointestinal tract. All these parameters can affect robustness and, thus, carry a risk of over- or underdosing the target volume and possibly compromising tumor control rates. The overall good local control rates of PBT reported here and elsewhere, confirm feasibility and robustness of PBT treatment plans for the treatment of NB. Plan comparison studies have shown that PBT is particularly advantageous for lateralized target volumes to protect the contralateral side (11, 33).

While RT is considered as a key element in the treatment of high-risk NB, the value of radiation for metastases in NB is seen controversially. While limited cohort studies with a comparison group could not find a positive effect (34, 35), institutional studies revealed promising results (25, 36). In our analysis, local tumor control was achieved for all metastases when irradiated. However, RT to metastatic lesions was only offered to children with limited dissemination at the time of RT defined as up to three MIBG-avid lesions.

Although RT is an integral part of the multimodality treatment of high-risk neuroblastoma, the role of RT with regard to the dose concept is still unclear (37). High local control rates were achieved after irradiation of the preoperative tumor bed with 21 Gy (22, 38–40). It was even discussed by Casey et al. whether lower doses could be sufficient as they obtained comparable results for 18 Gy (41). However, the extent of surgery and the response to high-dose chemotherapy were not taken into account at the radiation planning, so far. There is an on-going controversy about the impact of a macroscopically complete resection compared to an incomplete tumor resection in children with high-risk disease. Analyses of the German NB study NB97 did not show any significant difference for LC, PFS, and OS between the two groups (42). In contrast, the results of the HR-NBL1/SIOPEN study in patients with metastatic NB responding to induction therapy were recently published and showed a small but due to the high number of patients significant improvement for survival and local control rates after macroscopic complete resection (43). In our study, CME was only achieved in 13 patients. Still, only one child experienced local progression. However, out of 31 children with residual tumor at time of RT, 25 children received a dose higher than 30 Gy (RBE) for the residual tumor. In Europe, there is a debate, if, after subtotal resection a dose increase with 36 Gy may be advantageous. A retrospective study from the Memorial Sloan Kettering Cancer Centre showed that patients with residual tumor who had received a dose of more than 30 Gy remained free of local failure (100%), while 30% of those who were irradiated with a dose below 30 Gy experienced local failure (44). Simon et al. had comparable results for patients with residual tumor who received a dose of 36–40 Gy. The local control rate at 3 years in NB 97 for patients with residual tumor who underwent RT was 100% (45). In contrast, the preliminary results of the prospective American ANBL0532 study published recently displayed no benefit of a boost. In this study, 133 patients received preoperative tumor bed irradiation at 21.6 Gy and a boost to the residual tumor up to 36 Gy. No superior results for LC, EFS, or OS at 5 years were achieved when compared to the COG A3973 (NCT 00004188) study. After amendment, patients received only 21.6 Gy radiation of the tumor bed without any boost to the residue (46). The recently opened European collaborative study HR-NBL2 currently investigates the role of a boost after incomplete resection in a randomized fashion. These data are particularly relevant as there is evidence that a dose increase above 30Gy may also increase the likelihood of complications (31).

In contrast to these data but in line with other proton studies, we did not observe relevant, higher grade toxicity, although most of the patients received total doses above 30Gy.

The use of myeloablative chemotherapy (8, 9) and particularly those containing BuMel (47) has been shown to improve the outcome of high-risk NB patients. However, an increased radiosensitivity was assumed after the administration of Busulfan containing myeloablative chemotherapy regimens. Unfortunately, the data on the combination of BuMel and irradiation is very limited and mainly restricted to Ewing sarcomas. Therefore, dose limits applicable to NBs are difficult to define. Seddon et al. reported on a 17-year-old boy presenting with myelopathy after radiation therapy (maximum Dose to myelon: 50.2 Gy) and BuMel (48). Carrie et al. described morbidity-relevant gastrointestinal (GI) side effects (obstruction) after BuMel and pelvic irradiation (49). Bölling et al. evaluated complications attributable to RT after BuMel in the EuroEwing 99 trial with regard to the GI tract, lung, and spinal cord. After a mean follow-up of 7 months, 18 patients being examined did not show any spinal cord complication. After a short mean FU of 1 month, one out of five patients presented with lung dysfunction grade III after irradiation. However, this patient already had pulmonary dysfunction before RT. No higher grade adverse event regarding GI was reported (50). In another report of the EuroEwing 99 study, Whelan et al. presented a case with myelopathy after BuMel and irradiation (51). In our cohort, we had homogenously respected an interval of 60 to 90 days between BuMel and irradiation. In addition the maximum dose to GI tract, lung, and spinal cord was limited to 30 Gy (RBE). With this strategy, we have not observed any complication attributable to the combination of BuMel and RT. Another concern may be raised, regarding the tolerability of RT. Dinutuximab, a monoclonal antibody targeting the glycolipid antigen disialoganglioside expressed on NB cells, has been shown to promote a survival benefit in patients with high-risk NB (52). It is currently unclear whether the combination of RT and immunotherapy may induce additional acute or long term toxicity due to overlapping toxicity profiles (53). Ding et al. reported three patients with myelitis shortly after initiation of dinutuximab therapy

and hypothesized a combined effect between irradiation and immunotherapy. The authors postulated that the influence of RT to the blood-brain barrier could have increased the permeability of dinutuximab. Also in our series, one patient presented with a transient myelitis after the first block of dinutuximab following RT also visible within the MRI of the spinal canal related to the radiation field. Fortunately, the symptoms improved after administration of steroids, comparable to the cases presented by Ding et al. [36]. In general, we have to consider RT in NB as particularly challenging in the context of a very demanding and intense multimodal therapy concept.

The proximity of the target volume to the kidney makes nephrotoxicity a significant concern in many patients, particularly when higher RT doses have to be administered. Since residual tumor tissue often remains in the preaortic region close to the large vessel and the kidneys, there is a risk of relevant dose exposure to the kidneys in many patients. In order to protect the better kidney, a split renal function scintigraphy should be performed prior to radiation planning. With this approach we did not observe any clinical relevant radiation induced nephrotoxicity, up to date. Nevertheless, in one patient MRI identified a partial post-RT fibrosis of the kidney cortex as result of partial radiation exposure of the kidney without any subsequent clinical and biochemical evidence of global renal impairment. Interestingly, this patient was operated prior to induction chemotherapy. Therefore, the target volume was based on the initial tumor extension but not on the surgical bed after response to induction chemotherapy generating a very large radiation field.

In the present study, we have to recognize some limitations. The follow-up time is still short and any findings on long-term toxicity cannot be considered representative. Furthermore, patients included in our analysis were irradiated within different study protocols. Finally, we critically acknowledge the retrospective nature of our analysis and the restricted cohort size.

In summary, PBT is a highly conformal RT modality potentially improving the treatment burden. According to our data, PBT for children with NB is feasible with very little acute and early late toxicity. Tumor control rates were high, both for primary disease and metastases. However, results have to be confirmed in larger cohorts and with longer follow-up periods. Any RT in NB patients has to be part of an intensive multidisciplinary treatment regimen and will need intensive investigation with regard to oncological benefit and risk for adverse events.

DATA AVAILABILITY STATEMENT

The raw data supporting the conclusions of this article are provided by the authors without reservation, in compliance with data protection guidelines.

ETHICS STATEMENT

The studies involving human participants were reviewed and approved by the ethics committee of the University Duisburg Essen. Written informed consent to participate in this study was provided by the participants' legal guardian/next of kin. Written informed consent was obtained from the minor(s)' legal guardian/next of kin for the publication of any potentially identifiable images or data included in this article.

AUTHOR CONTRIBUTIONS

DJ, SB, BH, DA-K, JM, CBä, GP, JF, FK, TSt, SP, JD, TT, MS, CBl, ST, AE, RS, TSi, and BT contributed to the design and implementation of the research. DJ, SB, BH, DA-K, JM, CBä, GP, JF, FK, TSt, SP, JD, TT, AE, RS, TSi, and BT contributed to the analysis of the results and to the writing of the manuscript. All authors provided critical feedback and helped shape the research, analysis, and manuscript. All authors contributed to the article and approved the submitted version.

REFERENCES

1. Matthay KK, Maris JM, Schleiermacher G, Nakagawara A, Mackall CL, Diller L, et al. Neuroblastoma. *Nat Rev Dis Primer* (2016) 2:16078. doi: 10.1038/nrdp.2016.78
2. Sokol E, Desai AV. The Evolution of Risk Classification for Neuroblastoma. *Children* (2019) 6(2):27. doi: 10.3390/children6020027
3. Huang M, Weiss WA. Neuroblastoma and MYCN. *Cold Spring Harb Perspect Med* (2013) 3(10):a014415. doi: 10.1101/cshperspect.a014415
4. Irshad S, Pedley RB, Anderson J, Latchman DS, Budhram-Mahadeo V. The Brn-3b Transcription Factor Regulates the Growth, Behavior, and Invasiveness of Human Neuroblastoma Cells in Vitro and in Vivo. *J Biol Chem* (2004) 279:21617–27. doi: 10.1074/jbc.M312506200
5. von Schweinitz D. Neuroblastom und andere Nebennierentumoren bei Kindern und Jugendlichen. In: D von Schweinitz, B Ure, editors. *Kinderchirurgie: Viszerale und allgemeine Chirurgie des Kindesalters Springer Reference Medizin*. Berlin, Heidelberg: Springer (2019). p. 1–22. doi: 10.1007/978-3-662-53390-1_84-1
6. Simon T, Hero B, Schulte JH, Deubzer H, Hundsdoerfer P, von Schweinitz D, et al. GPOH Guidelines for Diagnosis and Treatment of Patients with Neuroblastic Tumors. *Klin Padiatr* (2017) 2017) 229:147–67. doi: 10.1055/s-0043-103086
7. Cohn SL, Pearson ADJ, London WB, Monclair T, Ambros PF, Brodeur GM, et al. The International Neuroblastoma Risk Group (INRG) classification system: an INRG Task Force report. *J Clin Oncol Off J Am Soc Clin Oncol* (2009) 27:289–97. doi: 10.1200/JCO.2008.16.6785
8. Berthold F, Boos J, Burdach S, Erttmann R, Henze G, Hermann J, et al. Myeloablative megatherapy with autologous stem-cell rescue versus oral maintenance chemotherapy as consolidation treatment in patients with high-risk neuroblastoma: a randomised controlled trial. *Lancet Oncol* (2005) 6:649–58. doi: 10.1016/S1470-2045(05)70291-6
9. Matthay KK, Reynolds CP, Seeger RC, Shimada H, Adkins ES, Haas-Kogan D, et al. Long-term results for children with high-risk neuroblastoma treated on a randomized trial of myeloablative therapy followed by 13-cis-retinoic acid: a children's oncology group study. *J Clin Oncol Off J Am Soc Clin Oncol* (2009) 27:1007–13. doi: 10.1200/JCO.2007.13.8925
10. Yu AL, Gilman AL, Ozkaynak MF, London WB, Kreissman SG, Chen HX, et al. Anti-GD2 Antibody with GM-CSF, Interleukin-2, and Isotretinoin for Neuroblastoma. *N Engl J Med* (2010) 363:1324–34. doi: 10.1056/NEJMoa0911123

11. Hillbrand M, Georg D, Gadner H, Pötter R, Dieckmann K. Abdominal cancer during early childhood: a dosimetric comparison of proton beams to standard and advanced photon radiotherapy. *Radiother Oncol J Eur Soc Ther Radiol Oncol* (2008) 89:141–9. doi: 10.1016/j.radonc.2008.06.012
12. Hill-Kayser C, Tochner Z, Both S, Lustig R, Reilly A, Balamuth N, et al. Proton versus photon radiation therapy for patients with high-risk neuroblastoma: The need for a customized approach. *Pediatr Blood Cancer* (2013) 60 (10):1606–11. doi: 10.1002/pbc.24606
13. Bagley AF, Grosshans DR, Philip NV, Foster J, McAleer MF, McGovern SL, et al. Efficacy of proton therapy in children with high-risk and locally recurrent neuroblastoma. *Pediatr Blood Cancer* (2019) 66:e27786. doi: 10.1002/pbc.27786
14. Hill-Kayser CE, Tochner Z, Li Y, Kurtz G, Lustig RA, James P, et al. Outcomes after Proton Therapy for Treatment of Pediatric High-Risk Neuroblastoma. *Int J Radiat Oncol Biol Phys* (2019) 104(2):401–8. doi: 10.1016/j.ijrobp.2019.01.095
15. Berthold F, Faldum A, Ernst A, Boos J, Dilloo D, Eggert A, et al. Extended induction chemotherapy does not improve the outcome for high-risk neuroblastoma patients: results of the randomized open-label GPOH trial NB2004-HR. *Ann Oncol Off J Eur Soc Med Oncol* (2020) 31:422–9. doi: 10.1016/j.annonc.2019.11.011
16. AWMF. *Detail*. Available at: https://www.awmf.org/leitlinien/detail/ll/025-008.html (Accessed April 24, 2020).
17. Taylor PA, Kry SF, Followill DS. Pencil Beam Algorithms Are Unsuitable for Proton Dose Calculations in Lung. *Int J Radiat Oncol Biol Phys* (2017) 99:750–6. doi: 10.1016/j.ijrobp.2017.06.003
18. Saini J, Maes D, Egan A, Bowen SR, St James S, Janson M, et al. Dosimetric evaluation of a commercial proton spot scanning Monte-Carlo dose algorithm: comparisons against measurements and simulations. *Phys Med Biol* (2017) 62:7659–81. doi: 10.1088/1361-6560/aa82a5
19. Gatcombe HG, Marcus RB, Katzenstein HM, Tighiouart M, Esiashvili N. Excellent local control from radiation therapy for high-risk neuroblastoma. *Int J Radiat Oncol Biol Phys* (2009) 74:1549–54. doi: 10.1016/j.ijrobp.2008.10.069
20. Ferris MJ, Danish H, Switchenko JM, Deng C, George BA, Goldsmith KC, et al. Favorable Local Control From Consolidative Radiation Therapy in High-Risk Neuroblastoma Despite Gross Residual Disease, Positive Margins, or Nodal Involvement. *Int J Radiat Oncol* (2017) 97:806–12. doi: 10.1016/j.ijrobp.2016.11.043
21. Haas-Kogan DA, Swift PS, Selch M, Haase GM, Seeger RC, Gerbing RB, et al. Impact of radiotherapy for high-risk neuroblastoma: a Children's Cancer Group study. *Int J Radiat Oncol* (2003) 56:28–39. doi: 10.1016/S0360-3016(02)04506-6
22. Casey DL, Kushner BH, Cheung N-KV, Modak S, LaQuaglia MP, Wolden SL. Local Control With 21-Gy Radiation Therapy for High-Risk Neuroblastoma. *Int J Radiat Oncol Biol Phys* (2016) 96:393–400. doi: 10.1016/j.ijrobp.2016.05.020
23. Pai Panandiker AS, Beltran C, Billups CA, McGregor LM, Furman WL, Davidoff AM. Intensity modulated radiation therapy provides excellent local control in high-risk abdominal neuroblastoma. *Pediatr Blood Cancer* (2013) 60:761–5. doi: 10.1002/pbc.24350
24. Robbins JR, Krasin MJ, Pai Panandiker AS, Watkins A, Wu J, Santana VM, et al. Radiation therapy as part of local control of metastatic neuroblastoma: the St Jude Children's Research Hospital experience. *J Pediatr Surg* (2010) 45:678–86. doi: 10.1016/j.jpedsurg.2009.11.003
25. Mazloom A, Louis CU, Nuchtern J, Kim E, Russell H, Allen-Rhoades W, et al. Radiation therapy to the primary and postinduction chemotherapy MIBG-avid sites in high-risk neuroblastoma. *Int J Radiat Oncol Biol Phys* (2014) 90:858–62. doi: 10.1016/j.ijrobp.2014.07.019
26. Liu KX, Naranjo A, Zhang FF, DuBois SG, Braunstein SE, Voss SD, et al. Prospective Evaluation of Radiation Dose Escalation in Patients With High-Risk Neuroblastoma and Gross Residual Disease After Surgery: A Report From the Children's Oncology Group ANBL0532 Study. *J Clin Oncol* (2020) 38(24):2741–52. doi: 10.1200/JCO.19.03316 JCO.19.03316.
27. Oshiro Y, Mizumoto M, Okumura T, Sugahara S, Fukushima T, Ishikawa H, et al. Clinical results of proton beam therapy for advanced neuroblastoma. *Radiat Oncol* (2013) 8:142. doi: 10.1186/1748-717X-8-142
28. Gillis AM, Sutton E, Dewitt KD, Matthay KK, Weinberg V, Fisch BM, et al. Long-term outcome and toxicities of intraoperative radiotherapy for high-risk neuroblastoma. *Int J Radiat Oncol Biol Phys* (2007) 69:858–64. doi: 10.1016/j.ijrobp.2007.04.006
29. Zhao Q, Liu Y, Zhang Y, Meng L, Wei J, Wang B, et al. Role and toxicity of radiation therapy in neuroblastoma patients: A literature review. *Crit Rev Oncol Hematol* (2020) 149:102924. doi: 10.1016/j.critrevonc.2020.102924
30. van Waas M, Neggers SJCMM, Raat H, van Rij CM, Pieters R, van den Heuvel-Eibrink MM. Abdominal radiotherapy: a major determinant of metabolic syndrome in nephroblastoma and neuroblastoma survivors. *PloS One* (2012) 7:e52237. doi: 10.1371/journal.pone.0052237
31. Ducassou A, Gambart M, Munzer C, Padovani L, Carrie C, Haas-Kogan D, et al. Long-term side effects of radiotherapy for pediatric localized neuroblastoma. *Strahlenther Onkol* (2015) 191(7):604–12. doi: 10.1007/s00066-015-0837
32. Lim PS, Pica A, Hrbacek J, Bachtiary B, Walser M, Lomax AJ, et al. Pencil Beam Scanning Proton Therapy for Paediatric Neuroblastoma with Motion Mitigation Strategy for Moving Target Volumes. *Clin Oncol R Coll Radiol G B* (2020) 32:467–76. doi: 10.1016/j.clon.2020.02.002
33. Hattangadi JA, Rombi B, Yock TI, Broussard G, Friedmann AM, Huang M, et al. Proton radiotherapy for high-risk pediatric neuroblastoma: early outcomes and dose comparison. *Int J Radiat Oncol Biol Phys* (2012) 83:1015–22. doi: 10.1016/j.ijrobp.2011.08.035
34. Kandula S, Prabhu RS, Nanda R, Switchenko JM, Cash T, Qayed M, et al. Outcomes After Radiation Therapy to Metastatic Sites in Patients With Stage 4 Neuroblastoma. *J Pediatr Hematol Oncol* (2015) 37:175–80. doi: 10.1097/MPH.0000000000000264
35. Polishchuk AL, Li R, Hill-Kayser C, Little A, Hawkins RA, Hamilton J, et al. Likelihood of bone recurrence in prior sites of metastasis in patients with high-risk neuroblastoma. *Int J Radiat Oncol Biol Phys* (2014) 89:839–45. doi: 10.1016/j.ijrobp.2014.04.004
36. Casey DL, Pitter KL, Kushner BH, Cheung N-KV, Modak S, LaQuaglia MP, et al. Radiation Therapy to Sites of Metastatic Disease as Part of Consolidation in High-Risk Neuroblastoma: Can Long-term Control Be Achieved? *Int J Radiat Oncol Biol Phys* (2018) 100:1204–9. doi: 10.1016/j.ijrobp.2018.01.008
37. Arumugam S, Manning-Cork NJ, Gains JE, Boterberg T, Gaze MN. The Evidence for External Beam Radiotherapy in High-Risk Neuroblastoma of Childhood: A Systematic Review. *Clin Oncol* (2018) 31(3):182–90. doi: 10.1016/j.clon.2018.11.031
38. Kushner BH, Wolden S, LaQuaglia MP, Kramer K, Verbel D, Heller G, et al. Hyperfractionated low-dose radiotherapy for high-risk neuroblastoma after intensive chemotherapy and surgery. *J Clin Oncol Off J Am Soc Clin Oncol* (2001) 19:2821–8. doi: 10.1200/JCO.2001.19.11.2821
39. Nazmy MS, Khafaga Y. Clinical experience in pediatric neuroblastoma intensity modulated radiotherapy. *J Egypt Natl Cancer Inst* (2012) 24:185–9. doi: 10.1016/j.jnci.2012.10.001
40. Jo JH, Ahn SD, Koh M, Kim JH, Lee S, Song SY, et al. Patterns of recurrence after radiation therapy for high-risk neuroblastoma. *Radiat Oncol J* (2019) 37:224–31. doi: 10.3857/roj.2019.00353
41. Casey DL, Kushner BH, Cheung N-KV, Modak S, Basu EM, Roberts SS, et al. Reduced-Dose Radiation Therapy to the Primary Site is Effective for High-Risk Neuroblastoma: Results From a Prospective Trial. *Int J Radiat Oncol Biol Phys* (2019) 104:409–14. doi: 10.1016/j.ijrobp.2019.02.004
42. Simon T, Häberle B, Hero B, von Schweinitz D, Berthold F. Role of surgery in the treatment of patients with stage 4 neuroblastoma age 18 months or older at diagnosis. *J Clin Oncol Off J Am Soc Clin Oncol* (2013) 31:752–8. doi: 10.1200/JCO.2012.45.9339
43. Holmes K, Poetschger U, Sarnacki S, Monclair T, Cecchetto G, Gomez Chacon J, et al. The influence of surgical excision on survival in high-risk neuroblastoma revisited after introduction of ch14.18/CHO immunotherapy in the HR-NBL1/SIOPEN trial. *J Clin Oncol* (2018) 36:10521–1. doi: 10.1200/JCO.2018.36.15_suppl.10521
44. Casey DL, Kushner BH, Cheung N-KV, Modak S, LaQuaglia MP, Wolden SL. Dose-escalation is needed for gross disease in high-risk neuroblastoma. *Pediatr Blood Cancer* (2018) 65:e27009. doi: 10.1002/pbc.27009
45. Simon T, Hero B, Bongartz R, Schmidt M, Müller RP, Berthold F. Intensified external-beam radiation therapy improves the outcome of stage 4 neuroblastoma in children > 1 year with residual local disease. *Strahlenther Onkol Organ Dtsch Rontgengesellschaft Al* (2006) 182:389–94. doi: 10.1007/s00066-006-1498-8
46. ASTRO. *Boost Radiation Offers No Additional Benefit in Children With High-Risk Neuroblastoma. PracticeUpdate* (2019). Available at: https://www.

practiceupdate.com/content/astro-2019-boost-radiation-offers-no-additional-benefit-in-children-with-high-risk-neuroblastoma/89978 (Accessed April 23, 2020).
47. Ladenstein R, Pötschger U, Pearson ADJ, Brock P, Luksch R, Castel V, et al. Busulfan and melphalan versus carboplatin, etoposide, and melphalan as high-dose chemotherapy for high-risk neuroblastoma (HR-NBL1/SIOPEN): an international, randomised, multi-arm, open-label, phase 3 trial. *Lancet Oncol* (2017) 18:500–14. doi: 10.1016/S1470-2045(17)30070-0
48. Seddon BM, Cassoni AM, Galloway MJ, Rees JH, Whelan JS. Fatal radiation myelopathy after high-dose busulfan and melphalan chemotherapy and radiotherapy for Ewing's sarcoma: a review of the literature and implications for practice. *Clin Oncol R Coll Radiol G B* (2005) 17:385–90. doi: 10.1016/j.clon.2005.03.004
49. *Carrie: The radiosensitization effect and toxicity... - Google Scholar*. Available at: https://scholar.google.com/scholar_lookup?title=The%20radiosensitization%20effect%20and%20toxicity%20of%20busulfan%20containing%20chemotherapy%20before%20radiotherapy%20for%20Ewing%E2%80%99s%20sarcomas&journal=Strahlenther%20Onkol&volume=185&issue=Sondernr.2&publication_year=2009&author=Carrie%2CC.&author=Deley%2CM.C.&author=Claude%2CL.&author=Alapetite%2CC.&author=Marandet%2CJ.&author=Habrand%2CJ.L.&author=Quetin%2CP.&author=Oberlin%2CO (Accessed July 21, 2020).
50. Bölling T, Dirksen U, Ranft A, Ernst I, Jürgens H, Willich N. Radiation toxicity following busulfan/melphalan high-dose chemotherapy in the EURO-EWING-99-trial: review of GPOH data. *Strahlenther Onkol Organ Dtsch Rontgengesellschaft Al* (2009) 185 Suppl 2:21–2. doi: 10.1007/s00066-009-1009-9
51. Whelan J, Le Deley M-C, Dirksen U, Le Teuff G, Brennan B, Gaspar N, et al. High-Dose Chemotherapy and Blood Autologous Stem-Cell Rescue Compared With Standard Chemotherapy in Localized High-Risk Ewing Sarcoma: Results of Euro-E.W.I.N.G.99 and Ewing-2008. *J Clin Oncol Off J Am Soc Clin Oncol* (2018) 36(31):JCO2018782516. doi: 10.1200/JCO.2018.78.2516 JCO2018782516.
52. Ladenstein R, Pötschger U, Valteau-Couanet D, Luksch R, Castel V, Ash S, et al. Investigation of the Role of Dinutuximab Beta-Based Immunotherapy in the SIOPEN High-Risk Neuroblastoma 1 Trial (HR-NBL1). *Cancers* (2020) 12 (2):309. doi: 10.3390/cancers12020309
53. Ding Y-Y, Panzer J, Maris JM, Castañeda A, Gomez-Chiari M, Mora J. Transverse myelitis as an unexpected complication following treatment with dinutuximab in pediatric patients with high-risk neuroblastoma: A case series. *Pediatr Blood Cancer* (2018) 65(1):e26732. doi: 10.1002/pbc.26732

Conflict of Interest: The authors declare that the research was conducted in the absence of any commercial or financial relationships that could be construed as a potential conflict of interest.

Copyright © 2021 Jazmati, Butzer, Hero, Ahmad Khalil, Merta, Bäumer, Plum, Fuchs, Koerber, Steinmeier, Peters, Doyen, Thole, Schmidt, Blase, Tippelt, Eggert, Schwarz, Simon and Timmermann. This is an open-access article distributed under the terms of the Creative Commons Attribution License (CC BY). The use, distribution or reproduction in other forums is permitted, provided the original author(s) and the copyright owner(s) are credited and that the original publication in this journal is cited, in accordance with accepted academic practice. No use, distribution or reproduction is permitted which does not comply with these terms.

frontiers in Oncology

REVIEW
published: 21 January 2021
doi: 10.3389/fonc.2020.613669

Biological and Mechanical Synergies to Deal With Proton Therapy Pitfalls: Minibeams, FLASH, Arcs, and Gantryless Rooms

Alejandro Mazal[1], Juan Antonio Vera Sanchez[1], Daniel Sanchez-Parcerisa[2,3,4], Jose Manuel Udias[2,3], Samuel España[2,3], Victor Sanchez-Tembleque[2,3], Luis Mario Fraile[2,3], Paloma Bragado[3,5], Alvaro Gutierrez-Uzquiza[3,5], Nuria Gordillo[6,7], Gaston Garcia[7], Juan Castro Novais[1], Juan Maria Perez Moreno[1], Lina Mayorga Ortiz[1], Amaia Ilundain Idoate[1], Marta Cremades Sendino[1], Carme Ares[1], Raymond Miralbell[1] and Niek Schreuder[8]*

[1] Centro de Protonterapia Quironsalud, Madrid, Spain, [2] Grupo de Física Nuclear and IPARCOS, U. Complutense Madrid, CEI Moncloa, Madrid, Spain, [3] Instituto de Investigación Sanitaria del Hospital Clínico San Carlos, Madrid, Spain, [4] Sedecal Molecular Imaging, Madrid, Spain, [5] Department of Biochemistry and Molecular Biology. U. Complutense, Madrid, Spain, [6] Department of Applied Physics, U. Autonoma de Madrid, Madrid, Spain, [7] Center for Materials Microanalysis, (CMAM), U. Autonoma de Madrid, Madrid, Spain, [8] Leo Cancer Care, Knoxville, TN, United States

Proton therapy has advantages and pitfalls comparing with photon therapy in radiation therapy. Among the limitations of protons in clinical practice we can selectively mention: uncertainties in range, lateral penumbra, deposition of higher LET outside the target, entrance dose, dose in the beam path, dose constraints in critical organs close to the target volume, organ movements and cost. In this review, we combine proposals under study to mitigate those pitfalls by using individually or in combination: (a) biological approaches of beam management in time (very high dose rate "FLASH" irradiations in the order of 100 Gy/s) and (b) modulation in space (a combination of mini-beams of millimetric extent), together with mechanical approaches such as (c) rotational techniques (optimized in partial arcs) and, in an effort to reduce cost, (d) gantry-less delivery systems. In some cases, these proposals are synergic (e.g., FLASH and minibeams), in others they are hardly compatible (mini-beam and rotation). Fixed lines have been used in pioneer centers, or for specific indications (ophthalmic, radiosurgery,…), they logically evolved to isocentric gantries. The present proposals to produce fixed lines are somewhat controversial. Rotational techniques, minibeams and FLASH in proton therapy are making their way, with an increasing degree of complexity in these three approaches, but with a high interest in the basic science and clinical communities. All of them must be proven in clinical applications.

Keywords: proton therapy, FLASH, minibeams, arc therapy, gantry

OPEN ACCESS

Edited by:
Antony John Lomax, Paul Scherrer Institut (PSI), Switzerland

Reviewed by:
Ulrich W. Langner, Lifespan, United States
William F. Hartsell, Northwestern University, United States

****Correspondence:***
Alejandro Mazal
alejandro.mazal@quironsalud.es

Specialty section:
This article was submitted to Radiation Oncology, a section of the journal Frontiers in Oncology

Received: *03 October 2020*
Accepted: *02 December 2020*
Published: *21 January 2021*

Citation:
Mazal A, Vera Sanchez JA, Sanchez-Parcerisa D, Udias JM, España S, Sanchez-Tembleque V, Fraile LM, Bragado P, Gutierrez-Uzquiza A, Gordillo N, Garcia G, Castro Novais J, Perez Moreno JM, Mayorga Ortiz L, Ilundain Idoate A, Cremades Sendino M, Ares C, Miralbell R and Schreuder N (2021) Biological and Mechanical Synergies to Deal With Proton Therapy Pitfalls: Minibeams, FLASH, Arcs, and Gantryless Rooms. Front. Oncol. 10:613669. doi: 10.3389/fonc.2020.613669

INTRODUCTION: ADVANTAGES AND PITFALLS IN PROTON THERAPY

Proton therapy has been evolving as the reference for conformal radiation therapy for decades and, in spite of an exponential growth, it is still limited to less than 1% of the patients treated with radiation therapy even in high-income countries. The primary advantages of proton therapy—compared with conventional photon beams—that justify its use and development are:

1. there is not a maximum of dose in the path of a beam;
2. it may have a small lateral penumbra in the path of a beam;
3. it is possible to irradiate homogeneously (or with a controlled inhomogeneity) a target in depth even with a single beam;
4. the range of particles can be placed anywhere by changing the energy of the beam;
5. there is a high gradient of dose after the range;
6. there is no practical dose beyond the distal gradient, i.e., the beam stops;
7. the radiobiological efficiency is managed in clinics with a rather low risk.

But there are also pitfalls:

1. the entrance dose can be higher than the usual with photon beams (no skin sparing), depending on parameters such as the proximity of the target volume to the skin, the thickness of the target, the delivery technique;
2. the lateral penumbra in depth, at depths close to the range and in the region of the target volume, can be higher than mid-energy photon beams (e.g., 6 MV) as such used in rotational VMAT techniques with photons;
3. there are large uncertainties on the position of the range in complex tissues including inhomogeneities, imposing large margins to get robustness of plans, and placing the higher Linear Energy Transfer (LET) beyond the target limits.
4. There are complex dose distributions and large uncertainties beyond implanted materials such as metallic screws, rods, prosthesis, …;
5. There is a neutron dose in the tissues around the target, even far from it; it has been reduced in the evolution of proton systems from passive to pencil beam, but still there, comparing with photons beams with energies lower than 10 MV;
6. It is complex to irradiate moving targets, even more when using scanned pencil beams, in spite of specific protocols of repainting and organ movement management (interplay effect, undesirable doses beyond the target,…);
7. Capital and operational costs are high, uptimes are sometimes limited and it is difficult to easily have backups in case of system failure.

In **Figure 1**, some of these advantages and pitfalls are presented for a single proton beam in particular compared to a single photon beam and for a final clinical dose distribution.

In practice, there are clinical cases where the dose gradient between a target and a close critical organ maybe better achieved with photon beams. But the integral dose distribution will always be easier to optimize with proton beams, given their finite range (no exit dose) that reduce the irradiation to large volumes of healthy tissues.

The advantages offered by proton therapy are stronger than the pitfalls, justifying the fact that more than 200,000 patients have been treated with protons in the world to date with more than 20,000 new treatments added per year. Proton therapy is a rational choice among the existing tools in radiation therapy for some clinical targets: pediatrics, ophthalmic, base of the skull, reirradiations. Most of the other clinical sites in radiation oncology are under investigation to quantify the real clinical advantage of the use of protons and the associated cost, through studies of tumor control, complications and quality of life. Concepts like "model-based approach" are used to evaluate individual cases, and Qualy, quality of life, cost-benefit and similar ones for a population-based study.

The use of photon beams is also still evolving, many more scholars are working actively in the photon therapy space and the pace of innovation is high. The development of any modality in radiation therapy (photons, electrons, neutrons, protons, heavy particles …) can be synergic and not opposed between them. Innovations such as the use of online magnetic resonance imaging, adaptive therapy and the combination with immunological approaches are examples of major improvements to be shared.

Several papers are included in this special issue to deal with some of the proton therapy pitfalls, trying to reduce or to eliminate them, or at least to control and mitigate their effect.

In this work we want to review and address biological and mechanical proposals to mitigate most of the mentioned pitfalls, using particular approaches to distribute the dose in space (minibeams) and time (FLASH effect) as well as to reduce complexity (rotational therapy) and cost (gantry less facilities), to make proton therapy more accessible to the benefit of more cancer patients.

BIOLOGY: REVISITING RADIATION BIOLOGY TO IMPROVE HEALTHY TISSUE PROTECTION

The location of the tumors and the nature of the treatments inevitably leads to a certain degree of undesired effects in surrounding tissues. Proton minibeam radiation therapy (pMBRT) and ultra-high dose rate (FLASH) radiotherapy (FLASH RT) are two innovative radiotherapy modalities where the potential to reduce normal tissue toxicity have already been demonstrated, compared to standard radiotherapy, potentially revolutionizing the radiotherapy field.

Recently several reviews on the tissue sparing and tumor control with Flash have been published, including a few oriented towards proton therapy (1). One of us and co-authors presented a review of minibeams and FLASH radiation therapy, with both approaches working independently or in synergy (2).

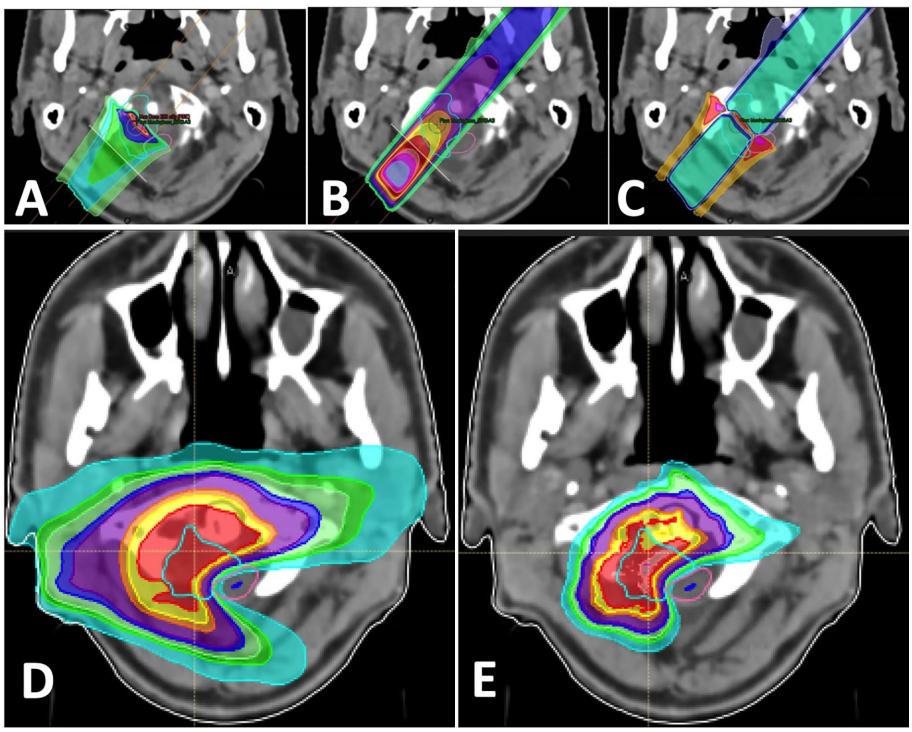

FIGURE 1 | Beams for a treatment of a base of skull tumor: **(A)** single proton beam; **(B)** single photon beam; **(C)** difference between single proton (higher dose in red) and photon beams (higher dose in blue); **(D)** combination of photon arcs; **(E)** combination of proton beams.

In this work we review some of the basic and new proposals on these subjects and how they are linked to advances in ongoing mechanical aspects of proton therapy such as proton arc therapy.

Flash

Recent pre-clinical studies have found that the "new" methodology named "FLASH", which consists of delivering single doses of 5 to 10 Gy in a single microsecond pulse or in times lower than 100 to 500 ms, produces a dramatic decrease of damage to normal tissues while keeping the anti-tumoral effect (3–6). This FLASH effect was described as early as the 1970s for intestinal tumors and skin lesions. One of the pioneers, J. Hendry, who, in the 1970s and 1980s, related the amount of oxygen with the radioprotection of tissues using high intensity pulsed electron beams, recently rediscussed the clinical potential application of FLASH and, finally supported the development of proton experiments while recommending to take care having a long follow up and a better understanding of parameters and effects (7, 8). The robustness of the FLASH effect has recently been reproduced in various animal models, such as mice, rats, zebrafish, pigs, and cats (5) for several organs such as lung, skin, gut, and brain (3, 4, 9, 10).

To prove the toxicity limiting capability of FLASH RT, Favaudon et al., used a lung fibrosis model in mice and demonstrated that thoracic irradiation of mice with FLASH dose rates (40–60 Gy/s) reduced the induction of pulmonary fibrosis when compared with conventional dose rates (0.03 Gy/s) where 100% of the mice develop lung fibrosis (3). In this study, they also used a xenograft model of head and neck squamous carcinoma, a xenograft model of breast cancer, and a syngeneic model of lung cancer and found that in all three models FLASH RT was as efficient as conventional radiotherapy in reducing tumor growth (3).

The reduced radiotoxicity of FLASH RT has also been shown by the irradiation of the mice abdomen. In a recent work, Diffenderfer et al., showed that after acute radiation of 10-week-old C57BL/6J mice with either 15 Gy whole abdominal FLASH proton RT (789 Gy/s) or standard proton RT (0.9 0.08 Gy/s) acute cell loss and late fibrosis were decreased in the mice irradiated with FLASH proton therapy, whereas the effect on tumor growth was similar with the two irradiation modalities (10). This is in agreement with previous studies where the protective effect of FLASH RT in the gut was also observed (11). Using proton beams, Abel et al. (12) reported differences between FLASH (and FLASH with pulsed beams) vs "conventional" radiation for doses higher than 15 Gy on the thorax region of mice using several endpoints such as weight, dermatitis, lung function and lung fibrosis, as well as gender differences (female mice having better response to FLASH but no difference on mode of cell death).

Furthermore, it has also been shown in several studies that FLASH radiotherapy also has less neurotoxic effects compared to conventional RT (9, 13–15). Montay-Gruel et al., reported that mice with whole brain irradiated with FLASH RT experienced

better preservation of memory and performed better in the behavioral studies compared to those irradiated with standard RT (9, 13).

The biological mechanism responsible for the reduced tissue toxicity following FLASH RT is yet to be fully explained. The reduced adverse long-term effects of FLASH irradiation observed in normal tissues compared to conventional dose rates and or tumor tissues have been explained by the different type and/or amount of the induced DNA damage. *In vitro* experiments suggested that the genomic instability induced in response to FLASH RT was much lower than at conventional dose rates (16, 17).

In addition to the DNA damage, several hypotheses have been proposed to explain the FLASH effect, such as the presence of free radicals or oxygen depletion that will trigger different biological responses depending on the status and metabolism of the cell (18). Oxygen depletion has been proposed to cause transient hypoxia and radio-resistance, and this is considered as the underlying mechanism, but *in vitro* data to support this assumption has been lacking until recently (19). To test the role of oxygen in the FLASH effect, Adrian et al., irradiated prostate cancer cells at different oxygen concentrations using either 600 Gy/s (FLASH) or 14 Gy/min (CONV) (20). Their results showed that in hypoxic conditions, cell survival increased in the cells irradiated with FLASH, while in normoxic conditions no differences were found between FLASH and conventional RT (20). A recent study by Montay-Gruel et al., proposes that oxygen depletion at ultra-high dose rates inhibits the production of reactive oxygen species (ROS) which promote radio-resistance (9). They report that increasing the local oxygen concentration reversed the protective effect of FLASH (9).

Furthermore, depletion of ROS using ROS scavengers sensitize zebrafish embryos to conventional therapy while having no effect in FLASH RT (9). The oxygen depletion hypothesis was used to explain the normal tissue radio-resistance to FLASH RT.

Besides local and transient oxygen depletion, radical-radical interaction is another hypothesized reason for the FLASH effect. FLASH irradiation results in a high local radical concentration available to interact with the DNA (21).

However, if tumors (or partial volumes of the tumors) are partially, but maybe not fully, hypoxic, how do they react with FLASH RT? The metabolic reorganization or the absence of proper antioxidant defenses, frequent in tumor cells, may accelerate the presence of irradiated induced radicals which may jeopardize tumor cell viability.

Nevertheless, more studies are necessary to validate these hypotheses experimentally for a full understanding of the biological effects induced by FLASH therapy.

The immune system and inflammation have also been proposed to play a role in FLASH RT protective effect of normal tissues. In their paper, Favaudon et al., found changes in the induction of the transforming growth factor beta (TGFb), a pro-inflammatory signal, which was reduced in FLASH irradiated mice (3). In addition, previous studies have shown an increased recruitment of T lymphocytes in tumors treated with FLASH-RT (22). Furthermore, a recent study in which they perform a genome-wide microarray analysis on mice that have been irradiated either with FLASH or conventional RT showed that immune system wide activation and maturation was downregulated in mice following FLASH RT (23). Therefore, these studies suggest that FLASH irradiation induces the response of the immune system in the irradiated tissue; however, the molecular mechanism behind this response remains to be explained.

Recently, Wardman (24) reviewed 60 years of experience with pulse radiolysis and highlighted 2 mechanistic approaches for the differentiated effect on normal versus tissue cells, i.e., the depletion of a chemical critical to the effect and/or the radical-radical reactions. Favaudon (25) also reviewed these two approaches, i.e., oxygen depletion vs radical recombinations, giving more weight to the second phenomena. He also stated that in both extremes of anoxia (or deep hypoxia) and hyperoxia there is no FLASH effect, making it important to know the oxygen pressure in the tumor and tissues to predict the effect. The group presented a chemical kinetic model supporting peroxyl radical recombination as the main effect (26) and, adding the results from Fouillade et al. (4), they conclude that part of the differential effect between tumors and healthy tissue could be related to DNA damage (dependent on oxygen and radicals) and double strand break repair protein 53BP1 for which tumors cells have a repair defect.

From the published data, we conclude that the main hypothesis explaining the FLASH benefit, is based on three main aspects, i.e., (a) a "window" of Oxygen concentration, (b) the kinetics of radicals and, (c) an intrinsic differentiation between tumor and healthy cells related to their DNA damage repair mechanisms. A correct understanding of the mechanisms behind FLASH effect may help to establish protocols aiming to decrease the harmful effects of ionizing radiation by preserving the healthy tissues surrounding the irradiated tumor while keeping the curative effect. A first clinical application has been reported (6) and new clinical trials are being approved. Furthermore the potential use of FLASH in pediatrics (e.g., in medulloblastoma) has been cited from studies in juvenile mice (27).

Mini-Beams

Minibeam radiation therapy (MBRT) is an innovative strategy for spatially fractionated radiotherapy that consists of using a series of narrow (sub-millimetric) parallel beams to deliver the dose. This results in dose profiles consisting of a pattern of peaks and valleys.

The approach has an old rational with spatially fractionated "GRID" radiation therapy with photons using patterns of large peaks and valleys or sectors, both in the 1-cm scale, to spare skin toxicity with orthovoltage devices (28) and to shrink malignancies for advanced and palliative cases, with Co´60 and linacs (29), but not with curative intention.

The rationale behind the new approach is that the smaller the beam size is, the higher the dose tolerances of the healthy tissue appears to be, and a curative aim can still be kept. This is known

as the dose-volume effect. Several studies have reported that MBRT is less neurotoxic than standard radiotherapy (30–35). The potential of the minibeams radiotherapy technique was studied in brain tumor bearing rats that were irradiated using X-ray minibeams. Deman et al., found that the survival time of irradiated glioma bearing rats was doubled when compared to untreated animals (30). This increase in glioma bearing rats' life span was similar to the one obtained through other radiotherapy techniques. However, no brain damage was found on X-ray minibeams irradiated in healthy rats suggesting healthy tissues have a higher tolerance to submillimetric spatially fractionated beams (30). These experiments suggest that X-ray minibeams can be used in brain tumor radiotherapy.

Prezado et al. modified a small animal irradiator to be able to perform MBRT experiments. As a proof of concept experiment, they irradiated a group of rats with standard radiation while the other group received MBRT, both groups with 20 Gy mean dose and evaluated 6.5 months after radiation. They found that the standard RT group have extensive brain damage while in the MBRT group no significant brain lesions were observed (31). *In vitro* studies have shown that MBRT induces clonogenic cell death of human glioma cell lines (33). In a recent report by the same group showed that proton MBRT (pMBRT) increases the therapeutic window for high grade gliomas (34). They showed that pMBRT causes less neurotoxicity than standard proton therapy and in addition it significantly reduces tumor growth (34). This opens the possibility for even more aggressive irradiation schemes.

In a recent study by Dos Santos et al., they compare the micro- and nanodosimetric characteristics of three different MBRT modalities: proton (pMBRT), photon (xMBRT) and electron (eMBRT). They found that pMBRT was the most effective at preserving normal tissue since it caused less energy deposition and lower number of DNA breaks both in peak and valley cell nuclei (35). Furthermore, pMBRT was also the most aggressive treatment in the tumors region, as it was associated with a higher number of complex DNA breaks and higher energy deposition, and energy per event, at the cell nucleus (35).

As mentioned above several studies have reported the therapeutic interest of the MBRT at preclinical level, but the biological mechanisms responsible for the described protection of healthy tissues are not fully understood to date. Classically, the protective effect of MBRT on healthy tissues has been associated with the apparent resistance of normal tissue vasculature to MBRT (36). Furthermore, it has been proposed that the efficiency of MBRT on reducing tumor growth is related to a preferential damaging effect on the tumor vasculature (37). When applied to the brain of rodents, microbeam irradiation does not modify blood volume or vascular density (36). In fact, the endothelial cell lining of the vessels in the microbeam paths remains intact (37). However, immature blood vessels are more sensitive to MBRT than mature blood vessels (38). This has led to the hypothesis that immature blood vessels in the tumor will be more sensitive to MBRT while the healthy tissue mature blood vessels will be resistant to MBRT. Several reports have shown that MBRT affects the tumor vasculature structure, nevertheless, the effect may vary depending on the tumor type. In general, MBRT induces a decrease in tumor blood vessels leading to decrease in perfusion and to tumor hypoxia (39, 40). However, in a mammary tumor model, MBRT increased pericyte numbers, suggesting a normalization of the vasculature structure and tumor oxygenation (41). Although MBRT preferentially affects the tumor vasculature structure, we shouldn't restrict the effects of MBRT to vascular effects only.

A study of the early transcriptomic responses of normal brain and glioma tissue in rats after MBRT irradiation showed that inflammation and immunity appear to be major contributors to MBRT efficacy (42). Pathways related with natural killer cells (NK) or CD8+ T lymphocytes were particularly represented in the irradiated tissue. Furthermore, they found changes in genes such as *HMGB1*, Toll-like receptors 1, 2, 7, C-type lectins 7A and CD36 in the irradiated tissue (42). These genes can trigger activation of innate or adaptive immune cells. Therefore, their hypothesis is that biochemical changes in irradiated cells, will activate these genes which in turn will promote inflammation or an immunological response (42). This is in agreement with data from Sprung et al. that have previously reported using a genome transcriptional screening that MBRT in mouse mammal tumors induced upregulation of immunity-related genes (43). Still more *in vitro* and *in vivo* experiments where the immune response within healthy tissue and/or tumor is studied in response to MBRT are necessary to fully understand the mechanisms behind MBRT. We conclude that there are still a lot of open questions about the mechanisms of action associated with MBRT.

Although the mechanisms of action and the biological effects of both FLASH and MBRT are still under study, both radiation modalities have the potential to become paradigm-changing technologies in the radiotherapy field. They can open the door to a new approach to the delivery of curative radiotherapy and may become an effective treatment for radioresistant tumors.

The Dose Matter: The Dosimetry of FLASH and Mini-Beams

The accurate measurement of the dose delivered in a FLASH irradiation with photons, protons or electrons is a challenging task mainly due to the high dose-rate beams employed in this radiotherapy technique. Because of this, redundant measurements are usually performed with dosimeters whose response is nearly independent of the dose-rate (44).

As in the case of conventional radiotherapy, ionization chambers may be employed to measure the absolute dose, but with some caution. For instance, it has been stated by Petersson et al. (45) that the factors that correct the raw charge collected by the dosimeter in a pulsed electron FLASH irradiation depend on the dose per pulse rather than on the dose-rate.

Faraday cups have also been employed as a dosimeter in FLASH radiotherapy. In this case, the integral charge measured is used to validate the ionization chamber measurements, as shown in different studies (10, 46).

Among the dosimeters with a response independent of the dose rate, radiochromic films are commonly employed to provide a redundant verification of the dose delivered as

shown in the works of Buonanno et al. (47) and Jaccard et al. (48). Also, alanine pellets have been satisfactorily employed together with radiochromic films to perform independent dose verifications in the first clinical FLASH treatment of a human patient (6). Other dose-rate independent dosimeters that have been employed for the measurement of ultrahigh dose-rate beams are the PTW microdiamond, the LYNX 2D scintillator the TLD-100 and the Methyl Viologen (44). A comprehensive review of dosimeters for FLASH including charge-based, chemicals and luminescence detectors has been presented recently (49) with interesting figures of merit in a spider chart diagram for each of them, underlying the importance of the luminescence methods for resolution in time and additional performances on measuring Oxygen tension and LET.

Finally, some experiments have been carried out to achieve real time monitoring of FLASH irradiations. For instance, Diffenderfer et al. (10) employed a NaI gamma detector to relate the prompt gamma rays detected to the dose rate of the irradiation while Oraiqat et al. (50) have stated that an ionizing radiation acoustic imaging technique may be employed to perform real-time deep tissue dosimetry.

The dosimetry of proton minibeams radiation therapy is challenging due to the fact that it should characterize the inhomogeneous entrance spatial dose distribution as well as the homogenous part of the dose distribution. The entrance dose distribution presents marked spatial variations in the millimetric and submilimetric scale thus a high spatial resolution dosimeter should be employed. On the other hand, the homogeneous part of the beam does not present markedly spatial variations thus conventional dosimeters such as ionization chambers may be used. For this reason, a two-step protocol has been proposed by Peucelle et al. (51) in order to measure proton minibeams obtained by means of a multi-slit collimator. The first step consists in absolute dose measurements performed with a thimble ionization chamber and the second step is performed with radiochromic films to characterize the peak-to-valley dose ratios.

Radiosurgery diodes have been employed as an alternative to or together with radiochromic films for measurements in the high modulated entrance dose region. In the work of De Marzi et al. (52), the high modulated entrance region is characterized by performing measurements with a radiosurgery p-type silicon diode. Microdiamond diodes have also been proposed and evaluated in the works of Meyer et al. (53) and Farr et al. (54). Also, a microdiamond diode has been employed to characterize carbon and oxygen mini-beams in the work of Martinez-Rovira et al. (55).

Finally, some experiences have been carried out with gel dosimetry as in the work of Annabell et al. (56), where fluorescent microscopy is employed to achieve higher spatial resolution dose measurements.

The Time Factor in Beam Delivery for FLASH: The Pulsed Structure of Clinical Beams and Its Relationship With the Kinetics of the Physicochemical Processes

While it is usual to talk about the high dose rate to achieve FLASH, it is important to understand how this dose is delivered in time, in particular the pulsed structure of the beam. In two extremes, we can mention the "continuous" irradiation provided by a cyclotron (acceleration at several MHz), and the low frequency pulses of a synchrotron (a few Hz) and synchrocyclotrons (typically 1 KHz), modified by different extraction methods. The latter is gaining industrial interest from the perspective to make compact accelerators.

Internally, a synchrocyclotron varies the frequency of acceleration to be synchronized with the particle mass when it acquires energy. Here we use the "S2C2 Proteus One synchrocyclotron" (IBA, Leuven) as an example. We measured the beam intensity arriving at the isocenter as a function of time in a clinical condition (**Figure 2**). The accelerating frequency varies from 90 to 30 MHz. At extraction, there are pulses of about 10 μs wide (**Figure 2A**) each 1 ms (**Figure 2B**), i.e., 1 KHz pulses.

In **Figure 2B**, we superposed published data (26) on the O_2 evolution from a concentration of 50 μmol/L, as if 10 Gy were delivered at 10^6 Gy/s in the first pulse of 10 μs wide. The potential interaction with the pulsed beam must be evaluated in any experimental study (e.g., delivering the 10 Gy in 10 or 100 pulses) for all the elements involved (Oxygen, radicals, etc.).

Other patterns of dose delivery in time must be considered. In some systems the dose deposition in a single "spot" is fractionated in two to three parts so a feedback system can measure and control the delivery of an accurate total integrated charge for the spot. At a larger scale of time, when using a "pencil beam scanning system", the dose at a given point in the medium will have contributions from contiguous points and lines (related to scanning times) and layers (related to time to change the beam energy). In an even larger scale of time, if more than one beam is planned, several seconds or minutes are required to rotate the gantry and/or a couch to position the next beam and even more time is added if any verification of the new beam and patient position is required. The possibility to deliver FLASH in a very small number of fractions will add the scale of a daily difference between irradiations.

It is of the utmost importance to evaluate in the research programs these scales of time in particular related to the chemical and biological process mentioned before.

MECHANICS: THE ADVANTAGES AND LIMITS OF ARCS AND GANTRY-LESS PROTON BEAMS

Proton arc therapy is under consideration nowadays to reduce calculation complexity and uncertainties, as well as to optimize the deposition of high LET in tissues. But proton gantries are much more cumbersome and expensive than gantries for photon beams. There is a renewed interest to evaluate fixed lines and rotate the patient to reduce costs. Both approaches, arcs and fixed lines, have advantages and pitfalls we evaluate here.

Proton Arc Therapy (PAT)

The notion of rotating the proton gantry during beam delivery, in a similar fashion as it is done for Volume Modulated Arc Therapy (VMAT) using photons, has been studied in detail by

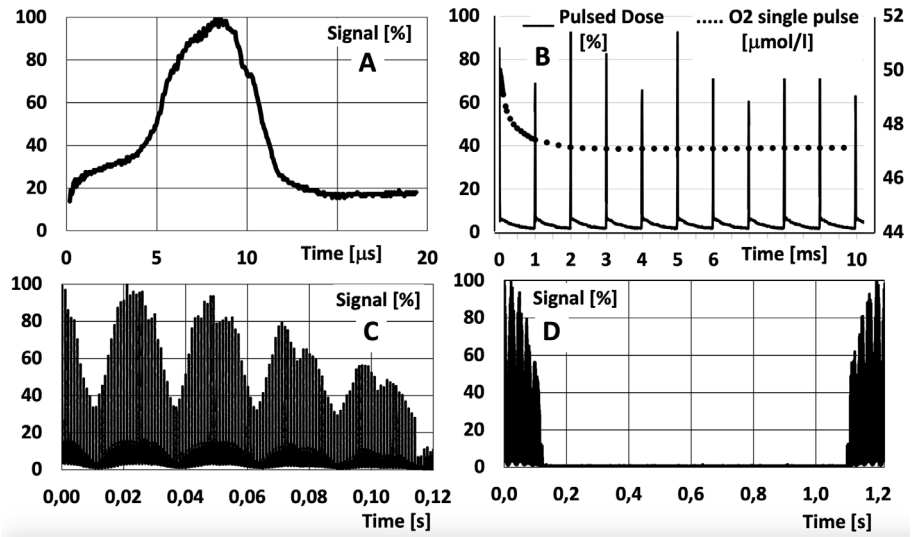

FIGURE 2 | Measurement at a fixed spot in a media when delivering protons with a scanned beam from a synchrocyclotron: **(A)** single spot; **(B)** a sequence of spots delivered in a same point at an extraction frequency of 1 kHz, superposed with the effect on oxygen (O_2) from a first pulse (see text); **(C)** effect cumulated dose in a point given by different lines scanned in a single layer (each packet is a line, the next packet is a contiguous line); **(D)** change of a layer in depth with a larger time to change energy (here about 1 sec). Measurements have been performed with a CeGAG scintillator coupled to a S13360-6075CS SiPM from Hamamatsu, read with a digital Picoscope.

various groups in the last two decades. Except from the first study (57), which used a rotational phantom to show the favorable physical properties of protons over electrons, most studies have been limited to dosimetric calculations in patients or phantoms. These studies showed that protons arcs have indeed a better longitudinal dose profile than photons (58, 59), and that increasing the number of incoming angles could have a positive impact on the resulting dose distribution, further reducing out-of-target dose (60–62) and secondary neutron dose for passively scattered protons (63).

However, none of these studies addressed in detail the feasibility and practical aspects of the proposed solutions. Treatment planning was typically performed with standard clinical software (by simply selecting an arbitrarily large number of fields). The effect of energy layer switching time (ELST), preventing different energy layers from being delivered simultaneously, from a single control point, was not contemplated.

A group at the University of Pennsylvania (Philadelphia, PA) did publish some work on the feasibility of delivering proton arcs using passively scattered (PS) beams (64, 65) but with the global market moving inevitably towards pencil beam scanning (PBS) solutions, no new developments involving PS beams were realistic at the time. The same group also explored the feasibility of arc techniques with PBS (66), showing that, with an adequate range selection system, single- and dual-energy proton arcs (named Proton Modulated Arc Therapy, or PMAT) could achieve similar dose coverage and organ-at-risk sparing capabilities as full-coverage 2-field and 4-field intensity-modulated proton therapy (IMPT) plans (67). The same study also showed limited improvement by using fully modulated arcs, warning that existing planning systems might not be able to produce optimal proton arc therapy plans by simply combining an arbitrarily large number of field angles in an IMPT plan, and that specific treatment-planning algorithms for proton arc therapy, either developed in-house (68, 69) or as an addition to existing systems (70) are probably required.

In 2016, a research group at Beaumont Health (Royal Oak, MI) published an article describing a PAT solution named SPArc, for Spot-scaning Proton Arc Therapy (70). It is based on a patented algorithm that optimizes the number of arc control points and the number of energy layers delivered from each angle. The algorithm was implemented in Raystation (RaySearch laboratories AB, Stockholm, Sweden) and used to plan two example patient cases, showing some potential for dose reduction in healthy tissues at a cost of increased delivery and treatment planning times. These time increased by a factor of ~2 and ~10, respectively, in comparison with equivalent static IMPT plans. This team has since published several studies analyzing possible dosimetric outcomes of SPArc in various tumor sites: prostate (71), non-small cell lung cancer (72), whole brain irradiation (73), head and neck (74) and left-side breast (75). This last location has been also explored by other teams (76). **Table 1** summarizes the most relevant data from these studies.

In general, it is hard to produce convincing evidence comparing two techniques based solely on treatment planning. The physical or biological rationale supporting superiority of a technique over another must be absolutely clear: in other words, these kind of studies have to prove that not only is SPArc better than IMPT in a selection of cases, but also that IMPT could not produce equivalent results if used differently (different planning objectives, different choice of fields, etc.). Also, as is usually the case with proton therapy, it is often unclear, and not necessarily

TABLE 1 | Analysis of published dosimetric studies comparing SPArc with IMPT.

Tumor site	Number of patients	Ratio of treatment times (SPArc/IMPT)*	Reference IMPT plans used clinically?	Demonstrated clinical relevance?	Reference
Prostate	9	2.0	No (VMAT)	No	(71)
Lung	14	1.2	No (IMRT)	No	(72)
Whole brain	8	0.9	No (VMAT)	No	(73)
Head and neck	14	1.1	No (combination IMPT with SFUD)**	Mean reduction of 31% in probability of salivary flow dysfunction.	(74)
Left-side breast	8	1.1	Yes	Mean reduction of 23% in probability of major coronary events, among other endpoints.	(75)

(*) Assuming a value of 1s for energy layer switching time.
(**) X. Ding, private communication. SFUD, Single-field, uniform dose.

obvious, that improved dose distributions automatically imply clinically relevant improved effects. Tumor-control probability (TCP) and normal-tissue complication probability (NTCP) models are therefore useful to prove this point, waiting for real clinical trials.

All five studies published to date by the Beaumont team show a clear potential of the SPArc technique to reduce out-of-target (integral) doses, and they do so without a foreseen major impact in treatment delivery time. However, only one of them (75) clearly demonstrates clinical relevance by comparing SPArc plans and clinically used IMPT plans in terms of NTCP, showing a predicted mean reduction of 23% in the probability of major coronary events caused by a reduction in the heart dose.

Plan robustness must also be considered when discussing recent developments in proton arc therapy. The general belief is that proton arc therapy is naturally more robust than IMPT, as it spreads the range uncertainty among different beam angles (61, 77). Dosimetric studies using SPArc seem to support this hypothesis: for all reported plans in all five sites, SPArc plans present equal or better robustness than their IMPT counterparts, evaluated in terms of mean area under the curve for root-mean-square dose volume histograms for relevant organs at risk, a metric introduced by Liu et al. (78).

Another interesting effect linked with PAT is radiobiological optimization (77). Increasing the number of beam angles allows for reducing the dose delivered by high-energy beams at the distal end of the target potentially placing the high-LET components close to a critical organ. The team at the University of Pennsylvania recently showed that PMAT plans effectively increase relative biological effectiveness (RBE) within the target (68). This finding was validated with an in-vitro study (79) and has also been reported by other authors in simpler PAT implementations (80). The clinical relevance of this radiobiological effect of PAT is yet to be established.

The aforementioned potential benefits of proton arc therapy, particularly in its SPArc implementation, instigated the development of a prototype system. A patent from U. of Maryland described in 2018 a method to deliver a proton beam while the gantry rotates around the patient, without changing the energy from the source but using an automatic energy modulator (81). In 2019, the first delivery of SPArc plans was reported by the Beaumont team (82) in their IBA Proteus One accelerator, with a technique that was named Proton Dynamic Arc Delivery, or PDAD. The delivered plans reported passing all quality assurance tests (flatness, symmetry, isocentricity), and the system was able to deliver a clinical plan over a 220-degree arc in 4 min.

Further work is required before SPArc (or any other implementation of PAT) becomes clinically available. The Beaumont team (82) cite machine stability (beam pauses, interlocks) and clinical workflow (development of DICOM standard, integration with TPS and Oncology Information System, QA program) as the main issues that need to be resolved. This should be complemented by an improvement in treatment calculation time, since the current status of the SPArc dose calculation algorithm, with over 2 h per patient (70), would hinder its incorporation into a clinical workflow. While recent developments in the SPArc dose optimization algorithm (83) have reported some advances, including a ~50% reduction in estimated irradiation time, a recent study (84) has identified several inherent weaknesses in the SPArc algorithm and proposed an alternative approach which can possibly reduce planning time by up to a factor of 10.

In conclusion, while PAT does not have the disruptive aura of other advanced technologies (such as FLASH or minibeams), it can indeed produce a positive effect in the quality of IMPT plans (due to better dose conformity, increased RBE and enhanced robustness). However, this effect must be backed up by more clinical studies. It could improve the logistics of proton treatments, like VMAT with photons, provided that fast and accurate treatment planning algorithms are developed. While its integration with other novel technologies (such as FLASH or minibeams) has not been studied in detail yet, arc strategies (in the form of arc-shoot-through techniques) have been proposed as an intermediate solution for achieving FLASH dose rates with pencil-beam scanned proton beams (85).

Gantries vs Fixed Beam Treatment Rooms—The Need for a Change in Paradigm Enabling Treating Patients in an Upright Orientation

In a recent paper Bortfeld et al. emphasized the need for particle beam therapy to become more available to more patients (86, 87). One of the three aspects that they list to "democratize" protons is to reduce the costs of proton systems by doing away with expensive gantry systems and adopt fixed beam treatment

rooms attaining multiple beam angles by rotating the patient in the beam. Fixed horizontal beams have been exploited in early systems to treat the patients in a seated position (88, 89) and at Fermi Lab, patients were treated in an upright position with neutrons (90, 91). Seated and upright treatments were until recently regarded as suboptimal arrangements forced on proton therapy when it was only available at physics research institutions, i.e., before the very large, expensive gantry systems were developed for and installed at hospital based and free-standing proton therapy clinics.

When the neutron therapy clinical results struggled to live up to the promises in the early eighties, people in the field reasoned that it is because they could not achieve the same conformality in dose than what was possible with gantry-based photon systems. This was mainly due to the lack of neutron gantries and not having multileaf collimators to allow for beam shaping to conform the beam to the target. That argument led to the development of isocentric neutron gantries and neutron multileaf collimators.

However, the proton depth dose curve (Bragg Peak) allows for a different paradigm in delivering the dose to a target. The fact that the beam stops and that fewer beams are typically used in proton treatment plans, defeats for some people the argument that proton gantries are essential. Furthermore, it is true that it's better to treat the patient in the same position as what the patient was scanned in mainly due to the displacement of organs when the patient is moved from a lying into an upright position. Intracranial lesions can be, and have been, treated in an upright position although the patient was scanned in a lying position. Multimodality imaging is an important aspect of treatment planning and target delineation and the best registration between different modality images is obtained with the patient in the same orientation. Like CT scanners most other imaging systems, i.e., PET, MRI, PET-CT, gamma Cameras and even Ultrasound scans are often designed to image the patient in a lying position. This notion further supports the thinking that radiation therapy treatments should be done in the lying position.

This paradigm is shifting, and several companies are now developing technologies that will allow for imaging and treating patients in an upright orientation (companies such as P-Cure, New-RT Corp Ltd, LEO and Advanced Oncotherapy). In **Figure 3**, we show an upright CT scanner and the upright patient positioner and that is currently being developed by one of these companies and that will soon be available for integration into existing proton therapy systems.

Clinical Potential Benefits of Upright Treatments

The potential advantages of treating the patient in a seated or upright position have been addressed by several scholars in the field. Verhey et al. reported in 1981 that patients can be immobilized effectively in the seated position with less unwanted motions than in a supine or decubitus position (92). McCarroll et al. reported on the benefits of treating thoracic and Head and neck patients in a seated position (93). Yang et al. reported that thoracic patients breathe easier and are more relaxed in an upright position while the lung volume is on average up to 25% larger compared to the supine position and the excursion of a lung tumor as a result of breathing motion is also smaller (94), depending on the location of the tumor in the lung. The WHO reported recently that 55% cancer deaths are from disease sites that are affected by breathing motion (95). Treating these cases in a seated or upright position could then result in improved patient comfort, less target motion and less lung volumes being irradiated.

Among the main benefits of having the patient immobilized in an upright position we can mention (a) the reduced risk of asphyxiation and (b) the reduced need to swallow that causes significant movement in the neck and esophageal regions (93). Applying anesthesia to patients in the upright position is common practice, e.g., in shoulder and posterior fossa surgery and might also be safer in some cases with respect to the risk of

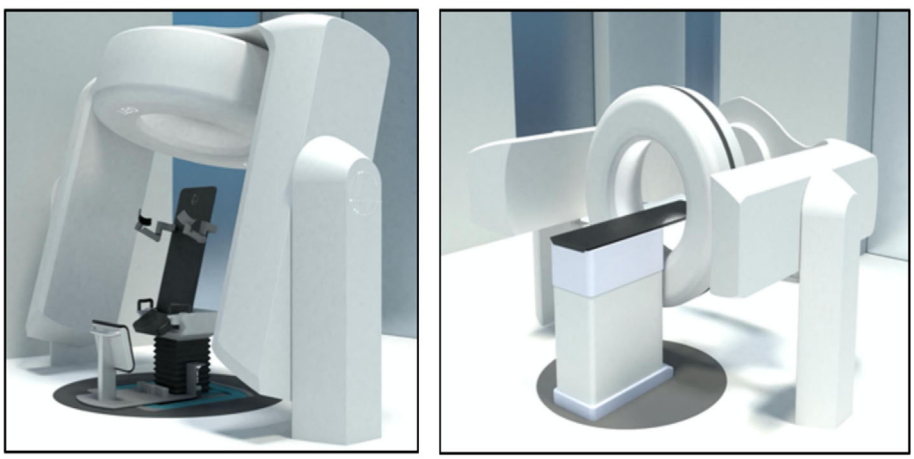

FIGURE 3 | The left panel shows an upright Dual Energy CT scanner together with the upright patient positioner for upright scanning and treatments that is under development. The right panels show the CT scanner integrated with a CT gurney for CT scanning in the lying down position (courtesy LEO Cancer Care Ltd).

asphyxiation, providing a proper support system for such patients is developed. It also depends on the airway management as well as the depth of anesthesia. Treating quadriplegic and paraplegic patients in the upright position should also be easy since it is standard practice to support such patients in upright positions for many clinical reasons.

Technical Benefits of Upright Treatments

Upright treatments may offer several technical benefits. Rotating a 100 to 250 Kg patient isocentrically is mechanically easier than moving a more than 50T gantry around the patient with the required precision. This of course means that one needs to focus on patient comfort and proper immobilization of the patient in the upright position. In a recent special edition of the British Journal of radiology (BJR), one of us (96) listed eight beam delivery specific technologies that proton therapy systems must be able to offer within the next ten years. Most of these technologies seems to be more attainable in a fixed beam configuration for mainly two reasons. Firstly, fixed beam arrangements provide much more free space around the isocenter compared to "closed" gantries, and the treatment envelope around the patient is much more accessible and predictable. The difference is lower with "open" gantries with partial isocentric rotation. Furthermore, the beam delivery nozzle could be retracted further to provide the required space to implement some of these technologies, e.g., on line axial CT at isocenter and proton imaging. Second, the fixed beam systems may be much less expensive, reducing the total project cost and so the barriers to their purchase.

Cone beam CT (CBCT) images of the patient could easily be obtained while rotating the patient precisely in a stationary x-ray beam measuring the transmission x-rays with stationary x-ray detectors. Proton radiography (P-Rad) and proton computed tomography (PCT) images can be obtained in a similar manner providing the proton beam energy is sufficient for the protons to traverse the specific anatomical region. Upright treatments require only fixed beam lines which will allow for moving the scanning magnet further away from the isocenter. This in turn will allow for faster beam scanning since less scanning power is required. The benefits of faster scanning are important in terms of organ motion, FLASH radiation therapy and PAT. Other benefits of moving the scanning magnet further away from the isocenter are a larger source to axis distance (SAD) and the ability to scan the beam to larger field sizes. If a fixed beam delivery nozzle is equipped with a collapsible vacuum section or a helium bag smaller spot sizes can be achieved. This will also allow for variable spots sizes since the beam control does not have to accommodate variations in the beam optics as a result of changes in the gantry angle. Implementing fast trimmer apertures would also be much easier since the gravitational forces on the trimmer components will be constant (96).

The benefits of upright treatments in reducing the cost of a proton therapy system seem self-evident. Fixed beams are cheaper to construct and much easier to maintain as they are comprised of few and mostly static components. Installing and commissioning fixed beam systems will also be faster which will result in significant project cost savings. The shielded volume for a fixed beam system is much smaller and the wall thicknesses can be reduced significantly over the bulk of the shielded volume since the primary beam will only be directed in one direction. This could allow for optimizing the treatment room layout resulting in significant cost reductions. The latter could also allow for improved treatment workflow and throughput efficiencies. The traditional clinical concerns around upright treatments could be outweighed by the potential benefits that upright treatments hold for many patients.

DISCUSSION AND CONCLUSIONS: THE LINK BETWEEN BIOLOGY AND MECHANICS

In spite of more than 50 years of application of protons, this is still a highly evolving branch of radiation therapy. It is synergic with the developments with photon and ion beams. A multidisciplinary and multicentric approach is necessary to advance in this field, as it is true for all the tools in the treatment of cancer.

In this work, we have reviewed aspects that can individually reduce some of the pitfalls of proton therapy. Even if they seem to be disconnected (biology and mechanics), some synergies or incompatibilities can be found between them based on the described process for each, as represented in **Figure 4**.

FLASH can reduce the damage to normal tissues under specific conditions including beam parameters (minimal dose, maximal time) and oxygenation. Different studies have shown that with the present devices it is difficult to achieve the technical conditions for FLASH (85) and even more in large volumes. In the short and mid-term it can be foreseen that FLASH will apply to treating smaller volumes close to or embedded in the target volume if the differential effect of FLASH, between tumoral and healthy cells, is not only related to oxygen, but also to cellular factors. While this scenario is the usual one in radiation therapy, specific situations should also be studied. One example could be re-irradiation in or close to critical organs, or in vascular areas, to cumulated doses of 110 to 140 Gy, where the risk of necrosis or injuries to vessels are high and with very different levels of oxygenation.

Minibeams could be applied in synergy with FLASH in order to avoid any movement, and optimized for large paths through healthy tissue and applied to small target volumes differentiating the benefit between tumoral and normal cells or, more specifically, organs [eg hippocampus, (14)].

In contrast, proton arc therapy is in principle not easily compatible with minibeams, and can also affect some mechanisms on the immune response to radiation therapy if large volumes are irradiated again with low doses.

It is important to conclude mentioning that even among the co-authors of this review, where we also include personal work of some of them, there is not a unanimous agreement on the potential effect of the proposed scenarios, interpretations and tools. It is not yet known how many logistical and flexible advantages will be lost without a gantry, how much the pattern of dose distribution with rotational techniques will change the

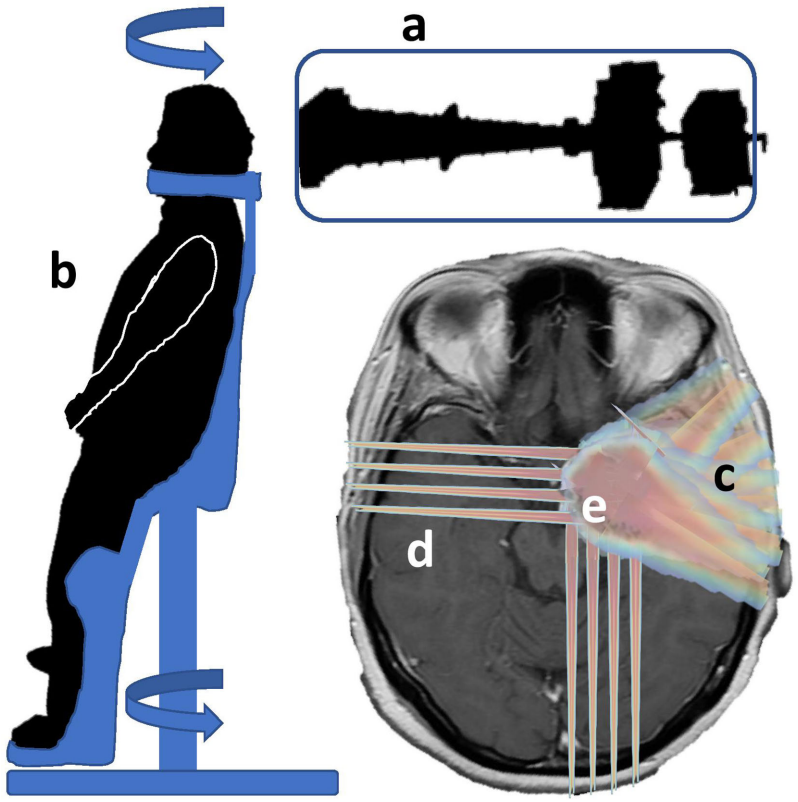

FIGURE 4 | Combination of biological and technical aspects to reduce pitfalls in proton therapy: the combination of a fixed line "a" with a rotational patient positioner "b" could reduce the investment cost. It is compatible with arc therapy, maybe for partial arcs "c" in order to avoid a large spread of low doses and keeping the original rationale for protons. Mini-beams could be applied for beam incidences traversing a large amount of healthy tissue "d" and, synergically with FLASH, be applied in specific regions "e" of the tumor and healthy tissues, protecting specific regions or organs.

response of tissues, how really mini-beams should be delivered to keep the tumor control with inhomogeneous dose, and where, why and how FLASH will be applied efficiently.

If we succeed, with one of these approaches, to reduce at least one or some of the pitfalls of proton therapy in its present status (such as cost, complexity, downtime, uncertainties and complications), it will be even easier to find a better place of protons as a therapy of choice for treating cancer with radiation therapy, in a multidisciplinary approach, for a wider population.

AUTHOR CONTRIBUTIONS

AM: manuscript design and figures. JV: dosimetry section. DS-P: arc therapy. JU, SE, VS-T, LF: time signal data. PB, AG-U: minibeams and FLASH. NG, GG: physics review. JC, JP: medical physics review. LM, AI, CA, RM: clinical review. MC: anesthesia review. NS: gantryless section. All: literature review. All authors contributed to the article and approved the submitted version.

FUNDING

This work was partially funded by Comunidad de Madrid (Project B2017/BMD-3888 PRONTO-CM "Proton therapy and nuclear techniques for oncology" and project 2017-T1/BMD-5468), Spanish Government (RTI2018-098868-B-I00, RTC-2015-3772-1, PID2019-104991RB-I00), European Regional Funds, EU Marie Sklodowska-Curie program (grant agreement 793576-CAPPERAM) is acknowledged. This is a contribution for the Moncloa Campus of International Excellence, "Grupo de Física Nuclear-UCM," Ref. 910059.

REFERENCES

1. Hughes JR, Parsons JL. FLASH Radiotherapy: Current Knowledge and Future Insights Using Proton-Beam Therapy. *Int J Mol Sci* (2020) 21:6492.
2. Mazal A, Prezado Y, Ares C, de Marzi L, Patriarca A, Miralbell R, et al. FLASH and minibeams in radiation therapy: the effect of microstructures on time and space and their potential application to protontherapy. *Br J Radiol* (2020) 93 (1107):20190807.
3. Favaudon V, Caplier L, Monceau V, Pouzoulet F, Sayarath M, Fouillade C, et al. Ultrahigh dose-rate FLASH irradiation increases the differential response between normal and tumor tissue in mice. *Sci Transl Med* (2014) 6(245):245ra93. doi: 10.1126/scitranslmed.3008973

4. Fouillade C, Curras-Alonso S, Giuranno L, Quelennec E, Heinrich S, Bonnet-Boissinot S, et al. FLASH irradiation spares lung progenitor cells and limits the incidence of radio-induced senescence. *Clin Cancer Res* (2020) 26(6):1497–50610.1158/1078-0432.CCR-19-1440
5. Vozenin M, De Fornel P, Petersson K, Favaudon V, Jaccard M, Germond J-F, et al. The Advantage of FLASH Radiotherapy Confirmed in Mini-pig and Cat-cancer Patients. *Clin Cancer Res* (2019) 25(1):35–42.
6. Bourhis J, Sozzi W, Jorge P, Gaide O, Bailat C, Duclos F, et al. Treatment of a first patient with FLASH-radiotherapy. *Radiother Oncol [Internet]* (2019) 139:18–22. doi: 10.1016/j.radonc.2019.06.019
7. Hendry J, Moore J, Hodgson B, Keene J. The Constant Low Oxygen Concentration in All the Target Cells for Mouse Tail Radionecrosis. *Radiat Res* (1982) 92(1):172.
8. Hendry J. Taking Care with FLASH Radiation Therapy. *Int J Radiat Oncol Biol Phys [Internet]* (2020) 107(2):239–42. doi: 10.1016/j.ijrobp.2020.01.029
9. Montay-Gruel P, Acharya M, Petersson K, Alikhani L, Yakkala C, Allen B, et al. Long-term neurocognitive benefits of FLASH radiotherapy driven by reduced reactive oxygen species. *Proc Natl Acad Sci U S A* (2019) 166 (22):10943–51.
10. Diffenderfer ES, Verginadis II, Kim MM, Shoniyozov K, Velalopoulou A, Goia D, et al. Design, Implementation, and in Vivo Validation of a Novel Proton FLASH Radiation Therapy System. *Int J Radiat Oncol* (2020) 106(2):440–8.
11. Schüler E, Trovati S, King G, Lartey F, Rafat M, Villegas M, et al. Experimental Platform for Ultra-high Dose Rate FLASH Irradiation of Small Animals Using a Clinical Linear Accelerator. *Int J Radiat Oncol Biol Phys* (2017) 97(1):195–203. doi: 10.1016/j.ijrobp.2016.09.018
12. Abel E, Girdhani S, Jackson I, Eley J, Katsis A, Marshall A, et al. Characterization of Radiation-Induced Lung Fibrosis and Mode of Cell Death Using Single and Multi-Pulsed Proton Flash Irradiation. *Int J Radiat Oncol* (2019) 105(1):E652–3. doi: 10.1016/j.ijrobp.2019.06.1033
13. Montay-Gruel P, Petersson K, Jaccard M, Boivin G, Germond J, Petit B, et al. Irradiation in a flash: Unique sparing of memory in mice after whole brain irradiation with dose rates above 100 Gy/s. *Radiother Oncol* (2017) 124 (3):365–9. doi: 10.1016/j.radonc.2017.05.003
14. Simmons D, Lartey F, Schüler E, Rafat M, King G, Kim A, et al. Reduced cognitive deficits after FLASH irradiation of whole mouse brain are associated with less hippocampal dendritic spine loss and neuroinflammation. *Radiother Oncol* (2019) 139:4–10. doi: 10.1016/j.radonc.2019.06.006
15. Montay-Gruel P, Bouchet A, Jaccard M, Patin D, Serduc R, Aim W, et al. X-rays can trigger the FLASH effect: Ultra-high dose-rate synchrotron light source prevents normal brain injury after whole brain irradiation in mice. *Radiother Oncol* (2018) 129(3):582–8. doi: 10.1016/j.radonc.2018.08.016
16. Fernet M, Ponette V, Deniaud-Alexandre E, Menissier-De Murcia J, De Murcia G, Giocanti N, et al. Poly(ADP-ribose) polymerase, a major determinant of early cell response to ionizing radiation. *Int J Radiat Biol* (2000) 76(12):1621–9.
17. Ponette V, Le Pechoux C, Deniaud-Alexandre E, Fernet M, Giocanti N, Tourbez H, et al. Hyperfast, early cell response to ionizing radiation. *Int J Radiat Biol* (2000) 76(9):1233–43.
18. de Kruijff RM. FLASH radiotherapy: ultra-high dose rates to spare healthy tissue. *Int J Radiat Biol* (2020) 96(4):419–23.
19. Wilson JD, Hammond EM, Higgins GS, Petersson K. Ultra-High Dose Rate (FLASH) Radiotherapy: Silver Bullet or Fool's Gold? *Front Oncol* (2020) 9 (1563):1563. doi: 10.3389/fonc.2019.01563.
20. Adrian G, Konradsson E, Lempart M, Bäck S, Ceberg C, Petersson K. The FLASH effect depends on oxygen concentration. *Br J Radiol* (2020) 93 (1106):20190702.
21. Spitz DR, Buettner GR, Petronek MS, St-Aubin JJ, Flynn RT, Waldron TJ, et al. An integrated physico-chemical approach for explaining the differential impact of FLASH versus conventional dose rate irradiation on cancer and normal tissue responses. *Radiother Oncol* (2019) xxxx:1–5. doi: 10.1016/j.radonc.2019.03.028
22. Rama N, Saha T, Shukla S, Goda C, Milewski D, Mascia AE, et al. Improved Tumor Control Through T-cell Infiltration Modulated by Ultra-High Dose Rate Proton FLASH Using a Clinical Pencil Beam Scanning Proton System. *Int J Radiat Oncol* (2019) 105(1, Supplement):S164–5.
23. Girdhani S, Abel E, Katsis A, Rodriquez A, Senapati S, KuVillanueva A, et al. Abstract LB-280: FLASH: A novel paradigm changing tumor irradiation platform that enhances therapeutic ratio by reducing normal tissue toxicity and activating immune pathways. *Cancer Res* (2019) 79(13 Supplement):LB-280-LB-280.
24. Wardman P. Radiotherapy Using High-Intensity Pulsed Radiation Beams (FLASH): A Radiation-Chemical Perspective. *Radiat Res* (2020). doi: 10.1667/RADE-19-00016
25. Favaudon V. Flash radiotheray at very high dose-rate: A brief account of the current situation. *Cancer/Radiotherapie* (2019) 23(6–7):674–6. doi: 10.1016/j.canrad.2019.07.127
26. Labarbe R, Hotoiu L, Barbier J, Favaudon V. A physicochemical model of reaction kinetics supports peroxyl radical recombination as the main determinant of the FLASH effect. *Radiother Oncol* (2020)153:303–10. doi: 10.1016/j.radonc.2020.06.001
27. Alaghband Y, Cheeks SN, Allen BD, Montay-Gruel P, Doan NL, Petit B, et al. Neuroprotection of radiosensitive juvenile mice by ultra-high dose rate flash irradiation. *Cancers (Basel)* (2020) 12(6):1–21.
28. Liberson F. The Value of a Multi-perforated Screen in Deep X-ray Therapy. *Radiology* (1933) 20(3):186–95.
29. Reiff J, Saiful Huq M, Mohiuddin M, Suntharalingam N. Dosimetric properties of megavoltage grid therapy. *Int J Radiat Oncol* (1995) 33 (4):937–42.
30. Deman P, Vautrin M, Edouard M, Stupar V, Bobyk L, Farion R, et al. Monochromatic minibeams radiotherapy: From healthy tissue-sparing effect studies toward first experimental glioma bearing rats therapy. *Int J Radiat Oncol Biol Phys* (2012) 82(4):E693–700.
31. Prezado Y, Dos Santos M, Gonzalez W, Jouvion G, Guardiola C, Heinrich S, et al. Transfer of Minibeam Radiation Therapy into a cost-effective equipment for radiobiological studies: a proof of concept. *Sci Rep [Internet]* (2017) 7 (1):17295. doi: 10.1038/s41598-017-17543-3
32. Prezado Y, Jouvion G, Hardy D, Patriarca A, Nauraye C, Bergs J, et al. Proton minibeam radiation therapy spares normal rat brain: Long-Term Clinical, Radiological and Histopathological Analysis. *Sci Rep* (2017) 7(1):1–7.
33. Guardiola C, Prezado Y, Roulin C, Bergs JWJ. Effect of X-ray minibeam radiation therapy on clonogenic survival of glioma cells. *Clin Transl Radiat Oncol* (2018) 13:7–13.
34. Prezado Y, Jouvion G, Patriarca A, Nauraye C, Guardiola C, Juchaux M, et al. Proton minibeam radiation therapy widens the therapeutic index for high-grade gliomas. *Sci Rep* (2018) 8(1):1–10.
35. Dos Santos M, Delorme R, Salmon R, Prezado Y. Minibeam radiation therapy: A micro- and nano-dosimetry Monte Carlo study. *Med Phys* (2020) 47 (3):1379–90.
36. Serduc R, Vérant P, Vial J-C, Farion R, Rocas L, Rémy C, et al. In vivo two-photon microscopy study of short-term effects of microbeam irradiation on normal mouse brain microvasculature. *Int J Radiat Oncol* (2006) 64(5):1519–27.
37. Bouchet A, Serduc R, Laissue J, Djonov V. Effects of microbeam radiation therapy on normal and tumoral blood vessels. *Phys Medica* (2015) 31(6):634–41.
38. Sabatasso S, Laissue JA, Hlushchuk R, Graber W, Bravin A, Bräuer-Krisch E, et al. Microbeam Radiation-Induced Tissue Damage Depends on the Stage of Vascular Maturation. *Int J Radiat Oncol* (2011) 80(5):1522–32.
39. Bouchet A, Lemasson B, Le Duc G, Maisin C, Bräuer-Krisch E, Siegbahn E, et al. Preferential effect of synchrotron microbeam radiation therapy on intracerebral 9l gliosarcoma vascular networks. *Int J Radiat Oncol Biol Phys* (2010) 78(5):1503–12.
40. Bouchet A, Lemasson B, Christen T, Potez M, Rome C, Coquery N, et al. Synchrotron microbeam radiation therapy induces hypoxia in intracerebral gliosarcoma but not in the normal brain. *Radiother Oncol* (2013) 108 (1):143–8.
41. Griffin RJ, Koonce NA, Dings RPM, Siegel E, Moros EG, Bruer-Krisch E, et al. Microbeam radiation therapy alters vascular architecture and tumor oxygenation and is enhanced by a galectin-1 targeted anti-angiogenic peptide. *Radiat Res* (2012) 177(6):804–12.
42. Bouchet A, Sakakini N, El Atifi M, Le Clec'h C, Brauer E, Moisan A, et al. Early Gene Expression Analysis in 9L Orthotopic Tumor-Bearing Rats Identifies Immune Modulation in Molecular Response to Synchrotron Microbeam Radiation Therapy. *PLoS One* (2014) 8(12):e81874.
43. Sprung CN, Yang Y, Forrester HB, Li J, Zaitseva M, Cann L, et al. Genome-Wide Transcription Responses to Synchrotron Microbeam Radiotherapy. *Radiat Res* (2012) 178(4):249–59.

44. Esplen NM, Mendonca MS, Bazalova-Carter M. Physics and biology of ultrahigh dose-rate (FLASH) radiotherapy: a topical review. *Phys Med Biol* (2020). doi: 10.1088/1361-6560/abaa28
45. Petersson K, Jaccard M, Germond J-F, Buchillier T, Bochud F, Bourhis J, et al. High dose-per-pulse electron beam dosimetry – A model to correct for the ion recombination in the Advanced Markus ionization chamber. *Med Phys* (2017) 44:1157–67.
46. Busold S, Heese J. Proton beam diagnostics for ultra-high dose rate irradiations. *Int J Part Ther* (2020) 6(4):116 PTC58–0621.
47. Buonanno M, Grilj V, Brenner D. Biological effects in normal cells exposed to FLASH dose rate protons. *Radiother Oncol* (2019) 139:51–5. doi: 10.1016/j.radonc.2019.02.009
48. Jaccard M, Durán M, Petersson K, Germond J-F, Liger P, Vozenin M, et al. High dose-per-pulse electron beam dosimetry: Commissioning of the Oriatron eRT6 prototype linear accelerator for preclinical use. *Med Phys* (2018) Feb45(2):863–74. doi: 10.1002/mp.12713
49. Ashraf MR, Rahman M, Zhang R, Williams BB, Gladstone DJ, Pogue BW, et al. Dosimetry for FLASH Radiotherapy: A Review of Tools and the Role of Radioluminescence and Cherenkov Emission. *Front Phys* (2020) 8(August):1–20.
50. Oraiqat I, Zhang W, Litzenberg D, Lam K, Ba Sunbul N, Moran J, et al. An ionizing radiation acoustic imaging (iRAI) technique for real-time dosimetric measurements for FLASH radiotherapy. *Med Phys* (2020) 47:5090–101. doi: 10.1002/mp.14358
51. Peucelle C, Nauraye C, Patriarca A, Hierso E, Fournier-Bidoz N, Martínez-Rovira I, et al. Proton minibeam radiation therapy: Experimental dosimetry evaluation. *Med Phys* (2015) 42(12):7108–13.
52. De Marzi L, Patriarca A, Nauraye C, Hierso E, Dendale R, Guardiola C, et al. Implementation of planar proton minibeam radiation therapy using a pencil beam scanning system: A proof of concept study. *Med Phys* (2018) 45 (11):5305–16.
53. Meyer J, Eley J, Schmid TE, Combs S, Dendale R, Prezado Y. Spatially fractionated proton minibeams. *Br J Radiol* (2019) 92(1095):20180466. doi: 10.1259/bjr.20180466
54. Farr JB, Moskvin V, Lukose RC, Tuomanen S, Tsiamas P, Yao W. Development, commissioning, and evaluation of a new intensity modulated minibeam proton therapy system. *Med Phys* (2018) 45(9):4227–37.
55. Martínez-Rovira I, González W, Brons S, Prezado Y. Carbon and oxygen minibeam radiation therapy: An experimental dosimetric evaluation: An experimental dosimetric evaluation. *Med Phys* (2017) 44(8):4223–9. doi: 10.1002/mp.12383
56. Annabell N, Yagi N, Umetani K, Wong C, Geso M. Evaluating the peak-to-valley dose ratio of synchrotron microbeams using PRESAGE fluorescence. *J Synchrotron Radiat* (2012) 19(3):332–9.
57. Sandison GA, Papiez E, Block C, Morphis J. Phantom assessment of lung dose from proton arc therapy. *Int J Radiat Oncol Biol Phys* (1997) 38(4):891–7. doi: 10.1016/s0360-3016(97)00059-x
58. Flynn RT, Barbee DL, Mackie TR, Jeraj R. Comparison of intensity modulated x-ray therapy and intensity modulated proton therapy for selective subvolume boosting: A phantom study. *Phys Med Biol* (2007) 52(20):6073–91. doi: 10.1088/0031-9155/52/20/001
59. Rechner LA, Howell RM, Zhang R, Etzel C, Lee AK, Newhauser WD. Risk of radiogenic second cancers following volumetric modulated arc therapy and proton arc therapy for prostate cancer. *Phys Med Biol* (2012) 57(21):7117–32. doi: 10.1088/0031-9155/57/21/7117
60. Hecht A. Improved Dose Characteristics From Proton Arc Therapy. *Med Phys* (2009) 36(6 Part 10):2551-2551 SU-FF-T-136.
61. Seco J, Gu G, Marcelos T, Kooy H, Willers H. Proton arc reduces range uncertainty effects and improves conformality compared with photon volumetric modulated arc therapy in stereotactic body radiation therapy for non-small cell lung cancer. *Int J Radiat Oncol Biol Phys* (2013) 87(1):188–94. doi: 10.1016/j.ijrobp.2013.04.048
62. Rah JE, Kim GY, Oh DH, Kim TH, Kim JW, Kim DY, et al. A treatment planning study of proton arc therapy for para-aortic lymph node tumors: Dosimetric evaluation of conventional proton therapy, proton arc therapy, and intensity modulated radiotherapy. *Radiat Oncol* (2016) 11(1):1–10. doi: 10.1186/s13014-016-0717-4
63. Sengbusch E, Pérez-Andújar A, DeLuca PM, Mackie TR. Maximum proton kinetic energy and patient-generated neutron fluence considerations in proton beam arc delivery radiation therapy. *Med Phys* (2009) 36 (2):364–72.
64. Sanchez Parcerisa D, Ainsley C, Carabe A. Fast Range Switching of Passively Scattered Proton Beams Using a Modulation Wheel and Dynamic Beam Current Modulation. *Int J Radiat Oncol* (2013) 87(2):S742. doi: 10.1016/j.ijrobp.2013.06.1966
65. Sánchez-Parcerisa D, Kondrla M, Shaindlin A, Carabe A. FoCa: A modular treatment planning system for proton radiotherapy with research and educational purposes. *Phys Med Biol* (2014) 59(23):7341–60.
66. Carabe-Fernandez A, Kirk M, Sanchez-Parcerisa D, Fager M, Burgdorf B, Stowe M, et al. Proton Modulated Arc Therapy Using Scanned Pencil Beams. *Med Phys* (2015) 42(6 Part22):3483–3.
67. Sanchez-Parcerisa D, Kirk M, Fager M, Burgdorf B, Stowe M, Solberg T, et al. Range optimization for mono- and bi-energetic proton modulated arc therapy with pencil beam scanning. *Phys Med Biol* (2016) 61(21):N565–74.
68. Bertolet A, Carabe A. Proton monoenergetic arc therapy (PMAT) to enhance LETd within the target. *Phys Med Biol* (2020) 65(16):165006.
69. Sánchez-Parcerisa D, Pourbaix JC, Ainsley CG, Dolney D, Carabe A. Fast range switching of passively scattered proton beams using a modulation wheel and dynamic beam current modulation. *Phys Med Biol* (2014) 59(7):N19–26. doi: 10.1088/0031-9155/59/7/N19
70. Ding X, Li X, Zhang JM, Kabolizadeh P, Stevens C, Yan D. Spot-Scanning Proton Arc (SPArc) Therapy: The First Robust and Delivery-Efficient Spot-Scanning Proton Arc Therapy. *Int J Radiat Oncol Biol Phys* (2016) 96 (5):1107–16. doi: 10.1016/j.ijrobp.2016.08.049
71. Ding X, Li X, Qin A, Zhou J, Yan D, Stevens C, et al. Have we reached proton beam therapy dosimetric limitations?–A novel robust, delivery-efficient and continuous spot-scanning proton arc (SPArc) therapy is to improve the dosimetric outcome in treating prostate cancer. *Acta Oncol (Madr)* (2018) 57(3):435–7.
72. Li X, Kabolizadeh P, Yan D, Qin A, Zhou J, Hong Y, et al. Improve dosimetric outcome in stage III non-small-cell lung cancer treatment using spot-scanning proton arc (SPArc) therapy. *Radiat Oncol* (2018) 13(1):1–9.
73. Ding X, Zhou J, Li X, Blas K, Liu G, Wang Y, et al. Improving dosimetric outcome for hippocampus and cochlea sparing whole brain radiotherapy using spot-scanning proton arc therapy. *Acta Oncol (Madr) [Internet]* (2019) 58(4):483–90. doi: 10.1080/0284186X.2018.1555374
74. Liu G, Li X, Qin A, Zheng W, Yan D, Zhang S, et al. Improve the dosimetric outcome in bilateral head and neck cancer (HNC) treatment using spot-scanning proton arc (SPArc) therapy: A feasibility study. *Radiat Oncol* (2020) 15(1):1–11.
75. Chang S, Liu G, Zhao L, Dilworth J, Zheng W, Jawad S, et al. Feasibility study: Spot-scanning Proton Arc therapy (SPArc) for left-sided breast irradiation. *Radiat Oncol* (2020) 15:232. doi: 10.1186/s13014-020-01676-3
76. Delso N, Stutzer K, Kirk M, Huang S, Sanchez Parcerisa D, Lin L, et al. Proton Modulated Arc Therapy Using Mono-Energetic Beams for the Treatment of Left-Sided Breast Cancer. *Med Phys* (2017) 44(6):SU-H2-GePD-T-06.
77. Carabe-Fernandez A, Bertolet-Reina A, Karagounis I, Huynh K, Dale RG. Is there a role for arcing techniques in proton therapy? *Br J Radiol* (2020) 93 (1107):20190469.
78. Liu W, Frank SJ, Li X, Li Y, Park PC, Dong L, et al. Effectiveness of robust optimization in intensity-modulated proton therapy planning for head and neck cancers. *Med Phys* (2013) 40(5):051711. doi: 10.1118/1.4801899
79. Carabe A, Karagounis I, Huynh K, Bertolet A, François N, Kim MM, et al. Radiobiological effectiveness difference of proton arc beams versus conventional proton and photon beams. *Phys Med Biol* (2020) 65 (16):165002. doi: 10.1088/1361-6560/ab9370
80. Toussaint L, Indelicato DJ, Holgersen KS, Petersen JBB, Stokkevåg CH, Lassen-Ramshad Y, et al. Towards proton arc therapy: physical and biologically equivalent doses with increasing number of beams in pediatric brain irradiation. *Acta Oncol (Madr)* (2019) 58(10):1451–6. doi: 10.1080/0284186X.2019.1639823
81. Yi BY, D´Souza WD, Langner U. Techniques for particle beam therapy. U.S. Patent and Trademark Office. US patent 20200022248 (2018). WO/2018/165423; Int app PCT/US2018/021541.
82. Li X, Liu G, Janssens G, De Wilde O, Bossier V, Lerot X, et al. The first prototype of spot-scanning proton arc treatment delivery. *Radiother Oncol* (2019) 137:130–6. doi: 10.1016/j.radonc.2019.04.032
83. Liu G, Li X, Zhao L, Zheng W, Qin A, Zhang S, et al. A novel energy sequence optimization algorithm for efficient spot-scanning proton arc (SPArc)

treatment delivery. *Acta Oncol (Madr)* (2020) 0(0):1–8. doi: 10.1080/0284186X.2020.1765415
84. Gu W, Ruan D, Lyu Q, Zou W, Dong L, Sheng K. A novel energy layer optimization framework for spot-scanning proton arc therapy. *Med Phys* (2020) 47(5):2072–84.
85. van de Water S, Safai S, Schippers J, Weber D, Lomax A. Towards FLASH proton therapy: the impact of treatment planning and machine characteristics on achievable dose rates. *Acta Oncol (Madr)* (2019) 58(10):1463–9.
86. Bortfeld TR, Loeffler JS. Three ways to make proton therapy affordable. *Nature* (2017) 549(7673):451–3.
87. Bortfeld TR, de Viana MF, Yan S. The societal impact of ion beam therapy. *Zeitschrift fur medizinische Physik* (2020) S0939-3889(20)30066-0. doi: 10.1016/j.zemedi.2020.06.007
88. Jones DTL, Schreuder AN, Symons JE, Yudelev M. ELSEVIER. The NAC Particle Therapy Facilities. In: U Amaldi, B Larsson, editors. *Hadrontherapy in Oncology*. New York: Elsevier Science BV (1994). p. 307–28.
89. Anferov V, Ball M, Berg GP, Broderick B, Collins J, East G, et al. The Indiana University Midwest Proton Radiation Institute. *Proc IEEE Part Accel Conf* (2001) 1:645–7.
90. Stanton D. "Neutron Therapy Facility resumes treating patients". In: *FermilabToday*. Batavia, IL, USA: Fermi National Accelerator Laboratory. Office of Science. US dept of Energy (2006). Available at: https://www.fnal.gov/pub/today/archive/archive_200.
91. Shah AP, Strauss JB, Kirk MC, Chen SS, Kroc TK, Zusag TW. Upright 3D Treatment Planning Using a Vertical CT. *Med Dosim* (2009) 34(1):82–6.
92. Verhey LJ, Goitein M, McNulty P, Munzenrider JE, Suit HD. Precise positioning of patients for radiation therapy. *Int J Radiat Oncol Biol Phys* (1982) 8(2):289–94.
93. McCarroll RE, Beadle BM, Fullen D, Balter PA, Followill DS, Stingo FC, et al. Reproducibility of patient setup in the seated treatment position: A novel treatment chair design. *J Appl Clin Med Phys* (2017) 18(1):223–9.
94. Yang J, Chu D, Dong L, Court LE. Advantages of simulating thoracic cancer patients in an upright position. *Pract Radiat Oncol* (2014) 4(1):e53–8. doi: 10.1016/j.prro.2013.04.005
95. Ferlay J, Colombet M, Soerjomataram I, Mathers C, Parkin DM, Piñeros M, et al. Estimating the global cancer incidence and mortality in 2018: GLOBOCAN sources and methods. *Int J Cancer* (2019) 144(8):1941–53.
96. Schreuder AN, Shamblin J. Proton therapy delivery: what is needed in the next ten years? *Br J Radiol* (2020) 93(1107):20190359.

Conflict of Interest: NS is the President of proton therapy for Leo Cancer Care, Ltd.

The remaining authors declare that the research was conducted in the absence of any commercial or financial relationships that could be construed as a potential conflict of interest.

Copyright © 2021 Mazal, Vera Sanchez, Sanchez-Parcerisa, Udias, España, Sanchez-Tembleque, Fraile, Bragado, Gutierrez-Uzquiza, Gordillo, Garcia, Castro Novais, Perez Moreno, Mayorga Ortiz, Ilundain Idoate, Cremades Sendino, Ares, Miralbell and Schreuder. This is an open-access article distributed under the terms of the Creative Commons Attribution License (CC BY). The use, distribution or reproduction in other forums is permitted, provided the original author(s) and the copyright owner(s) are credited and that the original publication in this journal is cited, in accordance with accepted academic practice. No use, distribution or reproduction is permitted which does not comply with these terms.

frontiers in Oncology

ORIGINAL RESEARCH
published: 02 February 2021
doi: 10.3389/fonc.2020.611514

A New Proton Therapy Solution Provides Superior Cardiac Sparing Compared With Photon Therapy in Whole Lung Irradiation for Pediatric Tumor Patients

Xue Sha[1†], Jinghao Duan[1†], Xiutong Lin[1], Jian Zhu[1,2], Ruohui Zhang[3], Tao Sun[1], Hui Wang[4], Xiangjuan Meng[1] and Yong Yin[1]*

[1] Department of Radiation Oncology, Shandong Cancer Hospital and Institute, Shandong First Medical University and Shandong Academy of Medical Sciences, Jinan, China, [2] Shandong Provincial Key Laboratory of Digital Medicine and Computer-Assisted Surgery, Qingdao, China, [3] Department of Radiation Oncology, The Fourth Hospital of Hebei Medical University, Shijiazhuang, China, [4] Department of Radiation Oncology, Qingdao Central Hospital, Qingdao, China

OPEN ACCESS

Edited by:
Beate Timmermann, Essen University Hospital, Germany

Reviewed by:
Yibao Zhang, Peking University Cancer Hospital, China
James Chow, University of Toronto, Canada

***Correspondence:**
Yong Yin
yinyongsd@126.com

[†]These authors have contributed equally to this work

Specialty section:
This article was submitted to Radiation Oncology, a section of the journal Frontiers in Oncology

Received: *29 September 2020*
Accepted: *14 December 2020*
Published: *02 February 2021*

Citation:
Sha X, Duan J, Lin X, Zhu J, Zhang R, Sun T, Wang H, Meng X and Yin Y (2021) A New Proton Therapy Solution Provides Superior Cardiac Sparing Compared With Photon Therapy in Whole Lung Irradiation for Pediatric Tumor Patients. Front. Oncol. 10:611514. doi: 10.3389/fonc.2020.611514

Objective: Whole lung irradiation (WLI) plays a crucial role in local control in pediatric patients with lung metastases and improves patient survival. The intention of this research was to explore the advantage of cardiac sparing between photons and protons during WLI. We also propose a new solution for cardiac sparing with proton techniques.

Methods: Eleven patients with pediatric tumors and pulmonary metastasis treated with 12 Gy WLI (all received volumetric-modulated arc therapy (VMAT)) in our institute between 2010 and 2019 were retrospectively selected. Each patient was replanned with intensity-modulated radiation therapy (IMRT), helical tomotherapy (HT), and two intensity-modulated proton radiotherapy (IMPT) plans (IMPT-1 and IMPT-2). IMPT-1 considered the whole lung as the planning target volume (PTV), utilizing the anteroposterior technique (0/180°). IMPT-2 was a new proton solution that we proposed in this research. This approach considered the unilateral lung as the PTV, and 3 ipsilateral fields were designed for each lung. Then, IMPT-2 was generated by summing two unilateral lung plans. The primary objective was to obtain adequate coverage (95% of the prescription dose to the PTV) while maximally sparing the dose to the heart. The PTV coverage, conformity index (CI), homogeneity index (HI), and dose–volume statistics of the heart and substructures were assessed by means of the averages of each comparison parameter.

Results: All treatment techniques achieved the target volume coverage required by clinical practice. HT yielded the best coverage and homogeneity for the target structure compared with other techniques. The CI from IMRT was excellent. For photon radiation therapy, the HT plan afforded superior dose sparing for the V_5, V_6, V_7, V_8, and D_{mean} of the heart and D_{mean} of the right ventricle (RV). IMRT displayed the most notable dose reductions in the V_9, V_{10}, V_{11}, and V_{12} of the heart and D_{mean} of the right atrium (RA). The VMAT plan was the least effective on the heart and substructures. However,

compared with photon radiation therapy, IMPT-1 did not show an advantage for heart protection. Interestingly, IMPT-2 provided significant superiority in cardiac sparing, including maximum dose sparing for the V_5, V_6, V_7, V_8, V_9 and D_{mean} of the heart and D_{mean} of the RA, RV, left atrium (LA) and left ventricle (LV) compared to all other techniques.

Conclusions: Considering the complex anatomical relation between target volumes and organs at risk (OARs), IMPT can provide a dose advantage for organs located outside of the target area rather than within or surrounding the area. It is hoped that advances in proton therapy (PT) plan design will lead to further improvements in radiotherapy approaches and provide the best treatment choice for individual patients.

Keywords: proton radiotherapy, cardiac sparing, whole lung irradiation, pediatric tumor, photon radiotherapy

INTRODUCTION

Malignant tumors are the second leading cause of death in children, with over 300,000 new cases diagnosed annually (1, 2). The lung is the most common site of metastasis, with approximately 20 to 25% of patients with Wilms tumor or Ewing sarcoma showing metastatic lesions on chest radiography at diagnosis (3). Whole lung irradiation (WLI) plays a crucial role in local control in patients with lung metastases, those who had incomplete resection, and those with an unfavorable histology, advanced stage, and high-risk chromosomal aberrations (4, 5). Published studies have indicated that WLI is an essential component in the current multimodality treatment and can achieve a survival rate of 90% (6–8).

With the increased proportion of survivors, the risk of late toxicities resulting from a combination of radiotherapy and toxic cardiac chemotherapy is becoming increasingly concerning. Advances in imaging science and radiotherapy technology have allowed precise tumor determination and delineation and high conformity to the target volume. However, due to the non-targeted radiation dose, the surrounding normal tissue is still at risk. Cardiac toxicity is a common delayed effect observed in pediatric patients after chemotherapy and WLI. Studies have revealed that in child survivors, WLI has led to a high prevalence of a variety of cardiac complications, including vascular heart disease, myocardial infarction, congestive heart failure (CHF) and pericardial disease (9). WLI has traditionally been combined with standard anterior/posterior field photon irradiation, resulting in poor heart-sparing potential. Therefore, to achieve a lower dose to the heart, new techniques, such as multiple field intensity-modulated radiation therapy (IMRT), volumetric-modulated arc therapy (VMAT), and helical tomotherapy (HT), are desirable. Although these techniques contribute to the reliable treatment delivery of the radiation dose to the diseased tissues, the crucial problem of overdose to the heart during treatment remains unsolved.

Proton therapy (PT), as a frontier radiotherapy technique, offers distinct physical properties that can contribute to an improvement in dose distribution with a subsequent reduction in the integral dose to the patient, supporting the potential value of proton beams in tumors close to the target volume. A series of studies have demonstrated that children with malignant tumors have good tolerance to proton beams, and this plan ensures good tumor control probability, prolonged survival, intelligence quotient protection and reduced risk of a secondary tumor (10). Consequently, we hope for an advantage of PT over photon therapy that will lead to improved indications for WLI. However, with the current proton treatment planning system (TPS), PT cannot provide an advantage for cardiac sparing in WLI. For this reason, we propose a new solution for cardiac sparing in proton techniques, and we expect this solution to reduce the exposure dose to the heart and diminish the complications associated with radiation-induced cardiac injury in pediatric patients receiving WLI. Our research may lead to improvements in the PT TPS and provides useful guidelines for selecting reasonable treatment techniques in WLI.

MATERIALS AND METHODS

Patient Eligibility

Eleven patients (median age, 3 years; range 2–17 years) with different histologies (five with Wilms tumor, three with rhabdomyosarcoma, two with Ewing sarcoma, and one with germ cell tumor) who received WLI in our institute between January 1, 2010 and December 31, 2019, were retrospectively selected. The retrospective analysis of the medical records was approved by the Institutional Review Board of Shandong Cancer Hospital. The characteristics of the patients are displayed in **Table 1**.

Target Volume and Organs at Risk Definitions

Patients were placed in a customized site-specific immobilization device for the treatment position, and computed tomography (CT) simulation provided images at 3 mm for both lungs. For patients who could not cooperate with positioning, chloral hydrate was injected to produce a sedative hypnotic effect, ensuring a precise posture. The target volume, clinical target volume (CTV), was defined as total lung extension from the apex

TABLE 1 | Patient characteristics.

Patient	Diagnosis	Primary site	Age at diagnosis/Sex	Stage	Dose (Gy)/fractions
1	Ewing sarcoma	Astragalus	11/Female	IV	12/10
2	Wilms tumor	Left kidney	2/Female	IV	12/10
3	Wilms tumor	Right kidney	3/Female	IV	12/10
4	Wilms tumor	Left kidney	7/Male	IV	12/10
5	Rhabdomyosarcoma	Arm	17/Male	IV	12/10
6	Rhabdomyosarcoma	Left kidney	3/Female	IV	12/10
7	Rhabdomyosarcoma	Abdomen	3/Male	IV	12/10
8	Wilms tumor	Right kidney	3/Male	IV	12/10
9	Wilms tumor	Right kidney	13/Male	IV	12/10
10	Germ cell tumor	Sacrococcyx	3/Female	IV	12/10
11	Ewing sarcoma	Astragalus	3/Female	IV	12/10

to the diaphragm using the acquisition window/level setting. The planning target volume (PTV) was delineated by expanding the 0.3 to 0.5 cm margin of the CTV. For inverse planning techniques, a heart-PTV structure that consisted of the volume overlap of the heart and the PTV was created to enhance the optimization process. OARs considered in the present study included the esophagus, liver, spinal cord, vertebral column, humerus, heart, right atrium (RA), right ventricle (RV), left atrium (LA) and left ventricle (LV) (contoured using the Radiation Therapy Oncology Group contouring atlas).

Treatment Planning

The prescribed dose was 12 Gy in all patients, and the daily fraction dose was 1.2 Gy. The primary objective was to obtain adequate coverage (95% of the prescription dose to the PTV) while maximally sparing the dose to the OARs, especially the heart and substructures. For each patient, five plans were created: IMRT, VMAT, HT, IMPT-1, and IMPT-2. All plans were generated by senior radiation physicists with more than ten years of experience designing radiotherapy plans. The beam arrangements are shown in **Figure 1**.

IMRT plans were performed with a Varian Trilogy linear accelerator using beam energies of 6 MV photons and beam angles of 0, 40, 80, 120, 160, 200, 240, 280 and 320° for cardiac sparing. The sliding window technique, by having the leaf pairs move across the field at a variable rate, was used to deliver the nine-field modulated plan on the Eclipse 13.6 TPS (Varian Medical Systems, Palo Alto, CA). The field sizes and weights of a series of beam segments were determined by iterative, automated optimization techniques. For the VMAT technique, two full arcs were delivered to 10 patients: a clockwise arc traveling from 181 to 179° and a counterclockwise arc traveling from 179 to 181°. The oldest patient with the largest lung volume required three full arcs. A collimator angle of 10° for the clockwise arc and 350° for the counterclockwise arc were used. HT plans were created with the Tomotherapy version 5.1.3 TPS using a HiArt unit (Accuray® Planning Station, Madison, WI, USA). In general, the parameters specified as part of the optimization process were the field width, pitch, and modulation factor. In the current research, a pitch of 0.287, a collimator width of 2.5 cm, and a modulation factor of 2.4 were selected.

Two IMPT plans were generated in the Varian Eclipse ProBeam proton system and used for multiple field optimization and selective robust optimization. IMPT-1 considered the whole lung as the PTV, utilizing the anteroposterior technique (0/180°). IMPT-2 included the sum of two IMPT plans that considered the unilateral lung as the PTV. For the left lung, the IMPT plan was designed with three fields, with gantry rotations of 40, 90, and 140°. For the right lung, the IMPT plan was designed with three felids, with gantry rotations of 220, 270, and 320°. For individual patients, the gantry rotation was adjusted to minimize the exposure to the heart as much as possible. The proton dose was determined using a relative biologic effectiveness (RBE) of 1.1 and is specified in cobalt gray equivalent (CGE) units (11). The non-linear universal proton optimizer (NUPO) algorithm was used to generate the plan, and the dose was calculated with the proton convolution superposition algorithm with a grid size of 0.25 cm. A positioning error of 3 mm and a range uncertainty of ±3% were taken into account during planning optimization.

Treatment Plan Analysis

Dose–volume data for the PTV and OARs obtained from dose-volume histograms (DVHs) were determined for each technique from the 11 scans. The following dosimetry parameters for the PTV were evaluated: target coverage, dose received by 2% of the target volume ($D_{2\%}$), dose received by 98% of the target volume ($D_{98\%}$), maximum dose (D_{max}), medial dose (D_{mean}), minimum dose (D_{min}), conformity index (CI), and homogeneity index (HI). The CI was calculated according to the following expression (12):

$$\mathrm{CI} = \frac{TV_{RI}}{TV} \times \frac{TV_{RI}}{V_{RI}}$$

where TV_{RI} is the target volume covered by the prescription isodose, TV is the target volume, and V_{RI} is the volume of the prescription isodose. The CI ranged from 0 to 1, where 1 indicated perfect overlap (identical structures). A value near 0 indicated the total absence of conformation, *i.e.*, the target volume was not irradiated.

$$\mathrm{HI} = \frac{D_{2\,\%} - D_{98\,\%}}{D_{prescription}}$$

where $D_{prescription}$ is the prescription dose of the target volume.

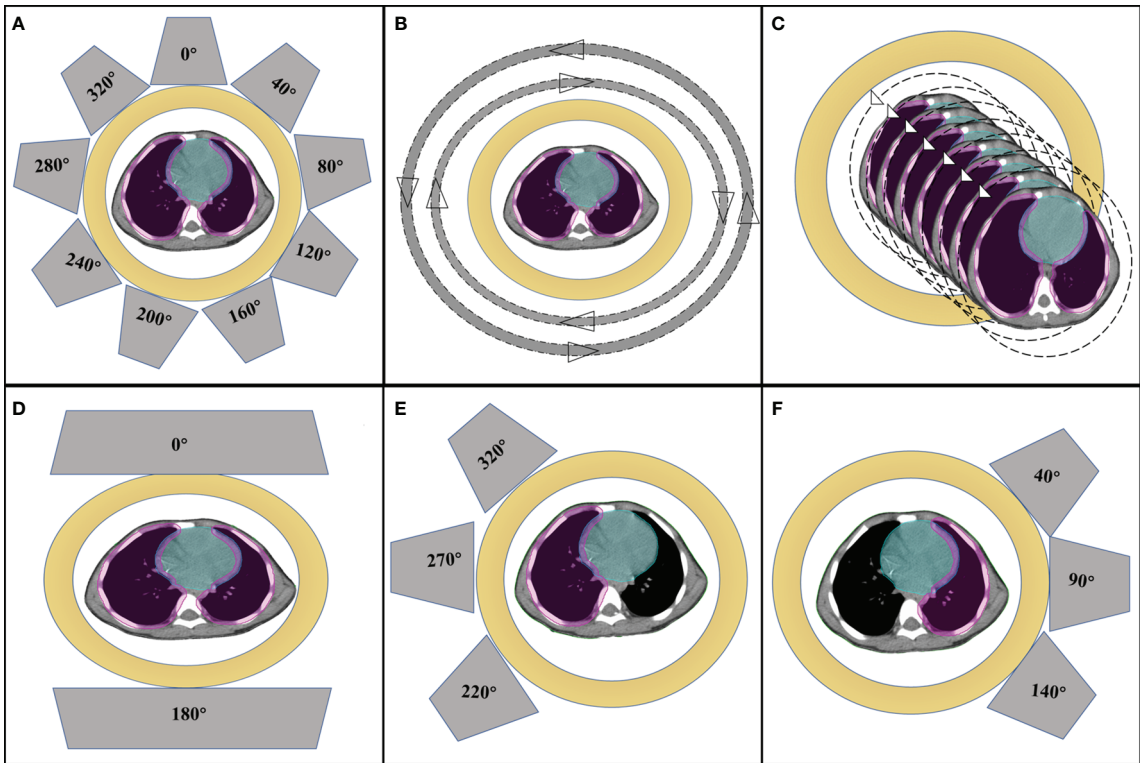

FIGURE 1 | Beam arrangements for **(A)** IMRT, **(B)** VMAT, **(C)** HT, **(D)** IMPT-1, **(E)** sum and **(F)** IMPT-2.

The HI ranged from 0 to 1, where 0 was the ideal value. A higher HI indicates poorer homogeneity.

The following dosimetric parameters were evaluated for the heart: V_5, V_6, V_7, V_8, V_9, V_{10}, V_{11}, and V_{12} (V_X represents the volume percentage receiving more than x Gy) and D_{mean}. Additional parameters analyzed included D_{mean} for the RA, RV, LA and LV. Additionally, to evaluate dose delivery efficiency, monitor units (MUs), control points (or segments) per fraction and beam on time were compared.

Statistical Analysis

The Wilcoxon matched-pairs signed-rank test was used to compare the dose differences between different radiotherapy techniques. Data analysis was performed with MATLAB software version R2018a (MathWorks, Chicago, IL, USA). *P*-values<0.05 were considered statistically significant.

RESULTS

Comparison of Target Volume Dosimetry

All treatment techniques achieved the target volume coverage required by clinical practice. HT plans yielded the best coverage for the target structure, with 98% (range 97–99%) of the PTV receiving 95% of the prescribed dose. Nevertheless, the coverage of the target volumes was equivalent between the IMRT, VMAT, IMPT-1 and IMPT-2 plans, and no significant difference was found in the present study. The maximum target dose was achieved with the IMPT-2 plan, and the minimum target dose was achieved with the VMAT plan. In general, the mean target doses were compromised, and all techniques resulted in similar D_{mean} values. Moreover, the CI was excellent with the IMRT plan, demonstrating the best consistency between the target volume and the shape of the radiation fields in the treatment delivery. Additionally, HT plans were associated with a favorable HI and reflected uniform dose distributions. Comparative dosimetry of the target volumes for five plans is reported in **Table 2**, and the cumulative DVHs of the PTV are shown in **Figure 2A**.

Cardiac Sparing

IMPT-2 resulted in marked cardiac sparing, yielding the lowest D_{mean} of the heart and substructures, the most focused dosimetric parameters of the heart. The D_{mean} values of the whole heart, RA, RV, LA and LV in the IMPT-2 plan were 5.5 ± 0.9, 8.3 ± 1.1, 2.8 ± 1.3, 4.2 ± 1.0, and 8.3 ± 1.1, respectively. Moreover, statistical analysis indicated significant differences between this plan and the other plans (*P*-values less than 0.05). ATIThis treatment planning study demonstrates that PT delivers higher tumor doses than photon therapy while sparing normal tissues.

For the photon plan, HT afforded superior dose sparing for the V_5, V_6, V_7, V_8, and D_{mean} of the heart, while the greatest reductions in the V_9, V_{10}, V_{11}, and V_{12} of the heart were observed with the IMRT plan. Concerning cardiac structures, IMRT resulted in the most notable dose reduction to the RA, and HT

TABLE 2 | Summary of the target volume dosimetry.

	IMRT	VMAT	HT	IMPT-1	IMPT-2	P < 0.05
D_2(Gy)	13.2 ± 0.1	13.1 ± 0.07	12.7 ± 0.1	13.0 ± 0.4	14.74 ± 1.24	a,b,d,f,g,h,i,j
D_{98}(Gy)	11.8 ± 0.1	11.8 ± 0.2	12.0 ± 0.1	11.9 ± 0.5	11.84 ± 0.09	b,f, g,h,j
D_{max}(Gy)	14.1 ± 0.3	13.6 ± 0.2	13.0 ± 0.1	14.6 ± 0.7	21.81 ± 3.93	a,b,c,d,e,f,g,h,i,j
D_{mean}(Gy)	12.6 ± 0.03	12.6 ± 0.007	12.5 ± 0.1	12.6 ± 0.001	12.75 ± 0.14	b,d,f,g,h,i,j
D_{min}(Gy)	8. 4 ± 1.2	5.6 ± 2.0	10.2 ± 0.4	6.6 ± 2.4	6.31 ± 1.72	a,b,c,d,e,f, g,i
Target coverage(%)	96.2 ± 0.4	96.2 ± 1.3	98.2 ± 0.5	96.0 ± 0.8	96.36 ± 1.03	b,f,i
CI	0.86 ± 0.02	0.84 ± 0.03	0.84 ± 0.03	0.84 ± 0.03	0.80 ± 0.05	b,g,j
HI	0.1 2 ± 0.01	0.11 ± 0.02	0.05 ± 0.01	0.10 ± 0.07	0.24 ± 0.11	b,d,f, g,h,i,j

IMRT, intensity-modulated radiation therapy; VMAT, volumetric-modulated arc therapy; HT, helical tomotherapy; IMPT, intensity-modulated proton therapy; Dx, dose received by x% of the volume; CI, conformity index; HI, homogeneity index; a, IMRT vs VMAT; b, IMRT vs HT; c, IMRT vs PT; d, VMAT vs HT; e, VMAT vs PT; f, HT vs PT; g, IMRT vs IMPT-2; h, VMAT vs IMPT-2; I, HT vs IMPT-2; j, IMPT-1 vs IMPT-2.

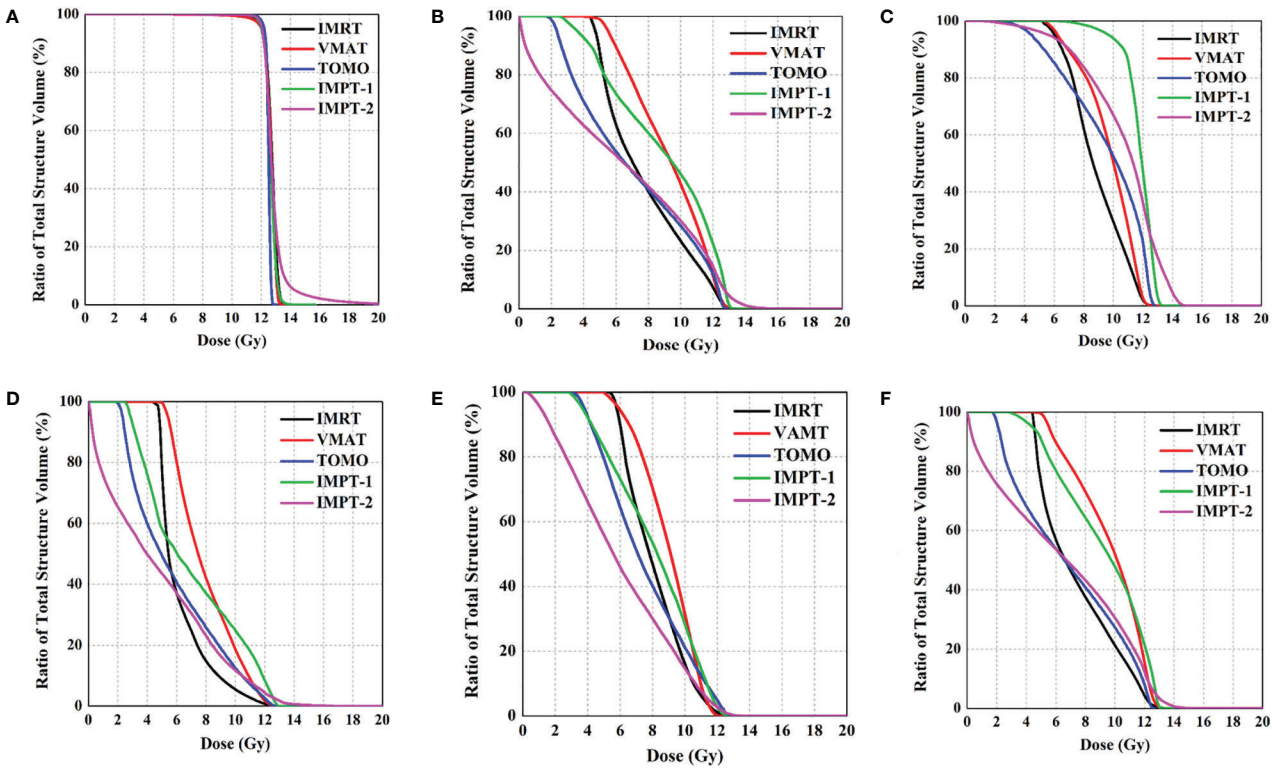

FIGURE 2 | Comparison of DVHs for the PTV and OARs. **(A)** PTV, **(B)** whole heart, **(C)** right atrium, **(D)** right ventricle, **(E)** left atrium, and **(F)** left ventricle.

displayed the most notable dose reduction to the RV. However, VMAT showed the poorest reduction in various dosimetric parameters of the heart. **Table 3** summarizes the various absorbed-dose parameters for cardiac structures, and cumulative DVHs are shown in **Figures 2B–E**. **Figure 3** shows schematic diagrams of the absorbed-dose distribution for the heart.

DISCUSSION

Unlike adult tumors, stage IV pediatric tumors usually have a satisfactory prognosis. For Wilms tumor patients, the survival analysis showed that the 16-year relapse-free survival (RFS) rate was 70%, and more than 80% of patients were expected to achieve 16-year overall survival (OS) (3). WLI is commonly employed in the treatment of pediatric malignancies, such as Wilms tumor, rhabdomyosarcoma and Ewing sarcoma, as part of the curative intent of the management of stage IV disease. Pediatric patients with sarcomas and pulmonary metastasis are usually treated with chemotherapeutic anthracyclines. In recent years, accumulating evidence has demonstrated that most of the above methods are correlated with adverse effects, including CHF and secondary malignant neoplasms (13). A few investigations have indicated that WLI is an important factor contributing to the development of heart failure in childhood

TABLE 3 | Dose–volume histogram (DVH) statistics for cardiac structures.

Heart	IMRT	VMAT	HT	IMPT-1	IMPT-2	P<0.05
V_5 (%)	79.6 ± 27.5	82.3 ± 27.7	60.1 ± 19.2	66.1 ± 23.0	44.5 ± 16.32	b,c,d,e,g,h,i,j
V_6 (%)	66.6 ± 12.2	80.4 ± 13.5	55.8 ± 4.0	62.4 ± 7.8	43.37 ± 8.46	b,d,e,g,h,i,j
V_7 (%)	53.7 ± 13.0	69.4 ± 14.6	47.5 ± 4.1	52.8 ± 7.0	38.69 ± 7.85	a,d,e,f,g,h,i,j
V_8 (%)	43.1 ± 11.7	58.5 ± 15.5	40.2 ± 4.0	49.4 ± 6.4	33.94 ± 6.99	a,c,d,f,h,j
V_9 (%)	33.6 ± 10.1	48.8 ± 17.2	33.7 ± 4.0	43.0 ± 6.0	29.21 ± 6.26	a,c,d,f,h,j
V_{10} (%)	24.7 ± 7.4	38.9 ± 18.9	27.2 ± 3.8	36.1 ± 5.9	24.11 ± 5.45	a,b,c,f,h,j
V_{11}(%)	16.2 ± 4.4	27.4 ± 16.9	20.9 ± 5.0	27.5 ± 5.3	18.47 ± 4.53	a,b,c,f,h,j
V_{12}(%)	7.4 ± 2.3	11.8 ± 9.0	10.5 ± 3.5	15.7 ± 3.9	11.17 ± 3.27	b,c,e,f,g,j
D_{mean}(Gy) RA	7.8 ± 0.7	8.7 ± 1.1	7.3 ± 0.4	7.8 ± 0.8	5.5 ± 0.9	b,d,f,g,h,i,j
D_{mean}(Gy) RV	8.9 ± 0.6	9.4 ± 1.0	9.0 ± 0.9	10.3 ± 0.9	8.3 ± 1.1	c,f,h,j
D_{mean}(Gy) LA	6.0 ± 1.1	6.7 ± 1.8	5.3 ± 0.9	5.0 ± 1.0	2.8 ± 1.3	c,e,g,h,i,j
D_{mean}(Gy) LV	7.8 ± 0.7	8.9 ± 1.3	7.5 ± 0.8	6.5 ± 1.0	4.2 ± 1.0	a,c,e,f,g,h,i,j
D_{mean}(Gy)	7.9 ± 0.7	9.5 ± 1.6	7.6 ± 0.5	8.5 ± 0.8	6.2 ± 1.3	a,c,d,f,g,h,i,j

RA, right atrium; RV, right ventricle; LA, left atrium; LV, left ventricle; a, IMRT vs VMAT; b, IMRT vs HT; c, IMRT vs PT; d, VMAT vs HT; e, VMAT vs PT; f, HT vs PT; g, IMRT vs IMPT-2; h, VMAT vs IMPT-2; I, HT vs IMPT-2; j, IMPT-1 vs IMPT-2.

cancer survivors (14–16). Furthermore, recent studies have indicated that irradiation of the heart can cause various disorders associated with the endocardium, myocardium, pericardium, coronary arteries, conduction system, and cardiac valves. Preliminary research has reported that a cardiac dose higher than 15 Gy is associated with cardiomyopathy or valvular disease (17). The Institute Gustave Roussy report indicated that the 20-year incidence of CHF was 18% after a heart dose >3.7 Gy and 9% after lower doses (18). Tukenova et al. studied 4,122 5-year survivors of a childhood cancer diagnosed before 1986 in France and the United Kingdom and confirmed that receiving radiation to the heart increased cardiovascular morbidity/mortality, with an estimated relative risk of 1.6 at a mean dose of 1 Gy (19). The American Wilms Tumor Study and Childhood Cancer Survivor Study showed that cardiovascular disease and secondary malignancies were the main causes of morbidity and mortality in long-term survivors (20, 21). Recently, a retrospective study of the pathophysiological observations of cardiovascular disorders in childhood cancer survivors linked anthracyclines (≥100 mg/m^2) alone or combined with ≥15 Gy chest radiotherapy (RT) with poor OS, and children younger than 5 years old at diagnosis were vulnerable to radiotherapy-related adverse effects and an increased risk for cardiac complications (22). Therefore, reducing the adverse effects of radiotherapy is of great significance to the management of these populations (9).

The above findings emphasize the need to focus on normal tissue sparing when designing radiotherapy plans. Based on these therapeutic risk factors associated with cardiac disease, researchers have attempted to explore the values of strategies to reduce cardiac exposure using new radiotherapy techniques. Additionally, radiation-induced cancers are more common in children than in adults because of increased susceptibility to secondary cancers (23). Other very important organs around the lungs include the vertebral column, humerus, esophagus, liver, and spinal cord. Increased evidence has demonstrated that advanced radiotherapy techniques allow radiation oncologists to improve treatment, leading to maximal therapeutic efficacy with minimal adverse effects. A study published by Christina et al. confirmed the advantages of IP-AP/PA and VMAT techniques over standard AP/PA in normal tissue sparing (9). Kalapurakal et al. reported a significant decrease in the doses delivered to the OARs in the cardiac-sparing IMRT technique for WLI and confirmed the feasibility of this technique in a clinical trial consisting of 20 patients (24).

As an increasing number of pediatric patients have access to new forms of radiotherapy, efforts to improve heart exposure have followed. In this research, we assessed dose reductions to the heart and substructures with IMRT, VMAT, HT, and IMPT plans in the treatment of children undergoing WLI. Regarding the three photon plans, the results indicated that HT significantly lowered the dose to the heart and yielded the best coverage and homogeneity to the target structure. Additionally, the HT plan afforded superior dose sparing for the V_5, V_6, V_7, V_8, and D_{mean} of the heart and D_{mean} of the RV. Previous research showed that HT has the ability to conformally avoid reducing doses to normal tissues that are close to tumor-bearing regions, resulting in the superior capability of homogeneous dose distributions within targeted regions. HT has improved patient care through image-guided positioning and adaptive plans and prolonged the overall treatment times; thus, it represents both a novel radiation treatment device and an innovative means of delivering radiotherapy. More importantly, unlike VMAT, HT has great flexibility in treating multiple targets within a large volume in a simple setup. Moreover, IMRT demonstrated excellent conformity and displayed the most notable dose reductions in the V_9, V_{10}, V_{11}, and V_{12} of the heart and D_{mean} of the RA. The VMAT plan was the least effective at sparing the heart and other normal tissues.

In recent years, with the development of radiotherapy technology, protons have gradually been used in the treatment of tumors. The major advantage of protons over traditional photons is that there is an obvious local high-dose region at the end of the dose range; this is referred to as the Bragg peak. The use of this property can ensure both a precise dose in the target area and low irradiation on the surrounding tissues and organs, improving the quality of life for cancer survivors,

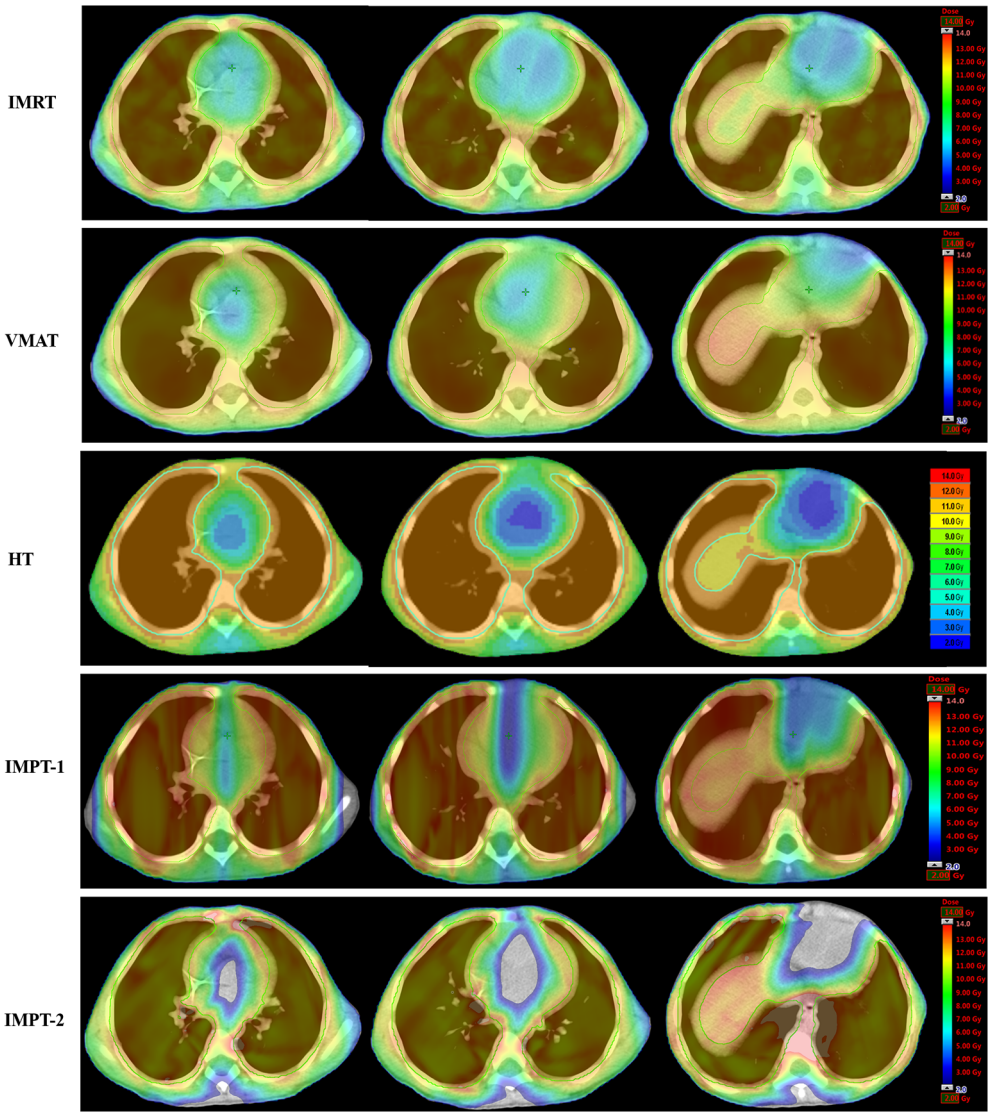

FIGURE 3 | Color wash of the absorbed-dose distribution (transverse plane) to the heart in four-year-old male patients.

particularly children. As a result, a low-to-intermediate radiation dose may increase the risk of functional impairment as well as radiation-induced malignancies (25). From a purely physics focused point of view, the dose distribution of protons is, in most cases, superior to that of photons, although the lateral dose fall-off is worse for protons at higher energies than for photons (refer to Engelsman, this issue). In contrast, a proton beam does not experience the lateral penumbra widening that a photon beam experiences in the lung, a great advantage for PT.

When we first designed the IMPT-1 plan, we used both lungs as the PTV, similar to when we designed the photon radiotherapy plan, and found that PT is equivalent to photon radiotherapy in reducing the cardiac dose but not providing a dose advantage in cardiac protection. During PT, the peak part is aimed at the focus of the tumor, and the tumor receives the largest amount of radiation, while the normal cells in front of the tumor receive only 1/3 to 1/2 of the peak energy, and the normal cells at the back of the tumor essentially do not experience any radiation damage. Considering the anatomical positions of the heart and lung, regardless of the radiation field, the heart is surrounded by the target area, not the back of the whole lung (26, 27). Published studies have indicated that the effectiveness and degree of IMPT dose sparing to various OARs depend on the intracranial tumor location (28). Considering the anatomical relation between the whole lung and heart, we proposed a novel proton radiotherapy solution for children with WLI that has rarely been reported in previous studies. This solution significantly reduces the dose to the heart and explores the advantages of proton radiotherapy. Therefore, this approach may decrease the incidence of long-term complications associated with WLI. The future of pediatric radiation oncology research will determine patients who will benefit the most from PT.

Currently, IMPT is not widely applied in clinical practice, and it is sensitive to organ movement. Thus, this problem needs to be solved by combining respiratory gating techniques; however, these techniques are still in the research and improvement stage (27). Furthermore, current estimates of the benefit of PT over photon therapy based on toxicity reduction will be realized only when survivorship has been achieved. IMPT is limited by its technology and infrastructure, making it challenging to use in clinical applications; moreover, there are few proton centers in other countries, and the treatment is very costly. Currently, there are many dosimetry studies and small cohort or short-term follow-up studies. As a new technique, PT is an immature treatment plan for tumors with different shapes and locations. Different planning systems and different linear accelerator (LINAC) machines produced by other manufacturers should be studied in future investigations to overcome the variance between treatment facilities. With the improvement in the proton TPS and its physical properties, we believe that PT will benefit more patients.

CONCLUSIONS

Our findings show that proton therapy, as a new radiotherapy modality that sums two PT plans and uses the unilateral lung as the PTV, is superior to the plan that uses the bilateral lung as the PTV for cardiac sparing in WLI. Considering the complex anatomical relation between target volumes and OARs, PT can provide a dose advantage for organs located outside the target area rather than within or surrounding the area. It is hoped that advances in PT plan design will lead to further improvements in radiotherapy approaches and provide the best treatment choice for individual patients.

DATA AVAILABILITY STATEMENT

The raw data supporting the conclusions of this article will be made available by the authors, without undue reservation.

ETHICS STATEMENT

The retrospective research of the medical records was approved by Institutional Review Board of the Shandong Cancer Hospital for this analysis.

AUTHOR CONTRIBUTIONS

XS, JD, and YY designed the study and wrote the initial draft of the manuscript. XL, TS, and HW contributed to the design of the study and the analysis and interpretation of data and assisted in the preparation of the manuscript. JZ, HW, and XM contributed to data collection and interpretation, and critically reviewed the manuscript. All authors contributed to the article and approved the submitted version.

FUNDING

This study was supported by the Key Support Program of Natural Science Foundation of Shandong Province (Grant No. ZR2019LZL017) and the Taishan Scholars Project of Shandong Province (Grant No. ts201712098 and No.tsqn201909140), and the Academic promotion program of Shandong First Medical University (Grant No. 2020RC003) and the National Natural Science Foundation of China (Grant No. 81901743).

REFERENCES

1. Steliarova-Foucher E, Colombet M, Ries LAG, Moreno F, Dolya A, Bray F, et al. International incidence of childhood cancer, 2001–10: a population-based registry study. *Lancet Oncol* (2017) 18:719–31. doi: 10.1016/S1470-2045(17)30186-9
2. Siegel R, Naishadham D, Jemal A. Cancer statistics, 2013. *CA Cancer J Clin* (2013) 63:11–30. doi: 10.3322/caac.21166
3. Green DM. The treatment of stages I-IV favorable histology Wilms' tumor. *J Clin Oncol* (2004) 22:1366–72. doi: 10.1200/JCO.2004.08.008
4. Ladenstein R, Potschger U, Le Deley MC, Whelan J, Paulussen M, Oberlin O, et al. Primary disseminated multifocal Ewing sarcoma: Results of the Euro-EWING 99 trail. *J Clin Oncol* (2010) 10:3284–91. doi: 10.1200/JCO.2009.22.9864
5. Donaldson SS, Meza J, Breneman JC, Crist WC, Laurie F, Qualman SJ, et al. Results from the IRS-IV randomized trial of hyperfractionated Radiotherapy in children with rhabdomyosarcoma—A report from the IRSG. *Int J Radiat Oncol Biol Phys* (2001) 51:718–28. doi: 10.1016/S0360-3016(01)01709-6
6. Grewal Amardeep S, Li Y, Grewal SK, Bagatell R, Balamuth N, Womer RB, et al. Role of Metastatic Site Irradiation in Pediatric Patients With Metastatic Ewing Sarcoma. *J Pediatr Hematol Oncol* (2020) 42:e305–9. doi: 10.1097/MPH.0000000000001752
7. Bolling T, Schuck A, Paulussen M, Dirksen U, Ranft A, Könemann S, et al. Whole lung irradiation in patients with exclusively pulmonary metastases of Ewing tumors.Toxicity analysis and treatment results of the EICESS-92 trial. *Strahlenther Onkol* (2008) 184:193–7. doi: 10.1007/s00066-008-1810-x
8. Nicolin G, Taylor R, Baughan C, Shannon C, Stevens S, Richardson D, et al. Outcome after pulmonary radiotherapy in Wilms' tumor patients with pulmonary metastases at diagnosis: A UK Children's Cancer Study Group, Wilms' tumor Working Group Study. *Int J Radiat Oncol Biol Phys* (2008) 70:175–80. doi: 10.1016/j.ijrobp.2007.05.053
9. Kalapurakal JA, Zhang Y, Kepka A, Zawislak B, Sathiaseelan V, Rigsby C, et al. Cardiac-sparing whole lung IMRT in children with lung metastasis. *Int J Radiat Oncol Biol Phys* (2013) 85:761–7. doi: 10.1016/j.ijrobp.2012.05.036
10. Mitin T, Zietman AL. Promise and pitfalls of heavy-particle therapy. *J Clin Oncol* (2014) 32:2855–63. doi: 10.1200/JCO.2014.55.1945
11. Paganetti H, Niemierko A, Ancukiewicz M, Gerweck LE, Suit HD. Relative biological effectiveness (RBE) values for proton beam therapy. *Int J Radiat Oncol Biol Phys* (2002) 53:407–21. doi: 10.1016/S0360-3016(02)02754-2
12. Feuvret L, Noël G, Mazeron JJ, Bey P. Conformity index: a review. *Int J Radiat Oncol Biol Phys* (2006) 64:333–42. doi: 10.1016/j.ijrobp.2005.09.028
13. Green DM, Grigoriev YA, Nan B, Takashima JR, Breslow NE. Correction to "congestive heart failure after treatment for wilms' tumor". *J Clin Oncol* (2003) 21:2447–8. doi: 10.1200/JCO.2003.99.005
14. Yeh ET, Tong AT, Lenihan DJ, Yusuf DW, Swafford J, Champion C, et al. Cardiovascular complications of cancer therapy: Diagnosis, pathogenesis and management. *Circulation* (2004) 109:3122–31. doi: 10.1161/01.CIR.0000133187.74800.B9

15. Guldner L, Haddy N, Pein F, Diallo I, Shamsaldin A, Dahan M, et al. Radiation dose and long term risk of cardiac pathology following radiotherapy and anthracycline for a childhood cancer. *Radiother Oncol* (2006) 81:47–56. doi: 10.1016/j.radonc.2006.08.020
16. Berry GJ, Jorden M. Pathology of radiation and anthracycline cardiotoxicity. *Pediatr Blood Cancer* (2010) 44:630–7. doi: 10.1002/pbc.20346
17. Mulrooney DA, Yeazel MW, Kawashima T, Mertens AC, Mitby P, Stovall M, et al. Cardiac outcomes in a cohort of adult survivors of childhood and adolescent cancer:Retrospective analysis of the Childhood Cancer Survivor Study cohort. *BMJ* (2009) 339:b4606. doi: 10.1136/bmj.b4606
18. Pein F, Sakiroglu O, Dahan M, Lebidois J, Merlet P, Shamsaldin A, et al. Cardiac abnormalities 15 years and more after adriamycin therapy in 229 childhood survivors of a solid tumor at the Institut Gustave Roussy. *Br J Cancer* (2004) 91:37–44. doi: 10.1038/sj.bjc.6601904
19. Tukenova M, Guibout C, Oberlin O, Doyon F, Mousannif A, Haddy N, et al. Role of cancer treatment in long-term overall and cardiovascular mortality after childhood cancer. *J Clin Oncol* (2010) 28:1308–15. doi: 10.1200/JCO.2010.30.8585
20. Cotton CA, Peterson S, Norkool PA, Takashima J, Grigoriev Y, Green DM, et al. Early and late mortality after diagnosis of Wilms tumor. *J Clin Oncol* (2009) 27:1304–9. doi: 10.1200/JCO.2008.18.6981
21. Termuhlen AM, Tersak JM, Qi L, Yasu Y, Green DM. Twenty-five year follow up of childhood Wilms tumor: A report from the Childhood Cancer Survivor Study. *Pediatr Blood Cancer* (2011) 57:1210–6. doi: 10.1002/pbc.23090
22. Armenian SH, Armstrong GT, Aune G, Chow EJ, Ehrhardt MJ, Ky B, et al. Cardiovascular disease in survivors of childhood cancer: Insights into epidemiology, pathophysiology, and prevention. *J Clin Oncol* (2018) 36:2135–44. doi: 10.1200/JCO.2017.76.3920
23. Bölling T, Könemann S, Ernst I, Willich N. Late Effects of Thoracic Irradiation in Children. *Strahlenther Onkol* (2008) 184:289–95. doi: 10.1007/s00066-008-1842-2
24. Kalapurakal JA, Gopalakrishnan M, Walterhouse DO, Rigsby DK, Rademaker A, Helenowski I, et al. Cardiac-Sparing Whole Lung IMRT in Patients With Pediatric Tumors and Lung Metastasis: Final Report of a Prospective Multicenter Clinical Trial. *Int J Radiat Oncol Biol Phys* (2019) 103:28–37. doi: 10.1016/j.ijrobp.2018.08.034
25. Armstrong GT, Stovall M, Robison LL. Long-term effects of radiation exposure among adult survivors of childhood cancer: results from the childhood cancer survivor study. *Radiat Res* (2010) 174:840–50. doi: 10.1667/RR1903.1
26. Greenberger BA, Yock TI. The role of proton therapy in pediatric malignancies: Recent advances and future directions. *Semin Oncol* (2020) 47:8–22. doi: 10.1053/j.seminoncol.2020.02.002
27. Weber DC, Habrand JL, Hoppe BS, Christine HK, Laack NN, Langendijk JA, et al. Proton therapy for pediatric malignancies: Fact, figures and costs. A joint consensus statement from the pediatric subcommittee of PTCOG, PROS and EPTN. *Radiother Oncol* (2018) 128:44–55. doi: 10.1016/j.radonc.2018.05.020
28. Adeberg S, Harrabi SB, Bougatf N, Vermaf V, Windisch P, Bernhardt D, et al. Dosimetric Comparison of Proton Radiation Therapy, Volumetric Modulated Arc Therapy, and Three-Dimensional Conformal Radiotherapy Based on Intracranial Tumor Location. *Cancers* (2018) 10:401. doi: 10.3390/cancers10110401

Conflict of Interest: The authors declare that the research was conducted in the absence of any commercial or financial relationships that could be construed as a potential conflict of interest.

Copyright © 2021 Sha, Duan, Lin, Zhu, Zhang, Sun, Wang, Meng and Yin. This is an open-access article distributed under the terms of the Creative Commons Attribution License (CC BY). The use, distribution or reproduction in other forums is permitted, provided the original author(s) and the copyright owner(s) are credited and that the original publication in this journal is cited, in accordance with accepted academic practice. No use, distribution or reproduction is permitted which does not comply with these terms.

frontiers in Oncology

ORIGINAL RESEARCH
published: 29 April 2021
doi: 10.3389/fonc.2021.621350

Enhanced Deep-Inspiration Breath Hold Superior to High-Frequency Percussive Ventilation for Respiratory Motion Mitigation: A Physiology-Driven, MRI-Guided Assessment Toward Optimized Lung Cancer Treatment With Proton Therapy

Frank Emert[1], John Missimer[1], Philipp A. Eichenberger[2], Marc Walser[1], Celina Gmür[2], Antony J. Lomax[1,3], Damien C. Weber[1,4,5] and Christina M. Spengler[2,6]*

[1] Center for Proton Therapy, Paul Scherrer Institute (PSI), Villigen, Switzerland, [2] Exercise Physiology Lab, Department of Health Sciences and Technology, Institute of Human Movement Sciences and Sport, ETH Zurich, Zurich, Switzerland, [3] Department of Physics, ETH Zurich, Zurich, Switzerland, [4] Department of Radiation Oncology, University Hospital Zurich, Zurich, Switzerland, [5] Department of Radiation Oncology, University Hospital Bern, Bern, Switzerland, [6] Zurich Center for Integrative Human Physiology (ZIHP), University of Zurich, Zurich, Switzerland

OPEN ACCESS

Edited by:
Alessio G. Morganti, University of Bologna, Italy

Reviewed by:
Yaacov Lawrence, Sheba Medical Center, Israel
Christina Tsien, Johns Hopkins Medicine, United States

***Correspondence:**
Frank Emert
frank.emert@psi.ch

Specialty section:
This article was submitted to Radiation Oncology, a section of the journal Frontiers in Oncology

Received: *26 October 2020*
Accepted: *18 February 2021*
Published: *29 April 2021*

Citation:
Emert F, Missimer J, Eichenberger PA, Walser M, Gmür C, Lomax AJ, Weber DC and Spengler CM (2021) Enhanced Deep-Inspiration Breath Hold Superior to High-Frequency Percussive Ventilation for Respiratory Motion Mitigation: A Physiology-Driven, MRI-Guided Assessment Toward Optimized Lung Cancer Treatment With Proton Therapy. Front. Oncol. 11:621350. doi: 10.3389/fonc.2021.621350

Background: To safely treat lung tumors using particle radiation therapy (PRT), motion-mitigation strategies are of critical importance to ensure precise irradiation. Therefore, we compared applicability, effectiveness, reproducibility, and subjects' acceptance of enhanced deep-inspiration breath hold (eDIBH) with high-frequency percussive ventilation (HFPV) by MRI assessment within 1 month.

Methods: Twenty-one healthy subjects (12 males/9 females; age: 49.5 ± 5.8 years; BMI: 24.7 ± 3.3 kg/m^{-2}) performed two 1.5 T MRI scans in four visits at weekly intervals under eDIBH and HFPV conditions, accompanied by daily, home-based breath-hold training and spirometric assessments over a 3-week period. eDIBH consisted of 8-min 100% O_2 breathing (3 min resting ventilation, 5 min controlled hyperventilation) prior to breath hold. HFPV was set at 200–250 pulses min^{-1} and 0.8–1.2 bar. Subjects' acceptance and preference were evaluated by questionnaire. To quantify inter- and intrafractional changes, a lung distance metric representing lung topography was computed for 10 reference points: a motion-invariant spinal cord and nine lung structure contours (LSCs: apex, carina, diaphragm, and six vessels as tumor surrogates distributed equally across the lung). To parameterize individual LSC localizability, measures of their spatial variabilities were introduced and lung volumes calculated by automated MRI analysis.

Results: eDIBH increased breath-hold duration by >100% up to 173 ± 73 s at visit 1, and to 217 ± 67 s after 3 weeks of home-based training at visit 4 ($p < 0.001$). Measures of

vital capacity and lung volume remained constant over the 3-week period. Two vessels in the lower lung segment and the diaphragm yielded a two- to threefold improved positional stability with eDIBH, whereby absolute distance variability was significantly smaller for five LSCs; ≥70% of subjects showed significantly better intrafractional lung motion mitigation under reproducible conditions with eDIBH compared with HFPV with smaller ranges most apparent in the anterior-posterior and cranial-caudal directions. Approximately 80% of subjects preferred eDIBH over HFPV, with "less discomfort" named as most frequent reason.

Conclusions: Both, eDIBH, and HFPV were well-tolerated. eDIBH duration was long enough to allow for potential PRT. Variability in lung volume was smaller and position of lung structures more precise with eDIBH. Subjects preferred eDIBH over HFPV. Thus, eDIBH is a very promising tool for lung tumor therapy with PRT, and further investigation of its applicability in patients is warranted.

Keywords: breath hold, enhanced DIBH, HFPV, proton therapy, lung cancer, motion mitigation, MRI, lung volume

INTRODUCTION

The safe, accurate, and effective delivery of a highly conformal dose to the tumor while sparing adjacent healthy tissues represents the central challenge in the delivery of external beam radiation therapy (1–4). A fundamental advantage of particle radiation therapy (PRT) is the steep dose gradient at the distal edge, which allows protons and carbon ions to deliver their therapeutic dose with a precisely defined, energy-dependent finite range distribution (4, 5). This highly sophisticated level of spatial precision requires exact knowledge of the tumor in space and time during the entire treatment, especially in the presence of motion (6, 7). This also includes the time-dependent distribution of the materials along the particle trajectory, since the materials' electron densities have a significant influence on particle range.

With respect to proton therapy for mobile tumors, e.g., lung tumors, using pencil beam scanning (PBS-PT), the following factors are the major challenges to delivering the intended dose distribution (7–10): (i) target failures due to interfractional tumor changes regarding position, shape, and size; (ii) dose blurring due to interfractional changes in the patient's anatomy due to density variations along the beam path, and (iii) intrafractional interplay between the dynamics of the beam and the motion of anatomical structures due to respiration, heartbeat, gastrointestinal peristalsis, and inertial organ relaxation. The problem of treating lung tumors with PBS-PT was already discussed in 1992 (11), and the delivery of such treatments has gradually evolved since (12, 13). All main components of proton therapy workflows are now time dependent, including motion analysis and modeling, multimodal imaging, contouring, treatment planning, dose delivery techniques, and integrated patient monitoring (14–17). So-called 4D treatment strategies and motion management concepts continue to be developed to cope with this temporal dependence and to meet the corresponding specific challenges of proton range uncertainties (18–21).

In practice, these approaches can be divided into techniques which either manipulate the treatment beam (e.g., tracking, gating, rescanning, robust optimization, etc.,) (22–25) or those that mitigate target motion (e.g., compression, breath hold, ventilation) (26, 27). Although, applications of combinations of these can be effective, the selected treatment approach generally depends on individual patient and tumor conditions (28), as well as on site-specific irradiation capabilities (17).

Of the different patient-assisted motion mitigation techniques available, suppression of ventilation via active or passive breath holding seems to be among the most promising (17). Important in this context is the duration of motion suppression and its influence on the stability of lung structure and volumes. For example, considering relationships between tumor volumes and field application durations for different rescanning scenarios based on the beam delivery characteristics of, e.g., Gantry-2 at our institution, realistic rescanning factors are 0–4 with a duration of 45–90 s for a single field irradiation for tumor volumes up to 1 L. Therefore, with the goal of one breath hold per irradiation field, breath-hold durations of more than 60–90 s are desirable. This is longer than the length of unassisted, voluntary breath holds that typically range between 30 and 70 s and are typically associated with chest wall movements when subjects approach the point of termination. Without training, a longer breath-hold duration can only be achieved either by physiological interventions prior to an active deep-inspiration breath hold (DIBH) or via passive "breath holding" using, for example, high-frequency mechanical ventilation, e.g., high-frequency percussive ventilation (HFPV) (27).

For active breath holding, however, the challenges are manifold. First, lung volume and chest wall positions need to be reproducible in relation to the planning CT (the basis for treatment). Since the largest breath-hold duration can be achieved with the largest lung volume, subjects must hold their breath at maximal inspiration, i.e., at total lung capacity (29, 30). However, measures of lung volumes are known to vary in response to a person's experience with performing this specific

inspiratory maneuver. This implies that on each measurement day, several full inspirations need to be performed until stable total lung capacity values are reached (31, 32). Second, breath holds may be more difficult in supine position, as active breath hold in daily life is used for stabilizing the trunk during lifting heavy objects or balancing, in contrast to the relaxed supine position. Furthermore, additional weight with abdominal obesity may cause further objective or subjective problems. Third, coughing is one of the most common symptoms of lung cancer. The majority of lung cancer patients are current or former smokers, potentially also suffering from chronic obstructive pulmonary disease (COPD) which is also accompanied by frequent coughing due to bronchitis. Tussive irritation may, in turn, lead to early termination of breath holding, a problem most likely to be mitigated through medication.

Perhaps the most limiting factor of breath-hold duration, however, is the so-called break-point, where perception of intolerable air hunger urges subjects to take a new breath. This depends on the interplay of multiple factors. First, rises in arterial CO_2-partial pressure (P_aCO_2) stimulate the respiratory motor output via chemoreceptors, giving rise to air hunger. Second, the ability of the subject to suppress respiratory motor output and/or tolerate the lack of rhythmical input from lung and chest wall stretch receptors (33, 34) also limit breath-hold duration. Third, also decreases in O_2-partial pressure (P_aO_2) that stimulate respiratory motor output *via* chemoreceptors also rise to air hunger—an effect important mainly during breath holding after prior hyperventilation. Importantly, the O_2 available depends on lung size that decreases with age, is lower in women, and is often reduced by tumor tissue itself. Also, during extended breath holds, lung volume can decrease, since less CO_2 is produced than the O_2 that is consumed. Last, the psychological state of a person also contributes to the level of perceived air hunger (35). Thus, an anxious person may reach the break-point earlier.

On the other hand, it has also been demonstrated that breath-hold duration can be extended using a variety of techniques. For instance, hyperventilation prior to breath holding decreases the starting P_aCO_2 and thus leads to delayed chemoreceptor and ventilatory stimulation. As a small risk for passing out exists with hyperventilation, however, the level of P_aCO_2 needs to be controlled for patient safety. Training of the subjects, by which they become familiar to the suppression of the automatic respiratory motor output and to the lack of stretch receptor input, has also been shown to extend breath-hold duration (36). Finally, extended breath-hold duration has been demonstrated by breathing a gas mixture with increased P_aO_2 leading to delayed chemoreceptor and thus ventilatory stimulation when P_aO_2 decreases (37, 38).

Similarly, passive breath holding via HFPV is not without challenges for conscious subjects. First, patients need to "hold" a mouthpiece tightly in their mouth while fully relaxing muscles of the chest and the diaphragm. It is yet unknown whether this technique can be trained by repeated application. Normally, a patient in need of HFPV is sedated or unconscious in the intensive care unit. Second, the pressure applied, and the level of muscle relaxation, greatly affects pulmonary compliance and therefore lung volume at a given pressure, thus, potentially affecting the location of anatomical structures. Finally, HFPV may induce motion artifacts due to the vibrating nature of this type of ventilation. Although, expected to be in the millimeter range, this could be of considerable importance for its application in proton therapy. Despite these limitations, as both active and passive breath-hold techniques can substantially reduce motion amplitudes, they could be of considerable interest in radio- and proton therapy as effective motion mitigation techniques.

The aim of the present study therefore, was to compare, in healthy volunteers, intrasession, and intersession variability of lung volumes, position of anatomical lung structures, and breath-hold durations between physiologically modified oxygen-enhanced DIBH (eDIBH) and HFPV over the duration of 3 weeks in order to simulate fractionated radiotherapy treatment regimes. Longitudinal breath-hold duration, lung volume measurement, and magnetic resonance imaging (MRI) were used to assess variability in volunteers performing daily breath-hold training.

MATERIALS AND METHODS

Participants

Twenty-one healthy subjects (12 males, 9 females) participated in the study (**Table 1**). Inclusion criteria were absence of physical and mental impairment or disease, age ≥40 years, and ability to give informed consent by signature. Subjects were excluded, if they had contraindications to MRI procedures, i.e., non-MRI-suitable electronic and metal implants or claustrophobia, impaired lung function, acute or chronic disease, known or suspected non-compliance, drug or alcohol abuse, inability to follow the procedures of the study (e.g., due to language problems, psychological disorders, or dementia of the participant), presence of any psychological or sociological condition potentially hampering compliance with the study protocol or, for women, pregnancy, or breastfeeding. Subjects were informed about all procedures, and all devices were shown and explained before subjects signed an informed consent prior to the first data collection. The study was approved by the Cantonal Ethics Committee North West and Central Switzerland (BASEC-ID: 2018-01295; Clinical trial number NCT03669341).

Study Protocol

Subjects visited the Center for Proton Therapy at the Paul Scherrer Institute (PSI, Villigen, Switzerland) for MRI acquisitions on four different occasions. Visits were interspersed by 6 days of home-based breath-hold training. A schematic of the study protocol is displayed in **Figure 1**. In addition, a fifth visit was arranged for four selected subjects who demonstrated long breath-hold durations whereby three MRI acquisitions were performed within the same breath hold.

At the first visit, subjects were thoroughly informed about all details of the study procedures, including a demonstration of all testing equipment. After signing the informed consent form, a questionnaire-based assessment regarding cardiovascular risk factors and exclusion criteria was performed. Then, subjects were briefly asked about activity, nutrition, and sleep over the past 24 h, which they were requested to keep as similar as possible

before each of the following visits to assure a similar metabolic and psychological status.

At all visits, after checking the current health status as well as activity, nutrition, and sleep over the past 24 h, lung function was assessed by performing forced spirometry. This served to exclude a potentially undiagnosed lung disease affecting lung volume and/or respiratory mechanics and to achieve maximal lung volumes for breath holding because forced spirometry, yielding FVC, requires repeated maximal inspiration until similar volumes are reached (31).

Thereafter, and as with home training, two DIBH of maximal duration were performed in sitting position, the first out of resting breathing, the second after three deep breaths (to decrease P_aCO_2 slightly and prolong breath-hold duration).

Next, the subjects were transferred to the MR scanner and positioned on the couch in supine position according to a positioning under treatment. Measurement devices for the assessment of heart rate (HR) and peripheral blood oxygen saturation (SpO_2) were used to assure subject's safety throughout the procedure. Also, respiratory CO_2 concentration was measured to control the level of hyperventilation. Subjects also were fitted with a face mask for delivery of 100% O_2 during hyperventilation prior to breath-holding in the MR scanner.

One enhanced DIBH (eDIBH) procedure was then performed to determine the maximum breath-hold duration. Thereafter, subjects were moved by the MR couch into the scanner ring head first and a laser alignment (for reproducible interfractional positioning between weekly visits including wing board settings) followed. During two immediately consecutive MRI acquisitions

TABLE 1 | Demographic data of subject cohort.

Parameter	Males ($n = 12$)	Females ($n = 9$)	p
Age [years]	50.7 ± 6.4	47.9 ± 4.6	0.496
Height [cm]	183.2 ± 5.3	167.8 ± 5.0	<0.001
Weight [kg]	89.0 ± 9.5	62.9 ± 9.5	<0.001
BMI [kg·m^{-2}]	26.5 ± 2.4	22.3 ± 2.7	0.003

Data presented as mean ± SD. BMI: Body mass index.

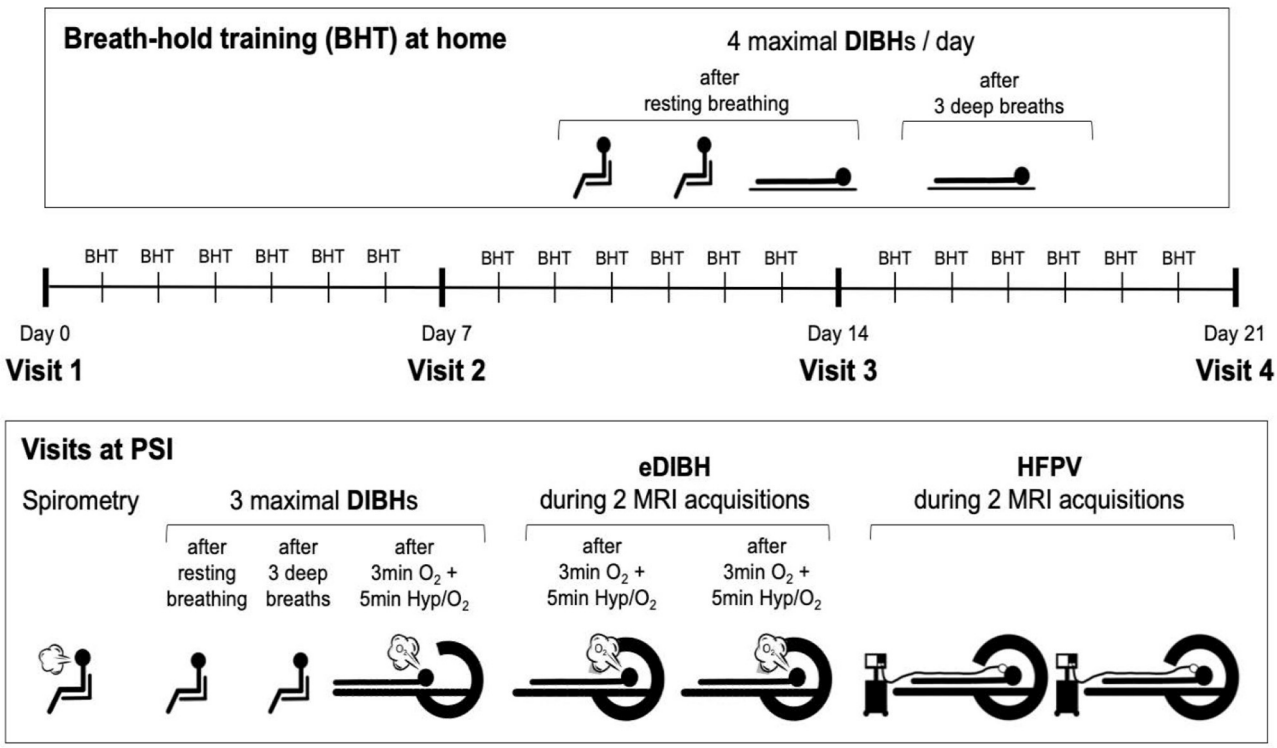

FIGURE 1 | Study protocol. Visits at the Paul Scherrer Institute (PSI) were interspersed by 6 days of home-based breath-hold training with four deep-inspiration breath holds (DIBHs) of maximal duration, two in sitting and two in supine position. The first three breath holds were performed out of resting breathing, the fourth after three deep breaths. At visits, first spirometry was performed, followed by two DIBHs of maximal duration in sitting position, the second one performed after three deep breaths. The third breath hold prior to magnetic resonance image (MRI) acquisitions was performed after ≥8 min of breathing 100% O_2 with hyperventilation (at an end-tidal CO_2-partial pressure of 20 mmHg) for the last 5 min prior to this maximal enhanced DIBH (eDIBH). This procedure was immediately followed by moving the subject into the MR scanner, initiating the eDIBH-procedure prior to each of two consecutive MRI acquisitions and maintaining it during image acquisitions. After moving the subject out of the MR scanner and installing the high-frequency percussion ventilator (HFPV), the subject was moved into the scanner ring again for two consecutive MRIs under HFPV conditions.

performed to simulate intrafractional treatment conditions with multiple fields, subjects were asked to perform two separate eDIBHs, one for each scan. Afterwards, subjects were moved out of the MR scanner to return to resting breathing and allowed to move (still on the couch).

Subsequently, details of the HFPV procedure were explained again and subjects were connected to the HFPV device. A first HFPV trial was performed outside the MR scanner for familiarization purposes, to adjust the HFPV settings accordingly and to test whether the tolerated HFPV duration was sufficient for a single MRI acquisition. Subjects were then repositioned and moved back into the MR scanner, where two consecutive MRI acquisitions were performed, in analogy to the two eDIBHs.

At the end of the first session, subjects additionally received instructions on performance and recording of their daily, home-based breath-hold training which was recorded in a personal logbook (see Section **Training and Measurements at Home** for details).

Measurements and Interventions During Each Visit

Lung Function Measurement

Forced spirometry was performed to assess FVC as well as maximal inspiratory and expiratory flow rates via a hand-held spirometer (Spirobank, MIR, Rome, Italy). Measurements were performed according to criteria of the American Thoracic Society and the European Respiratory Society (31). An adequate test required a minimum of three acceptable maneuvers and meeting the reproducibility criteria according to the ATS/ERS statement. If these criteria were not met, additional trials were performed until criteria were met but no more than eight maneuvers were performed.

Motion Suppression Techniques

The eDIBH procedure was performed as follows: In resting, supine position, subjects breathed 100% O_2 via face mask for at least 8 min with (i) 3 min resting breathing followed by (ii) controlled hyperventilation where subjects were coached to perform deep inspirations and expirations such that a $P_{ET}CO_2$ of 20 mmHg (2.67 kPa) was maintained for 5 min, followed by (iii) a maximal deep inspiration, which was sustained for as long as possible. A second and third eDIBH was performed during the following MR scans, where eDIBH was maintained during image acquisition for 70 s.

HFPV is based on the administration of small volumes of air, so-called percussions, with adjustable pressures and frequencies. These percussions can replace spontaneous ventilation allowing prolonged apnea-like suppression of respiratory motion while maintaining adequate oxygen diffusion and CO_2 removal.

The HFPV procedure was performed using a jet ventilator (Monsoon® Jet Ventilation, ACUTRONIC Medical Systems, Hirzel, Switzerland), positioned in the MR control room (outside the magnetic scanner region). The ventilator was connected by an 8-m pressure tube to an open circuit breathing-adapter (Phasitron®, Percussionaire Suisse, Ardon, Switzerland) that subjects held in their mouth via mouthpiece with a nose clip in place. The familiarization trial outside the MR scanner was performed using 1.0-bar pressure pulses at a frequency of 250 pulses min^{-1}. Individual adjustments of pressure and frequency were made according to subjective comfort and the subjects' ability to relax while being passively ventilated. During the MRI acquisitions, individualized pressure pulses ranged from 0.8 to 1.2 bar with a frequencies of 225–250 pulses min^{-1}.

MR Positioning and Image Acquisition

Subjects were immobilized on the MR couch using (i) a removable wing board attached to it with a central head support and adjustable fixation rods, which were held by both hands with arms supported overhead, and (ii) a knee support without additional fixation devices.

For all image acquisitions in the MR scanner (MAGNETOM Aera, 1.5 T, Siemens Healthcare AG, Zurich, Switzerland) a T2-weighted, 2D-steady-state free precision (SSFP) sequence was used. Voxel spacing was 0.7617 by 0.7617 mm^2 in plane with a plane separation of 2.2 mm; the reconstructed image plane consisted of an array of 512 × 512 pixels. Approximately 100 coronal 2D image planes were acquired in about 70 s.

Visit 5 for Selected Subjects

Four subjects that were capable of maintaining eDIBH for at least 4 min were recruited for an additional session to assess changes in lung volume during prolonged breath-holding. During this fifth visit, only the eDIBH procedure was performed. The visit consisted of two separate MRI acquisitions, each with three consecutive MR sequences, and each performed over a period of 210 s during a single eDIBH.

Subjective Assessment of Interventions

At the end of visit 4, acceptance of breath-hold training at home and levels of "comfort/tolerability" of eDIBH or HFPV procedures during the MRI acquisition were assessed using visual analog scales with the anchors "feasible"/"not feasible" and "well-tolerable"/"not tolerable." Finally, the subjects were asked which of the two techniques for respiratory motion mitigation they would prefer as a patient.

Training and Measurements at Home

Home-based breath-hold training consisted of four maximal DIBHs per day for a total of 18 days in order to get used to these respiratory maneuvers including full inspirations. The first and second DIBH was performed in sitting position, out of resting breathing as this is more comfortable and to allow comparison with the same breath-hold technique in lying position. The third and fourth DIBH were performed in lying position, with the first of these two also starting from resting breathing (to be compared with sitting) while the second was initiated after three deep inspirations and expirations to show the subject that "hyperventilation" increases breath-hold duration and to get them used to long-duration breath holds. Breath-hold durations were recorded by the subject in a logbook and correct recording was double-checked at each lab visit.

Data Analysis and Statistics

Anthropometric data were compared between sexes using the Mann-Whitney *U* test.

Breath-Hold Duration, Forced Vital Capacity, and Subjective Assessment

In order to evaluate the effects of sex and repeated visits, breath-hold durations as well as forced vital capacities were analyzed using two-way analysis of variance (ANOVA) with repeated measures and Bonferroni corrections for *post-hoc* analyses. If data were not normally distributed, a related-sample Friedman test was performed and the Wilcoxon signed rank test used for *post-hoc* analysis. Effects of breath-hold methods and sex in time-averaged home training (18 days average), visit (four visits average), and subjective data were analyzed using paired *t*-tests or Wilcoxon matched-pairs signed rank test. For correlation analysis between breath hold and spirometry variables, Pearson's correlation coefficient was calculated if data were normally distributed and Spearman's correlation coefficient if data were not normally distributed. One subject was excluded from all breath-hold analyses due to incomplete data. GraphPad Prism 2019 (GraphPad Software, La Jolla California, USA) was used for statistical analysis and data presentation.

Lung Volume Analysis

Based on the repeated MRI acquisitions using both eDIBH and HFPV inter- and intrafractional lung volumes and displacements have been determined and compared. Total lung volumes were determined from each acquired MRI using an automatic segmentation program developed in-house. Using functions provided by the Image Processing Toolbox of MatLab (R2018b, The MathWorks, Inc., Natick, Massachusetts, USA), the program imported and saved image data in DICOM format. The algorithm first processed the image volume as suggested in the step "Mark the Foreground Objects" in the MatLab documentation section: "Marker-Controlled Watershed Segmentation." A voxel threshold was selected by an adaptive algorithm for each image plane and the segmentation effected using the functions bwlabel.m and regionprops.m. The final step in the algorithm was the application of the 3D-clustering program, spm_cluster.m of the statistical parametric mapping package SPM12 (https://www.fil.ion.ucl.ac.uk/spm/software/spm12/). Two-way unbalanced ANOVAs evaluated the effects of visit, motion-mitigation method, and sex. For the four subjects studied for lung volume decreases during the acquisitions (fifth visit), the volumes were normalized by the initial volumes to yield a fractional decrease during the acquisition.

Measuring Intra- and Interfractional Lung Displacements

To simulate potential intra- and interfractional variations in lung volume and form as part of a radiotherapy treatment, in this study, it has been assumed that the breath-hold duration of a patient with eDIBH is sufficient for the complete irradiation of one field. That is, each single MRI reflects lung position and shape for an individual irradiation field, with each fourfold weekly repetition of two consecutive MRI sequences then representing four irradiation fractions, each consisting of two fields. As such, variations between MRIs in the same session represent inter-field variations, whereas, variations between sessions represent potential interfraction variations. In addition, variations of intrafield conditions, i.e., intrabreath-hold changes in lung volume, were evaluated by the acquisition of the three consecutive MRIs within one eDIBH in selected subjects.

In order to investigate the spatial variation of key anatomical lung structures (LSCs) over therapy sessions, a reference point was selected ($\mathrm{Ref_{SC}} = \mathrm{LSC_4}$) which does not move during respiration in the supine position. The chosen reference point was a prominent paravertebral part of one of the posterior intercostal veins on the level of the middle thoracic vertebral column (T4–T8). As shown in **Figure 2**, the selected anatomical structures subject to movement were (i) the ribs in the apex areas of the lung ($\mathrm{LSC_1}$), (ii) the carina tracheae ($\mathrm{LSC_2}$), (iii) the diaphragm ($\mathrm{LSC_3}$), and (iv) the branching points of six specific lung vessels representing hypothetic intrapulmonal tumor locations ($\mathrm{LSC_5}$-$\mathrm{LSC_{10}}$). The distribution of the six vessels observed an even division in the craniocaudal direction. With an extension from the apex to the costodiaphragmatic cavity, projections on the junctions of the T5/T6 vertebras and T9/T10 were selected, which defined three segments of approximately equal length. On each side of a segment were then located two vessels. Using Velocity®, trained medical assistants located the reference point and anatomical structures manually; two of the authors (FE and MW) checked the locations. The set of difference vectors $\underline{\mathbf{r}}_\mathrm{i}$ between the locations, $\mathrm{Ref_{SC}}$ and $\mathrm{LSC_i}$, is denoted as an intrapulmonary lung structure metric. Using these metrics, two analyses have been performed.

First, the radial distance $r_\mathrm{i} = |\underline{\mathbf{r}}_\mathrm{i}|$ of the distance vector $\underline{\mathbf{r}}_\mathrm{i}$, was determined for each MRI acquisition. From the sets of eight MRIs (two scans at four visits) acquired for each subject, the mean radial distances of each lung structure $\mu(r_\mathrm{i}, M)$ and their standard deviations $\sigma(r_\mathrm{i}, M)$ were determined for each method M: eDIBH or HFPV. The ratios $\sigma(r_\mathrm{i}, \mathrm{eDIBH})/\mu(r_\mathrm{i},\ \mathrm{eDIBH})$ and $\sigma(r_\mathrm{i}, \mathrm{HFPV})/\mu(r_\mathrm{i},\ \mathrm{HFPV})$ yielded fractional variations, for which medians, maxima, and distributions of ranks according to the Wilcoxon signed rank test could be compared. In addition, the logarithm of the ratio of fractional variations.

$$\gamma = \log\left[\frac{\frac{\sigma(r_\mathrm{i},\mathrm{eDIBH})}{\mu(r_\mathrm{i},\mathrm{eDIBH})}}{\frac{\sigma(r_\mathrm{i},\mathrm{HFPV})}{\mu(r_\mathrm{i},\mathrm{HFPV})}}\right]$$

of the two methods provided a comparison of methods for each subject and lung structure.

Second, as shown schematically in **Figure 3**, we evaluated (i) the distributions in each subject after corrections for interfractional shifts due to repositioning and (ii) intrafractional differences due to different lung volumes during the consecutive eDIBH or HFPV MRI acquisitions. The analysis consisted of three steps.

(A) After contouring, the spatial distributions of all 10 LSCs were determined in the DICOM reference system of all 16 MRIs: 8 × eDIBH and 8 × HFPV, without positioning correction.
(B) Interfractional shifts were described as rigid-body transformations. These were treated in Velocity® as pairwise image registrations with respect to the reference

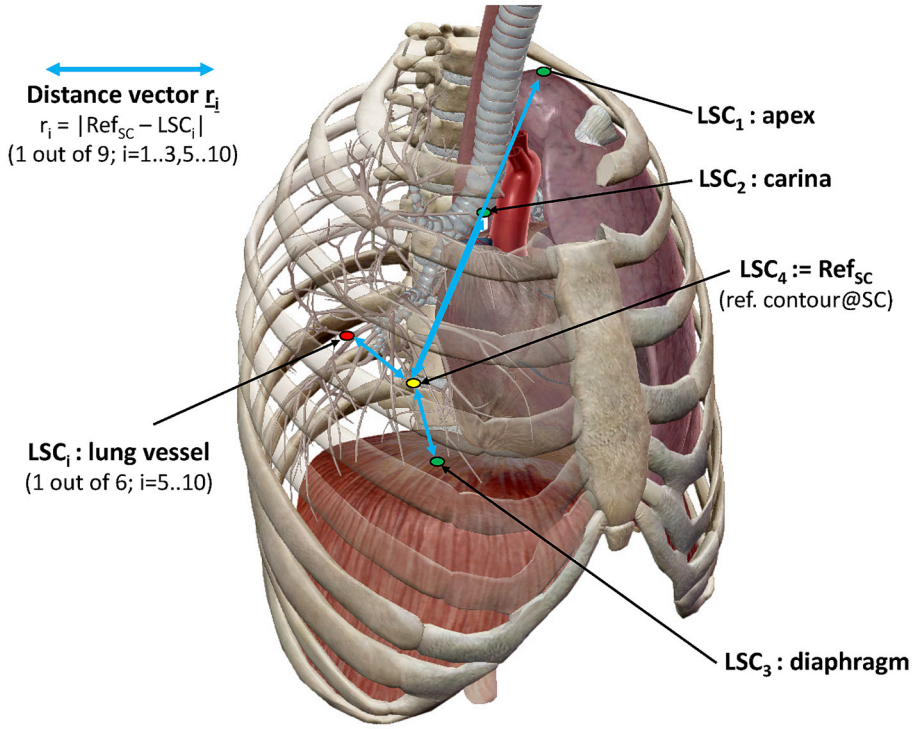

FIGURE 2 | Representation of lung structure metric with selected LSCs. LSC distribution as described in the text (image courtesy of Visible Body®).

point Ref_{SC} on the spine between the first MRI of visit 1 (MRI_1) as reference and the following MRIs from visits 2 to 4 (MRI_3 to MRI_8). The transformation between MRI_1 and the second MRI of visit 1 (MRI_2) was assumed to be negligible. In the other registrations, the MRIs were superimposed in such a way that the spinal column structure was optimally covered. The resulting six transformation matrices were then exported as DICOM registration objects and imported into MatLab. In order to simulate the 3D positioning offset correction applied in Gantry-2 before each irradiation fraction, only the translation components of the transformation were included in the analysis. These interfractional translation corrections were applied to the corresponding spatial distributions of the LSCs given in (A). For each subject and method, the resulting LSC distributions in Cartesian DICOM space yield clusters of position variabilities.

(C) The standard deviations about the mean positions of each LSC-specific cluster yielded a 95% CL ellipsoid, the volume of which, denoted "volume of variability" (VolOfVar), represented an empirical measure of spatial variability. Division of the VolOfVar by the mean subject lung volume delivered a fractional volume of variability. As for the radial distances, the logarithm of the ratio of fractional variations between the two methods for each subject and lung structure yielded a subject-specific comparison of variability.

RESULTS

Breath-Hold Duration and Subject Acceptance

Subjective Acceptance

On a scale ranging between 0 and 10, where 0 was the best rating, the subjects rated home-based training as being "feasible": 2.2 ± 2.1, as they also rated eDIBH and HFPV methods: 1.4 ± 1.1 and 2.2 ± 2.5, respectively. Both methods were also rated "tolerable" for patients: 1.8 ± 2.2 and 2.5 ± 2.7, respectively. Wilcoxon signed rank tests evidenced no difference between the two methods in neither "feasibility" nor "tolerability." However, 14 of the 21 subjects preferred eDIBH to HFPV; an experience of "less discomfort" during eDIBH was named as the most frequent reason.

Effect of Breath-Hold Training in Sitting Position Over Time

Breath-hold training at home revealed no change in breath-hold duration in sitting subjects across 18 training days and 4 visits (**Figure 4**), while a significant effect of time was detected in breath-hold durations assessed at visits ($p = 0.035$), despite breath-hold durations at visits being similar to those assessed at home at these specific time-points ($p = 0.444$). The difference was located between visit 1 and visit 2 ($p = 0.034$). Three deep breaths prior to a maximal DIBH significantly increased breath-hold duration at home in males (18-day average without 77 ± 28 s

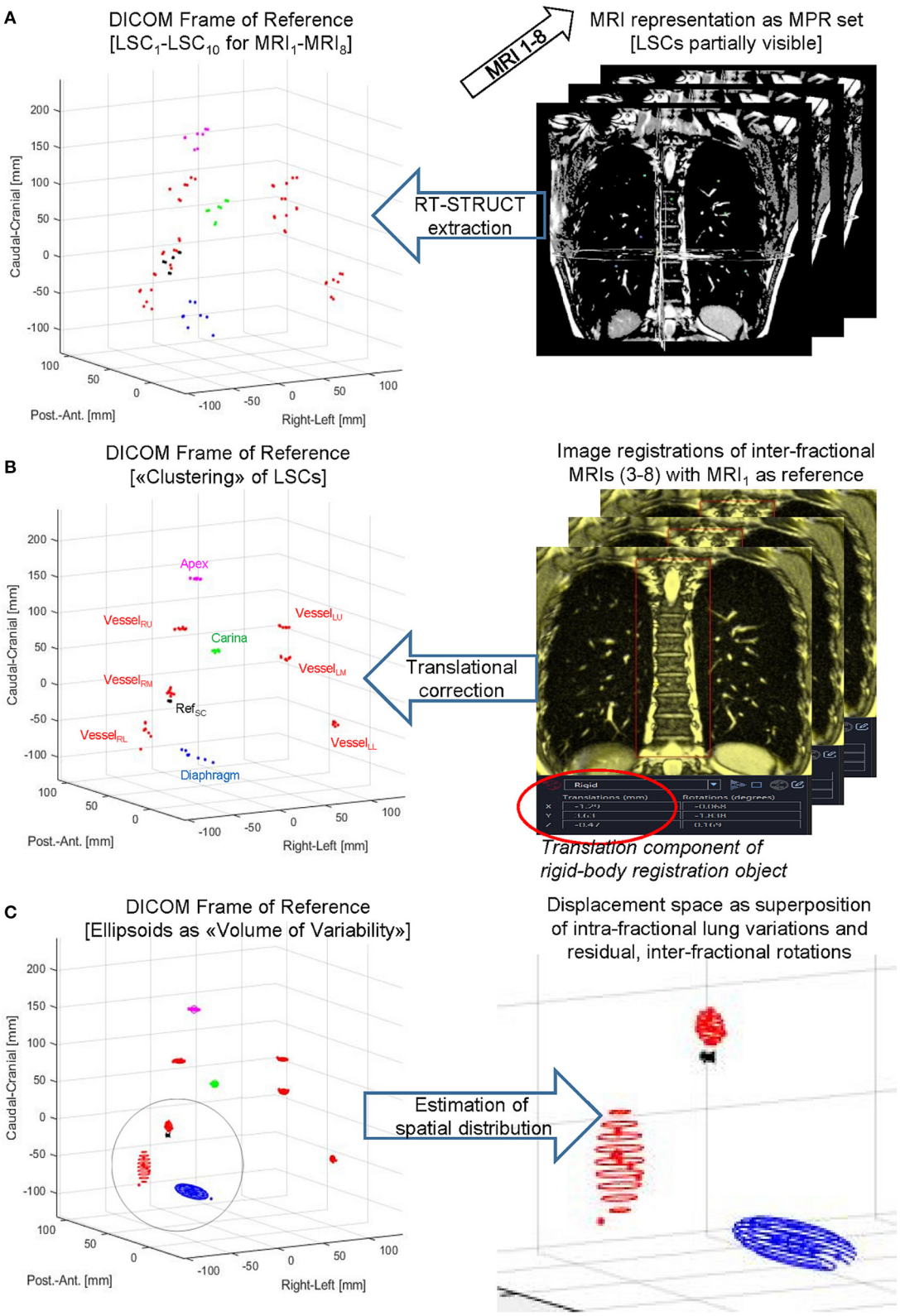

FIGURE 3 | LSC volumes of variability. Principal steps of displaying, processing, and analyzing a lung structure metric for a subject-specific set of eight MRIs acquired for eDIBH or HFPV. Top to bottom: LSCs were contoured as RT-STRUCT sets in Velocity® **(A)** followed by DICOM export/import into MatLab to enable visualization in the common DICOM Frame of Reference. Subsequently **(B)** translation corrections determined by rigid-body image registrations were applied to the LSC distributions identified on left side graph, and **(C)** rotational ellipsoids to approximate their spatial distributions were calculated as described in the text.

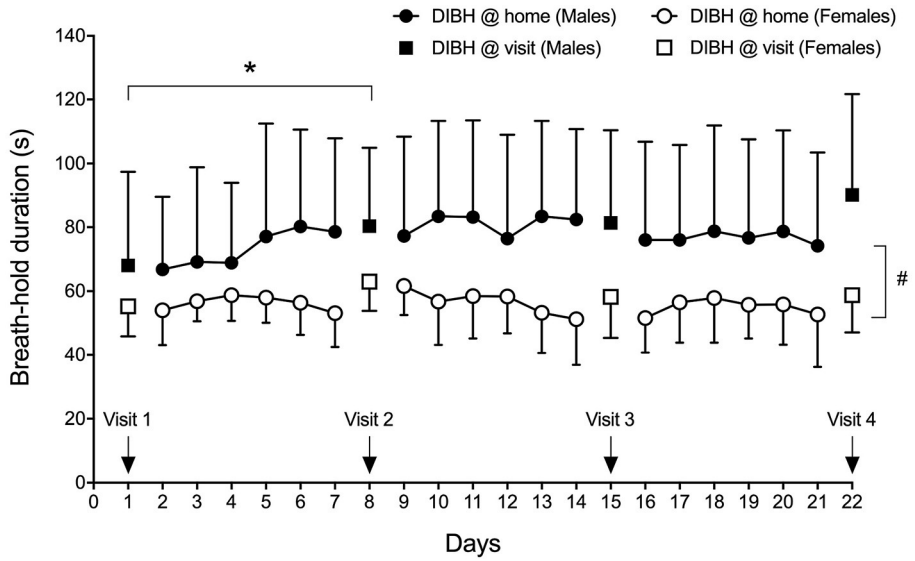

FIGURE 4 | Sex-specific group mean maximal DIBH durations (± standard deviation) at home and at visits. *$p < 0.05$; #$p = 0.010$.

and with three deep breaths 120 ± 46 s; $p < 0.001$) and females (from 56 ± 9 s to 84 ± 18 s; $p < 0.001$). Also during visits, 3 deep breaths increased breath-hold duration in males (average of four visits without deep breaths: 80 ± 26 s, average of four visits with three deep breaths: 111 ± 38 s, $p < 0.001$) and in females (from 59 ± 7 s to 76 ± 11 s; $p < 0.001$). A significant time-effect was detected that was located *post-hoc* between Visit 1 and Visit 2. A significant sex effect was detected with males having longer breath-hold durations during home trainings ($p = 0.010$) as well as at visits ($p = 0.038$).

Breath-Hold Duration Before MRI Acquisition (eDIBH) in Lying Position

Enhanced deep-inspiration breath hold duration assessed prior to the MRI acquisition, i.e., eDIBH duration, was significantly lower in visit 1 than in the following visits in the entire group. However, only in males, these differences were present without significant differences between visits in females (**Figure 5**). Individual breath-hold durations show, that all but one subject reached the required 90 s eDIBH duration at all four visits. DIBH durations assessed in sitting position at home were significantly correlated with eDIBH durations in lying position assessed prior to MRI acquisitions (**Figure 6**). The correlation coefficients for the different visits were similar: visit 1: $r^2 = 0.520$, $p < 0.001$; visit 2: $r^2 = 0.392$, $p = 0.003$; visit 3: $r^2 = 0.637$, $p < 0.001$; visit 4: $r^2 = 0.567$, $p < 0.001$. Similarly, sitting breath-hold durations at visits were significantly correlated with eDIBH durations; $r^2 = 0.672$, $p < 0.001$.

Lung Volume Analysis

Full Inspiration (Forced Vital Capacity)—Changes Within and Between Days

Across visits, measures of FVC did not differ significantly: visit 1: 5.05 ± 1.25 L; visit 2: 5.06 ± 1.24 L; visit 3: 5.05 ± 1.24 L; visit 4: 5.07 ± 1.26 L; $p = 0.42$. However, a sex effect was detected with males having a larger FVC than females (average across four visits in males: 5.93 ± 0.89 L; in females: 3.89 ± 0.37 L, $p < 0.001$). Also, FVC correlated significantly with eDIBH duration ($r^2 = 0.306$; $p < 0.001$) although—when sexes were analyzed separately—a significant correlation was present in males only ($r^2 = 0.279$; $p < 0.001$).

To determine FVC according to ATS/ERS criteria (31), an average number of 5 ± 1 attempts (range 3–8) was necessary to achieve maximal values on visit 1 while on visit 4 an average of 3 ± 0 attempts (range 3–4) was needed. On visit 1, all but two subjects reached maximal values at the fourth attempt at the latest, while on visit 4, all but one subject reached maximal values at or prior to the third attempt. Maximal within-subject differences between selected best values ranged between 0.3 and 3.6%.

Lung Volumes

The segmentation algorithm yielded the lung volumes presented in **Table 2**. In addition, their intrafractional variations for each method at each visit were derived.

As indicated in **Table 2**, an unbalanced two-way ANOVA showed no significant variation over visits, $p < 0.88$, but a significant difference between methods, $p < 0.0001$. Further ANOVAs yielded for neither method a significant variation over visit, $p < 0.99$ for eDIBH and $p < 0.48$ for HFPV, but significant difference between sexes, $p < 0.00001$, in both cases. The average difference between males and females for lung volume as measured by eDIBH was 2 L, as for FVC.

In neither of the ANOVAs of the intrafractional variations was there a significant difference over the course of the four visits: $p < 0.32$ for eDIBH and $p < 0.77$ for HFPV. The standard deviations of the intrafractional variations are with the exception of the last visit twice as large for HFPV as for eDIBH and smaller than

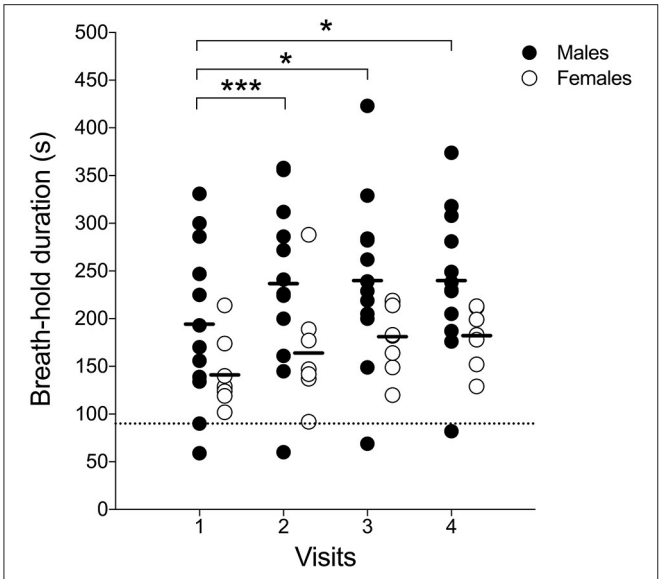

FIGURE 5 | Individual subject's maximal-enhanced deep-inspiration breath hold (eDIBH) duration; black line: group average, dashed line: 90 s duration. $^{*}p < 0.01$; $^{***}p < 0.001$.

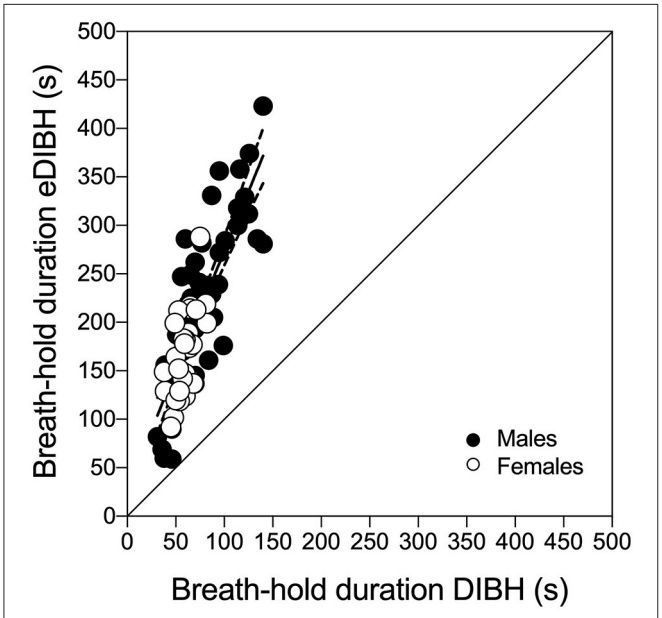

FIGURE 6 | Individual subject's maximal deep-inspiration breath hold (DIBH) durations out of resting breathing in sitting position compared with maximal-enhanced deep-inspiration breath hold (eDIBH) duration in lying position at all visits. Best-fit line with 95% confidence bands.

the lung volume standard deviations given in the upper part of **Table 2**.

Variation of Lung Volume Over Time for eDIBH

Analysis of the variation of intrabreath-hold lung volumes for the four subjects most capable of long breath-hold durations (**Figure 7**) showed that the decrease in lung volume over the course of the first 70 s acquisition was 5% or less in each of the four subjects. The more pronounced decrease in subject 6 (006-1) was rather due to an image artifact than to a physiological effect. The measured, maximum 5% decrease in lung volume over a period corresponding to the radiation time of a single field was thus below the 10% threshold, which was determined to be a sufficient determination accuracy for the automated calculation of lung volumes.

Lung Topography Analysis

Intrafractional Displacement of Lung Structure Metrics

The first analysis of lung structure metric evaluates the positional variability of the lung structures *via* the relative errors of radial distances r_i between Ref_{SC} and LSC_i, i.e., the quotient of the standard deviation and the mean value of the LSC_i distributions over all subjects. The analysis yielded no significant correlation between the relative errors of lung structures and the relative errors of the computed lung volumes. They can therefore serve as intrinsic measures of variability.

As given in **Table 3**, the medians and maxima for almost all structures are consistently less for eDIBH than for HFPV. In addition, the Wilcoxon signed rank test yielded significant differences between methods for the diaphragm, the carina, and vessels in the lower region of both lungs, $Vessel_{LL}$ and $Vessel_{RL}$, and one in the left mid-lung section, $Vessel_{LM}$. This indicates a significantly lower positional variability for eDIBH than for HFPV.

Confirmation of this result on a subject basis was established by plotting the logarithm of the ratio of relative errors between eDIBH and HFPV, denoted as γ ratio, for each subject and LSC. This yielded the three-dimensional bar plot in the upper part of **Figure 8**. Augmented by the corresponding ratio of lung volumes, it summarizes the relative variability of the two motion mitigation methods. A negative logarithm indicates that the variability is less for eDIBH, a positive value that the variability is less for HFPV.

Of the 200 log ratios, 140, i.e., 70%, show less variability for eDIBH. The subject distribution presented in the resulting table at the bottom of **Figure 8** showed in 11 subjects between 8 and 10 γ ratios favoring eDIBH, whereas, four subjects exhibit between 0 and 3 of such ratios. Thus, of the 15 subjects showing a clear distinction, 73% of the subjects show less variability for eDIBH. The distribution in **Figure 8** can be modeled by a binomial distribution with the two options eDIBH or HFPV, resulting in a probability of 0.87 for eDIBH. This value indicates that the above estimates of less variability for eDIBH are not arbitrary.

Interfractional Displacement of Lung Structure Metrics

To simulate proton therapy treatment conditions for Gantry-2@PSI, where setup uncertainties are compensated by linear 3D offset movements of the couch, the inter-fractional displacements (contained in the 6 DoF-MRI registration objects) were corrected by applying their 3D translation components to the respective

TABLE 2 | All data presented in [l] as mean ± SD.

	Visit 1	Visit 2	Visit 3	Visit 4
		Lung volumes over course of visits [l]		
eDIBH men	6.40 ± 1.44	6.58 ± 1.20	6.58 ± 1.22	6.59 ± 1.12
eDIBH women	4.61 ± 0.54	4.51 ± 0.78	4.39 ± 0.95	4.38 ± 0.90
HFPV men	5.48 ± 1.41	5.24 ± 1.18	5.67 ± 1.51	5.29 ± 1.73
HFPV women	3.20 ± 0.72	3.48 ± 0.94	3.81 ± 0.74	3.74 ± 0.51
		Intra-fractional variation of lung volumes [l]		
eDIBH	0.160 ± 0.256	0.153 ± 0.364	0.056 ± 0.255	0.020 ± 0.285
HFPV	−0.108 ± 0.640	−0.056 ± 0.617	−0.176 ± 0.542	−0.001 ± 0.291

Top: the means and standard deviations of lung volumes over the course of four visits as determined by gender for eDIBH and HFPV; bottom: the means and standard deviations of the differences between successive measurements of lung volumes for each method at each visit.

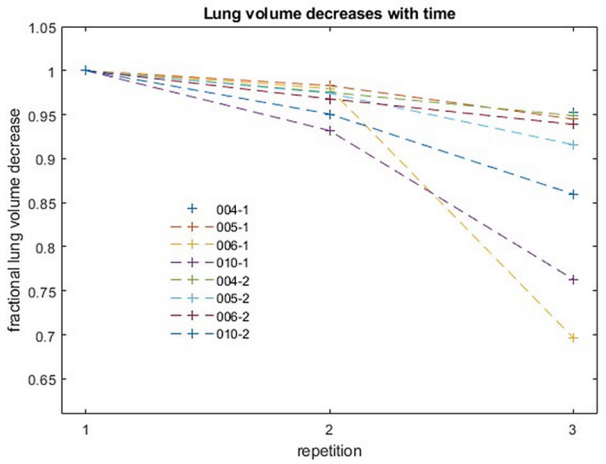

FIGURE 7 | Fractional decreases of lung volume with repetition for four subjects. Each acquisition lasted 70 s. Successive acquisitions were performed with an interruption of a few seconds for restarting the MR sequence.

TABLE 3 | Median and maximum relative error [%] of radial distances between reference (Ref_{SC}) and selected anatomical structures (LSC_i), including significance of difference between corresponding distributions of eDIBH and HFPV according to Wilcoxon signed rank test.

Relative errors of radial distances to reference/significance of difference					
LSC	**eDIBH**		**HFPV**		***p***
	Median [%]	**Maximum [%]**	**Median [%]**	**Maximum [%]**	
Apex	0.7980	1.3164	0.7876	3.2929	0.167
Carina	2.4417	3.8687	3.3148	7.1217	0.014
Diaphragm	2.6896	9.3390	7.7671	25.0294	0.001
$Vessel_{LU}$	1.1106	2.0416	1.2444	3.8462	0.218
$Vessel_{LM}$	1.5520	3.0509	2.3186	3.5505	0.025
$Vessel_{LL}$	1.7521	7.5847	3.7943	13.1986	0.010
$Vessel_{RU}$	1.4460	1.9090	1.4487	4.3269	0.314
$Vessel_{RM}$	2.2613	7.0645	2.3931	6.3809	0.247
$Vessel_{RL}$	3.6881	16.3864	7.7566	21.1520	0.014

lung structure distributions (see **Figure 3**). Their remaining spatial uncertainties are thus composed of (i) the interfractional rotational components and (ii) the interbreath-hold variations. Geometrically, rotations around the AP axis result in lateral displacements. Their amount depends on the distance to the rotation center Ref_{SC} in CC direction. Since the spatial shifts of lung structures due to respiratory movements are least pronounced in RL (39), the contribution of uncorrected setup rotations is greatest in the lateral spatial direction. Assuming a CC distance of a pulmonary vessel from Ref_{SC} of 100 mm, an AP rotation of 3° delivers a lateral offset of about 5 mm. A comparison with **Figure 9** reveals this value to be a good approximation to the upper limits for the σ_{RL} distributions of $Vessel_{LU}$ and $Vessel_{RU}$ displayed in the top row. Larger RL displacements were measured only for the apex: ∼6–7 mm and diaphragm: ∼8–10 mm, as these lung structures are farthest from the reference point in the CC direction. There are no significant differences between eDIBH and HFPV regarding RL displacements.

In accordance with the intrafractional displacements discussed in Section **Intra-Fractional Displacement of Lung Structure Metrics**, the most significant differences between eDIBH and HFPV in spatial variability are found in the CC and AP directions for the diaphragm, carina and for the vessels of the lower and middle left lung segment.

Analogous to the relationship between rotational distribution and RL shifts, the contributions of pitch and roll components to the linear shifts of lung structures in the CC and AP direction can be estimated geometrically. Calculations reveal that only about 10–20% of these displacements are caused by the uncorrected rotations about the RL and CC axes, respectively; the variation in lung volumes due to eDIBH or HFPV represent the dominant factor.

This presentation of lung structure variability in Cartesian space concludes with analysis of comparison of the relative

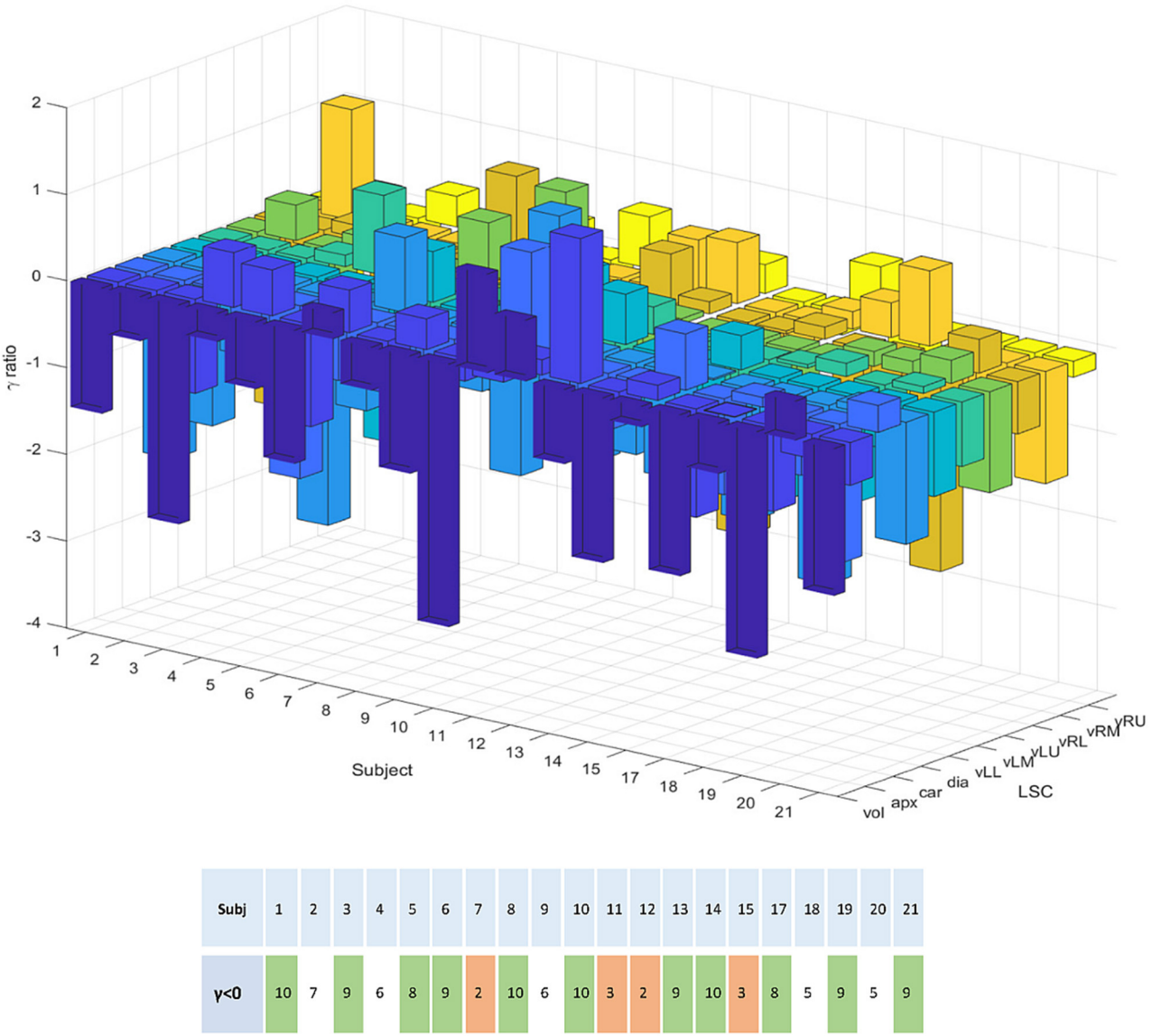

FIGURE 8 | The 3D bar plot displays the logarithm of the ratio, denoted γ, of relative errors in lung structure radial distances and volumes between the motion mitigation methods, eDIBH and HFPV, for each subject, and lung structure or volume. The lower table assigns to each subject the number of values for which the γ ratio is negative, indicating less variability with eDIBH. Green indicates numbers >7, orange those <4. White indicates intermediate numbers.

volumes of variability: $\text{VolOfVar}_{\text{eDIBH}}$ and $\text{VolOfVar}_{\text{HFPV}}$, determined by the ratio between the 95% CL ellipsoid volume and the mean subject lung volume for each subject and lung vessel structure.

The logarithm of the ratio of eDIBH and HFPV relative volumes is shown in **Figure 10** as 2D bar plots. Of the 120 ratios which could be determined, 85 showed less variability with eDIBH, i.e., 71%, confirming the analysis of relative errors in radial distances presented earlier. However, only 10 of the 20 subjects showed exclusively less variability with eDIBH, whereas, three showed exclusively less variability with HFPV; the remaining seven subjects exhibited mixed variabilities.

DISCUSSION

External beam radiation therapy is a highly effective modality in the treatment of lung tumors, yielding similar outcomes as surgery, particularly for early stage non-small-cell lung carcinoma [NSCLC; (40, 41)]. Appropriate respiratory motion management approaches (17), however, are of great importance, especially for PBS-PT (42). As such, breath holding is an effective method to minimize respiratory motion, which is well-established in conventional RT treatments of breast cancer and mediastinal lymphoma (43–46). Its combination with hyperventilation and/or preoxygenation

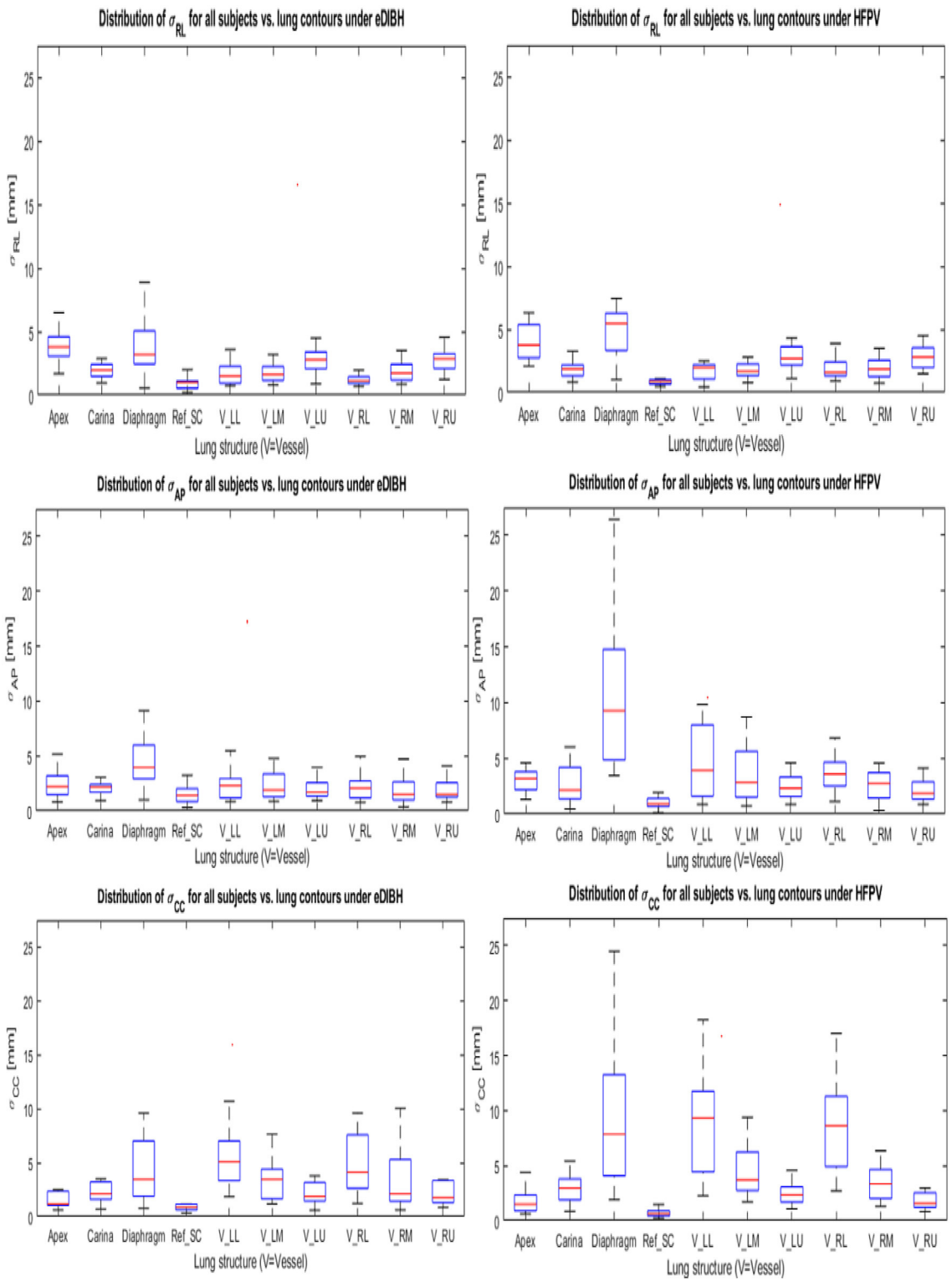

FIGURE 9 | Standard deviations about the mean positions of each LSC-specific cluster in Cartesian coordinates for eDIBH and HFPV (see Section **Measuring Intra- and Interfractional Lung Displacements** and **Figure 3**). The coordinates are labeled in table notation: RL (top row), AP (middle row), and CC (lower row).

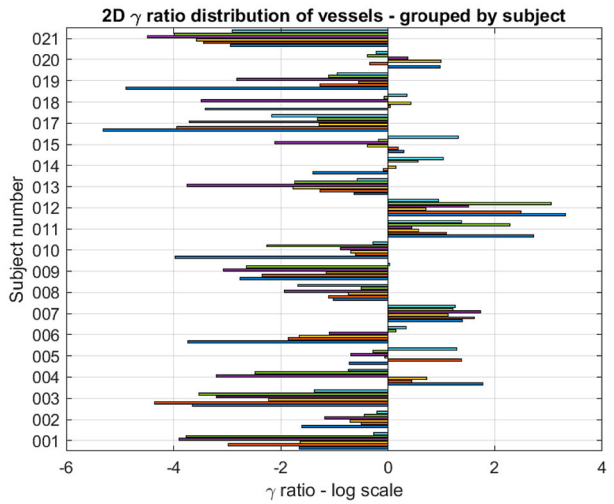

FIGURE 10 | For each subject and lung vessel are plotted the logarithm of the ratio of relative volumes of variability determined from the 95% CL ellipsoids of variability between the eDIBH and HFPV. Negative values indicate lesser variability with eDIBH, positive values lesser variability with HFPV.

for breast irradiation with photons has already been reported (47).

Several studies investigated the use of DIBH for lung cancer RT (26, 39, 48–50). However, clinical breath-hold implementations in proton therapy of lung tumors are currently predominated by device-assisted breath-hold techniques (17, 51–53). Training or coaching, however, is deemed necessary for patient applications, with autonomous breath holding with or without monitoring being the exception. To the authors' knowledge, however, no reports of practical implementation for patient-controlled DIBH supported by physiological measures (hyperventilation, preoxygenation, breath-hold training) are available for application in proton therapy, and only few studies have related breath-hold duration to treatment delivery time. Indeed, the Particle Therapy Cooperative Group (PTCOG) guidelines (54) for implementing PBS-PT in thoracic malignancies consider DIBH to be a realistic clinical treatment approach. However, they also caution that small highly mobile tumors potentially causing large baseline drifts are a significant risk for a consistent DIBH application. Research and clinical practice in the field of motion management for particle therapy, however, has primarily focused on adapting to motion (rescanning, gating, etc.,) rather than effectively mitigating it by eliminating or reducing patient organ motion, e.g., through breath hold.

Following the assumption that effective motion management starts with mitigation, the change in breath-hold duration with breath-hold training and the use of hyperventilation combined with oxygenation were investigated in the present study with 21 healthy subjects. Using MRI assessment to simulate realistic PT treatment conditions, the newly proposed eDIBH and the established HFPV application for respiratory motion suppression were investigated with respect to lung volume variability and reproducibility of lung topographies. The aim of these measurements was the evaluation of applicability and effectiveness of both methods. Since the use of eDIBH envisages breath-hold training prior to the start of proton therapy, not only the effect on breath-hold duration over the study period was analyzed, but also subjects' acceptance of the eDIBH approach compared to the HFPV method was determined.

The main results of the present study demonstrated that by the use of breath-hold training and DIBH enhanced by prior hyperventilation in hyperoxic conditions, breath-hold durations could be increased from 173 ± 73 s on visit 1 to 217 ± 67 s on visit 4, with maximal eDIBH durations in all but one individual subject reaching an eDIBH duration of ≥90 s already at visit 1. The achieved breath-hold durations were similar or longer than the time required to deliver representative PBS proton treatment fields at PSI's Gantry-2 for typical lung tumors. A recent study using a different method to extend breath-hold duration in pulmonary patients (a majority with stage III lung cancer) reported a mean breath-hold duration of 78 s (range 29–223 s) during conventional RT treatment (55). Thus, the increase in breath-hold duration by eDIBH in the healthy subjects of the present study is likely transferrable to lung cancer patients allowing irradiation of adequate PBS-PT fields. Importantly also, lung volumes determined prior to and during breath holds, did not change over the course of four visits. In addition, an important advantage of eDIBH found in this work results from the fact that subjective tolerance of eDIBH was similar to HFPV and presumed, by study subjects, tolerable for patients. Also, home training was given a good rating. Indeed, of the 18 subjects expressing a distinct preference, 14 (∼80%) preferred eDIBH to HFPV. Also, during the study, no adverse events occurred with eDIBH, but one subject was unable to tolerate HFPV.

Detailed analysis showed that lung volumes determined with spirometry and during eDIBH in the MR were larger in males than females. This translated into a tendency for shorter eDIBH duration in females compared to males. Nevertheless, in this female cohort, breath-hold duration was still long enough for a PRT with 141 ± 36 s already on visit 1. The fact that breath-hold duration in both sexes did not change significantly after visit 2 suggests that 1 week of individual home-based breath-hold training with four daily maximal DIBHs, including reassurance of the possibility to extend breath-holds, e.g., by prior deep breathing (56), is sufficient to achieve maximal breath-hold durations. Also, the good correlation found in this study between maximal sitting DIBHs at home and maximal eDIBHs could possibly allow to predict in future patients, already after 1 week of home-based DIBH-training, whether individual patients' breath holds will be of sufficient duration for effective irradiation.

While sufficiently long breath hold durations are essential, it is equally crucial to achieve consistently similar lung volumes and lung topographies over all irradiation days. As for reproducibility of lung volume, no significant difference in FVC and in inter-fractional variability was observed over the course of four visits, with intrafractional deviations being <10% of the standard

deviation of uncertainty of the volume measurements. Thus, lung volume was reproducible and stable over the study course, especially also within each visit. During extended breath holds over the duration of three consecutive, identical MRI sequences, however, as tested on a sub-set of subjects, lung volume was found to decrease significantly after the second sequence repetition. This effects results from the ongoing metabolism where burning a mixture of carbohydrate and fat produces a smaller volume of CO_2 than the volume of O_2 consumed in a given time period (respiratory quotient <1.0). Nevertheless, such volume reductions stayed below 5% over the first and second MRI sequence, which is less than the uncertainty in intrafractional volume determination.

The advantages of eDIBH became evident in the analysis of lung structure positional variability based on a lung structure metric. Five of nine absolute distances between mobile lung structures and a static reference structure at the spine showed, averaged over all subjects, significantly less variability of relative error for eDIBH than for HFPV. These were the carina, diaphragm, and the vessels in the left and right lower lung segment and in the left-middle lung region. The introduction of a subject- and lung structure-specific measure to determine distance variability between eDIBH and HFPV defined by the logarithmic ratio of their relative errors indicated that eDIBH exhibited at least a 70% advantage compared to HFPV. This result was derived from the total number of ratios calculated, as well as by the overall number of subjects showing less variability for eDIBH.

In addition, an approximation of the intrafractional, spatial distribution of the 10 lung structures across all MRIs of each subject provided —after correction of the interfractional translations and separately for eDIBH and HFPV—their individual so-called Volume of Variability. In analogy to the variability of distances, the logarithmic ratio of $VolOfVar_{eDIBH,}$ and $VolOfVar_{HFPV}$ confirmed that the spatial variability for all investigated pulmonary vessels is smaller under eDIBH than for HFPV in 71% of cases. The distributions of positional standard deviations of the 10 lung structures in all three Cartesian dimensions showed that standard deviations are least for the reference structures on which the registrations were based, and most for the diaphragm and for vessels in the lower left and right lung segment. Their magnitude is higher by a factor of 3 for the diaphragm using HFPV than for eDIBH and by a factor of 2 for $Vessel_{LL}$ and $Vessel_{RL}$ with differences between the methods being most apparent in the anterior-posterior and cranial-caudal directions.

In summary, the present results can be interpreted in three ways. Physically, the eDIBH approach has significant and clear advantages over the HFPV method with respect to local reproducibility and stability of lung conditions over time. In practical application, both approaches are feasible under irradiation conditions with proton therapy, whereby both the subjective preference of the study participants and the lower resource requirements speak in favor of eDIBH. Physiologically, the results suggest that the eDIBH procedure could benefit patients that need to achieve a breath-hold duration of $\geq$60–90 s for irradiation therapy. Although, it can be expected that such durations can be achieved in cancer patients without lung morbidity and despite such breath-hold durations having been reported in lung cancer patients (55), further investigations are needed to test the extent to which compromised lung function influences overall breath-hold performance.

In articles related to radiotherapy, average breath-hold durations of around 22 s are reported for breath holds starting from resting breathing (47). This is 2- to 3-fold less than breath holds reported in the present study but in those studies, no or much less emphasis was put on achieving maximal lung volumes at the start of those breath holds. Thus, although the present results are very promising, more research is needed in lung tumor patients in order to ascertain the benefit of the present eDIBH procedure in this patient population.

CONCLUSIONS

Both, eDIBH, and HFPV were well-tolerated and eDIBH duration was long enough to allow potential PRT. Variability in lung volume and anatomical position of lung structures is smaller with eDIBH. Also, if given the opportunity to choose, subjects prefer eDIBH. Thus, eDIBH is a very promising tool for lung tumor therapy with PRT, and further investigation of its applicability in patients is warranted.

DATA AVAILABILITY STATEMENT

Raw data supporting the conclusions of this article are provided by the authors upon reasonable request.

ETHICS STATEMENT

The studies involving human participants were reviewed and approved by Cantonal Ethics Committee North West and Central Switzerland. The patients/participants provided their written informed consent to participate in this study.

AUTHOR CONTRIBUTIONS

FE, PE, MW, DW, and CS contributed to the conception and design of the work. FE, MW, and CG were involved in the acquisition of the data. FE, JM, MW, CG, PE, and CS analyzed and interpreted the data. FE, JM, PE, CS, and AL drafted the manuscript. All authors contributed to the manuscript and approved the submitted version.

ACKNOWLEDGMENTS

The authors would like to thank all participants for their time and patience invested in the study.

REFERENCES

1. Mayles P, Nahum A, Rosenwald JC (editors). *Handbook of Radiotherapy Physics: Theory and Practice*. 1st ed. Boca Raton, FL: CRC Press (2007). doi: 10.1201/9781420012026
2. International Commission on Radiation Units and Measurements. *ICRU Report 50: Prescribing, Recording, and Reporting Photon Beam Therapy*. Washington, DC: International Commission on Radiation Units and Measurements (1993).
3. International Commission on Radiation Units and Measurements. *ICRU Report 62, Prescribing, Recording, and Reporting Photon Beam Therapy (Supplement to ICRU Report 50)*. Bethesda, MD: International Commission on Radiation Units and Measurements (1999).
4. International commission on radiation units and measurements. ICRU report 78, prescribing, recording, and reporting proton-beam therapy. *J Int Comm Radiat Unit Meas*. (2007) 7:11–150. doi: 10.1093/jicru/ndn001
5. Durante M, Paganetti H. Nuclear physics in particle therapy: a review. *Rep Prog Phys*. (2016) 79:096702. doi: 10.1088/0034-4885/79/9/096702
6. Palta J, Yeung D. Precision and uncertainties in proton therapy for nonmoving targets. In: Paganetti H, editor. *Proton Therapy Physics*. 1st ed. Boca Raton, FL: CRC Press (2012). p. 413–33. doi: 10.1201/b11448-14
7. Engelsman M, Bert C. Precision and uncertainties in proton therapy for moving targets. In: Paganetti H, editor. *Proton Therapy Physics*. 1st ed. Boca Raton, FL: CRC Press (2012). p. 435–59. doi: 10.1201/b11448-15
8. Bert C, Durante M. Motion in radiotherapy: particle therapy. *Phys Med Biol*. (2011) 56:R113–44. doi: 10.1088/0031-9155/56/16/R01
9. Bert C, Herfarth K. Management of organ motion in scanned ion beam therapy. *Radiat Oncol*. (2017) 12:170. doi: 10.1186/s13014-017-0911-z
10. Bert C, Grözinger SO, Rietzel E. Quantification of interplay effects of scanned particle beams and moving targets. *Phys Med Biol*. (2008) 53:2253–65. doi: 10.1088/0031-9155/53/9/003
11. Phillips MH, Pedroni E, Blattmann H, Boehringer T, Coray A, Scheib S. Effects of respiratory motion on dose uniformity with a charged particle scanning method. *Phys Med Biol*. (1992) 37:223–34. doi: 10.1088/0031-9155/37/1/016
12. Wink KCJ, Roelofs E, Solberg T, Lin L, Simone CB II, Jakobi A, et al. Particle therapy for non-small cell lung tumors: where do we stand? A systematic review of the literature. *Front Oncol*. (2014) 4:292. doi: 10.3389/fonc.2014.00292
13. Grassberger C, Dowdell S, Sharp G, Paganetti H. Motion mitigation for lung cancer patients treated with active scanning proton therapy. *Med Phys*. (2015) 42:2462–9. doi: 10.1118/1.4916662
14. Bert C, Rietzel E. 4D treatment planning for scanned ion beams. *Radiat Oncol*. (2007) 2:24. doi: 10.1186/1748-717X-2-24
15. Dong L, Yang J, Zhang Y. Image processing in adaptive radiotherapy. In: Brock KK, editor. *Image Processing in Radiation Therapy*. 1st ed. Boca Raton, FL: CRC Press (2013). p. 1–20.
16. Kubiak T. Particle therapy of moving targets-the strategies for tumour motion monitoring and moving targets irradiation. *Br J Radiol*. (2016) 89:20150275. doi: 10.1259/bjr.20150275
17. Keall PJ, Mageras GS, Balter JM, Emery RS, Forster KM, Jiang SB, et al. The management of respiratory motion in radiation oncology report of AAPM Task Group 76. *Med Phys*. (2006) 33:3874–900. doi: 10.1118/1.2349696
18. Lomax AJ, Böhringer T, Bolsi A, Coray D, Emert F, Goitein G, et al. Treatment planning and verification of proton therapy using spot scanning: initial experiences. *Med Phys*. (2004) 31:3150–7. doi: 10.1118/1.1779371
19. Lomax AJ. Intensity modulated proton therapy and its sensitivity to treatment uncertainties 1: the potential effects of calculational uncertainties. *Phys Med Biol*. (2008) 53:1027–42. doi: 10.1088/0031-9155/53/4/014
20. Knopf AC, Stützer K, Richter C, Rucinski A, da Silva J, Phillips J, et al. Required transition from research to clinical application: report on the 4D treatment planning workshops 2014 and 2015. *Phys Med*. (2016) 32:874–82. doi: 10.1016/j.ejmp.2016.05.064
21. Trnkova P, Knaeusl B, Actis O, Bert C, Biegun AK, Boehlen TT, et al. Clinical implementations of 4D pencil beam scanned particle therapy: report on the 4D treatment planning workshop 2016 and 2017. *Phys Med-Eur J Med Phys*. (2018) 54:121–30. doi: 10.1016/j.ejmp.2018.10.002
22. Riboldi M, Orecchia R, Baroni G. Real-time tumour tracking in particle therapy: technological developments and future perspectives. *Lancet Oncol*. (2012) 13:e383–91. doi: 10.1016/S1470-2045(12)70243-7
23. De Ruysscher D, Sterpin E, Haustermans K, Depuydt T. Tumour movement in proton therapy: solutions and remaining questions: a review. *Cancers*. (2015) 7:1143–53. doi: 10.3390/cancers7030829
24. Lu HM, Brett R, Sharp G, Safai S, Jiang S, Flanz J, et al. A respiratory-gated treatment system for proton therapy. *Med Phys*. (2007) 34:3273–8. doi: 10.1118/1.2756602
25. Kanehira T, Matsuura T, Takao S, Matsuzaki Y, Fujii Y, Fujii T, et al. Impact of real-time image gating on spot scanning proton therapy for lung tumors: a simulation study. *Int J Radiat Oncol Biol Phy*. (2017) 97:173–81. doi: 10.1016/j.ijrobp.2016.09.027
26. Boda-Heggemann J, Knopf AC, Simeonova-Chergou A, Wertz H, Stieler F, Jahnke A, et al. Deep inspiration breath hold-based radiation therapy: a clinical review. *Int J Radiat Oncol Biol Phy*. (2016) 94:478–92. doi: 10.1016/j.ijrobp.2015.11.049
27. Péguret N, Ozsahin M, Zeverino M, Belmondo B, Durham AD, Lovis A, et al. Apnea-like suppression of respiratory motion: first evaluation in radiotherapy. *Radiother Oncol*. (2016) 118:220–6. doi: 10.1016/j.radonc.2015.10.011
28. Zhang Y, Huth I, Weber DC, Lomax AJ. A statistical comparison of motion mitigation performances and robustness of various pencil beam scanned proton systems for liver tumour treatments. *Radiother Oncol*. (2018) 128:182–8. doi: 10.1016/j.radonc.2018.01.019
29. Flume PA, Eldridge FL, Edwards LJ, Mattison LE. Relief of the 'air hunger' of breathholding. A role for pulmonary stretch receptors. *Respirat Physiol*. (1996) 103:221–32. doi: 10.1016/0034-5687(95)00094-1
30. Waurick S, Rammelt S, Rassler B, Teller H. Breathing–homeostatic function and voluntary motor activity. *Pflugers Archiv*. (1996) 432(Suppl. 3):R120–6.
31. Miller MR, Hankinson J, Brusasco V, Burgos F, Casaburi R, Coates A, et al. ATS/ERS Task Force. Standardisation of spirometry. *Eur Respir J*. (2005) 26:319–38. doi: 10.1183/09031936.05.00034805
32. Wanger J, Clausen JL, Coates A, Pedersen OF, Brusasco V, Burgos F, et al. Standardisation of the measurement of lung volumes. *Eur Respir J*. (2005) 26:511–22. doi: 10.1183/09031936.05.00035005
33. Fowler WS. Breaking point of breath-holding. *J Appl Physiol*. (1954) 6:539–45. doi: 10.1152/jappl.1954.6.9.539
34. Flume PA, Eldridge FL, Edwards LJ, Houser LM. The fowler breathholding study revisited: continuous rating of respiratory sensation. *Respirat Physiol*. (1994) 95:53–66. doi: 10.1016/0034-5687(94)90047-7
35. Herzog M, Sucec J, Van Diest I, Van den Bergh O, Chan P-YS, Davenport P, et al. Reduced neural gating of respiratory sensations is associated with increased dyspnoea perception. *Eur Respir J*. (2018) 5:1800559. doi: 10.1183/13993003.00559-2018
36. Bain AR, Drvis I, Dujic Z, MacLeod DB, Ainslie PN. Physiology of static breath holding in elite apneists. *Exp Physiol*. (2018) 103:635–51. doi: 10.1113/EP086269
37. Parkes MJ. Breath-holding and its breakpoint. *Exp Physiol*. (2006) 91:1–15. doi: 10.1113/expphysiol.2005.031625
38. Parkes MJ. The limits of breath holding. *Sci Am*. (2012) 306:74–9. doi: 10.1038/scientificamerican0412-74
39. Josipovic M, Persson GF, Dueck J, Bangsgaard JP, Westman G, Specht L, et al. Geometric uncertainties in voluntary deep inspiration breath hold radiotherapy for locally advanced lung cancer. *Radiother Oncol*. (2016) 118:510–4. doi: 10.1016/j.radonc.2015.11.004
40. Baker S, Dahele M, Lagerwaard FJ, Senan S. A critical review of recent developments in radiotherapy for non-small cell lung cancer. *Radiat Oncol*. (2016) 11:115. doi: 10.1186/s13014-016-0693-8
41. Harada H, Murayama S. Proton beam therapy in non-small cell lung cancer: state of the art. *Lung Cancer*. (2017) 8:141–5. doi: 10.2147/LCTT.S117647
42. Vyfhuis M, Onyeuku N, Diwanji T, Mossahebi S, Amin NP, Badiyan SN, et al. Advances in proton therapy in lung cancer. *Ther Adv Respir Dis*. (2018) 12:1–16. doi: 10.1177/1753466618783878
43. Latty D, Stuart KE, Wang W, Ahern V. Review of deep inspiration breath-hold techniques for the treatment of breast cancer. *J Med Radiat Sci*. (2015) 62:74–81. doi: 10.1002/jmrs.96

44. Bergom C, Currey A, Desai N, Tai A, Strauss JB. Deep inspiration breath hold: techniques and advantages for cardiac sparing during breast cancer irradiation. *Front Oncol*. (2018) 8:87. doi: 10.3389/fonc.2018.00087
45. Aznar MC, Maraldo MV, Schut DA, Lundemann M, Brodin NP, Vogelius IR, et al. Minimizing late effects for patients with mediastinal Hodgkin lymphoma: deep inspiration breath-hold, IMRT, or both? *Int J Radiat Oncol Biol Phys*. (2015) 92:169–74. doi: 10.1016/j.ijrobp.2015.01.013
46. Baues C, Marnitz S, Engert A, Baus W, Jablonska K, Fogliata A, et al. Proton versus photon deep inspiration breath hold technique in patients with hodgkin lymphoma and mediastinal radiation : a planning comparison of deep inspiration breath hold intensity modulation radiotherapy and intensity modulated proton therapy. *Radiat Oncol*. (2018) 13:122. doi: 10.1186/s13014-018-1066-2
47. Roth J, Engenhart-Cabillic R, Eberhardt L, Timmesfeld N, Strassmann G. Preoxygenated hyperventilated hypocapnic apnea-induced radiation (PHAIR) in breast cancer patients. *Radiother Oncol*. (2011) 100:231–5. doi: 10.1016/j.radonc.2011.02.017
48. Wong JW, Sharpe MB, Jaffray DA, Kini VR, Robertson JM, Stromberg JS, et al. The use of active breathing control (ABC) to reduce margin for breathing motion. *Int J Radiat Oncol Biol Phys*. (1999) 44:911–9. doi: 10.1016/S0360-3016(99)00056-5
49. Hanley J, Debois MM, Mah D, Mageras GS, Raben A, Rosenzweig K, et al. Deep inspiration breath-hold technique for lung tumors: the potential value of target immobilization and reduced lung density in dose escalation. *Int J Radiat Oncol Biol Phys*. (1999) 45:603–11. doi: 10.1016/S0360-3016(99)00154-6
50. Mah D, Hanley J, Rosenzweig KE, Yorke E, Braban L, Ling CC, et al. Technical aspects of the deep inspiration breath-hold technique in the treatment of thoracic cancer. *Int J Radiat Oncol Biol Phys*. (2000) 48:1175–85. doi: 10.1016/S0360-3016(00)00747-1
51. Remouchamps VM, Letts N, Vicini FA, Sharpe MB, Kestin LL, Chen PY, et al. Initial clinical experience with moderate deep-inspiration breath hold using an active breathing control device in the treatment of patients with left-sided breast cancer using external beam radiation therapy. *Int J Radiat Oncol Biol Phys*. (2003) 56:704–15. doi: 10.1016/S0360-3016(03)00010-5
52. Giraud P, Morvan E, Claude L, Mornex F, Le Pechoux C, Bachaud JM, et al. Respiratory gating techniques for optimization of lung cancer radiotherapy. *J Thorac Oncol*. (2011) 6:2058–68. doi: 10.1097/JTO.0b013e3182307ec2
53. Mazars P, Garcia R. 12 Study of the anatomy position reproducibility during deep inspiration breath hold. *Phys Med*. (2018) 56:45–6. doi: 10.1016/j.ejmp.2018.09.094
54. Chang JY, Zhang X, Knopf A, Li H, Mori S, Dong L, et al. Consensus guidelines for implementing pencil-beam scanning proton therapy for thoracic malignancies on behalf of the PTCOG thoracic and lymphoma subcommittee. *Int J Radiat Oncol Biol Phys*. (2017) 99:41–50. doi: 10.1016/j.ijrobp.2017.05.014
55. Peeters S, Vaassen F, Hazelaar C, Vaniqui A, Rousch E, Tissen D, et al. Visually guided inspiration breath-hold facilitated with nasal high flow therapy in locally advanced lung cancer. *Acta Oncol*. (2020). doi: 10.1080/0284186X.2020.1856408. [Epub ahead of print].
56. Klocke FJ, Rahn H. Breath holding after breathing of oxygen. *J Appl Physiol*. (1959) 14:689–93. doi: 10.1152/jappl.1959.14.5.689

Conflict of Interest: The authors declare that the research was conducted in the absence of any commercial or financial relationships that could be construed as a potential conflict of interest.

Copyright © 2021 Emert, Missimer, Eichenberger, Walser, Gmür, Lomax, Weber and Spengler. This is an open-access article distributed under the terms of the Creative Commons Attribution License (CC BY). The use, distribution or reproduction in other forums is permitted, provided the original author(s) and the copyright owner(s) are credited and that the original publication in this journal is cited, in accordance with accepted academic practice. No use, distribution or reproduction is permitted which does not comply with these terms.

frontiers in Oncology

ORIGINAL RESEARCH
published: 12 May 2021
doi: 10.3389/fonc.2021.599018

Clinical Implementation of Proton Therapy Using Pencil-Beam Scanning Delivery Combined With Static Apertures

Christian Bäumer[1,2,3,4], Sandija Plaude[1,2], Dalia Ahmad Khalil[1,2,5], Dirk Geismar[1,2,3,5], Paul-Heinz Kramer[1,2], Kevin Kröninger[4], Christian Nitsch[4], Jörg Wulff[1,2] and Beate Timmermann[1,2,3,5]*

[1] West German Proton Therapy Centre Essen, Essen, Germany, [2] West German Cancer Center (WTZ), University Hospital Essen, Essen, Germany, [3] German Cancer Consortium (DKTK), Heidelberg, Germany, [4] Faculty of Physics, TU Dortmund University, Dortmund, Germany, [5] Department of Particle Therapy, University Hospital Essen, Essen, Germany

Proton therapy makes use of the favorable depth-dose distribution with its characteristic Bragg peak to spare normal tissue distal of the target volume. A steep dose gradient would be desired in lateral dimensions, too. The widespread spot scanning delivery technique is based, however, on pencil-beams with in-air spot full-widths-at-half-maximum of typically 1 cm or more. This hampers the sparing of organs-at-risk if small-scale structures adjacent to the target volume are concerned. The trimming of spot scanning fields with collimating apertures constitutes a simple measure to increase the transversal dose gradient. The current study describes the clinical implementation of brass apertures in conjunction with the pencil-beam scanning delivery mode at a horizontal, clinical treatment head based on commercial hardware and software components. Furthermore, clinical cases, which comprised craniopharyngiomas, re-irradiations and ocular tumors, were evaluated. The dosimetric benefits of 31 treatment plans using apertures were compared to the corresponding plans without aperture. Furthermore, an overview of the radiation protection aspects is given. Regarding the results, robust optimization considering range and setup uncertainties was combined with apertures. The treatment plan optimizations followed a single-field uniform dose or a restricted multi-field optimization approach. Robustness evaluation was expanded to account for possible deviations of the center of the pencil-beam delivery and the mechanical center of the aperture holder. Supplementary apertures improved the conformity index on average by 15.3%. The volume of the dose gradient surrounding the PTV (evaluated between 80 and 20% dose levels) was decreased on average by 17.6%. The mean dose of the hippocampi could be reduced on average by 2.9 GyRBE. In particular cases the apertures facilitated a sparing of an organ-at-risk, e.g. the eye lens or the brainstem. For six craniopharyngioma cases the inclusion of apertures led to a reduction of the mean dose of 1.5 GyRBE (13%) for the brain and 3.1 GyRBE (16%) for the hippocampi.

Keywords: proton therapy, pencil-beam scanning, aperture, quality assurance, radiation protection, brain tumors, ocular tumors

OPEN ACCESS

Edited by:
Brian Timothy Collins, Georgetown University, United States

Reviewed by:
Shahed Nicolas Badiyan, Washington University in St. Louis, United States
Dalong Pang, Georgetown University, United States

****Correspondence:***
Christian Bäumer
christian.baeumer@uk-essen.de

Specialty section:
This article was submitted to Radiation Oncology, a section of the journal Frontiers in Oncology

Received: *26 August 2020*
Accepted: *06 April 2021*
Published: *12 May 2021*

Citation:
Bäumer C, Plaude S, Khalil DA, Geismar D, Kramer P-H, Kröninger K, Nitsch C, Wulff J and Timmermann B (2021) Clinical Implementation of Proton Therapy Using Pencil-Beam Scanning Delivery Combined With Static Apertures. Front. Oncol. 11:599018. doi: 10.3389/fonc.2021.599018

INTRODUCTION

The depth dose characteristics with its distinct Bragg Peak facilitate a conformation advantage of proton beam treatment fields over hard X-ray fields. In lateral directions, however, the lateral dose fall-off limits the options to cover the target volume while keeping the dose to organs at risk low. This holds particularly true for the pencil-beam scanning delivery method (PBS), which has gained importance over passive delivery techniques with collimating apertures in the last few years. The conjunction of pencil-beam scanning with apertures constitutes a hybrid of PBS and passive beam delivery facilitating a good lateral dose fall-off (1–6). PBS-with-apertures can be technically realized through static apertures, multi-leaf collimators or dynamic collimators, which are synchronized with the PBS delivery (7–10). The concerns toward PBS with static apertures are similar to those toward passive delivery techniques: extra costs of the aperture production, extra time for the radiation therapy technologists to exchange beam shaping devices during a treatment session, less flexibility for plan adaptation, and radiation protection issues regarding handling and storage. The advantage of PBS with static apertures is the possibility to realize small air gaps in clinical treatment plans, which is beneficial for the lateral dose gradient (5, 11). Previously, multi-leaf collimators featured large air gaps (11). Recently, dynamic adaptive collimators, which enable small air gaps, were clinically introduced (9, 10). These dynamic collimators are necessary to compensate for wide PBS spots from a gantry-mounted cyclotron. Auxiliary beam-shaping hardware for proton PBS is used mainly for targets at shallow to medium depths, because the contribution of scattering in the patient dominates the lateral dose gradient at large radiological depths. The technical design of the proton treatment machine dictates the options for the clinical user to employ PBS-with-apertures. For instance, in the current study the mechanics supporting PBS with static apertures is available, because a multi-modal proton nozzle supporting active and passive delivery modes is used. Alternatively, dedicated PBS nozzles can be equipped with an extra holder for apertures.

The current work gives an account of the implementation of PBS with static, field-specific apertures in our proton therapy facility. The hardware and software set-up and the quality assurance (QA) are described in Section 2. This section also contains a description of the treatment planning techniques together with the design of the in-silico study, which compares the dose distribution of clinically applied treatment plans using brass apertures with the respective plans without supplementary apertures. Section 3 presents the results of the *in silico* plan comparison. We considered pediatric patients, re-irradiations, and small target volumes including eye tumors and stereotactical treatments as potential cases, which would benefit from the addition of apertures to PBS treatment fields. Section 4 discusses the possible clinical benefits of the supplement of PBS fields with apertures and the possible radiation protection issues.

MATERIALS AND METHODS

Proton Therapy Equipment

The delivery of proton fields was facilitated by the ProteusPlus therapy machine (IBA, Lovain-La-Neuve, Belgium) operated in spot-by-spot PBS mode. Proton acceleration and beam delivery are controlled by the treatment control system (TCS). Protons are accelerated in the isochronous cyclotron to the maximum kinetic energy of about 228 MeV. The energy can be reduced continuously down to 100 MeV downstream of the cyclotron with a wheel mounted wedge. The beam is cleaned up with analyzing magnets and slits and subsequently lead to a fixed-beam treatment room with horizontally mounted treatment head. **Table 1** gives an overview of the spot sizes, which are typical of the fields applied in the frame of the current study. The treatment head used for the current study was the so-called "universal nozzle" which supports single scattering, double scattering, uniform scanning, and PBS. It contains thin transmission monitor ionization chambers and a snout. The snout of type "Snout180" can be moved in beam direction to optimize the air gap. It provides slots for two brass apertures and a holder for range shifters (PBS) or range compensators. The patients were positioned (30 cases in supine position) on a PatLog air plate couch which was mounted to the patient positioning system (PPS). The PPS can be translated in three directions and rotated in the horizontal plane by ±180°. Additionally, angular corrections in pitch and roll directions are feasible up to ±3°. The patient set-up was verified with the X-ray based patient positioning and verification system (PPVS) which comprised three orthogonal X-ray panels. Generally, the X-ray imaging of the PPVS constitutes the geometrical reference for the isocenter position. The X-ray panel-A images in beam direction. It is used for quality assurance of the spot position (*Quality Assurance*).

Aperture Production and Use

The brass material was composed of 58% copper, 39% zinc and 3% lead. In our milling-machine shop (MMS) non-divergent brass apertures with a thickness of 3.3 cm were fabricated with a computer numerical control milling machine (Leadwell/

TABLE 1 | Pencil-beam scanning in-air spot characteristics of the treatment plans of the current study.

Energy (MeV)	σ (mm)	Comment
100	8.1	minimum energy among all cases
110	7.4	median of the lowest energy of all cases
130	6.5	median energy of all cases
150	5.3	median of the highest energy of all cases
170	4.6	maximum energy among all cases

Fields were applied with the IBA universal nozzle of the fixed-beam treatment room of WPE. σ refers to the standard deviation derived from a fit of a Gaussian distribution to the lateral spot profile. Proton energy values of the layers were rounded, because spot characteristics were measured in the isocenter plane in steps of 10 MeV in the clinical commissioning.

Taiwan). The milling head diameter was 1 cm. Aiming for an efficient production and treatment workflow, the actual number of apertures used was optimized per treatment field. It depended on the residual range R80 (in water) at the exit of the snout, i.e. it accounted for the energy degradation of an optional range shifter. In any case a field-specific aperture was mounted in the downstream slot (see *Proton Therapy Equipment*). If R80 exceeded 15.5 cm, a second field-specific aperture was mounted in the upstream slot. Otherwise, an open ring aperture was inserted in the upstream slot.

Treatment Planning and Dosimetric Analysis

A total of 31 patients (average age of 16 y, median age of 10 y, 21 patients <18y) were planned and treated in a fixed gantry room using PBS-with-apertures. The target volumes (5.4 to 229.0 cm^3, median 33 cm^3) were located in the skull. Cases were diagnosed, e.g., with craniopharyngimonas (n = 6) and ependymomas (n = 4). Some cases (n = 5) were retreatments. **Table 2** provides more detailed information.

The treatment planning system (TPS) RayStation (versions 6 and 7; RaySearch Laboratories, Stockholm/Sweden) was used (12). Dose distributions were simulated with the Monte Carlo (MC) dose engine (13), which transported primary and secondary protons with a Class II method. Secondary deuterons and alpha particles were tracked in the continuous slowing down approximation, i.e. their energy loss was accounted for while scattering, straggling and nuclear interactions were disregarded. The source of primary protons was located upstream of the beam shaping devices. Thus, the MC transport accounted for effects like edge scattering at the inner aperture surface and large-angle scattering in the range shifter. Secondary neutral particles were not simulated in the MC dose engine.

In the initial planning phase the RayStation optimization module was used to customize the spot fluences of the treatment plan. Robust optimizations were performed with an isotropic 3 mm isocenter shift and 3.5% density uncertainty. Treatment plan optimizations started with a single-field uniform dose strategy. This proved to be adequate for most cases. In other cases a restricted multi-field optimization with dose modulations up to ±20% per field was realized. The resulting plan, which fulfilled most of the clinically relevant dose requirements, could already be applied clinically. In the scope of the current study, it served as a reference for a typical PBS treatment plan. It will be called "uncollimated plan" in the following. Starting with the uncollimated plan, apertures were inserted for all fields specifying a lateral margin for the PTV coverage and blocking of adjacent organs at risk (OAR), if necessary. The margin accounts for the dose fall-off between the 50% and >90% isodose lines with the 50% isodose line coinciding with the projected aperture edge for a uniform field and a homogenous phantom. It was, thus, adapted for each individual field. The spot positions exceeded the aperture boundary by typically 5 mm in the beams-eye-view isocenter plane ("overscan"). **Figure 1** shows an example of the beams-eye view of an uncollimated treatment field compared to its collimated implementation.

The number of fields and their arrangement were chosen depending of the localization of the target volume. For the treatment of ocular tumors on average 1.6 fields were used, since for the most of these cases the target volume is superficial, small and with a simple geometry. Centrally located target volumes like craniopharyngiomas and tumors of the ventricle system were treated with three fields, i.e. two lateral and one vertex field, to decrease the dose to temporal lobes and hippocampi. For the target volumes in the skull base and those located more asymmetrically against the middle line of the brain, two fields were chosen to avoid treating from contralateral side. The air gap was chosen as small as possible to reduce the lateral penumbra while avoiding the possible collision. For fields delivering dose to shallow radiological depths range shifters were used. The range shifter was placed downstream of the aperture. The thinnest range shifter was chosen from a set of three range shifters for each individual field.

TABLE 2 | Overview of all cases which were treated with PBS-with-apertures and which were evaluated in the current study.

Localization	Diagnosis	Number of patients/retreatments	Average age (years)	V_{PTV} (cm^3)
Orbital tumors	Retinoblastoma	3	3	9.0
	Embryonal Rhabdomyosarcoma	1	12	16.2
	Optic nerve Glioma	1	14	113.8
	Choroidal Melanoma	1	51	8.6
	Choroidal Hemangioma	1	20	12.0
Base of skull tumors	Optic Posterior Pathway Glioma	1	8	67.0
	Brainstem Glioma	1	2	31.5
	Clivuschordoma	1	58	20.9
Intracranial tumors				
(infratentorial)	Ependymoma	6/2	9	22.5
	Atypical Teratoid Rhabdoid tum.	1/1	6	30.8
(supratentorial, midline)	Craniopharyngioma	7/1	12	97.6
	Neurocytoma	1	20	27.0
	Germ Cell tumor	3/1	8	52.4
	Astrocytoma	1	37	38.7
(supratentorial, unilateral)	Astrocytoma	2	42	173.7

For patient groups the age and the average volume of the PTV (V_{PTV}) are listed.

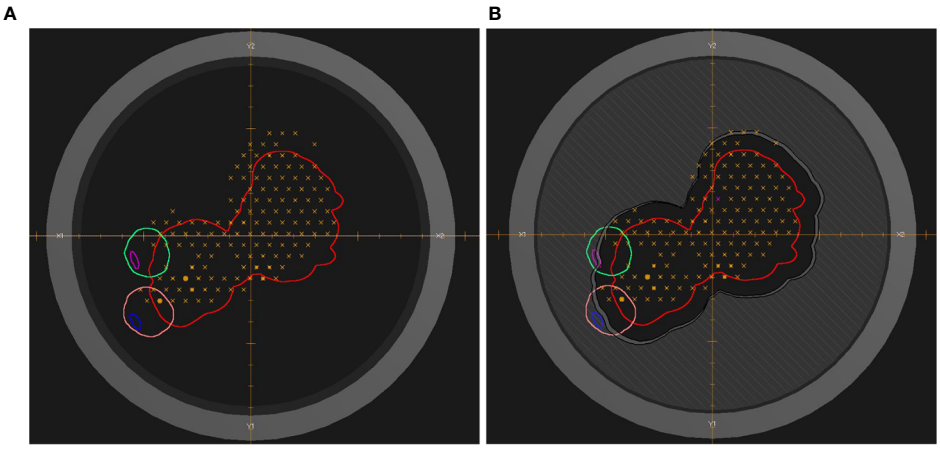

FIGURE 1 | Beams-eye view of a treatment field of the uncollimated plan **(A)** and the treatment plan with apertures **(B)**. The red contour indicates the PTV. The pink (blue) and green (magenta) contours indicate the eye (lens). The dark gray hatched area visualizes the brass of the aperture. The dark gray annular ring represents the snout holder. Orange crosses and circles indicate the centers of individual pencil-beam scanning spots of one of the energy layers. The dose distribution of the treatment plan is shown in **Figure 6**.

The following quantities were used to evaluate the dosimetric performance of PBS-with-apertures:

- $\Delta V_{20\text{-}80\%}$: quantifies the dose reduction in the dose gradient around the PTV. Maes et al. (5) compared the distance between the 20 and 80% isodose line of PBS fields with and without apertures, in order to characterize the lateral penumbra. Since the patient anatomy is not homogeneous [as in Ref. (5)] and the geometry of targets is quite complicated, a difference of volume between 80 and 20% isodose lines was analyzed with operations on regions-of-interest in RayStation. $\Delta V_{20\text{-}80\%}$ combines the 80–20% fall-off distance of Ref. (5) with the 10 mm ring surrounding the PTV of Refs. (8, 14).
- CI 50% (the conformity index of the 50% dose level of the prescription dose) was used to quantify improvements of the dose conformity (14). CI 50% was computed in RayStation as the ratio between the volume of region of interest (ROI) covered by 50% isodose line and the volume of the PTV.

For the three retinoblastoma cases (**Table 2**) the 20 and 50% isodose lines would partly lie in a volume outside the body and external contours. RayStation forces the corresponding regions of these isodose lines to the external contour. The dose statistics for the considered OARs like optic nerve, brainstem, thalamus, and hippocampus were assessed with RayStation using a dose computation on a 2 mm grid. Accounting for the variation of clinical goals, location, shape and volume of the target as well as the dose concept, relevant dose differences included in the plan comparison were defined as follows. A relevant dosimetric improvement for an OAR reported in *Dosimetric Advantages Of Supplementary Static Apertures: Results* exceeds a dose level of 20% of prescribed dose with at least 3% difference between uncollimated PBS and PBS-with-apertures. The first criterion was not applied to the eye lens with a tolerance dose level of 5 GyRBE.

Craniopharyngioma cases were selected for a more detailed analysis in terms of some clinically relevant dosimetric parameters of the OARs. Six clinically delivered treatment plans were analyzed and compared. The prescribed treatment dose was 54 GyRBE.

Data Workflow

Information about the field-specific apertures was passed within a DICOM RTIonplan from RayStation *via* the oncology information system (Mosaiq, Elekta, Stockholm/Sweden) to the TCS containing mounting position, material, label, thickness and a series of 2D points along the aperture contour. In RayStation and in the DICOM transfer a double set of identical apertures in the consecutive slots was coded by a single aperture of 6.5 cm thickness. Mosaiq provided an additional description for the beam shaping devices called "number of pieces". This value was manually set in the course of the planning process. Mosaiq also facilitated the electronic interface to the MMS. It also acted as a record&verify system. In this frame, the field-specific apertures were tagged with a barcode label and scanned prior to field application.

Quality Assurance

Table 3 provides an overview of the implemented QA procedures. Generally, the QA program of a medical proton accelerator facility should be in line with the report of the AAPM task group 224 (15). That report does not cover the QA processes for PBS-with-apertures but for PBS combined with static field-shaping MLCs. Alternatively, the tolerance of the leaf position accuracy might be taken from TG 224, which is ±2 mm or ±1 mm if field patching or matching is performed. Aiming at an overall beam to target accuracy of less than 1 mm, we adopted the tighter limit of ±1 mm and defined a dedicated PBS-A QA-program as outlined in **Table 3**. In general, one has to test the co-incidence of three independent coordinate-systems: x-ray

TABLE 3 | Overview of quality assurance procedures. "MPE review" refers to the clinical release of a treatment plan by a certified medical physicist ("medical physics expert").

Parameter	Warning level	Tolerance level	Test interval	Test device/comment
Co-incidence of coord. of X-ray field and PBS field	0.5 mm	1 mm	monthly	Lynx2D (EBT3 as alternative) with radio-opaque fiducial
Co-incidence of coord. of X-ray field and PBS field	–	1.5 mm	daily	spot positioning test Sun Nuclear DailyQA3
Co-incidence of aperture & PBS	–	1 mm	monthly	Lynx2D
Relative spot position	– –	<5% of spots >1 mm max 1.5 mm	monthly	Lynx2D
Outline of fabricated aperture	–	1 mm	field-specific	visual test with print-out
Dose plane of fields: γ -test	$\gamma < 1$ for <95%	$\gamma < 1$ for <90%	field-specific	DigiPhant; global γ 3%/2 mm, 10% dose threshold
Number of apertures correct	–	pass/fail	field-specific	Python script; MPE review

EBT3 is a radiochromic film of the vendor Ashland. Lynx2D is a scintillation screen with electronic readout (IBA dosimetry). "coord." is used as abbreviation for "coordinates". The Python script runs within the RayStation treatment planning system.

imaging, PBS and aperture. This means the origin of those need to be aligned at a common isocenter. The positioning of the aperture relative to the PBS field is impacted by the aperture manufacturing, but more importantly by the snout movement and aperture mounting mechanism. The co-incidence of aperture versus proton isocenter is tested on monthly basis with a tolerance of ±1 mm. The impact of this possible misalignment is evaluated for each individual treatment field in our TPS, as detailed in the next section. The daily QA procedures in our center (16) were not adapted. Furthermore, the outline of the milled opening of a fabricated aperture is visually compared against a printed hard copy from the TPS.

Robustness Analysis

As shown in previous works [see, e.g., Refs. (17, 18)] the geometrical expansion of a structure with a margin could fail to prevent underdosage of the target volume and overdosage of organs-at-risk in particle therapy. Consequently, a robustness evaluation based on perturbed dose scenarios was established as part of our treatment planning QA adhering to the concept of Ref. (18). Using the built-in function of RayStation to compute a perturbed dose distribution, a simultaneous set-up shift in all cardinal directions with the same sign combined with a rescaling of the mass density, was performed for all treatment plans. Considering a shift and a rescaling with both signs, this yielded four perturbed scenarios. The parameters of the perturbations were chosen to get a confidence level of 90%.

If apertures are used for field shaping, a systematic offset of spot positions and a systematic offset of the aperture contribute to the set-up error. The spot position offset and the aperture offset could have different signs and different values as outlined in the previous section. This kind of perturbation scenario is not covered by the built-in perturbation tool of RayStation. In our customized Python script four copies of the clinical plan were created which would serve as perturbed scenarios of the nominal plan. In each copy the coordinates of the aperture contour were shifted by ±1 mm independently in each lateral direction. The dosimetrist selected the worst case scenario of the four so-established perturbed scenarios of misaligned apertures, which is in turn were used as a starting scenario of the conventional perturbation analysis.

DOSIMETRIC ADVANTAGES OF SUPPLEMENTARY STATIC APERTURES: RESULTS

The overall reduction of the dose-volume between 80 and 20% isodose lines ($\Delta V_{20\text{-}80\%}$) is depicted in **Figure 2**. A clear dose reduction of the volume around the target volume is visible. The addition of collimated apertures reduces $\Delta V_{20\text{-}80\%}$ on average by 17.6% (median 13.8%). For the full cohort of 31 cases the mean brain dose could be reduced on average by 1.2 GyRBE through apertures. The CI of the 50% isodose line increased on average by 15.3% (median 12.1%) when PBS-with-apertures was used. **Table 4** shows the dosimetric improvements per tumor entity.

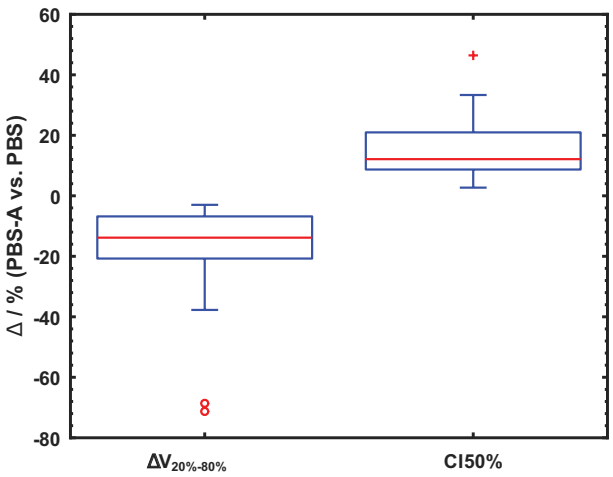

FIGURE 2 | Percentage difference of $\Delta V_{20\text{-}80\%}$ and CI 50% between PBS plans with and without collimating apertures visualized in a box-whisker plot. $\Delta V_{20\text{-}80\%}$, volume between 20 and 80% isodose lines; CI 50%, conformity index of 50% isodose line; PBS, uncollimated pencil beam scanning; PBS-A, pencil beam scanning with apertures. The boxes (whisker) indicate the 25th and 75th percentiles (1.5 times interquartile range). Data points outside the three times (1.5 and three times) the interquartile range are indicated by open circles (plus symbol). Median values are indicated by red lines.

This table reflects the variation of the dosimetric impact of auxiliary apertures among cases.

The most noticeable improvement regarding dose sparing is a dose reduction of the hippocampi, which varied between 1.6 and 4.7 GyRBE with a mean value of 2.9 GyRBE. The level of the mean dose for the hippocampi of the considered cases was on average 20.3 GyRBE. **Figure 3** provides an overview of the dose reduction facilitated with field-specific apertures for selected OARs. In case of bi-lateral structures, the value refers to the structure receiving the higher dose.

The target volumes of the six craniopharyngioma cases are located near the most important OARs like brainstem, optic nerves, chiasma and hippocampi. Usually target volumes overlap with OARs. For this reason almost no difference was observed for the dose maximum (D_{max}) or the dose receiving 1% of a considered volume (D_1). Therefore, the average dose of OARs (D_{mean}) was compared even for serial-type OARs. An absolute dose difference was calculated and summarized in **Figure 4**. The biggest benefit of using PBS-with-apertures was achieved for thalamus, brainstem, and hippocampus reducing D_{mean} by 5.5, 5.6 and 3.1 GyREBE, respectively. The rather large variation in dose reduction for the thalamus could be explained by the varying proximity to the target volumes. **Figure 5** shows the exemplary dose distribution of a case, which benefited most from the use of apertures in terms of sparing of both thalami.

For two cases the PBS-with-aperture technique facilitated a qualitative improvement of OAR sparing by reducing the mean dose for the eye lens below 5 GyRBE. This would not have been achieved with open PBS fields. For these two cases OAR sparing had the highest priority. Consequently, the PTV coverage was compromised in the uncollimated plans. **Figure 6** provides an example of the dose distribution for one of these cases.

Two retreatment cases were planned with a similar approach. Here, the maximum dose to the brainstem could be reduced. **Figure 7** provides an example. The primary goal was the sparing of the brainstem. The dose gradient at the interface between PTV and brainstem is squeezed (**Figure 7A**) compared to the uncollimated plan (**Figure 7B**). The OAR constraints could already be met with uncollimated plans for the other 27 cases. In those cases the apertures facilitate an extra sparing of normal tissue.

TABLE 4 | Percentage difference in $\Delta V_{20\text{-}80\%}$ and CI 50% for PBS-with-aperture plans compared with uncollimated PBS plans.

Tumor entity	Vol. 20–80%	CI-50%
Orbital tumors	−27.0%	18.0%
Craniopharyngioma	−13.6%	13.6%
Ependymoma	−16.0%	8.0%
Astrocytoma	−3.3%	7.8%
Retreatment	−30.4%	21.0%
Other brain tumors	−7.7%	17.3%

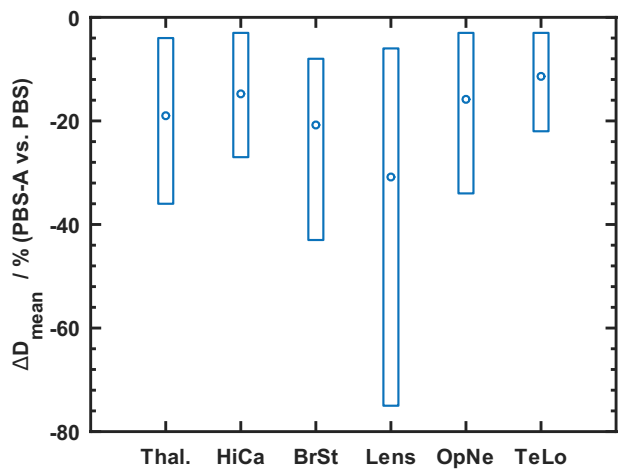

FIGURE 3 | Summary of the mean dose (D_{mean}) reduction for OARs using PBS-with-apertures ("PBS-A") indicated by circles. The boxes show the full range of achieved reductions. The shown structures are Thal, thalamus; Hica, hippocampus; BrSt, brainstem; OpNe, eye lens, optical nerve; TeLo, temporal lobe.

DISCUSSION

Clinical Benefits of Treatment Plans Using Apertures

The benefits of PBS-with-apertures could be assessed by comparing with previous studies, which used a similar technique (2, 19–21). Furthermore, the dosimetric improvements were compared to *in silico* studies of PBS combined with dynamic collimation (8, 14). As pointed out in Ref. (14), that technique is supposed to be superior to PBS with static apertures in terms of conformality and served, thus, as a

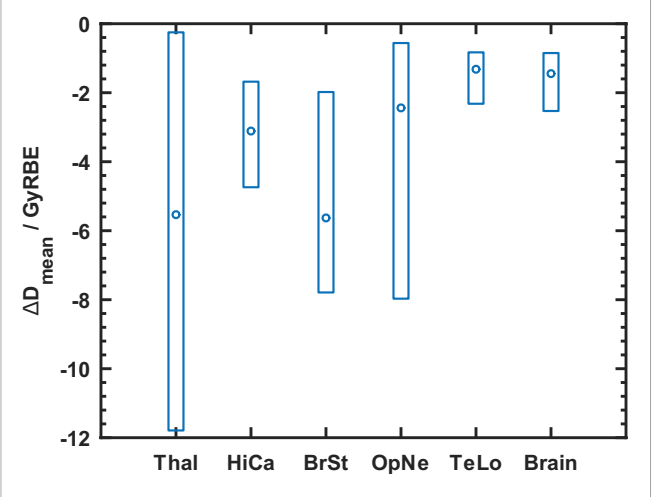

FIGURE 4 | Dose reduction to organs-at-risk (OAR) for craniopharyngioma cases comparing plans with aperture ("PBS-A") with uncollimated plans ("PBS"). Percentage difference of D_{mean} for organs-at-risk between the plans with and without apertures. The boxes show the full range of achieved reductions. The shown structures are Thal, thalamus; HiCa, hippocampus; BrSt, brainstem; OpNe, optical nerve; TeLo, temporal lobe; and brain.

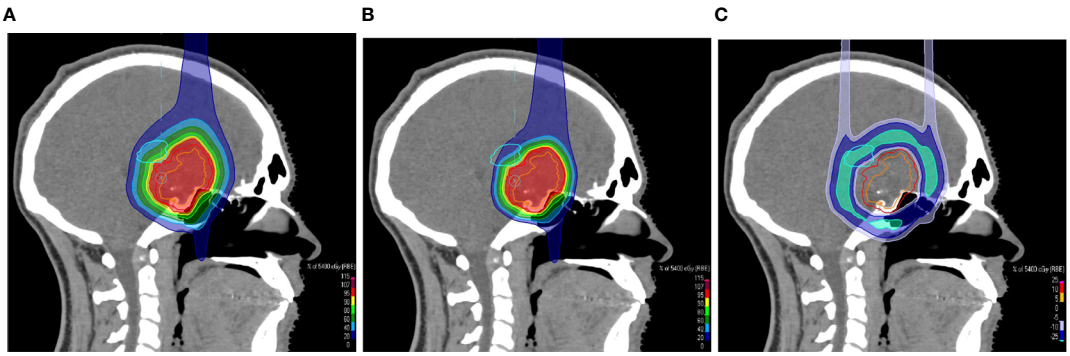

FIGURE 5 | Sagittal CT slices overlaid with a colorwash representation of the dose distribution of the uncollimated plan **(A)** and the treatment plan with apertures **(B)** for the treatment of a suprasellar craniopharyngioma. The screenshots of the treatment planning in RayStation show the dose sparing of the left thalamus, which is indicated by the light blue contour. **(C)** shows the dose difference between the plans.

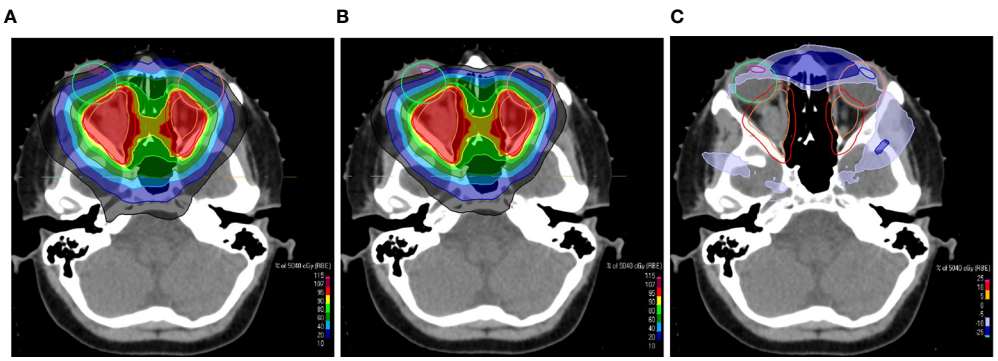

FIGURE 6 | Transversal CT slices overlaid with a colorwash representation of the dose distribution of the uncollimated plan **(A)** and the plan with apertures **(B)** for the treatment of an opticus glioma. The screenshots of the treatment planning in RayStation show the dose sparing of the eye lenses, which are indicated by the blue and magenta contours. **(C)** shows the dose difference between the plans. The beams eye view of one of the treatment fields is shown in **Figure 1**.

best case of proton PBS with extra beam shaping hardware. To the best of our knowledge, the current study is together with Ref. (19) the only one about patients treated with PBS in conjunction with supplementary collimators. In this regard it's the first study evaluating intracranial and orbital tumors. Furthermore, the patient cohort is clearly larger as in the previous studies mentioned above.

The current study identified a benefit for the hippocampi. For cases with a relevant sparing of the hippocampi the dose could be reduced on average by about 3 GyRBE (**Figure 4**). References (22, 23) stressed the clinical relevance of dosimetric improvements of this size for the hippocampi. Therefore, optimal sparing of the hippocampi is increasingly considered an important aim in treatment planning. For instance, the SIOP PNET 5 trial (ClinicalTrials.gov identifier: NCT02066220) and the SIOP Ependymoma Program II (ClinicalTrials.gov Identifier: NCT02265770) require contouring and dose reporting of the hippocampi. Clinical data about side effects are sparse and recent studies regarding neurocognitive impairment appear to be inconsistent (24, 25). The dose reductions achieved in the current paper are expected to reduce the probability of neurocognitive impairment (24, 26), which is currently hard to quantify with normal-tissue complication probability (NTCP)-models (23, 25, 27).

This study found a mean reduction of $\Delta V_{20\text{-}80\%}$ by 13.6%. Reference (14) reported about a 5.2% reduction of the mean dose of a 10 mm thick ring surrounding the PTV. That study also pointed out that the mean dose to the 10 mm ring could be reduced with dynamic collimation on average by 13.7%. The average reduction of mean dose to the healthy brain with energy-layer specific dynamic collimation was on average 25% in Ref. (8).

As for almost all uncollimated plans the dose to the OARs was already well below the tolerance level, a benefit of supplementary apertures for a risk-adapted adjustment of the high-dose volume was reported only in two out of 31 cases. Of course, tabulated OAR tolerances cannot be applied to the retreatment cases, which clearly benefit from a general reduction of the dose (**Figure 7**). In two retreatment cases only PBS-with-apertures achieved an acceptable brainstem dose. Furthermore, the

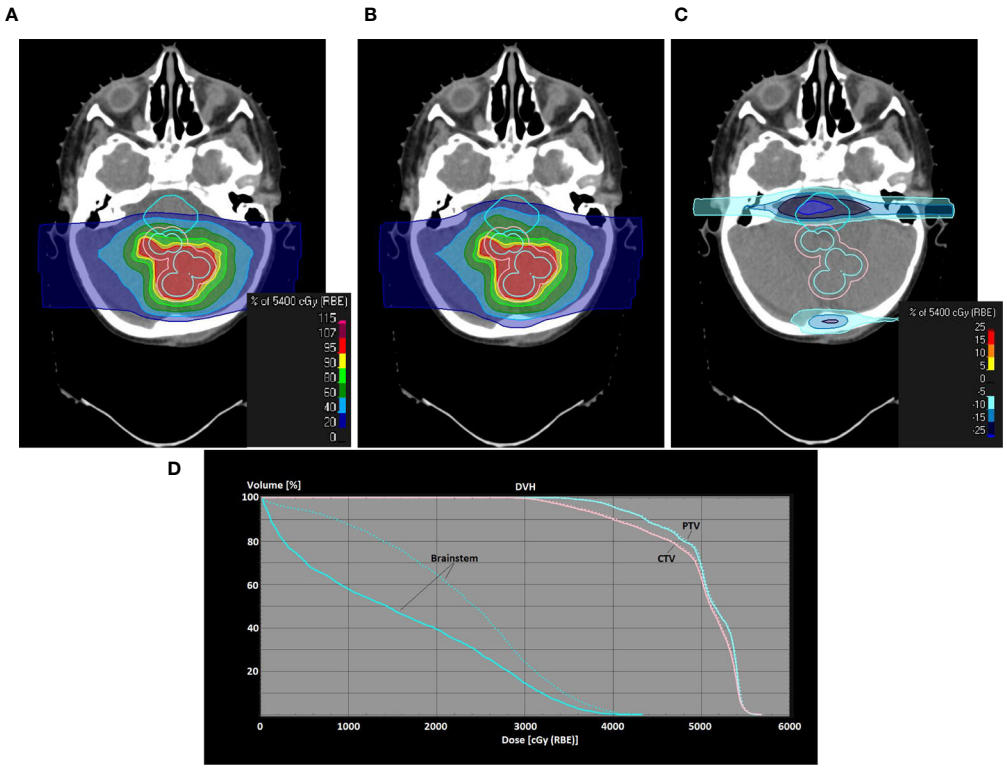

FIGURE 7 | Use of PBS-with-apertures for one of the retreatment cases (metastasis of an atypical teratoid rhabdoid tumor in the fossa posterior). Screenshots of treatment planning in RayStation are shown. Dose distributions in a transversal plane are shown as colorwash **(A–C)** PBS-with-apertures, uncollimated PBS plan, dose difference between PBS-with-apertures and uncollimated PBS plans; **(D)** dose volume histogram showing the difference for the brainstem and the target volumes between uncollimated (dashed line) and collimated (solid line) plans. PTV/CTV/brainstem is contoured with an orange/light blue/cyan line.

expected reduction of side effects also includes secondary malignancies. For instance, three cases of the considered eye treatments were retinoblastoma. Generally, we expect the biggest impact on normal-tissue complication, if the spatial extent of the involved structures and distances between them are on the scale of the dose fall-off, which is about 1 cm (4). The advantage at small spatial distances makes PBS-with-apertures a viable technique for localizations in the skull or for pediatric patients. The cochleae and the pituitary gland are examples for small-sized structures, which potentially develop less late effects through dose sparing with collimators. As pointed out in Ref. (28), there is evidence for a correlation of late end-points, e.g. hearing loss and endocrine dysfunctions, with absorbed dose in proton therapy. However, there are still uncertainties in the radiobiological models, including a possible influence of a heterogeneous dose distribution in the OARs. The clinical impact of the dose reduction of OARs by several GyRBE, which could be achieved by the insertion of apertures, was difficult to predict. Thus, future studies should seek to improve the NTCP-models, considering both the proton beam radiation quality (29, 30) and the irradiation of pediatric patients (31).

The outcome of the current dosimetric study could be regarded as a minimum achievement, which could be expected from field-specific apertures, because a horizontal beam-line was used. Reference (20) performed a similar comparison for two cases with a gantry-mounted nozzle of the same type as used here. Reductions of the mean dose of the cochlea of about 50% were reported. Dose sparing of abdominal organs was on the order of 20%. These relative improvements are clearly larger than the ones reported in this study indicating the synergy of PBS, field-specific apertures and a gantry. One may emphasize in this context the relevance of the choice of the beam ports in proton therapy, especially if an OAR is in the vicinity of the target volume. The strong distal dose gradient would provide an effective means to separate the high dose volume from the nearby OAR. However, the position of the distal dose fall-off in the patient is subject to uncertainties stemming from the range uncertainty of the proton machine (≈1 mm) and the stopping power estimation (≈3.5%). Moreover, the distal edge of proton fields features larger linear-energy transfers which are presumably associated with an elevated relative biological effectiveness [see, e.g., Refs. (32, 33)]. This is especially a concern for pediatric cases (34, 35). As a consequence, the treatment planning in our proton center seeks to avoid the ranging out of fields on common OAR tissue for more than one third of the fraction dose, as discussed in (35). This limitation motivates the importance for a sharp transveral dose fall-off and, thus, additional collimation of PBS fields. We further

conceive the blocking of the myelon, e.g. for infratentorial targets, and the blocking of vertebrae to avoid spine deformation for pediatric patients as possible clinical applications of PBS-with-apertures. This was not covered in the current study due to a quite limited cohort size and the lack of a gantry. The restriction to a horizontal treatment head is the main reason why extracranial targets have not been treated with PBS-with-apertures in our center.

The improvements of the dose distribution, which have been identified in this study, could be limited by the arrangement of beam modifiers. As shown in previous studies (4, 6) the reversed order of aperture and range shifter, i.e. the aperture downstream of the range shifter, features a steeper transversal dose gradient for divergent scanning fields. The usage of a corresponding snout would allow for an improved CI 50% and even less dose burden to healthy tissue. This comes at the expense of a limited effect of the fluence modulation on dose shaping due to broadened PBS spots. Albeit an easy mechanical modification, the current work only considered the nominal configuration of the Snout180 adhering to the intended use of the proton machine according to its vendor. For more information about the fundamentals of trimming PBS spots with a metal collimator, it is referred to Ref. (7).

Out-of-Field Dose and Radiation Protection Issues

One may note that the RayStation MC dose engine does not simulate secondary neutral particles. Thus, the out-field-dose, i.e. scattered dose far away from the target volume, is not covered in the presented dose distributions. In a MC study (36) it was found that the inclusion of a brass aperture causes a higher neutron fluence than the nominal PBS field configuration without aperture. Thus, the neutron contribution to the out-of-field dose equivalence increases when supplementing PBS with brass apertures. The same study assessed, however, that the use of a brass aperture leads to a reduction of the overall out-of-field dose. A similar conclusion was drawn in Ref. (37) in which the impact of a dynamic collimator was investigated. Using a thick graphite range shifter and a pair of nickel trimmers, the secondary neutron ambient dose equivalence was typically 70% larger as compared to the uncollimated field configuration. According to the MC simulation study of Ref. (38) hadronic interactions in nickel cause about 8% less neutron fluence/dose than in brass. As the impact of secondary neutrons was mainly evaluated in simulations, which depend on the models for neutron interactions (39), more experimental data are needed. Furthermore, this study did not investigate the effect of an increased linear-energy transfer (LET) of protons scattered from the aperture edge. Ueno et al. found a small increase of the dose-averaged LET when field-specific collimators were added (40).

The radiation protection of personnel concerns mainly the manual procedure of unmounting the apertures, which is performed by RTTs or physicists. Reference (41) showed with gamma-ray spectrometry and with MC simulations that the short-term radioactivation is dominated by the isotopes ^{63}Zn, and ^{60,61,62}Cu. The delayed, secondary radiation from these nuclei is a minor radiation protection concern, because the equivalent dose rate induced by the emitted photons is on the level of the natural background radiation. The long-lived isotopes, which are most relevant for storage and disposal, are ^{57,58}Co, ^{65}Zn, and ^{54}Mn (41). Assuming a dose prescription of 50 GyRBE, the accumulated activity after 30 fractions of long-lived isotopes is at the level of the exemption limit for recycling, especially for ^{65}Zn. The need for a long-term storage prior to clearance depends on the irradiation volume of the aperture and the energy spectrum of the incident protons (42). Thus, individual measurements of activity or equivalent dose rate are necessary and a storage room for decay has to be available (43).

SUMMARY

The addition of field-specific apertures to pencil-beam scanning treatment fields was successfully introduced at a proton therapy center which is based on commercial equipment. Pencil-beam scanning with custom-fabricated apertures has been clinically released in a treatment room with a horizontal beam line. The extra hardware effort mainly concerns a computer controlled milling machine and space for the decay of radioactivated apertures. The additional effort for quality assurance is moderate and can be derived from established procedures. In treatment planning, supplementary apertures were combined with robust optimization and integrated into the robustness evaluation.

Selected patients were treated with supplementary apertures. The *in silico* study indicated dosimetric advantages by comparison with treatment plans using uncollimated fields. The biggest dosimetric advantage was assessed for organs at risk in the vicinity of the high-dose, e.g. the hippocampus or the thalamus. Furthermore, the conformity index improved by typically 10–20% which is related to an overall decreased dose burden to healthy brain tissue. Apertures can facilitate the sparing of an organ-at-risk while keeping the dose coverage of the target, which was achieved in 4/31 cases.

DATA AVAILABILITY STATEMENT

The original contributions presented in the study are included in the article/supplementary material. Further inquiries can be directed to the corresponding author.

ETHICS STATEMENT

Ethical review and approval was not required for the study on human participants in accordance with the local legislation and institutional requirements. Written informed consent to participate in this study was provided by the participants' legal guardian/next of kin.

AUTHOR CONTRIBUTIONS

CB and SP wrote the manuscript. CB performed the clinical commissioning tests. SP evaluated the dose metrics and compiled the statistics. DG, SP, P-HK, DA, and BT did the treatment planning

of the patients. JW took care of the extension of the QA program. CN and KK assessed the radioprotection aspects. All authors contributed to the article and approved the submitted version.

FUNDING

The authors are thankful to the HARMONIC project. The HARMONIC project (Health effects of cArdiac uoRoscopy and MOderN radIotherapy in paediatriCs) has received funding from the Euratom research and training programme 2014-2018 under grant agreement No 847707.

ACKNOWLEDGMENTS

The authors would like to thank the dosimetrists of the medical physics group of the WPE. Many thanks to M. Bäcker, M. Gerhardt and S. Ibisi (TU Dortmund) for their support regarding the radioactivation of brass.

REFERENCES

1. Engelsman M, Schwarz M, Dong L. Physics Controversies in Proton Therapy. *Semin Radiat Oncol* (2013) 23:88–96. doi: 10.1016/j.semradonc.2012.11.003
2. Moteabbed M, Yock TI, Depauw N, Madden TM, Kooy HM, Paganetti H. Impact of Spot Size and Beam-Shaping Devices on the Treatment Plan Quality for Pencil Beam Scanning Proton Therapy. *Int J Radiat Oncol Biol Phys* (2016) 95:190–8. doi: 10.1016/j.ijrobp.2015.12.368
3. Yasui K, Toshito T, Omachi C, Kibe Y, Hayashi K, Shibata H, et al. A Patient-Specific Aperture System With an Energy Absorber for Spot Scanning Proton Beams: Verification for Clinical Application. *Med Phys* (2015) 42:6999–7010. doi: 10.1118/1.4935528
4. Bäumer C, Janson M, Timmermann B, Wulff J. Collimated Proton Pencil-Beam Scanning for Superficial Targets: Impact of the Order of Range Shifter and Aperture. *Phys Med Biol* (2018) 63:085020. doi: 10.1088/1361-6560/aab79c
5. Maes D, Regmi R, Taddei P, Bloch C, Bowen S, Nevitt A, et al. Parametric Characterization of Penumbra Reduction for Aperture-Collimated Pencil Beam Scanning (PBS) Proton Therapy. *Biomed Phys Eng Express* (2019) 5:035002. doi: 10.1088/2057-1976/ab0953
6. Bäumer C, Fuentes C, Janson M, Matic A, Timmermann B, Wulff J. Stereotactical Fields Applied in Proton Spot Scanning Mode With Range Shifter and Collimating Aperture. *Phys Med Biol* (2019) 64:155003. doi: 10.1088/1361-6560/ab2ae7
7. Hyer DE, Hill PM, Wang D, Smith BR, Flynn RT. A Dynamic Collimation System for Penumbra Reduction in Spot-Scanning Proton Therapy: Proof of Concept. *Med Phys* (2014) 41:091701. doi: 10.1118/1.4837155
8. Moignier A, Gelover E, Wang D, Smith B, Flynn R, Kirk M, et al. Theoretical Benefits of Dynamic Collimation in Pencil Beam Scanning Proton Therapy for Brain Tumors: Dosimetric and Radiobiological Metrics. *Int J Radiat Oncol Biol Physics* (2016) 95:171–80. doi: 10.1016/j.ijrobp.2015.08.030
9. Kang M, Pang D. Commissioning and Beam Characterization of the First Gantry-Mounted Accelerator Pencil Beam Scanning Proton System. *Med Phys* (2019) 47(8):3496–510. doi: 10.1002/mp.13972
10. Vilches-Freixas G, Unipan M, Rinaldi I, Martens J, Roijen E, Almeida IP, et al. Beam Commissioning of the First Compact Proton Therapy System With Spot Scanning and Dynamic Field Collimation. *Br J Radiol* (2020) 93:20190598. doi: 10.1259/bjr.20190598
11. Daartz J, Maughan RL, Orton CG. The Disadvantages of a Multileaf Collimator for Proton Radiotherapy Outweigh its Advantages. *Med Phys* (2014) 41:020601. doi: 10.1118/1.4824437
12. Bäumer C, Geismar D, Koska B, Kramer P, Lambert J, Lemke M, et al. Comprehensive Clinical Commissioning and Validation of the Raystation Treatment Planning System for Proton Therapy With Active Scanning and Passive Treatment Techniques. *Physica Med* (2017) 43:15–24. doi: 10.1016/j.ejmp.2017.09.136
13. Saini J, Maes D, Egan A, Bowen SR, James SS, Janson M, et al. Dosimetric Evaluation of a Commercial Proton Spot Scanning Monte-Carlo Dose Algorithm: Comparisons Against Measurements and Simulations. *Phys Med Biol* (2017) 62:7659. doi: 10.1088/1361-6560/aa82a5
14. Smith B, Gelover E, Moignier A, Wang D, Flynn RT, Lin L, et al. Technical Note: A Treatment Plan Comparison Between Dynamic Collimation and a Fixed Aperture During Spot Scanning Proton Therapy for Brain Treatment. *Med Phys* (2016) 43:4693–9. doi: 10.1118/1.4955117
15. Arjomandy B, Taylor P, Ainsley C, Safai S, Sahoo N, Pankuch M, et al. AAPM Task Group 224: Comprehensive Proton Therapy Machine Quality Assurance. *Med Phys* (2019) 46:e678–705. doi: 10.1002/mp.13622
16. Lambert J, Bäumer C, Koska B, Ding X. Daily QA in Proton Therapy Using a Single Commercially Available Detector. *J Appl Clin Med Phys* (2014) 15:151–63. doi: 10.1120/jacmp.v15i6.5005
17. Albertini F, Hug EB, Lomax AJ. Is it Necessary to Plan With Safety Margins for Actively Scanned Proton Therapy? *Phys Med Biol* (2011) 56:4399–413. doi: 10.1088/0031-9155/56/14/011
18. Korevaar EW, Habraken SJ, Scandurra D, Kierkels RG, Unipan M, Eenink MG, et al. Practical Robustness Evaluation in Radiotherapy – a Photon and Proton-Proof Alternative to PTV-based Plan Evaluation. *Radiother Oncol* (2019) 141(2019):267–74. doi: 10.1016/j.radonc.2019.08.005
19. Yasui K, Toshito T, Omachi C, Hayashi K, Tanaka K, Asai K, et al. Evaluation of Dosimetric Advantages of Using Patient-Specific Aperture System With Intensity-Modulated Proton Therapy for the Shallow Depth Tumor. *J Appl Clin Med Phys* (2017) 19:132–7. doi: 10.1002/acm2.12231
20. Liu CB, Song YT, Liu HD, Xue HZ, Feng HS. Quantifying Lateral Penumbra Advantages of Collimated Spot-Scanning Beam for Intensity-Modulated Proton Therapy. *Nucl Sci Techniques* (2019) 30:168. doi: 10.1007/s41365-019-0687-y
21. Su Z, Indelicato DJ, Mailhot RB, Bradley JA. Impact of Different Treatment Techniques for Pediatric Ewing Sarcoma of the Chest Wall: IMRT, 3DCPT, and IMPT With/Without Beam Aperture. *J Appl Clin Med Phys* (2020) 21:100–7. doi: 10.1002/acm2.12870
22. Uto M, Mizowaki T, Ogura K, Hiraoka M. Non-Coplanar Volumetric-Modulated Arc Therapy (VMAT) for Craniopharyngiomas Reduces Radiation Doses to the Bilateral Hippocampus: A Planning Study Comparing Dynamic Conformal Arc Therapy, Coplanar VMAT, and non-Coplanar VMAT. *Radiat Oncol* (2016) 11:86. doi: 10.1186/s13014-016-0659-x
23. Florijn MA, Sharfo AWM, Wiggenraad RG, van Santvoort JP, Petoukhova AL, Hoogeman MS, et al. Lower Doses to Hippocampi and Other Brain Structures for Skull-Base Meningiomas With Intensity Modulated Proton Therapy Compared to Photon Therapy. *Radiother Oncol* (2020) 142:147–53. doi: 10.1016/j.radonc.2019.08.019
24. Gondi V, Hermann BP, Mehta MP, Tomé WA. Hippocampal Dosimetry Predicts Neurocognitive Function Impairment After Fractionated Stereotactic Radiotherapy for Benign or Low-Grade Adult Brain Tumors. *Int J Radiat Oncol Biol Physics* (2012) 83:e487–93. doi: 10.1016/j.ijrobp.2011.10.021
25. Jaspers J, Mendez Romero A, Hoogeman M, van den Bent M, Wiggenraad R, Taphoorn M, et al. The Hippocampal Ntcp Model Could Not be Validated Within the eortc-22033 Low-Grade Glioma Trial. *Int J Radiat Oncol Biol Physics* (2018) 102:S8. doi: 10.1016/j.ijrobp.2018.06.114. Proceedings of the Amercian Society for Radiation Oncology.
26. Zureick AH, Evans CL, Niemierko A, Grieco JA, Nichols AJ, Fullerton BC, et al. Left Hippocampal Dosimetry Correlates With Visual and Verbal Memory Outcomes in Survivors of Pediatric Brain Tumors. *Cancer* (2018) 124:2238–45. doi: 10.1002/cncr.31143
27. Dutz A, Agolli L, Bütof R, Valentini C, Baumann M, Lühr A, et al. Neurocognitive Function and Quality of Life After Proton Beam Therapy for Brain Tumour Patients. *Radiother Oncol* (2020) 143:108–16. doi: 10.1016/j.radonc.2019.12.024
28. De Marzi L, Feuvret L, Boulé T, Habrand JL, Martin F, Calugaru V, et al. Use of Geud for Predicting Ear and Pituitary Gland Damage Following Proton and Photon Radiation Therapy. *Br J Radiol* (2015) 88:20140413. doi: 10.1259/bjr.20140413

29. Langendijk JA, Boersma LJ, Rasch CR, van Vulpen M, Reitsma JB, van der Schaaf A, et al. Clinical Trial Strategies to Compare Protons With Photons. *Semin Radiat Oncol* (2018) 28:79–87. doi: 10.1016/j.semradonc.2017.11.008. Proton Radiation Therapy.
30. Paganetti H, Beltran CJ, Both S, Dong L, Flanz JB, Furutani KM, et al. Roadmap: Proton Therapy Physics and Biology. *Phys Med Biol* (2021) 66:05RM01.
31. Constine L, Ronckers C, Hua CH, Olch A, Kremer L, Jackson A, et al. Pediatric Normal Tissue Effects in the Clinic (PENTEC): An International Collaboration to Analyse Normal Tissue Radiation Dose–Volume Response Relationships for Paediatric Cancer Patients. *Clin Oncol* (2019) 31:199–207. doi: 10.1016/j.clon.2019.01.002. Paediatric Radiation Oncology.
32. Lühr A, von Neubeck C, Krause M, Troost EG. Relative Biological Effectiveness in Proton Beam Therapy – Current Knowledge and Future Challenges. *Clin Trans Radiat Oncol* (2018) 9:35–41. doi: 10.1016/j.ctro.2018.01.006
33. Eulitz J, Troost E, Raschke F, Schulz E, Lutz B, Dutz A, et al. Predicting Late Magnetic Resonance Image Changes in Glioma Patients After Proton Therapy. *Acta Oncol* (2019) 58:1536–9. doi: 10.1080/0284186X.2019.1631477
34. Peeler CR, Mirkovic D, Titt U, Blanchard P, Gunther JR, Mahajan A, et al. Clinical Evidence of Variable Proton Biological Effectiveness in Pediatric Patients Treated for Ependymoma. *Radiother Oncol* (2016) 121:395–401. doi: 10.1016/j.radonc.2016.11.001
35. Haas-Kogan D, Indelicato D, Paganetti H, Esiashvili N, Mahajan A, Yock T, et al. National Cancer Institute Workshop on Proton Therapy for Children: Considerations Regarding Brainstem Injury. *Int J Radiat Oncol Biol Physics* (2018) 101:152–68. doi: 10.1016/j.ijrobp.2018.01.013
36. Dowdell SJ, Clasie B, Depauw N, Metcalfe P, Rosenfeld AB, Kooy HM. Et alMonte Carlo Study of the Potential Reduction in Out-of-Field Dose Using a Patient-Specific Aperture in Pencil Beam Scanning Proton Therapy. *Phys Med Biol* (2012) 57:2829. doi: 10.1088/0031-9155/57/10/2829
37. Smith BR, Hyer DE, Hill PM, Culberson WS. Secondary Neutron Dose From a Dynamic Collimation System During Intracranial Pencil Beam Scanning Proton Therapy: A Monte Carlo Investigation. *Int J Radiat Oncol Biol Physics* (2019) 103:241–50. doi: 10.1016/j.ijrobp.2018.08.012
38. Brenner DJ, Elliston CD, Hall EJ, Paganetti H. Reduction of the Secondary Neutron Dose in Passively Scattered Proton Radiotherapy, Using an Optimized Pre-Collimator/Collimator. *Phys Med Biol* (2009) 54:6065–78. doi: 10.1088/0031-9155/54/20/003
39. Chen H, Matysiak W, Flampouri S, Slopsema R, Li Z. Dosimetric Evaluation of Hybrid Brass/Stainless-Steel Apertures for Proton Therapy. *Phys Med Biol* (2014) 59:5043. doi: 10.1088/0031-9155/59/17/5043
40. Ueno K, Matsuura T, Hirayama S, Takao S, Ueda H, Matsuo Y. Et alPhysical and Biological Impacts of Collimator-Scattered Protons in Spot-Scanning Proton Therapy. *J Appl Clin Med Phys* (2019) 20:48–57. doi: 10.1002/acm2.12653
41. Bäcker CM, Bäumer C, Gerhardt M, Kröninger K, Nitsch C, Rullkötter H, et al. Evaluation of the Activation of Brass Apertures in Proton Therapy Using Gamma-Ray Spectrometry and Monte Carlo Simulations. *J Radiol Prot* (2020) 40:848–60. doi: 10.1088/1361-6498/ab9f42
42. Lee SH, Cho S, You SH, Shin D, Park SY, Lee SB, et al. Evaluation of Radioactivity Induced by Patient-Specific Devices in Proton Therapy. *J Korean Phys Soc* (2012) 60:125–28. doi: 10.3938/jkps.60.125
43. Walker PK, Edwards AC, Das IJ, Johnstone PAS. Radiation Safety Considerations in Proton Aperture Disposal. *Health Phys* (2014) 106:523–7. doi: 10.1097/hp.0b013e3182a2a725

Conflict of Interest: The authors declare that the research was conducted in the absence of any commercial or financial relationships that could be construed as a potential conflict of interest.

Copyright © 2021 Bäumer, Plaude, Khalil, Geismar, Kramer, Kröninger, Nitsch, Wulff and Timmermann. This is an open-access article distributed under the terms of the Creative Commons Attribution License (CC BY). The use, distribution or reproduction in other forums is permitted, provided the original author(s) and the copyright owner(s) are credited and that the original publication in this journal is cited, in accordance with accepted academic practice. No use, distribution or reproduction is permitted which does not comply with these terms.

frontiers in Oncology

ORIGINAL RESEARCH
published: 03 September 2021
doi: 10.3389/fonc.2021.617787

A Comparative Study of Two *In Vivo* PET Verification Methods in Clinical Cases

Junyu Zhang[1,2,3,4,5†], *Yan Lu*[2,3,6†], *Yinxiangzi Sheng*[2,3,6], *Weiwei Wang*[2,3,6], *Zhengshan Hong*[2,3,7], *Yun Sun*[1,2,3], *Rong Zhou*[4,5] *and Jingyi Cheng*[1,2,3*]

[1] Department of Nuclear Medicine, Shanghai Proton and Heavy Ion Center, Fudan University Cancer Hospital, Shanghai, China, [2] Shanghai Key Laboratory of Radiation Oncology, Shanghai, China, [3] Shanghai Engineering Research Center of Proton and Heavy Ion Radiation Therapy, Shanghai, China, [4] College of Physics, Sichuan University, Chengdu, China, [5] Key Laboratory of Radiation Physics and Technology, Ministry of Education, Chengdu, China, [6] Department of Medical Physics, Shanghai Proton and Heavy Ion Center, Shanghai, China, [7] Department of Radiotherapy, Shanghai Proton and Heavy Ion Center, Shanghai, China

Purpose: Positron emission tomography (PET) range verification is an important method that can help improve the confidence in proton therapy for clinical applications. Two kinds of verification methods are implemented and compared based on clinical cases in this study.

Method: The study is conducted on 14 breast cancer patients following proton irradiation treatment. Verification is done by calculating the depth error between the numerically predicted values with the measured PET image along the beam direction. Point-based and segment-based methods are applied and compared. The verification results are presented as depth error means and standard deviations in a region of interest (ROI).

Results: The mean value of the depth error of all 14 cases is within the range of [–3, 3] mm for both point-based and segment-based methods, and only one case result calculated by the point-based method is slightly beyond –3 mm. When comparing the mean depth error from the two methods, the paired *t*-test result shows that the *p*-value is 0.541, and the standard deviation of the segment-based method is smaller than that of the point-based method.

Conclusion: In breast cancer case verification application, point-based and segment-based methods show no significant difference in the mean value of results. Both methods can quantify the accuracy of proton radiotherapy to the millimeter level.

Keywords: proton therapy, breast cancer, positron emission tomography, depth verification, methods comparison

OPEN ACCESS

Edited by:
Beate Timmermann, Essen University Hospital, Germany

Reviewed by:
Piergiorgio Cerello, National Institute of Nuclear Physics, Italy
Wen Chien Hsi, Baptist Hospital of Miami, United States

***Correspondence:**
Jingyi Cheng
jcheng13@fudan.edu.cn

[†]*These authors have contributed equally to this work*

Specialty section:
This article was submitted to Radiation Oncology, a section of the journal Frontiers in Oncology

Received: *15 October 2020*
Accepted: *16 August 2021*
Published: *03 September 2021*

Citation:
Zhang J, Lu Y, Sheng Y, Wang W, Hong Z, Sun Y, Zhou R and Cheng J (2021) A Comparative Study of Two In Vivo PET Verification Methods in Clinical Cases. Front. Oncol. 11:617787. doi: 10.3389/fonc.2021.617787

INTRODUCTION

A proton beam demonstrates a good dose distribution with a clear edge because of the presence of the Bragg peak on the dose depth deposition curve. Proton therapy is widely utilized to treat solid tumors close to critical organs, as the clear dose edge is good at sparing normal tissue while destroying tumor tissue. The range verification methods, which are necessary to check the

irradiation accuracy, are applied to patients during or/and after proton therapy to ensure the proton beam delivered the dose to tumor tissue precisely.

Many *in vivo* non-invasive verification methods are developed (1); positron emission tomography (PET) is one of the most widely used verification techniques following proton irradiation. Positron emitter isotopes are generated by proton beam decay and release a positron. The positron annihilates with an electron and releases a pair of annihilation photons, which is recorded by the coincident detecting system. Using a suitable reconstruction algorithm, the positron distribution image can be reconstructed to reveal quantified information about beam irradiation.

Proton therapy PET verification has been developed through many phantom-based studies (2–5) and clinical cases (6–9). PET verification is assessed by comparing the measured PET image with the predicted PET image using two widely employed methods (3, 10): point-based and segment-based. The point-based method determines the PET depth by a marked point on the PET activity curve along the beam direction, while the segment-based method determines the depth difference relying on a segment of the curve. Several published articles report that the point-based method has a lower robustness against noise and other fluctuations (11, 12), whereas the segment-based method provides higher robustness to curve fluctuation (3, 10). However, these reports have few descriptions on the implementation of the segment-based method, and the comparison between these two methods is not described thoroughly.

Here, we are going to evaluate point-based and segment-based verification methods and investigate the difference between the two methods in clinical application. Both methods are implemented and employed to verify PET depth range. The comparison is performed on breast cancer cases of PET examination following proton therapy.

MATERIALS AND METHODS

Patient Set and PET Prediction

This retrospective study was approved by the ethics committee of Shanghai Proton and Heavy Ion Center, and the requirement for informed consent was waived. In this work, 14 breast cancer patients were analyzed, whose information is listed in **Table 1**. After proton beam treatment, patients underwent a PET scanning *via* the nuclear medicine PET device. All patients have two irradiation fields. In the treatment plans, fractional dose on the clinical target volume (CTV) was 2.0 or 2.66 Gray of photon Equivalent dose (GyE) in different cases, with a boost area (if exists) 20% higher than the CTV area. The relative biological effect (RBE) of proton beam is a fixed value 1.1.

TABLE 1 | Patient Information.

Case No.	Age (years)	Dose prescription/ (GyE/fx)		Dose distribution	Fields	Time course/min		ΔR_{50} - Field 1/mm		ΔR_{50} - Field 2/mm		ΔR_{shift} - Field 1/mm		ΔR_{shift} - Field 2/mm	
		CTV	Boost			Delay	Acq	CTV	Boost	CTV	Boost	CTV	Boost	CTV	Boost
1	41	2.66	–	Uniform	2	6	20	–0.51 ± 2.51	–	–0.51 ± 2.35	–	–0.90 ± 2.09	–	–1.05 ± 1.99	–
2	50	2.66	–	Uniform	2	13	20	–1.46 ± 3.05	–	–1.52 ± 3.10	–	–1.61 ± 2.28	–	–1.69 ± 2.33	–
3	74	2.00	–	Uniform	2	15	20	0.73 ± 2.45	–	0.69 ± 2.34	–	0.60 ± 1.82	–	0.59 ± 1.78	–
4	35	2.66	–	Uniform	2	13	20	0.78 ± 2.55	–	0.78 ± 2.65	–	0.70 ± 2.04	–	0.73 ± 2.32	–
5	44	2.00	–	Uniform	2	13	20	–2.63 ± 4.71	–	–2.53 ± 4.43	–	–2.59 ± 2.75	–	–2.66 ± 2.84	–
6	61	2.66	–	Uniform	2	9	20	2.18 ± 3.79	–	2.16 ± 3.72	–	2.25 ± 4.67	–	2.13 ± 4.12	–
7	48	–	2.50	boost	2	7	20	–	–1.41 ± 2.64	–	–1.45 ± 2.36	–	–1.88 ± 1.86	–	–1.91 ± 1.71
8	48	–	2.00	boost	2	14	20	–	1.81 ± 1.87	–	1.32 ± 1.74	–	1.42 ± 1.52	–	1.29 ± 1.52
9	39	2.67	3.20	SIB	2	7	20	–3.43 ± 3.36	–2.34 ± 3.83	–3.44 ± 3.56	–2.50 ± 4.34	–2.79 ± 2.08	–1.78 ± 1.52	–2.72 ± 2.03	–1.97 ± 1.67
10	63	2.00	2.40	SIB	2	9	20	–1.16 ± 3.24	1.48 ± 2.32	–1.14 ± 3.29	1.54 ± 2.11	–1.28 ± 2.65	0.95 ± 1.57	–1.22 ± 2.66	0.93 ± 1.36
11	49	2.67	3.20	SIB	2	8	20	–2.35 ± 3.12	–2.38 ± 2.04	–2.50 ± 3.16	–2.41 ± 1.99	–1.86 ± 2.21	–1.52 ± 1.36	–1.86 ± 2.16	–1.54 ± 1.25
12	50	2.67	3.20	SIB	2	9	20	0.45 ± 2.79	0.45 ± 2.79	0.60 ± 2.19	0.94 ± 2.40	0.66 ± 1.69	1.24 ± 1.45	0.70 ± 1.72	1.37 ± 1.55
13	42	2.67	3.20	SIB	2	11	20	–0.99 ± 4.42	–0.75 ± 2.22	0.26 ± 5.39	–0.23 ± 1.60	–1.14 ± 1.81	–0.04 ± 1.30	–1.94 ± 2.89	0.09 ± 0.76
14	33	2.67	3.20	SIB	2	8	20	–1.20 ± 2.91	1.68 ± 2.00	1.10 ± 6.24	–2.38 ± 3.00	–1.78 ± 1.82	–2.67 ± 1.95	0.69 ± 3.25	–1.71 ± 2.60

Given patient computer tomography (CT) data and treatment plan, the predicted PET image can be calculated by an analytical method (13). A group in Ludwig-Maximillian Universität (LMU) has developed a PET prediction module based on the Treatment Planning System (TPS) working frame (14), which calculates the predicted PET by convolving the dose with a filter function spot by spot and finally generates the PET distribution with washout (10, 15). This module is applied in this work as the source of predicted PET data.

PET Acquisition and Data Preprocess

In this work, the patient PET data are acquired by "offline" PET, which means that patients after proton irradiation will be transferred over a distance to the PET device; thus, the signal intensity decreased before the acquisition. Patients needed around 5–10 min to transport from the treatment room to the PET room. PET images are acquired by Biograph mCT (16) (Siemens), a PET/CT coupled device that acquires PET and CT data under the same geometry frame. It took us 20 min to acquire patient data. Furthermore, we reconstructed the images with ordered subsets expectation maximization algorithm (17, 18). In addition, CT attenuation correction was applied to reduce the signal attenuation caused by self-absorption. Since the predicted PET follows patient plan CT frame and measured PET follows the PET-CT frame, the plan CT is rigidly co-registered to the PET-CT and thus predicted and measured PET can be compared under one geometry frame.

Because of the low intensity of the PET signal, the reconstructed PET image has a lot of ripples, and the image has lost the accurate PET activity information; thus, measured PET is not suitable for a direct comparison with the predicted PET. A simple moving-average smoothing was applied to the original measured image to smoothen the ripples and then normalized to the scale of the predicted image (19). It is now possible to compare the predicted and measured PET to verify their range.

Depth Error Verification

Verification Result of an Irradiation Field

In each treatment plan, there could be one or more irradiation fields to provide a sufficient dose covering to the tumor tissue. In the treatment, the planned dose is delivered to the tumor tissue marked in "region of interest (ROI)", which covers a certain 3-D region of the patient body (**Figures 1A, B**). One-dimensional PET scoring lines are drawn along the beam direction perpendicular to the beam's eye view (BEV) plane (10). From the BEV, as shown in **Figure 1C**, the PET curve scoring line is uniformly distributed with an identical fixed interval (3 mm in our cases).

Obviously, not all the data from the scoring lines are useful to us. As the CTV is of our concern, we project this 3-D ROI on the BEV plane as a 2-D area, which circled a group of scoring lines (**Figure 1D**, just a sketch not real case). Only the scoring lines inside the ROI will be involved to calculate the mean value and standard deviation of the depth error of an irradiation field. This method of observing from the beam sight has been reported in many studies (6, 20–22). The comparison between two 3D-PET images is then degraded to one-dimensional curve problems; the statistical result of a case is then generated from the collection of one-dimensional curve comparison results.

R_{50} Method: Point-Based

In our verification cases, the predicted and measured PET curves had similar shapes and edges, but the distal edges did not have the same position and slope. R_{50} is defined as the position where the PET intensity is 50% of its maximum (3). The predicted PET curve is set as a reference, and a horizontal marking line is drawn at half of the maximum level. The horizontal line marked out two points at the distal side of the curves while the depth error calculated based on R_{50} is defined as $\Delta R_{50} = R_{50,pred} - R_{50,meas}$. This process is shown in **Figure 2**.

R_{shift} Method: Segment-Based

Contrary to the R_{50} method, if we are not concerned about a certain point but a segment of the curve, then the depth error evaluation reflects the feature of the entire segment rather than a single point. One method to calculate the depth error for a segment of a curve is the R_{shift} method (3, 10, 20).

The kernel of the shift method is to find a shift distance δ that minimizes the difference between predicted and measured PET curves [Eq. (1)], this difference is presented as a cost function $f(\delta)$ [Eq. (2)].

$$\Delta R_{shift} = \delta_0 \text{ where } f(\delta_0) = \min\{f(\delta)\} \tag{1}$$

$$f(\delta) = \begin{cases} \int_{z_{\min}}^{z_{\max}} \left| A_{pred}(Z) - A_{meas}(Z-\delta) \right| dz, \text{ continuous} \\ \sum_{i=0}^{M} \left| A_{pred}(Z_i) - A_{meas}(Z_i-\delta) \right|, \text{ discrete} \end{cases} \tag{2}$$

In Eq. (2), A(z) is the PET activity depth distribution along the beam direction (for prediction and measurement, respectively) and δ is specified as a depth shift between two curves. The reason of the entire curve deviation between predicted and measured PET activity data is not fully understood in this work; by specifying the integral region [Z_{min} and Z_{max} in Eq. (2)], we focus on the curve difference in the distal edge area rather than the entire curve. We specify the Z_{min} as the peak position of the predicted PET curve and the Z_{max} as 20% of the maximum location (**Figure 2**).

In Eq. (2), the cost function $f(\delta)$ describes the difference between continuous curves in a region, but the data stored in the computer are always discrete data lists. Therefore, cost function $f(\delta)$ has both continuous and discrete descriptions. Here, in the discrete description of Eq. (2), $i \in [0, M]$ is a list subscript index corresponding to the region [Z_{min}, Z_{max}] presented as a discretization data list Z_i, and the value of δ should be chosen discretely with the same value interval of Z_i, which is 3 mm, the same as our data grid voxel size and the curve's spatial resolution. The value of δ is set in [–15,15]mm with a range step of 3 mm and $f(\delta)$ is plotted in **Figure 3**.

Obviously, there is a minimum value point on the $f(\delta)$ curve. If our δ sampling density was high enough, we can easily locate the minimum point of the $f(\delta)$ curve and the corresponding δ would be the ΔR for curves. In our case, however, the value of δ sampling step was 3 mm, which is not small enough. Here, we can use derivative interpolation to accurately find the minimum point of the $f(\delta)$ curve. In $f(\delta)$ discrete list, there is a minimum $f(\delta_m)$ with corresponding δ_m, which is in the discrete δ list

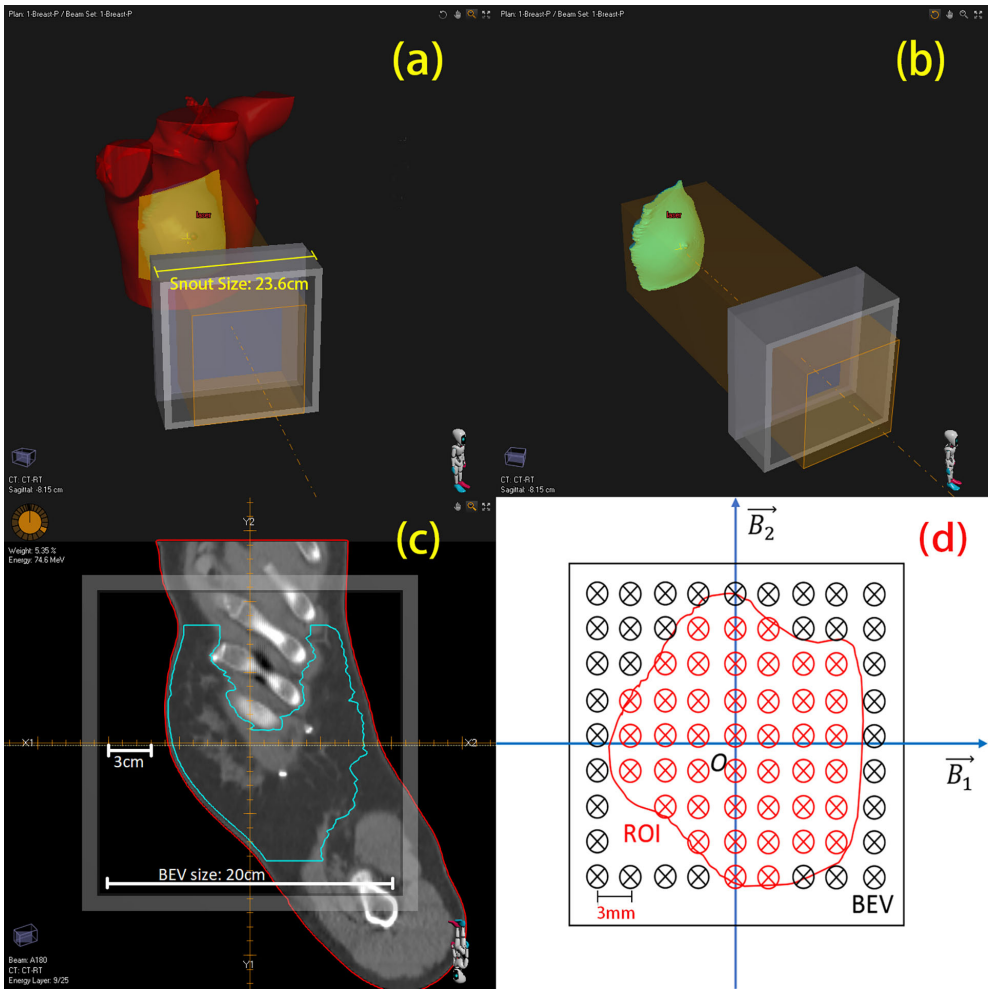

FIGURE 1 | 3-D view of region of interest (ROI) and mapping to BEV (beam's eye view). **(A)** A single beam irradiates to the patient's breast. **(B)** Irradiating to the patient CTV. **(C)** One slice image of CTV on BEV. **(D)** Sketch of scoring lines inside (red) and outside (black) the ROI; scoring line interval is 3 mm.

(**Figure 3**); the point is recorded as point $m[\delta_m, f(\delta_m)]$. On the left and right side of point m, there are point $L[\delta_{m-1}, f(\delta_{m-1})]$ and point $R[\delta_{m+1}, f(\delta_{m+1})]$. Obviously, the minimum point $[\delta_0 f(\delta_0)]$ of $f(\delta)$ is between L and R. Then, we calculate the left and right derivative of point m:

$$f_L^{'} = \frac{f(\delta_m) - f(\delta_{m-1})}{\delta_m - \delta_{m-1}} \text{ and } f_R^{'} = \frac{f(\delta_{m+1}) - f(\delta_m)}{\delta_{m+1} - \delta_m} \quad (3)$$

We know that $f(\delta_m)$ is smaller than $f(\delta_{m-1})$ and $f(\delta_{m+1})$, so $f_L^{'} < 0$ *and* $f_R^{'} > 0$; therefore, there must be a $f'(\delta_0) = 0$ and the corresponding δ_0 is exactly the ΔR_{shift} we want. We can easily estimate the δ_0 by linearly interpolating $f_L^{'}$ *and* $f_R^{'}$:

$$\delta_0 = \delta_m - \Delta\delta \left[\frac{f_R^{'} + f_L^{'}}{2(f_R^{'} + f_L^{'})} \right] \quad (4)$$

Here, $\Delta\delta$ = 3mm is our data grid voxel size, and δ_m can be searched from the discrete $f(\delta)$ list. The δ_0 in Eq. (4) is the point where $f(\delta)$ is minimized; thus, the integration in Eq. (1) is minimized, so the δ_0 here is the ΔR_{shift} we want.

RESULTS

Both R_{50} and R_{shift} methods are applied to analyze the depth error of two fields of each patient. Depending on different types of dose distribution, depth error is scored and calculated for CTV, boost area, or both. The statistical result is in **Table 1**.

Table 1. Enrolled breast cancer patient information: age, planning dose, field, time course, and all their depth error. All patients are two-field cases. Patients may have different delay times before positron emission tomography scanning, but the data acquisition (Acq) time is the same for all cases. The ΔR_{50} and ΔR_{shift} are scored in the CTV region and boost region (if exist). Different dose distribution strategies: Uniform: a dose is

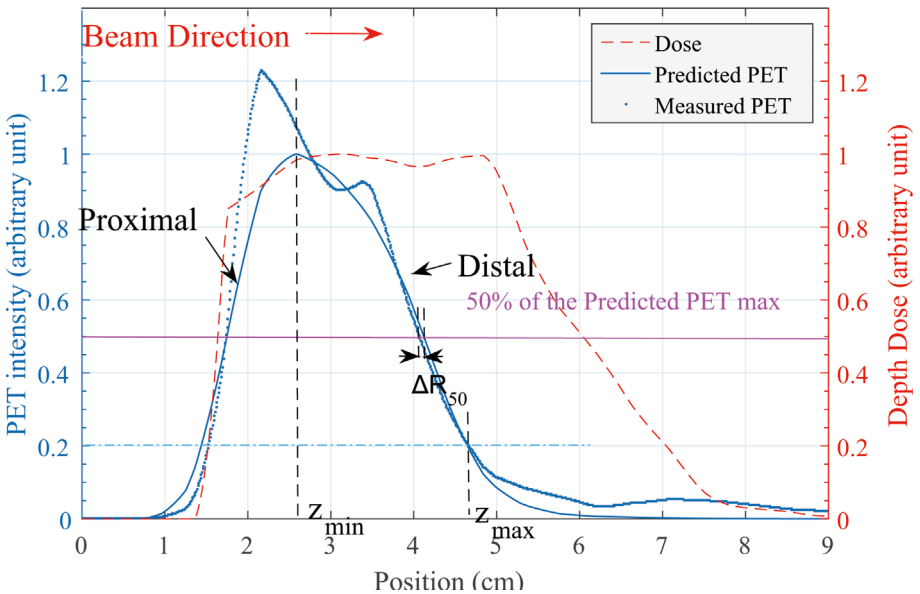

FIGURE 2 | Predicted and measured PET 1-D curve. Along the beam direction, the depth error at distal edge is our concern. Definition of ΔR_{50} is shown in this figure. z_{min} and z_{max} location of the R_{shift} method is defined on the predicted PET curve.

uniformly distributed in the CTV region in each fraction; Boost: dose is delivered to the tumor bed region in one fraction; SIB (simultaneous integrated boost): uniform and boost dose are simultaneously delivered in one fraction.

The mean value and standard deviation in **Table 1** is calculated as:

$$\text{mean} = \bar{x} = \frac{1}{n}\Sigma_{i=1}^{n} x_i,\ \text{std}: \sigma = \frac{1}{n}\sqrt{\Sigma_{i=1}^{n}(x_i - \bar{x})^2} \qquad (5)$$

The mean value of the depth error in all these 14 cases is within the range of [−3, 3] mm for both R_{50} and R_{shift} methods, except case 9 CTV region with the R_{50} method. The mean value and standard deviation of depth error of all cases are plotted in **Figure 4**, where the predicted PET depth is deeper than the measured PET if the ΔR is a positive value and *vice versa*. We can see that most patients have similar mean depth error calculated by R_{50} and R_{shift} methods in both field 1 and field 2. To evaluate whether the mean depth error from the two methods has

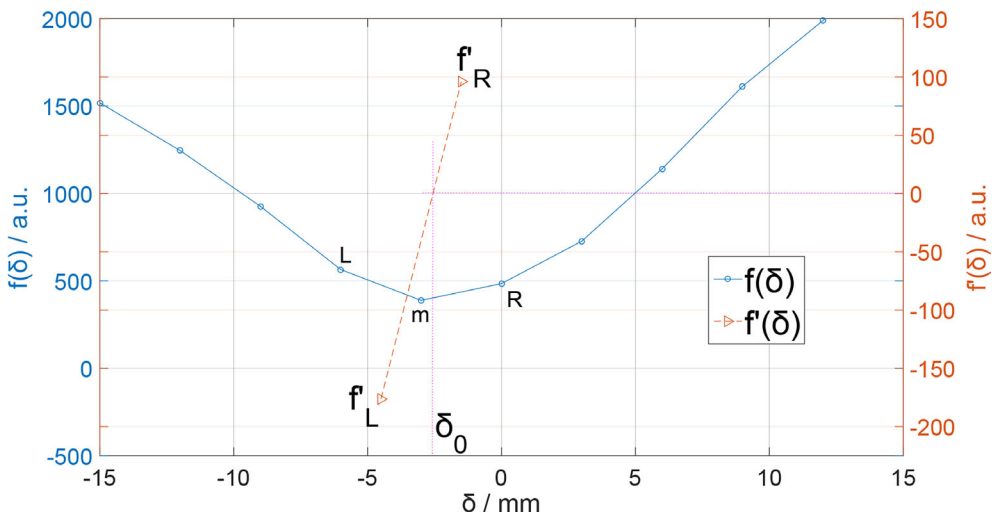

FIGURE 3 | $f(\delta)$ and $f'(\delta)$ for seeking δ_0. The position of δ_0 is located where $f'(\delta_0) = 0$.

significant difference, a paired Student's *t*-test is applied. Setting the confidence level $\alpha = 0.01$ and testing all the mean value of depth error, we get $p = 0.541 > \alpha$ which means the mean value of depth error has no significant difference between R_{50} and R_{shift} methods. Moreover, we also find that all cases have a smaller standard deviation of depth error calculated by R_{shift} rather than R_{50} except case 6. This can be roughly explained as the segment-based method refers more information to calculate a depth error result, which leads to higher robustness compared to R_{50}, thus presenting a smaller standard deviation.

Besides a global result analysis in **Figure 4**, a detailed result of a case is shown in **Figure 5**. The CTV and boost ROI is projected on the BEV plane whose edge circles an area, as shown in **Figures 5A–D**. Inside the boost region, we can see several positive ΔR pixels, and in **Table 1**, we can see that the mean value of ΔR of case 10 in the boost region is a positive number. In addition, the result of the R_{shift} method (**Figures 5B, D**) shows a smoother ΔR distribution than the R_{50} method (**Figures 5A, C**). The ΔR distribution in the boost region is also plotted as a histogram in **Figures 5E, F**, which indicates that R_{50} and R_{shift} methods give similar mean depth errors but different distribution widths.

DISCUSSION

Z_{min} and Z_{max} in R_{shift} Integration

In our calculations with the R_{shift} method (*Section R50 Method: Point-Based*), the integration range $[z_{min}, z_{max}]$ in Eq. (1) is simply specified as the range from the peak position to 20% of the peak value on the distal tail of the curve. Herein, the dose delivery is limited within the breast area with a high carbon component and low biological washout rate. Therefore, the PET image shows a smooth single peak curve if we score the data along the beam direction. Under this condition, we do not need to define a complex method to find out a specific z_{min} and z_{max} for Eq. (1). Frey provides a method (20) to locate z_{min} and z_{max} that can optimize the curve shape of $f(\delta)$ to achieve a more reasonable depth error result. In our study, however, the anatomical structure is not complex, which provides good stability to the result, so that z_{min} and z_{max} need no further optimization.

"Off-line" PET and "In-beam" PET

"Off-line" PET is applied in this work. The "off-line" PET scanner with a full ring detector system has been widely used

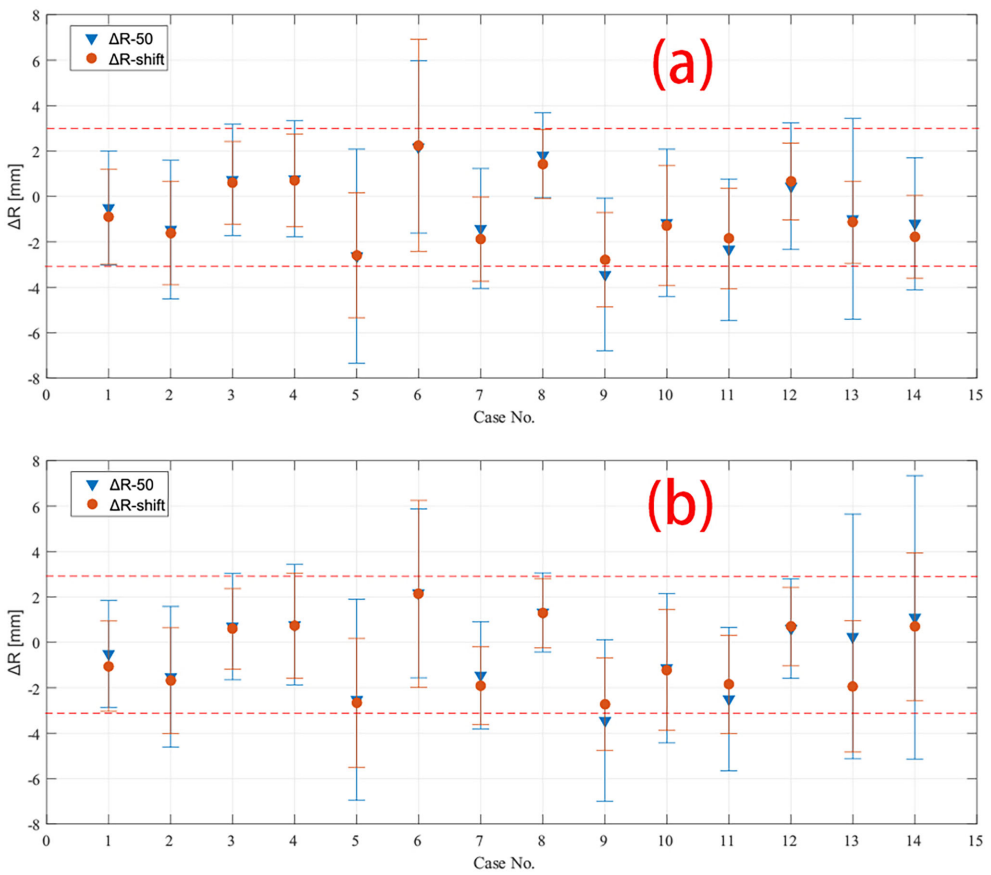

FIGURE 4 | Depth error of all 14 cases calculated by both R_{50} and R_{shift} methods in **(A)** field 1 and **(B)** field 2. The mean and standard deviation of depth error in CTV region of all cases are plotted except case 7 and 8, which have only data in boost region to be plotted. The red dashed line marked –3 mm and 3 mm in the plot.

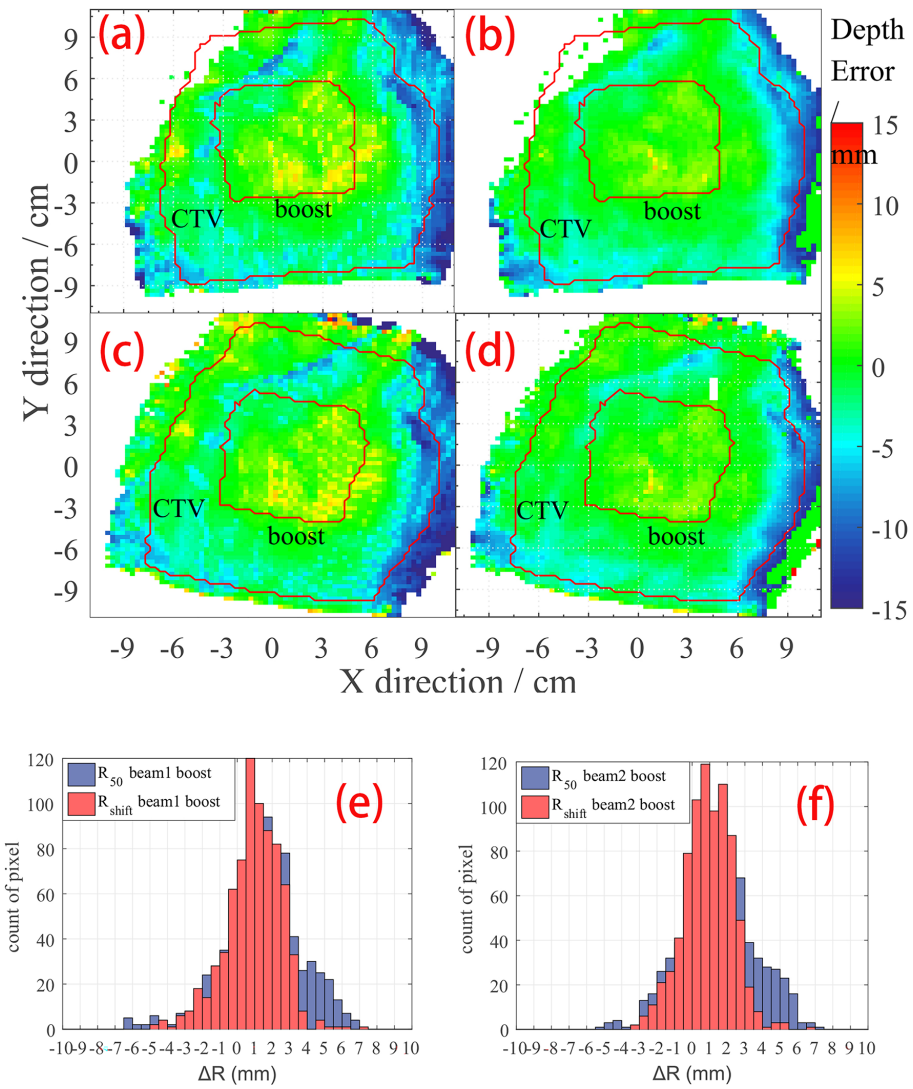

FIGURE 5 | ΔR detail result of case no. 10. The CTV and boost areas are marked within the red curve. **(A)** R_{50} depth error map on beam 1; **(B)** R_{shift} depth error map on beam 1; **(C)** R_{50} depth error map on beam 2; **(D)** R_{shift} depth error map on beam 2. Histogram of depth error statistic on boost region on **(E)** beam 1 view, and **(F)** beam 2 view of case no. 10.

in nuclear medicine clinical application. Mature device and reconstruction algorithm reduces the cost of use. However, the long transport time makes the contribution of short-lived isotopes undetectable; also, the co-registration between plan-CT and PET-CT may introduce additional geometrical error.

"In-beam" PET, on the other hand, can acquire the induced PET signal in time and thus collect the activity contributed by short-life isotopes. Higher signal intensity gives higher image accuracy and thus better comparison results in data analyzing. However, the in-beam PET requires a complex PET scanner installed inside the treatment room, and it is hard to construct a full ring to avoid blocking the beam path. A PET scanner with an incomplete ring will introduce more noise to data reconstruction and will need a more accurate reconstruction algorithm.

The breast cancer cases in this work have a relative higher yield of long-life isotope (like carbon-11); thus, "off-line" PET is applicable in this work.

CONCLUSIONS

PET could be used in depth error verification after proton therapy. Point-based and segment-based methods show no significant difference in the mean depth error result, which is within [−3, 3] mm. The segment-based methods have higher robustness with smaller standard deviation, while the point-based method has a relatively larger standard deviation. Both point-based and segment-based methods are suitable in the data

analysis of our breast cancer cases, while the point-based method is more appropriate because of the low cost in the calculation.

DATA AVAILABILITY STATEMENT

The original contributions presented in the study are included in the article/supplementary material. Further inquiries can be directed to the corresponding authors.

ETHICS STATEMENT

The studies involving human participants were reviewed and approved by the Ethics Committee of Shanghai Proton and Heavy Ion Center. The patients/participants provided their written informed consent to participate in this study. Written informed consent was obtained from the individual(s) for the publication of any potentially identifiable images or data included in this article.

AUTHOR CONTRIBUTIONS

JZ was responsible for writing the original draft. YL was responsible for writing the original draft and review. YXS and WW were responsible for methodology. ZH was responsible for data curation. JC was responsible for conceptualization. RZ was responsible for supervision. YS was responsible for funding acquisition. All authors contributed to the article and approved the submitted version.

FUNDING

This project was supported by the Shanghai Municipal Health Commission (Grant No. 202040279), the Pudong New Area Science and Technology Development Foundation (No. PKJ 2020-Y56), and the Natural Science Foundation of Shanghai (21ZR460300).

REFERENCES

1. Kraan AC. Range Verification Methods in Particle Therapy: Underlying Physics and Monte Carlo Modeling. *Front Oncol* (2015) 5:150. doi: 10.3389/fonc.2015.00150
2. Bauer J, Unholtz D, Kurz C, Parodi K. An Experimental Approach to Improve the Monte Carlo Modelling of Offline PET/CT-Imaging of Positron Emitters Induced by Scanned Proton Beams. *Phys Med Biol* (2013) 58:5193–213. doi: 10.1088/0031-9155/58/15/5193
3. Knopf A, Parodi K, Paganetti H, Cascio E, Bonab A, Bortfeld T. Quantitative Assessment of the Physical Potential of Proton Beam Range Verification With PET/Ct. *Phys In Med And Biol* (2008) 53:4137–51. doi: 10.1088/0031-9155/53/15/009
4. Nishio T, Sato T, Kitamura H, Murakami K, Ogino T. Distributions of β+ Decayed Nuclei Generated in the CH2 and H2O Targets by the Target Nuclear Fragment Reaction Using Therapeutic MONO and SOBP Proton Beam. *Med Phys* (2005) 32:1070–82. doi: 10.1118/1.1879692
5. Ferrero V, Bisogni MG, Camarlinghi N, Fiorina E, Giraudo G, Morrocchi M, et al. Double-Field Hadrontherapy Treatment Monitoring With the INSIDE In-Beam PET Scanner: Proof of Concept. *IEEE Trans Radiat Plasma Med Sci* (2018) 2:588–93. doi: 10.1109/TRPMS.2018.2870478
6. Sebastian PN, Bauer J, Welzel T, Rief H, Jäkel O, Haberer T, et al. Clinical Implementation and Range Evaluation of In Vivo PET Dosimetry for Particle Irradiation in Patients With Primary Glioma. *Radiother Oncol* (2015) 115:179–185. doi: 10.1016/j.radonc.2015.03.022
7. Parodi K, Harald P, Shih HA, Michaud S, Loeffler JS, DeLaney TF, et al. Patient Study of In Vivo Verification of Beam Delivery and Range, Using Positron Emission Tomography and Computed Tomography Imaging After Proton Therapy. *Int J Of Radiat Oncol Biol Phys* (2007) 68:920–34. doi: 10.1016/j.ijrobp.2007.01.063
8. Knopf A-C, Parodi K, Paganetti H, Bortfeld T, Daartz J, Engelsman M, et al. Accuracy of Proton Beam Range Verification Using Post-Treatment Positron Emission Tomography/Computed Tomography as Function of Treatment Site. *Int J Radiat Oncol Biol Phys* (2011) 79:297–304. doi: 10.1016/j.ijrobp.2010.02.017
9. Ferrero V, Fiorina E, Morrocchi M, Pennazio F, Baroni G, Battistoni G, et al. Online Proton Therapy Monitoring: Clinical Test of a Silicon-Photodetector-Based in-Beam PET. *Sci Rep* (2018) 8:4100. doi: 10.1038/s41598-018-22325-6
10. Knopf A, Parodi K, Bortfeld T, Shih HA, Paganetti H. Systematic Analysis of Biological and Physical Limitations of Proton Beam Range Verification With Offline PET/CT Scans. *Phys Med Biol* (2009) 54:4477. doi: 10.1088/0031-9155/54/14/008
11. Min CH, Zhu X, Winey BA, Grogg K, Testa M, Fakhri GE, et al. Clinical Application of In-Room Positron Emission Tomography for In Vivo Treatment Monitoring in Proton Radiation Therapy. *Int J Radiat Oncol Biol Phys* (2013) 86:183 – 189. doi: 10.1016/j.ijrobp.2012.12.010
12. Min CH, Zhu X, Grogg K, Fakhri GE, Winey B, Paganetti H. A Recommendation on How to Analyze In-Room PET for In Vivo Proton Range Verification Using a Distal PET Surface Method. *Technol Cancer Res Treat* (2014) 14:320–5. doi: 10.1177/1533034614547457
13. Parodi K, Bortfeld T. A Filtering Approach Based on Gaussian–powerlaw Convolutions for Local PET Verification of Proton Radiotherapy. *Phys Med Biol* (2006) 51:1991. doi: 10.1088/0031-9155/51/8/003
14. Frey K, Bauer J, Unholtz D, Kurz C, Kraemer M, Bortfeld T, et al. TPSPET-A TPS-Based Approach for In Vivo Dose Verification With PET in Proton Therapy. *Phys In Med And Biol* (2014) 59:1–21. doi: 10.1088/0031-9155/59/1/1
15. Mizuno H, Tomitani T, Kanazawa M, Kitagawa A, Pawelke J, Iseki Y, et al. Washout Measurement of Radioisotope Implanted by Radioactive Beams in the Rabbit. *Phys Med Biol* (2003) 48:2269–81. doi: 10.1088/0031-9155/48/15/302
16. Jakoby BW, Bercier Y, Conti M, Casey ME, Bendriem B, Townsend DW. Physical and Clinical Performance of the mCT Time-of-Flight PET/CT Scanner. *Phys In Med And Biol* (2011) 56:2375–89. doi: 10.1088/0031-9155/56/8/004
17. Shepp LA, Vardi Y. Maximum Likelihood Reconstruction for Emission Tomography. *IEEE Trans Med Imaging* (1982) 1:113. doi: 10.1109/TMI.1982.4307558
18. Hudson HM, Larkin RS. Accelerated Image Reconstruction Using Ordered Subsets of Projection Data. *IEEE Trans Med Imaging* (1994) 13:601–9. doi: 10.1109/42.363108
19. Zhang J, Lu Y, Hsi W, Zhang J, Sheng Y, Shi L, et al. Evaluation of Proton Therapy Accuracy Using a PMMA Phantom and PET Prediction Module. *Front Oncol* (2018) 8:523. doi: 10.3389/fonc.2018.00523
20. Frey K, Unholtz D, Bauer J, Debus J, Min CH, Bortfeld T, et al. Automation and Uncertainty Analysis of a Method for in-Vivo Range Verification in Particle Therapy. *Phys Med Biol* (2014) 59:5903–19. doi: 10.1088/0031-9155/59/19/5903
21. Chen W, Bauer J, Kurz C, Tessonnier T, Handrack J, Haberer T, et al. A Dedicated Software Application for Treatment Verification With Off-Line PET/CT Imaging at the Heidelberg Ion Beam Therapy Center. *J Physics: Conf Ser* (2017) 777:12–21. doi: 10.1088/1742-6596/777/1/012021
22. Handrack J, Tessonnier T, Chen W, Liebl J, Debus J, Bauer J, et al. Sensitivity of Post Treatment Positron Emission Tomography/Computed Tomography to Detect Inter-Fractional Range Variations in Scanned Ion Beam Therapy. *Acta Oncol* (2017) 56:1451–8. doi: 10.1080/0284186X.2017.1348628

Conflict of Interest: The authors declare that the research was conducted in the absence of any commercial or financial relationships that could be construed as a potential conflict of interest.

The reviewer WH declared a past co-authorship with the authors to the handling editor.

Publisher's Note: All claims expressed in this article are solely those of the authors and do not necessarily represent those of their affiliated organizations, or those of the publisher, the editors and the reviewers. Any product that may be evaluated in this article, or claim that may be made by its manufacturer, is not guaranteed or endorsed by the publisher.

Copyright © 2021 Zhang, Lu, Sheng, Wang, Hong, Sun, Zhou and Cheng. This is an open-access article distributed under the terms of the Creative Commons Attribution License (CC BY). The use, distribution or reproduction in other forums is permitted, provided the original author(s) and the copyright owner(s) are credited and that the original publication in this journal is cited, in accordance with accepted academic practice. No use, distribution or reproduction is permitted which does not comply with these terms.

Advantages of publishing in Frontiers

OPEN ACCESS
Articles are free to read for greatest visibility and readership

FAST PUBLICATION
Around 90 days from submission to decision

HIGH QUALITY PEER-REVIEW
Rigorous, collaborative, and constructive peer-review

TRANSPARENT PEER-REVIEW
Editors and reviewers acknowledged by name on published articles

Frontiers
Avenue du Tribunal-Fédéral 34
1005 Lausanne | Switzerland

Visit us: www.frontiersin.org
Contact us: frontiersin.org/about/contact

REPRODUCIBILITY OF RESEARCH
Support open data and methods to enhance research reproducibility

DIGITAL PUBLISHING
Articles designed for optimal readership across devices

FOLLOW US
@frontiersin

IMPACT METRICS
Advanced article metrics track visibility across digital media

EXTENSIVE PROMOTION
Marketing and promotion of impactful research

LOOP RESEARCH NETWORK
Our network increases your article's readership